RUHR-UNIVERSITÄT BOCHUM

SFB 837
Interaction Modeling in Mechanized Tunneling

Chenyang Zhao

A Contribution to Modeling of Mechanized Tunnel Excavation

Bochum 2018

Heft 65

Schriftenreihe des Lehrstuhls für
Grundbau, Boden- und Felsmechanik

Herausgeber: Tom Schanz

ISSN 2190-3255

A Contribution to Modeling of Mechanized Tunnel Excavation Chenyang Zhao 65

ISSN 2190-3255

Ruhr-Universität Bochum
Schriftenreihe Grundbau, Boden- und Felsmechanik
Heft 65

Herausgeber:
Prof. Dr. -Ing. habil. Tom Schanz
Ruhr-Universität Bochum
Fakultät für Bau- und Umweltingenieurwissenschaften
Lehrstuhl für Grundbau, Boden- und Felsmechanik
44801 Bochum
Telefon: 0234/ 3226135
Telefax: 0234/ 3214236
Internet: www.gbf.ruhr-uni-bochum.de

ISSN 2190-3255

A Contribution to Modeling of Mechanized Tunnel Excavation

Dissertation

as a requirement of the degree of
Doktor-Ingenieur (Dr.-Ing.)

at the Faculty of
Civil and Environmental Engineering
Ruhr-Universität Bochum

submitted by
Chenyang Zhao
from Jiangsu, China

Reviewers
Prof. Dr. techn. Günther Meschke
Prof. David M. Potts, BSc PhD (Cantab) DSc FICE FREng FCGI
Ao.Univ.-Prof. Dipl.-Ing. Dr.techn. Helmut F. Schweiger, M.Sc.

Bochum, March 2018

This work is dedicated to my beloved parents and Jingyi

Vorwort des Herausgebers

Die vorliegende Arbeit von Herrn Chenyang Zhao entstand im Rahmen des Teilprojektes A5 "Adaptive Konstitutivbeschreibung des Baugrundes unter besonderer Berücksichtigung der Destrukturierung" des SFB 837 "Interaktionsmodelle für den maschinellen Tunnelbau". Dieses Projekt und damit auch die Arbeit von Herrn Zhao wurde von Prof. Tom Schanz initiiert und geleitet. Prof. Tom Schanz verstarb am 12. Oktober 2017 völlig unerwartet vor Fertigstellung der Arbeit. Am Abschluss der Arbeit hatten Frau Dr. Maria Datcheva und Herr Dr. Arash Lavasan entscheidenden Anteil.

Der maschinelle Tunnelvortrieb ist ein komplexer Vorgang, in dem, neben den Bodeneigenschaften, verschiedene Einzelprozesse mit ihren Wechselwirkungen bestimmen, welche Beanspruchungen der Tunnelausbau erfährt und welche Auswirkungen der Vortrieb im Boden in der Umgebung des Tunnels und an der Oberfläche in Form von Setzungen hat. Die Bodeneigenschaften im Bereich des Tunnelvortriebs variieren und auch bei umfänglicher Erkundung bleiben Unsicherheiten bezüglich der Bodeneigenschaften. Gleichzeitig werden die Anforderungen an die Berechnungsmodelle zur Prognose von Auswirkungen des Tunnelvortriebs, insbesondere zu Setzungen immer höher. Angestrebt werden Echtzeitmodellierungen, bei welchen das verwendete Modell mit Messgrössen regelmässig abgeglichen und kalibriert wird. Dieses verlangt effiziente aber auch ausreichend komplexe Rechenmodelle. Hier setzt die Arbeit von Herr Zhao an, welche sich mit Strategien zur numerischen Simulation des maschinellen Tunnelvortriebs beschäftigt.

Zunächst zeigt Herr Zhao den Einfluss der Wahl des Stoffmodells am Beispiel von Setzungsmulden infolge Tunnelausbruchs bei Geländeoberflächen ohne und mit Bebauung berechnet mit einem 2D Modell. Weiterhin diskutiert er den Einfluss der Modellierung der Ringspaltverpressung, der Abbildung der Filtration des Mörtels in des Porenraum des Bodens und der Steifigkeitsentwicklung des Mörtels auf die mit einem 3D Modell berechneten Ausbaubeanspruchungen und Verformungen im Boden und an der Geländeoberfläche bei Böden mit unterschiedlicher Durchlässigkeit. Aus den Ergebnissen wird deutlich, dass sowohl die Wahl eines ausreichend komplexen Stoffmodells als auch die zutreffende Abbildung der einzelnen Teilprozesse des Tunnelvortriebs entscheidend für die Qualität der Berechnungsergebnisse sind.

Anschliessend wendet Herr Zhao drei innovative Modellierungstechniken auf den maschinellen Tunnelbau an. Er beschränkt den Einsatz höherwertiger Stoffmodelle auf den Nahbereich

um die Vortriebsmaschine und verwendet im Fernbereich einfache Stoffmodelle (Adaptive constitutive modeling). Im zweiten Schritt trennt er den Nahbereich als Teilmodell vom Gesamtmodell, wobei an den Rändern des Teilmodells die Reaktionen des Gesamtmodells übergeben werden (Submodeling). Im letzten Schritt ersetzt er das Gesamtmodell durch ein sogenanntes Metamodel (Hybrid Modeling). Mit dem Metamodell werden der Reaktionen des Gesamtmodells schnell berechnet, ohne die aufwändige numerische Vorwärtssimulation durchzuführen. Dieser letzte Schritt erlaubt es nun in kurzer Zeit Sensitivitätsstudien zum Einfluss einzelner Stoffparameter auf die Berechnungsergebnisse vorzunehmen, unsichere Stoffparameter anhand von Messdaten durch Rückrechnung zu bestimmen und Messprogramme zu optimieren. Hiermit leistet Herr Zhao einen eigenständigen und wertvollen Beitrag zur effizienten numerischen Simulation eines komplexen Systems.

Bochum, Juni 2018 Dr.-Ing. Diethard König

Acknowledgements

This research was carried out in the Chair of Foundation Engineering, Soil and Rock Mechanics, Ruhr-Universität Bochum. First and foremost, I would like to thank my supervisor Prof. Tom Schanz who gave me a chance to start my study in RUB and provided me a lot of precious scientific support during my research work. His wisdom and personality deeply impressed me. I will be ever grateful for his support, and am sorry that he has not lived to see me graduate. His memory will be with me always.

I would like to thank Prof. Günther Meschke for his continuous support on my PhD work when Prof. Schanz' life was taken prematurely.

I gratefully thank Prof. David M. Potts (Imperial College London) and Prof. Helmut F. Schweiger (Graz University of Technology) for acting as reviewers of my thesis. Their critical and constructive comments significantly improved this work.

My sincere gratitude also goes to Dr. Arash Lavasan and Prof. Maria Datcheva (Bulgarian Academy of Sciences) for their continuous help and lots of constructive suggestions during my research work, which guides me through the long academic puzzlement to a sudden enlightenment.

Thanks go to Prof. Andrew Whittle (Massachusetts Institute of Technology) for giving me the opportunity to join his team for my research visit. It has been an invaluable experience and highly motivated me for my further research.

I gratefully acknowledge the chance to be part of the Collaborative Research Center SFB 837 and learning about all aspects of mechanized tunneling from the greatest teachers together with many inspiring colleagues. Thanks for the excellent interactions. I also would like to appreciate the financial support by the China Scholarship Council during my PhD study.

I would give my warm gratitude to my colleagues in RUB who provide me so much help in my work and life. Especially the "A5-C2" group in the tunneling project where I learned a lot from the great teamwork, and the "Mittagspause" group where I enjoyed and got used to the life in Germany. I would like to say a big "thank you"! The years in RUB are the most meaningful time in my life so far. The precious experience with them has rooted in my mind forever.

Last but not least, I sincerely thank my family and friends for their endless love and amazing support during my PhD study. Infinite thanks to my beloved Jingyi for her love, support, understanding and being always by my side.

Bochum, March 2018 Chenyang Zhao

Abstract

The goal of this research is to investigate the effects of sub-systems during mechanized tunnel excavation via numerical analyses and to develop the advanced process simulation techniques for the purpose of optimization of the computational costs during numerical simulation.

In the first part of this thesis the influence of the most important sub-systems (face support, tunnel volume loss, tail void grouting, lining installation and progressive excavation) on the system behavior, e.g., ground movements, pore water pressures, lining forces and deformations, is investigated. Special attentions are paid to the tunneling induced volume loss at the ground surface that may endanger the existing buildings. The components of the surface volume loss are studied and modification of the empirical Gaussian distribution curve which is widely used to describe the settlement trough is proposed. By taking into account the tunnel advance speed and soil's permeability, different hydro-mechanical coupling (consolidation) analysis schemes are introduced for numerical simulation of tunnel excavation in saturated soil. Furthermore, the effects of grout features in the near field around the tunnel, namely grout hardening induced stiffness evolution and grout infiltration induced permeability evolution, are investigated.

In the second part of this thesis three advanced process simulation techniques are introduced for numerical simulation of tunneling process. Adaptive constitutive modeling aims to adequately describe the soil behavior in different sub-domains of the model by assigning appropriate constitutive models. The objective of submodeling is to cut a region of interest from the initial global model and to continue the following simulation in this small scale model only. Furthermore, hybrid modeling is proposed to combine the capacity of the process-oriented submodeling to accurately describe the complex tunneling induced system behavior with the computational efficiency of metamodel (or surrogate model). This approach is a powerful tool for parametric study (e.g., soil parameters identification and tunneling process parameters optimization). By using these approaches, the computation costs of tunneling simulation are saved and these methods benefit the design of experiments.

Finally two tunnel case studies are conducted to validate the aforementioned methodologies, it is shown that the validated numerical model is very well capable to predict the tunneling induced system behavior, and the sensitivity field is a powerful tool for design of optimal sensor location.

Contents

List of Figures

List of Tables

Nomenclature

β, κ	Material parameters during infiltration analysis
β_i	Normalized sensitivity information at each point
Δ	Differential displacement
η	Dynamic viscosity
γ_s	Unit weight of slurry
$\gamma_{0.7}$	Shear strain level at which shear stiffness degrades to 70% of initial value
$\gamma_{\text{unsat}}, \gamma_{\text{sat}}$	Unsaturated and saturated unit weight of soil
κ^*	Modified swelling index
λ^*	Modified compression index
μ_e	Safety factor for earth force
μ_w	Safety factor for water pressure
ν	Poisson's ratio
ν_{ur}	Poisson's ratio during unloading and reloading
ϕ	Porosity
ψ'	Dilation angle
ρ	Density
ρ^*, α^*	Realtive bending and axial stiffness
$\sigma'_1, \sigma'_2, \sigma'_3$	Effective principle stresses

σ_h, σ_v Horizontal and vertical stresses

COV Coefficient of variance

OCR Over consolidation ratio

θ Lode angle

φ' Effective friction angle

A Section area

A_1, A_2, B_1, B_2 Fitting parameters for modification of the empirical method

c Local concentration of fines

c' Cohesion

D Tunnel head diameter

d Lining diameter

E Young's Modulus

E_s Soil secant stiffness

E_{50}^{ref} Sceant primary triaxial loading stiffness

E_{oed}^{ref} Tangential oedometer loading stiffness

E_{ur}^{ref} Elastic uloading/reloading stiffness

G Shear modulus

G_0^{ref} Initial shear modulus at small strain

I Second moment of area

I_1' First invariant of stress

i_z Horizontal distance from tunnel center line to the inflection point

J_2 Second invariant of stress

K Bulk modulus

k^{f} Permeability

K_0 Coefficient of lateral earth pressure at rest

K_s Subgrade modulus of the spring between lining and soil

K_z Model parameter of settlement trough

L, H, B Length, height and width of the structure

M Storage modulus

m Exponent power for non-linear stiffness

$M^{DR,\mathrm{sag}}, M^{DR,\mathrm{hog}}$ Modification factor for sagging and hogging

N, M, u_r Axial forces, bending moments and radial displacements of lining

$n^{\mathsf{sa}}, n^{\mathsf{sn}}, n^{\mathsf{a}}, n^{\mathsf{f}}$ Volume fraction of four constituents

p Fluid pore pressure

p' Effective mean stress

p^{ref} Reference pressure

q Deviatoric stress

r Raduis of the tunnel

R_f Failure ratio

R_s Surface volume loss ratio

R_t Tunnel volume loss ratio (contraction factor)

R_{int} Reduction factor of interface properties

S Average settlement of the building

S_e Effective earth force at tunnel face

S_f Total force applied on the tunne face

S_i First order index

S_w Water pressure at tunnel face

$S_{\max}$ Maximum settlement

$s_{\text{stiffness}}$ Grout hardening parameter

$s_{d,\text{crown}}$ Slurry force at tunnel crown

S_{Ti} Stotal effect index

SA_i Sensitivity information at each point

W Strain energy

V_g Soil volume change

V_s Surface volume loss

V_t Tunnel volume loss

V_{exc} Notional excavation volume

V_{lining} Final lining volume

X Horizontal distance between center lines of tunnel and building

Y Tunnel overburden depth

Z_0 Depth of the tunnel center

1 Introduction

1.1 Motivation and objectives

Due to the growing population in the urban areas, an efficient and economic infrastructure is required for the improvement of both the mobility in the cities and the quality of urban life. Nowadays, mechanized excavation using Tunnel Boring Machine (TBM) has become a popular method to utilize the underground space for traffic infrastructure, and it offers the possibility to efficiently control traffic related emissions. The impact of the tunnel construction process on the surrounding underground has to be kept minimal due to the presence of sensitive and valuable surface and sub-surface constructions. Shield supported tunnel construction is an appropriated way to fulfill these requirements. Fig. 1.1 shows the illustration of a typical slurry shield TBM, and there are many sub-systems involved during tunneling process. The tunnel face is excavated by a cutting head and the machine advances by jacks reacting on the installed lining segments. In the chamber behind the cutting head, bentonite slurry and excavated residual are respectively used for slurry-shield TBM and earth-pressure-balance TBM to avoid the collapse of the soil in front of TBM. The lining segments are installed as the permanent structure to support the excavated tunnel. Since the volume loss around the tunnel is induced by the overcut zone and conicity of TBM, grout is injected in the annular gap between the lining segments and surrounding soils to compensate the surface settlements.

In order to provide reliable predictions of the system behavior in the tunneling process, numerical simulation approach, such as Finite Element (FE) method, has been widely applied. In the numerical model, the aforementioned sub-systems should be considered in a reasonable manner.

- Tunneling induced ground movements

Tunnel excavation inevitably induces deformation in the soil domain around the tunnel and changes the stress distribution. As a result, the change of stresses and deformations propagates up to the ground surface and form a surface settlement trough which may

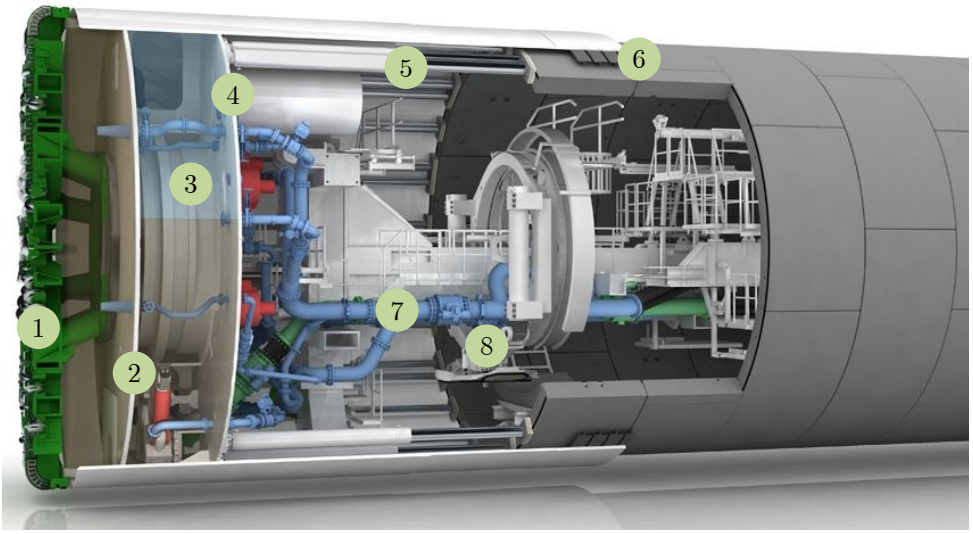

Figure 1.1: Illustration of a typical slurry shield tunnel boring machine: (1) cutting wheel, (2) submerged wall, (3) air cushion, (4) bulkhead, (5) thrust cylinders, (6) tail void grouting, (7) slurry circuit, (8) erector (Source: Herrenknecht AG)

consequently endanger the existing buildings. Therefore, it is essential to develop a platform that can accurately predict the system responses during tunnel excavation, and to evaluate the relation between ground deformations and correlated factors affecting the magnitude, orientation and location of the surface displacement profiles. Since there is rare studies to evaluate the influence of tunnel volume loss on surface volume loss, this research aims to evaluate the components of surface volume loss and to obtain a general correlation between them. In the numerical simulation, uncertainty of model response is generated due to the propagation of input parameters uncertainty, assumptions used in the constitutive model, etc. It is necessary and valuable to evaluate how the uncertainty of model response can be correlated to the uncertainty of input parameters. Within this framework, sensitivity analysis is conducted to distinguish the relative importance of the influencing factors in determining the ground movements and adjacent building's behavior. Furthermore, the sensitivity distribution can be utilized in the entire domain to gain the knowledge for optimum monitoring concept.

- Hydro-mechanical coupled analysis

In the numerical simulation of tunnel excavated below the water level, hydro-mechanical coupling (consolidation) analysis is essential. By taking into account the TBM advance rate and soil's permeability, different consolidation schemes can be developed and their effects on the model responses are evaluated in this research. Furthermore, when the grout

is injected in the annular gap, fine particles in the suspension move under the influence of grouting pressure. This phenomenon is called infiltration. When the fines flow into the surrounding soil, porosity of the soil may decrease. As a result, the permeability and viscosity of soil changes and this highly affects the consolidation process of the system. However, the effect of infiltration in tunneling simulation is normally not considered. Due to this reason, this study aims to consider the effects of infiltration in conjunction with grout hardening during consolidation analyses.

- Advanced process simulation

In 3D tunneling simulation, the numerical model is created to be large enough to avoid the influence of boundary effect. As the sequential excavation method is employed to simulate the tunneling process, the steady-state solution with a constant shape of the settlement trough is only reached after many steps of excavation. Consequently, the simulation of the FE-model is extremely computational cost consuming. Furthermore, when sophisticated constitutive model is applied to describe the soil behavior, it may need smaller time steps and elements that will make the convergence difficult, even questionable. In order to provide a model that is robust, representative and cost-economy for explaining the complex behavior in the near field of the tunnel, advanced process simulation techniques are developed.

Since there are many parameters involved in the sophisticated constitutive model, on the one hand, it is expensive and even impossible to obtained these parameters via laboratory and in-situ tests. On the other hand, in the process of parameter identification, uncertainties are inevitably embedded in these model parameters. Due to these reasons, the idea of adaptive modeling is to apply most appropriate constitutive models in the most relevant sub-domains to describe the soil behavior with the advancement of TBM. The idea of Submodeling technique is to reduce the problem to a smaller scale, by means of cutting out a local part of the large scale model. The following simulation of the tunneling problem will be conducted in the small scale model which is called submodel. As the complex soil behavior is observed in the near field, it is necessary to apply sophisticated constitutive model to describe the soil behavior in the local zone of interest. While for the global model, basic soil constitutive model can be applied to describe the system behavior. By adopting these advanced process simulation techniques, the computational cost of the numerical simulation is reduced. Furthermore, this approach can be used to guide the experimental/in-situ tests that are conducted to obtain the constitutive parameters.

1.2 Contents of the thesis

This thesis consists of eight chapters, of which the contents can be briefly summarized as:

- Chapter 1: Introduce the motivation, objectives and the organization of this thesis.
- Chapter 2: Present a literature overview on the mechanized tunnel excavation techniques and corresponding numerical simulation methods. The influence of tunneling excavation on the ground movements and advanced process simulation techniques are discussed as well.
- Chapter 3: The general description of the finite element model and numerical simulation method used in this research are introduced.
- Chapter 4: Components of the tunneling induced surface volume loss are studied. The numerical results are analyzed to improve the empirical method which is used to predict the tunneling induced surface settlement trough. In the case where there is building located on the ground surface, the influence of soil-tunnel-building system characters on the settlements and tilt of building is evaluated.
- Chapter 5: Numerical simulation of mechanized tunnel excavation in saturated soil is conducted. Special attention is paid to the hydro-mechanical coupling analysis in the near field around the tunnel.
- Chapter 6: Advanced process simulation techniques for tunneling simulation are proposed and the corresponding methodologies are explained.
- Chapter 7: Two case studies of Western Scheldt tunnel and tunneling model tests are conducted for model validation via back analysis and design of optimal sensor locations, respectively.
- Chapter 8: Based on the works in this study, conclusions are drawn and the works in the next step are suggested.

2 State of the art

2.1 Introduction of mechanized tunnel excavation techniques in soils

There is a basic distinction between conventional tunneling methods and mechanized tunnel excavation techniques. The conventional tunneling can be defined as the construction of underground openings of any shape with a cyclic construction process composed of the following steps (ITA 2009): (1) excavation, (2) mucking and (3) placement of the primary support elements. The Conventional tunneling methods mainly use standard equipment and allow access to the tunnel excavation face at almost any time, which is very flexible in situations or areas that require a change in the structural analysis or design. In fact, the conventional tunneling allows a very flexible process where many changes can be easily applied during construction (e.g., variation of ring closure time, increase or decrease length of excavation, ground treatment according to the geological conditions, etc.). In contrast, mechanized tunneling are all the techniques where excavation is performed mechanically by means of different machines. These machines not only carry out the excavation of the ground, they also provide support against the surrounding soils. In comparison with the conventional tunneling methods, on the one hand, the advantages of mechanized tunnel excavation techniques can be summarized as follows (ITA 2001): (1) enhanced health and safety conditions for the workforce, (2) industrialization of the tunneling process, (3) possibility of crossing complex hydro-geological conditions, and (4) good quality of the finished products. On the other hand, mechanized tunneling has drawbacks as well, such as lack of flexibility, difficult application to unexpected geological conditions, not economically optimized for short tunnels and time-consuming for the machine installation.

The mechanized tunneling can be divided into two types, namely open face tunneling and closed face tunneling. Open face construction of tunnels involves tunneling methods without applying permanent support to the tunnel face. While for closed face tunneling, face support such as a pressurized slurry, earth pressure balance or compressed air, is

continuously applied to avoid the collapse of soils. The author is aware of the fact that there are many more tunneling methods than the ones mentioned above. However, for the sake of convenience, this thesis mainly focuses on these basic tunneling methods.

2.1.1 Open face shield tunneling

As the name suggests, the shield simply provides within a tunnel a working area which is protected against the collapse of soil in that section which has been recently excavated, and in which no tunnel lining or other means of support have been installed. Obviously, when tunnel is been driven through stable ground, no shield is necessary. Open face shield tunneling was firstly introduced by Marc Isambard Brunel, who built the Thames tunnel in London (1825-1843) using a rectangular shield construction. The shield was made of cast-iron and the tunnel lining was a bricklayer construction. Thames tunnel was advanced by means of screw jacks which thrust against the finished masonry of the tunnel. Cast-iron lining advocated by Brunel in the 1818 patent was not utilized in Thames tunnel, this is probably due to the fact that a rectangular tunnel was decided upon and almost a necessary consequence a masonry tunnel was preferred to a cast-iron one (Stack 1982). Although Brunel was the first to suggest using a circular shield, J.H. Greathead designed and built a circular shield for the construction of new Thames tunnel (1869-1870). Of interest are the main differences between Brunel's old tunnel and Greathead's first tunnel (Stack 1982). Brunel's tunnel brickwork is 11.2 m wide by 6.8 m high, Greathead's tunnel consists of an iron tube of 2.0 m in diameter. The old tunnel was constructed within a shield weighting 109 t and accommodating 36 workmen, while the new tunnel was driven by a shield weighting 2.3 t and accommodating at most 3 workmen at a time. Since the new tunnel was finished in less than one year, its cost was only 1/30 of the old tunnel. Because of the statically favorable shape of a circular tunnel, the circular shield with the installation of lining segments became the archetype of modern shield tunneling (Möller 2006).

Shield tunneling is particular well suited for tunnel construction in soft grounds which need continuous radial support. The shield has to be designed to be able to bear all ground and working load within allowable deformations. It is usually made of thick steel plates at its front, to transfer the high axial working forces of the jack from the lining to the ground. The tail of shield is not as thick as the shield front, this is because that only radial ground load applies on the shield. For the advancement of the TBM shield, the diameter of shield tail is usually smaller than that of shield front, which is call conicity shape of TBM shield. The inner shield diameter is larger than the outer diameter of tunnel lining,

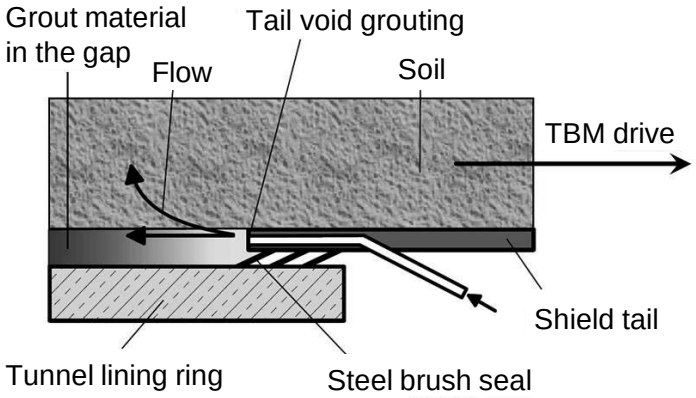

Figure 2.1: Schematic illustration of tail void grouting

which enables the installation of precast lining segments. Due to the different diameters of lining and shield, an annular gap is remained between the newly installed lining and surround soil. The schematic illustration of tail void grouting is shown in Fig. 2.1. Grout mortar is usually injected in the annular gap to compensate the soil deformations. The sealing consists of steel brushes filled with grease. The advancement of tunnel is achieved by the jacks installed in the TBM shield which push the shield away from the installed lining segments.

As mentioned before, open face shield tunneling is used when the geological condition is fairly good and has enough stand-up time for at least one cycle. An unstable tunnel face can be improved by applying steel plates that are connected to hydraulic jacks to provide a certain amount of face pressure. On the one hand, when the support from the machine cannot meet the balance of the soils in front of the tunnel, the soils may roll into the shield and the ground movements and adjacent building will be significantly influenced. On the other hand, when the tunnel is excavated below the initial ground water level, the ground water level should be lowered for open face shield tunneling or using ground freezing technique. Due to these reasons, closed face shield tunneling methods are developed to overcome the deficiencies of open face shield tunneling.

2.1.2 Closed face shield tunneling

Closed face shield tunneling is used when the geological condition is so unfavorable that the tunnel face becomes unstable without instant application of support pressure. Balance between acting earth pressure and resisting support pressure is essential. To prevent the

undesirable collapse of soils, not only maintenance of equipment and detailed geological investigation, but also the application of proper support pressure on the tunnel face are required. Depending on the ground conditions, the face support can be categorized into four types as following:

- Mechanized support

In this case, the cutting wheel itself provides the required face support. Although the pressure applied in mechanical support is more or less continuous, this method is only suitable for predominantly stable cohesive grounds above the ground water level.

- Compressed air

In compressed air closed shields the rotating cutting wheel acts as the means of excavation whereas face support is ensured by compressed air at a sufficient level to balance the hydrostatic pressure of the ground. These machines are specially suited for excavation in unstable soil with medium to low permeability levels, where water is present. Higher permeability can be reduced locally by injecting bentonite slurry onto the excavation face.

- Earth Pressure Balance (EPB) shield

EPB shield is used for the excavation of soils where face support and counter-effect of ground water pressure are obtained by means of the material excavated by the cutting wheel, which serves as support medium itself. This kind of TBM is used to excavate grounds with limited or self-supporting capacity. In granulometric terms, EPB shields are mainly used for excavating in silts or clays with sand (ITA 2001).

- Slurry shield

Slurry shields are TBM fitted with a full face cutterhead which provides face support by pressurizing boring fluid inside the chamber. The suspension is pumped into the excavation chamber where it reaches the face and penetrates into the ground forming the filter cake, or the impermeable bulkhead (fine ground) or impregnated zone (coarse ground) which guarantees the transfer of counter pressure to the excavation face. This kind of TBM is most suited for tunnels through unstable ground subjected to high groundwater pressure or water inflow that must be stopped by supporting the face with a boring fluid subjected to pressure. In granulometric terms, slurry shields are mainly suitable for excavation in sand and gravels with silts (ITA 2001).

2.2 Introduction of numerical simulation techniques for tunneling

With the significant development in the computational technology, nowadays numerical analysis is becoming more and more popular for simulation of mechanized tunnel excavation in both engineering practice and academic research. The related studies can be found in Potts & Zdravković (2001); Pickhaver (2006); Möller & Vermeer (2008); Zhao et al. (2015); Ninić & Meschke (2017). There are rare projects that are carried out without the support of numerical analyses. However, it should be noted that numerical analysis as a design tool for tunneling projects was often criticized in 1960s (Möller 2006). There is no doubt that the empirical and analytical solutions are efficient and convenient for the preliminary study. Whereas nowadays more reliable predictions of the system behavior due to tunnel excavation are required for the purpose of optimum design and safety. These cannot be achieved by the traditional engineering experience, intuition and analytical methods where a large amount of simplifications are adopted. In contrast, the numerical modeling methods provide a good opportunity to simulate the tunnel excavation process and soil-tunnel interaction behavior in a realistic manner. Furthermore, the parametric study which can be applied to improve the design can be easily conducted within numerical analysis, identification of the system through different likely scenario can be carried out as well. Generally, the available modern numerical tools include Finite Element Method (FEM), Finite Difference Method (FDM), Distinct Element Method (DEM), etc. Different approaches have their own advantages and disadvantages (Shah et al. 2017). In this thesis, attention will be paid to the FEM of mechanized tunnel excavation. Overall the proper use of numerical tools requires sufficient background knowledge in both geotechnical engineering and understanding of numerical method itself. Within this framework, the following sections introduce the key aspects in tunneling simulation.

2.2.1 Soil constitutive models

Constitutive model is applied to describe the soil behavior during mechanized tunnel excavation, which dominates the system behavior. Although a large number of constitutive models have been developed, the majority are predominantly used for research-oriented purpose (Surarak 2010). In this section, five constitutive models that are widely applied in tunneling simulation are demonstrated, namely Linear Elastic (LE) model,

Mohr-Coulomb (MC) model, Soft Soil (SS) model, Hardening Soil (HS) model and Hardening Soil with small strain stiffness (HSS) model.

- Linear Elastic (LE) model

In LE model, the material is assumed to be elastic and stiffness is constant with the variation of stress/strain. Two model parameters, namely Young's modulus (E) and Poisson's ratio (ν), are used. Since the realistic soil behavior is highly non-linear and irreversible. LE model is usually insufficient to capture the essential features of soil. While it is valuable to validate the numerical simulation model using LE model based on the analytical solution where soil domain is considered as an elastic material.

- Mohr-Coulomb (MC) model

MC model is one of the most broadly referred constitutive models that offers reasonable results for frictional soils (Vakili et al. 2013). This linear elastic-perfectly plastic model is relevant for simple stress paths. Vermeer & de Borst (1984) indicated that this model exhibits fairly accurate stress-strain variation for granular material. However, the post-failure volume changes may become inconvenient when the plasticity launches with achieving the failure envelope. Additionally, a single constant stiffness (e.g., stress and strain independent) has been adopted to model for all load cases (e.g., loading, unloading and reloading) which can result in questionable results for complex stress paths and large domains with wide range of stress variation. Accordingly, although the basic MC model is sufficient for stability analysis which deals with shear strength of frictional soil, it is essentially inadequate for the problems consist of deformation analysis or cyclic loading.

The soil behavior in MC model is defined by five parameters, i.e. Young's modulus (E) and Poisson's ratio (ν) for material elasticity; and effective friction angle (φ'), cohesion (c') and dilation angle (ψ') for plastic range. The volume changes and the rate of plastic strain variation are controlled by a non-associated flow rule where the potential surface is defined by dilation angle. Despite the deficiencies of MC model for many geotechnical application, the model is popularly adopted in practice due to the straightforward parameter determination process through laboratory tests (e.g., direct shear test and triaxial test). Although, measurement of the parameters and numerical calculation based on MC model are rather straightforward, it may lead to questionable results for complex loading conditions.

The MC yield surface (f) can be introduced in terms of the stress invariants and Lode angle as follows (Zienkiewicz & Humpheson 1977):

$$f = \sqrt{J_2} + \frac{m(\theta_l, \varphi') \cdot \sin\varphi'}{3} I_1' - m(\theta_l, \varphi') \cdot c' \cdot \cos\varphi' = 0 \tag{2.1}$$

$$I_1' = (\sigma_1' + \sigma_2' + \sigma_3') = 3p' \tag{2.2}$$

$$\sqrt{J_2} = \sqrt{\frac{1}{6}[(\sigma_1' - \sigma_2')^2 + (\sigma_2' - \sigma_3')^2 + (\sigma_1' - \sigma_3')^2]} = \frac{q}{\sqrt{3}} \tag{2.3}$$

$$\theta = \tan^{-1}[\frac{1}{\sqrt{3}}(\frac{2\sigma_2' - \sigma_1' - \sigma_3'}{\sigma_1' - \sigma_3'})] \quad , \quad (-30^\circ \leq \theta \leq 30^\circ) \tag{2.4}$$

$$m(\theta, \varphi') = \frac{\sqrt{3}}{\sqrt{3}\cos\theta + \sin\theta \cdot \sin\varphi'} \tag{2.5}$$

where, σ_1', σ_2' and σ_3' are the effective principle stresses, I_1' and J_2 respectively represent the first and second invariants of stress and p', q and θ state effective mean stress, deviatoric stress and Lode angle, respectively.

- Hardening Soil (HS) model

The Hardening Soil model (HS) proposed by Schanz (1998) and Schanz et al. (1999) is an appropriate model to simulate the mechanical behavior of soft and stiff soils. The shear failure in this model obeys Mohr-Coulomb failure criterion while the plasticity is governed by a double hardening law that acts on a cone-cap yield surface. In contrast to MC model, the yield surface of HS model can be isotropically expanded due to plastic straining. In the plastic range, the variation of the yield surface f is controlled by deviatoric and volumetric hardening rules, which can be seen in Fig. 2.2. Here $\tilde{q}$ is a similar deviatoric stress quantity as defined for the cap yield surface in HS model: $\tilde{q} = \sigma_1' + (\alpha - 1)\sigma_2' - \alpha\sigma_3'$, $\alpha = (3 + \sin\varphi')/(3 - \sin\varphi')$. For the deviatoric hardening section, a non-associated flow rule is assumed where yield (f) and potential (g) surfaces are functions of friction $f(\varphi')$ and dilation $g(\psi')$ angles, respectively. It is worth mentioning that mobilized dilatancy angle (ψ_m') controls the rate of plastic strain, and ψ_m' can be expressed as a function of mobilized friction angle (φ_m') as: $\sin\psi_m' = (\sin\varphi_m' - \sin\varphi_{cv}')/(1 - \sin\varphi_m'\sin\varphi_{cv}')$, here φ_{cv}' is the critical state friction angle, and φ_m' is stress level dependent: $\sin\varphi_m' = (\sigma_1' - \sigma_3')/(\sigma_1' + \sigma_3' - 2c'\cot\varphi_p')$, where φ_p' is the failure angle. While for the volumetric hardening rule that controls the size of cap yield surface, the plastic flow is associated. Furthermore, soil deformability is described conveniently by three stress dependent stiffnesses: the secant primary triaxial loading stiffness (E_{50}^{ref}), the tangential oedometer loading stiffness ($E_{\text{oed}}^{\text{ref}}$) and the elastic unloading/reloading stiffness ($E_{\text{ur}}^{\text{ref}}$) where all these stiffnesses correspond

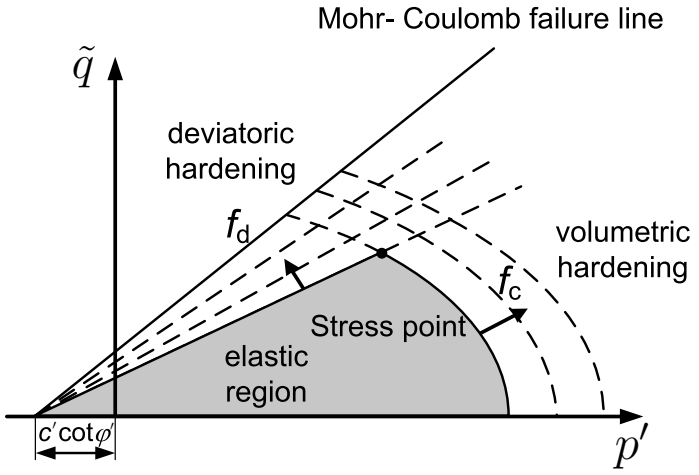

Figure 2.2: Yield surface of HS model, after Brinkgreve et al. (2014)

Table 2.1: Description of model parameters of HS model

Parameter	Description
γ_{unsat}	Unsaturated unit weight
γ_{sat}	Saturated unit weight
φ'	Effective friction angle (peak value)
ψ'	Dilatancy angle
c'	Effective cohesion
K_0^{NC}	K_0 value for normal consolidation
E_{50}^{ref}	Secant stiffness in triaxial test
E_{oed}^{ref}	Tangent stiffness for oedometer loading
E_{ur}^{ref}	Unloading-reloading stiffness
ν_{ur}	Poisson ratio
OCR	Over consolidation ratio
p^{ref}	Reference stress
m	Exponent power
R_f	Failure ratio

to reference pressure p^{ref}. The HS model parameters and corresponding description are given in Table 2.1.

Although this model is more accurate than basic MC model, a comprehensive knowledge about further advanced parameters is required. Likewise MC model, the HS model parameters can be extracted from conventional laboratory tests (i.e. triaxial and oedometer tests for non-monotonic loading). Accordingly, beside the difficulties arising from the testing procedure, the uncertainties embedded in the parameters and the cost of experimental efforts are two main concerns.

Additionally, it should be mentioned that softening behavior of material cannot be captured by HS model. The stiffness and strength in HS model are time independent, which means HS model does not account for the the creep behavior of material.

- Hardening Soil model with small strain (HSS)

Hardin & Drenvich (1972) illustrated that the soil stress dependent shear modulus is also strain dependent. Atkinson & Sallfors (1991) illustrated that the range of variation of shear strain varies for various geotechnical applications. HSS model is a modification of HS model that accounts for degradation of shear stiffness with shear strain evolution during loading (Benz 2006). In addition, the development of high small strain stiffness upon reversal loading can also be accommodated by HSS model. These aspects are addressed in the model through initial shear modulus at small-strain G_0^{ref} and the extra material threshold $\gamma_{0.7}$ (the shear strain level at which the shear stiffness degrades to about 70% of initial shear modulus). On account of these features, the HSS model provides better prediction for displacements in comparison with MC and HS models particularly under non-monotonic loading. However, complex cyclic soil lab tests at both small and intermediate strain states are on demand to measure these extra parameters.

Although the HSS model justifies the stiffness in the elements based on their strain level, the softening and creep behavior of material cannot be captured in HSS model.

- Soft Soil (SS) model

SS model has been developed within the critical state soil mechanics framework, which is similar to that of Modified Cam Clay (MCC) model. In SS model, λ^* and κ^* are respectively modified compression and swelling indices. To distinguish between reloading and the primary loading, a stress history parameter, namely pre-consolidation pressure (p_p), is adopted. This pre-consolidation pressure can be specified by the value of over-consolidation ratio (OCR). The SS model parameters and corresponding description are given in Table 2.2.

Table 2.2: Description of model parameters of SS model

Parameter	Description
γ_{unsat}	Unsaturated unit weight
γ_{sat}	Saturated unit weight
φ'	Effective friction angle (peak value)
ψ'	Dilatancy angle
c'	Effective cohesion
K_0^{NC}	K_0 value for normal consolidation
λ^*	Modified compression index
κ^*	Modified swelling index
ν_{ur}	Poisson ratio
OCR	Over consolidation ratio

The yield surface of SS model is shown in Fig 2.3. As seen, on the one hand, the ellipse shape yield surface which is similar to that of MCC model describes the irreversible volumetric strain in primary compression, and forms the cap of yield contour. On the other hand, a perfectly-plastic MC type yield function is used to model the failure state. It should be noted that the critical state parameter M does not govern the failure line. The failure line and the elliptical yield surface can be controlled separately. In comparison to HS and HSS models, the deviatoric hardening law is not considered in SS model. Consequently, less model parameters are required in SS model.

2.2.2 Sub-systems in the tunneling process

There are many sub-systems involved in the tunneling process, e.g., face support, overcut and conicity of TBM shield, jack forces, tail void grouting, lining installation, progressive excavation, TBM steering, etc. One the one hand, the numerical analysis should take into account these sub-systems for realistic prediction of the system behavior (Kasper & Meschke 2004). On the other hand, due to the complexity of the numerical model and computational cost required for modeling, simplifications should be applied to the tunneling systems (Fargnoli, Boldini & Amorosi (2015); Zhao, Lavasan, Barciaga, Hölter, Datcheva & Schanz (2014)). Therefore, it is essential to adequately simulate the most important sub-systems. In this section, four key sub-systems and corresponding simulation techniques are introduced.

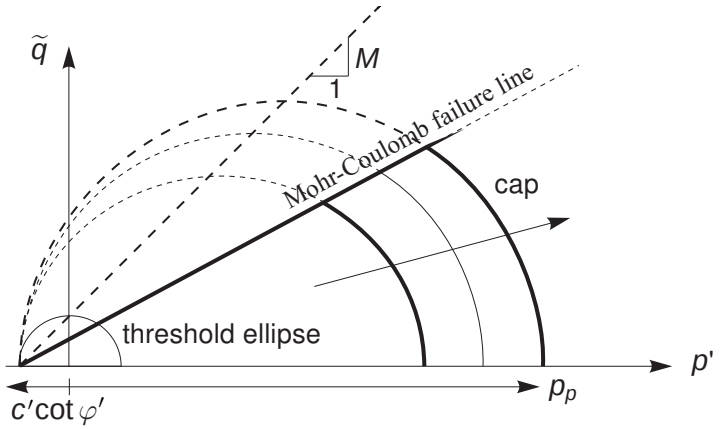

Figure 2.3: Yield surface of SS model, after Brinkgreve et al. (2014)

Face support

One of the most important objectives of mechanized tunneling is to keep the face of the tunnel stable while the flow of ground water towards the cutting head is prevented. Regardless of the stabilizing method, the face pressure should be kept at a level that excavation condition is ensured (Broms & Bennermark 1967; Davis et al. 1980). Apparently, irrelevant face pressure condition can lead to either soil collapse in front of the TBM (low pressure) or blow-out and subsequent loss of support medium (high pressure). Since the range of face pressure depends on the ground condition, excavation methods and overburden pressure, different methods are proposed to design the face support system. The existing solutions mostly take into account: (a) micro stability as the stability of a single grain or an ensemble of grains at the tunnel face (Nanninga 1970; Müller-Kirchenbauer 1977; Kilchert & Karstedt 1984), (b) macro stability such as limit equilibrium analysis to assess the soil body in front of the TBM (Atkinson & Potts 1977; Anagnostou & Kovári 1994, 1996) and limit analysis approaches (Leca & Dormieux 1990; Mollon et al. 2011, 2013*a*), (c) loss of support medium which deals with blow-out failure due to high support pressure (Balthaus 1989; Mori et al. 1991; Bezuijen et al. 1996). The concept and main assumptions for some typical methods are briefly shown in Table 2.3.

Additionally, according to German code (ZTV 2012), safety factor is taken into account when determining the required face pressure. The total force applied on the TBM face can be given as

$$S_f = \mu_e S_e + \mu_w S_w, \tag{2.6}$$

with S_e the effective earth force, S_w the water pressure, μ_e the safety factor for earth force and μ_w the safety factor for water pressure. μ_e and μ_w are suggested to 1.5 and 1.05,

Table 2.3: Overview of the face support design methods

Reference	**Description**
Horn (1961)	3D model with triangular wedge
Broms & Bennermark (1967)	Empirical lower and upper plasticity 2D solution
Atkinson & Potts (1977)	Unlined cavity in dry cohesionless material
Davis et al. (1980)	Lower and upper bound limit solution of a lined tunnel
Krause (1987)	Limit equilibrium analysis using shear stress on sliding planes
Mohkam & Wong (1989)	Limit equilibrium model using a log-spiral shaped wedge via variational analysis
Balthaus (1989)	A wedge shaped body to prevent blow out
Leca & Dormieux (1990)	Conical body using upper and lower bound analyses
Mori et al. (1991)	Soil fracturing developed for normally consolidated soil
Jancsecz & Steiner (1994)	3D wedge body incorporating the soil arching effect
Anagnostou & Kovári (1994)	Wedge model for stability analysis of slurry shield tunnel
Anagnostou & Kovári (1996)	Wedge model for stability analysis of EPB tunnel
Bezuijen et al. (1996)	Soil fracturing developed for highly over-consolidated soil
Broere (2001)	Multi-layered wedge model with 2D/3D arching effect
Kim & Tonon (2010)	Numerical simulation analysis incorporating earth and water pressures with safety factor

respectively. Then the slurry force at crown of chamber can be calculated as:

$$s_{d,\text{crown}} = \frac{S}{\frac{1}{4}\pi D^2} - \gamma_s \frac{D}{2} \pm 10\,\text{kPa}, \tag{2.7}$$

with γ_s=12 kN/m^3 the unit wight of slurry and 10 kPa the control tolerance during excavation. The value of pressure increases with depth and the gradient is 12 kPa/m. To prevent the blow-out, the German code advices that face pressure at the crown of chamber should fulfill the following equation:

$$1 \leq \frac{0.9\sigma_{v,\text{crown}}}{s_{d,\text{crown}}}, \tag{2.8}$$

with $\sigma_{v,\text{crown}}$ the total vertical stress at tunnel crown.

In case of tunneling beneath the ground water level, the face support is achieved by a pressured support medium that is filled into the excavation chamber. This support medium transmits the support pressure into the soil skeleton, the inflow of ground water

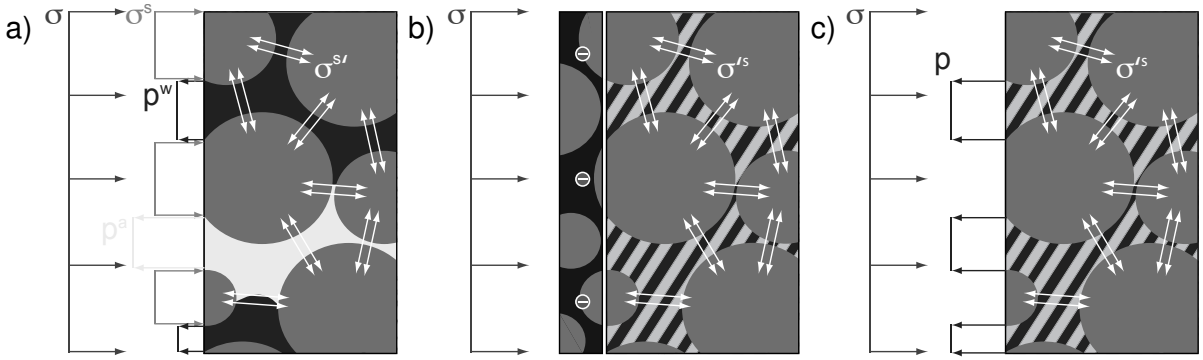

Figure 2.4: Prescribed boundary conditions at tunnel face: (a)stresses within the three-phase continua (total stress σ, effective stress σ'^s, partial soil stress σ^s and fluid pressure p^w,p^a); (b) situation for an impermeable filter cake sealing the heading face (total stress fixed and fluid flows prescribed to zero); (c) situation for no filter cake sealing the heading face (total stress and fluid pressure fixed), after Nagel (2009)

into the chamber is prevented by displacing the ground water or by establishing a filter cake to seal the heading face. Fig. 2.4 shows the boundary conditions at the tunnel face, there are two situations for the filter cake should be distinguished. One is that a perfect filter cake is formed and seals the heading face, the support pressure is applied through this filter cake onto the soil skeleton (see Fig. 2.4(b)). The other is that no filter cake seals the heading face and the support medium interacts directly with the pore fluids (see Fig. 2.4(c)). Although a filter cake can establish automatically from infiltration of the benonite suspension into the pore volume, support without filter cake may be given in certain situations. For instance, the advance in coarse soil and pores may be too large for plastering by bentonite particles. During advance of the TBM, the establishing filter cake may be excavated faster than the bentonite infiltrates into the pore volume. Subsequently, the generated excess pore pressure for the soil domain in front of the tunnel face may decrease during stand still of the machine as the filter cake re-establishes (Bezuijen et al. 2004).

According to Nagel (2009), two types of support models of modeling face pressure via FE simulation should be distinguished. One is called membrane model, where total stresses are prescribed and the fluid flows are set to zero representing the situation with a perfect filter cake. The other is called penetration model prescribing total stresses and fluid pressures for simulation of face support with a filter cake. In the numerical simulation of Möller (2006), the tunnel face support is modeled as a mechanical distributed load applied on the soil domain (total stress and the flow was not considered). This horizontal

Reference	**support pressure**	**Value [kPa]**
Broms & Bennermark (1967)	s_{min}	>93
Davis et al. (1980)	s_{min}	>136
Jancsecz & Steiner (1994)	s_{min}	>160
Anagnostou & Kovári (1994)	s_{min}	>172
Bezuijen et al. (1996)	s_{max}	<230
Lifting of soil body	s_{max}	<255
ZTV (2012)	$s_{d,center}$	204

Table 2.4: The convenient range of the face support pressure for the tunnel in present study (s_{min} and s_{max} are respectively minimal and maximal designed support pressure at the depth of tunnel center line)

load increases with depth from tunnel crown towards invert, and the gradient of the face pressure equals the unit weight of the betonite slurry in the chamber. This kind of method of modeling the face support is adopted in this study during tunneling simulation.

Assume a tunnel is excavated in a saturated and homogeneous soil. The tunnel has a diameter of 8.5 m and the depth of overburden equals the diameter of the tunnel. Water level is at the ground surface. Saturated unit weight (γ_{sat}) of soil is 20 kN/m^3. Unit weight of water γ_w=10 kN/m^3 and coefficient of horizontal stress $K_0 = 1 - \sin\varphi = 0.577$.

Table 2.4 represents the required face pressure at the center of the tunnel face using different methods. As seen, the relevant minimum and maximum support pressures at the center of the tunnel are determined respectively as 93 kPa and 255 kPa. To justify the applicability of these approaches in numerical modeling, a series of analyses have been conducted to define the most appropriate face pressure which logically satisfies (i) no soil movement towards the TBM head (micro-macro collapse), and (ii) no zero effective stress ahead of the TBM (local liquefaction/instability and piping). As ZTV (2012) recommends the face pressure of 204 kPa at the tunnel center line, this distribution of face pressure is firstly applied in the simulation. It is worth to be noted that the gradient of the face pressure is assumed to be equal to 12 kPa/m based on the unit weight of bentonite.

Fig. 2.5 shows the excess pore pressure distribution and soil deformation at the tunnel face using the face pressure suggested by ZTV (2012). As seen, the soil domain below the tunnel center line may flow into the tunnel chamber due to insufficient pressure. One the one hand, this can make the excavation process convenient in reality. On the other hand, the local soil body collapse may endanger the superstructure. Furthermore,

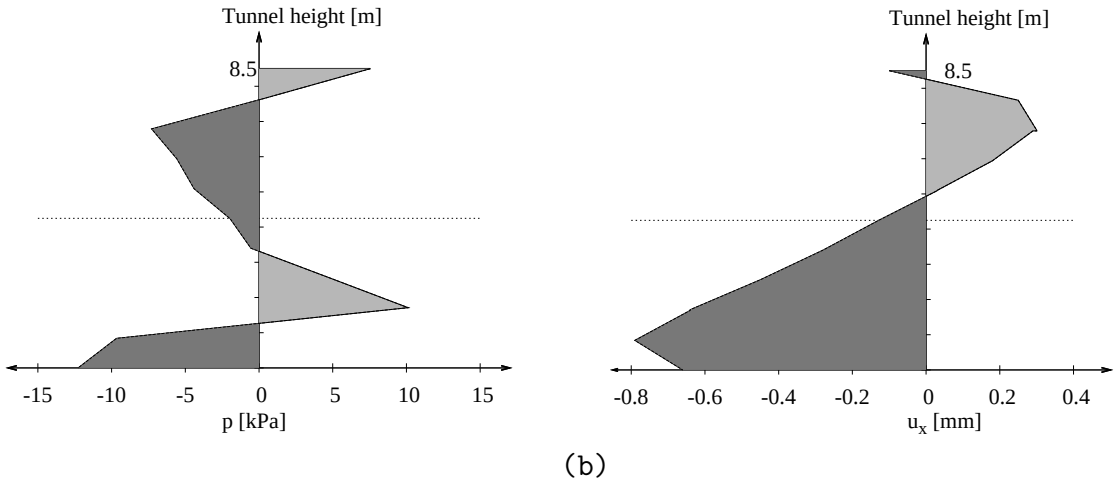

Figure 2.5: The distribution of the excess pore pressure (positive is suction) and deformation (positive is outward displacement) at the tunnel face for the face support designed based on ZTV (2012); (a) pore pressure distribution, (b) horizontal displacement

the current face pressure may result in zigzag distribution of both positive and negative excess pore pressure, this may result in convergence problem in the numerical solution. Accordingly, the face pressure has been increased by 15 kPa and the model responses in front of TBM are re-assessed. Fig. 2.6 illustrates the distribution of the pore pressure and soil deformation at the tunnel face with the modified face support pressure. As seen, the model responses are logical by acquiring uniform pore pressure distribution and no movement of the soil towards the TBM. Thus, the face support pressure in the numerical simulation of this thesis is defined in this manner.

Volume loss

In the mechanized tunnel excavation process, the ground settlement trough highly depends on the soil deformation around the tunnel. This results in a "displacement-to-displacement" kind of problem, in which the displacement field at surface is expected to be determined on the basis of the changes at extra boundary conditions in the tunnel (Sagaseta 1987). The ground deformation caused by tunneling is characterized by the term of "surface volume loss" (V_s). Möller (2006) summarized that the boundary change which induced surface volume loss in case of shield tunneling in soil can be composed of the following primary components, as shown in Fig. 2.7:

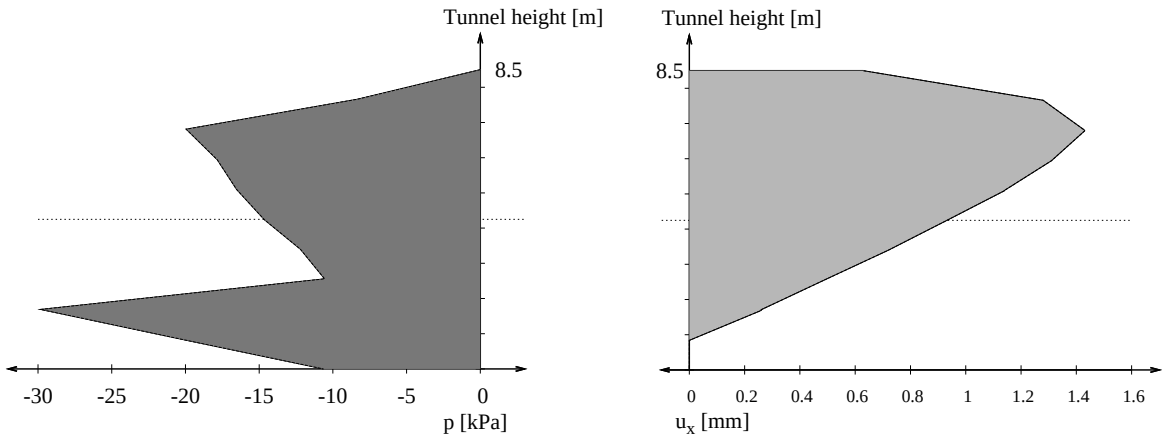

Figure 2.6: The distribution of the excess pore pressure (positive is suction) and deformation (positive is outward displacement) at the tunnel face for modified support pressure; (a) pore pressure distribution, (b) horizontal displacement

(a) Ground deformations at the tunnel face due to the unbalanced face pressure. Soil may move towards the excavation chamber as a result of excavation and relaxation ahead of tunnel face.

(b) Radial displacements around the tunnel shield, due to the overcut zone or shield conicity and self-weight, or yawing and pitching motion of the shield steering. Although bentonite mixture and grout mortar are respectively applied at tunnel face and tail void, due to the drop of flow pressure in the gap between shield and surrounding soil, soil can still move into the cavity when the soil pressure is larger than the support pressure.

(c) Radial displacements towards the tail void, due to the intermediate gap between the excavation profile and the relatively smaller diameter of lining

(d) Radial displacements of the lining segments

(e) Long term deformation of the lining segments

Apart from the above mentioned items, consolidation and creep of the grout/soil and stress redistribution in the near field around the tunnel can also trigger the variation of boundary conditions in the domain. Generally, tunnel volume loss (V_t) is defined as the difference between the final lining volume (V_{lining}) and the notional excavated tunnel volume per unit length (V_{exc}) which can be seen in Fig. 2.8. Hence, the tunnel volume

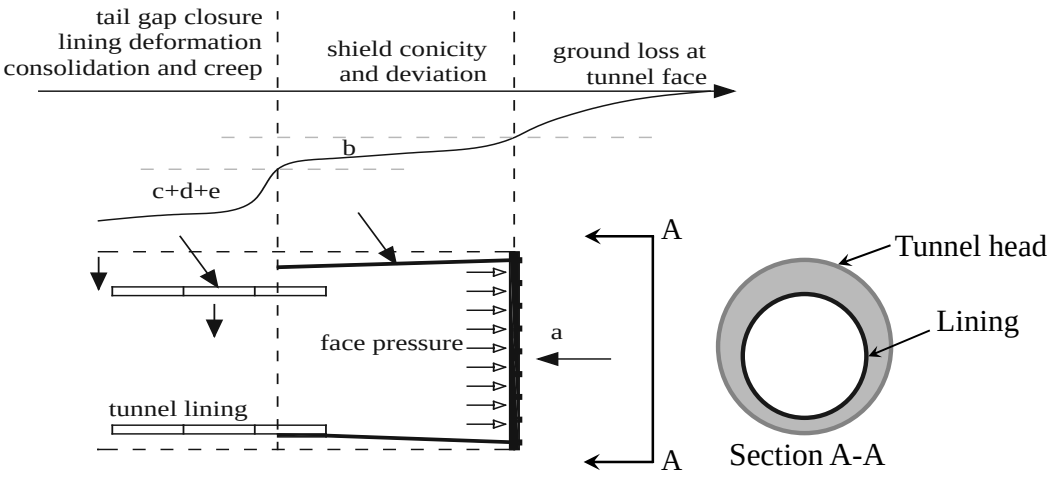

Figure 2.7: Components of surface volume loss for shield tunneling, after Möller (2006)

loss ratio (R_t) is defined as:

$$R_t = V_t/V_{\text{exc}} = \frac{V_{\text{exc}} - V_{\text{lining}}}{V_{\text{exc}}} = \frac{D^2 - d^2}{D^2} \tag{2.9}$$

where D and d are the diameters of the tunnel head and final lining segments, respectively. According to Shirlaw et al. (2004), the diameter of lining is normally 1.5% to 8% smaller than the tail of TBM shield, which is equivalent to a tunnel volume loss between 3% and 15% for full gap closure.

The surface volume loss ratio (R_s) is expressed as ratio of the surface settlement trough (V_s) and the notional excavated volume of the tunnel per unit length (V_{exc}):

$$R_s = V_s/V_{\text{exc}} = \frac{V_s}{\pi D^2/4}. \tag{2.10}$$

It should be noted that the volume of surface settlement trough is equivalent to the volume of soil on the tunnel boundary converging into the tunnel in case of tunneling in incompressible soil. To be specific, this means the Poisson ratio of soil equals 0.5, and compressibility is not assumed the inverse of stiffness. However, if tunneling is performed in compressible soil, it may be expected that $V_s > V_t$ due to compaction or $V_s < V_t$ due to dilation of the soil around the tunnel (Mair & Taylor 1997). It should be noted that both dilation and compaction can happen around the same tunnel, which depends on the position. Furthermore, V_s only captures the vertical movements at the surface boundary, while V_t captures the radial movements towards the circular lining. Both of them are not a full-picture of strain tensor, therefore their correlation is doomed to some level of imprecision.

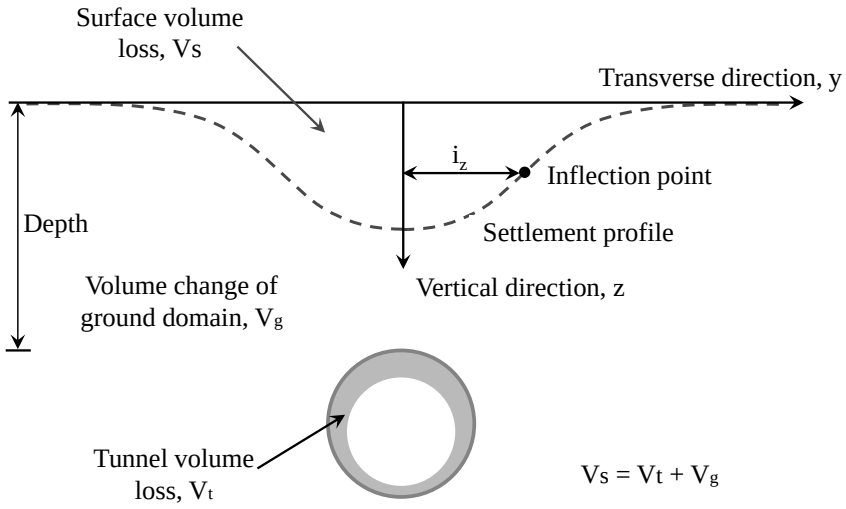

Figure 2.8: Schematic illustration of the tunneling induced volume loss in the transverse direction, after Peck (1969)

In order to model the tunnel volume loss of shield excavation, Rowe et al. (1983) proposed the first gap method. They consider the tunnel volume loss in terms of a vertical gap between lining and notional excavation boundary. Starting from initial stresses, the tunnel is excavated and the lining is installed with a certain gap at tunnel crown. The ground is unsupported and free to displace until contact to the lining is made. The shortcoming of this approach is that the gap between the lining and surrounding soil may cause numerical convergence problem due to local collapse of soil. Addenbrooke et al. (1997) apply stress reduction method and the unloading factor is replaced by a control of surface volume loss. Starting from the initial conditions, the stresses inside the tunnel are reduced stepwise and the resulting surface volume loss is calculated simultaneously. As soon as the prescribed surface volume loss is reached, the lining segments are activated. The shortcoming of this method is that the stress distribution inside the tunnel are manually modified and it might not reflect the reality of shield excavation. And it is not suitable to use one single unloading factor for precise prediction of settlements and lining forces (Möller 2006). If the surface volume loss is unknown, it is difficult to apply this method to predict the tunneling induced system behavior. Vermeer & Brinkgreve (1993) developed contraction factor method to model the tunnel volume loss. In their approach, after tunnel excavation the lining segments are directly activated. after that, the lining is stepwise contracted until its contraction factor matches a prescribed value. In numerical simulation, the contraction is introduced as the predefined volumetric strain which is not caused by any extra load. The value of contraction factor is expressed as a percentage, representing the ratio of the

area reduction and the notional excavated area. According to this definition, the value of contraction factor is identical to the tunnel volume loss ratio (R_t) when the lining deformation induced tunnel volume loss is excluded. The contraction factor technically aims at simulation of local soil deformations due to the partial collapse of soil in the overcut zone to fill the intermediate gap between the lining and excavation boundary. The shortcoming of this method is that the soil around the tunnel is forced to deform according to the prescribed value, this might not reflect the reality. For example, tunnel excavation induced heave at tunnel invert might be overestimated by using contraction method.

Lavasan & Schanz (2017) studied the influence of the different methods that can be applied to numerically simulate the tunnel volume loss on the model responses. Their results indicates that each of those methodologies has their specific limitations, advantages and deficiencies. Accordingly, decision on the numerical simulation method should be taken with a careful attention to the desired outputs of the numerical model.

Tail void grouting

As mentioned in the previous section, the outer diameter of lining segments is less than the inner diameter of tunnel shield. Therefore, a gap is formed between the lining and surrounding soil after TBM shield passes the observation section. Due to this reason, the grout mortar is injected in the annular gap to compensate the soil deformation. Dias & Bezuijen (2015) explained that the process of tail grouting can be understood as a volumetric problem. Once the TBM advances, it leaves behind a gap between the soil, which is previously supported by the shield, and the lining ring that was newly installed. Within this framework, by injecting a volume of grout equal to the volume of the gap, soil convergence can be avoided. However, the logic fails whenever the ground deforms faster than the process of grout injection, especially when the grout is still fluid. They pointed out that the focus has to change from controlling the injected volume to keeping the gap pressurized.

The grout materials can be categorized into two groups, namely single component grout and two-component grout. The first is formed by mixing mainly cement, fly-ash, sand, bentonite and water. It is an active mixture with a low fluidity and the grout mixture is filled into tail void by pressurizing of the injection pump. The stiffness and strength of the grout mixtures increases with time due to cement hydration. The following equation is widely applied to simulate the time dependent stiffness $E(t)$ of the grout (*CEB-FIP*

model code 1990; Schweiger 2014):

$$E(t) = E_{28}\left[\exp\left(s_{\text{stiffness}}(1-\sqrt{\frac{t_{28}}{t}})\right)\right]^{0.5} \quad \text{for } t \leq t_{28}, \tag{2.11}$$

where t_{28} is the time at 28 days in the corresponding time units, the cement parameter $s_{\text{stiffness}}$ controls how fast the stiffness increases with time, usually taking a value smaller than 1. This kind of time dependent stiffness for grout mixture has been applied in many tunneling problems (Schweiger et al. 2014; Saurer et al. 2014; Paternesi et al. 2016). Normally the stiffness and strength of the grout material is not generated for the first several hours after injection. Therefore, it is reasonable to assume that the grout has a constant low value of stiffness in that period. While it can reach high values (15-20 MPa at 28 days) of mechanical strength, even if it is not really necessary for good back-filling. It should be noted that this type of grout mixture is very negatively influenced by variations in its ingredients, which may result in pipes choking (Thewes & Budach 2009).

For the two-component grout material, the first component consists of mainly cement and bentonite and second component is accelerator based on sodium silicate. These two liquids are pressurized with the injection pumps separately and mixed at the injection point in the tail void. The mix gels a few seconds after the addition of the accelerator (normally 10-12 seconds, during which the TBM advances approximately 10-15 mm according to Peila et al. (2011)). The gel exhibits a thixotropic consistency and starts developing mechanical strength almost instantaneously. Peila et al. (2011) and Peila et al. (2015) conducted tests on hardening process of the grout mixture and plotted the increase of uniaxial compressive strength with respect to curing times. It is found that compressive strength varies from approximately 0.1 to 1 MPa at early stages, and the value is greater than 4.5 MPa after 120 days. Furthermore, the grout material initially corresponds to a fluid (Poisson's ratio is close to 0.5), and progressively hardens, reducing the Poisson's ratio and increasing the elastic stiffness. Within this framework, Shah et al. (2016) conducted numerical simulation of tunnel excavation with time dependent hardening behavior of two-component grout. The elastic stiffness $E(t)$ and Poisson's ratio $\nu(t)$ are determined as:

$$E(t) = E_{28}\left(1-e^{\alpha_s t}\right), \nu(t) = 0.5-(E(t)-6K(t)), \text{ for } t \leq t_{28}, \tag{2.12}$$

where α_s controls how fast the stiffness increases with time, $K(t)$ is the bulk modulus at time t. It should be noted that these equations are validated based on the experimental results of Peila et al. (2015).

The grout materials is a kind of mixtures of a liquid (mostly water) and small particles (fines) floating within the fluid. Under the effect of grouting pressure, the fines may move

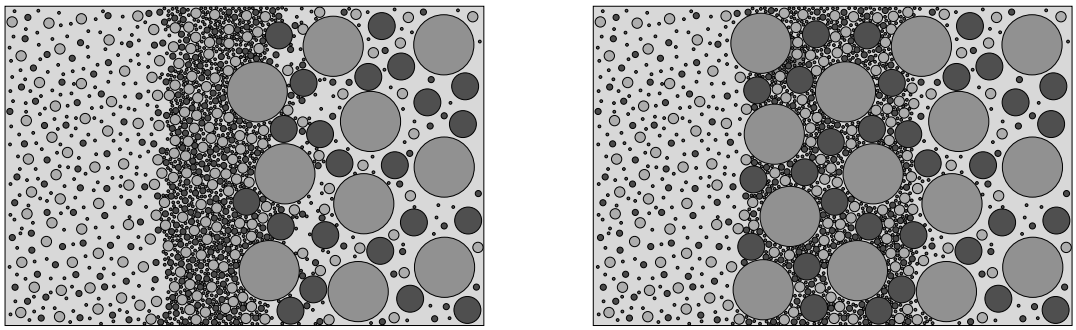

Figure 2.9: Illustration of formation of external filter cake (Left) and internal filter cake (Right), after Schaufler et al. (2013*a*)

from the grout into the surrounding soils. This phenomena is called infiltration process. The deposition of fines in the pore space of the porous medium results in considerable changes of the materials properties. On the one hand, the mechanical property, such as stiffness, is changed due to a reduction of pore space and additional materials coming from the deposited fines. On the other hand, the hydraulic properties, such as permeability and effective viscosity, are modified. Schaufler (2015) pointed out that deposition is triggered/controlled in two ways: hydraulic reasons trigger the process whereas geometrical properties on the micro-scale control the process. Depending on the initial conditions of the porous medium and complex fluid (e.g., pore constriction size distribution, hydraulic gradient, etc.), there are two types of infiltration processes. First is steady infiltration where deposition of fines takes place rather slowly due to an initially big pore space and low permeability. Second is rapid infiltration which is caused by a high hydraulic gradient and initially small constriction size leading to a highly localized clogging effect. Fig. 2.9 shows the illustration of formation of a filtration cake caused by clogging effect. As seen, it can be distinguished between external and internal filter cakes. Schaufler et al. (2013*a*) showed that an external filter cake is formed when the constriction sizes of the pore channels are smaller than the average diameter of the fluidized fines. Hence, the fines are deposited on the border, and more particles accumulate at the interface. Subsequently, a layer with reduced permeability can be observed. In contrast, the internal filter cake is formed when the fines can penetrate over a certain distance into the surrounding soil. Within this framework, the mechanical and hydraulic properties are significantly changed in the domain where grout is injected. Therefore, attention should be paid to the effect of grout infiltration in numerical simulation of mechanized tunnel excavation.

Fargnoli, Gragnano, Boldini & Amorosi (2015) numerically investigated the effect of tunnel excavation on the existing building, in their work the multi-story building is explicitly modeled by using different beam and plate elements that represent the column, floor, retaining wall, etc. While the grouting pressure is simplified as a distributed mechanical load and the grout material is not explicitly simulated. Masini et al. (2014) proposed an analytical model to describe the pressure filtration of grout induced soil volume change in both 1D and 3D scales. In their approach the amount of soil particles flowing out from the slurry grout is neglected, which means the source of filtration is dehydration of grout. The influencing factors that affect the permeability of filtered grout are studied, while the variation of grout permeability during filtration process is not considered. Kasper & Meschke (2004) studied the effect of stiffness and permeability of grout material properties in shield tunneling. They found that development of grout stiffness is more influential than the permeability on the final surface settlements and lining forces. However, the influence of grout stiffness and permeability on the short-term system behavior is not evaluated. Ninić & Meschke (2017) conducted tunneling simulation and many important aspects were considered in their numerical model. The evolution of stiffness and permeability of the tail void grout was considered as well. However, they considered the grout hardening induced permeability evolution only and the time dependent permeability was fitted based on the experimental results. The effect of grout infiltration on the hydraulic properties of surrounding soil was not investigated. Talmon & Bezuijen (2009) studied the time dependent thickness of the filter cake formation due to grout consolidation. Their results were validated on the real measurements of the Groene Hart tunnel. They found that short after lining installation, the fluid-like non-consolidated grout commences to dewatering and forms a grout cake due to deposition of the grout particles inside the grout layer. However, such infiltration at the interface between the grout and soil may occur in the soil layer rather than the grout when the tunnel is excavated in soil with higher permeability. As a result, the soil's permeability and hydraulic boundary conditions around the tunnel change, which may highly affect the model responses due to hydro-mechanical interaction. Therefore, it is valuable to include the grout infiltration induced permeability evolution in the numerical simulation of mechanized tunnel excavation, and to study its effect on the tunneling induced surface settlements and lining forces. Within this framework, this research aims to investigate the influence of grout infiltration induced permeability evolution on the model responses (e.g., surface settlements, stress path, pore pressure variation, lining forces and deformation, etc.). In the work of Schaufler et al. (2013*a*), one dimensional infiltration analysis in cohesionless soils is conducted based on theory of porous medium (TPM). They consider the filtration pro-

cess as a phase transition process of fines and the material parameters can be estimated without explicit numerical calculations (the details will be explained in section 5.2.2). Thereafter, the time and space dependent permeability is obtained. Within this framework, this approach is applied in the numerical simulation of tunneling in this thesis, the details will be introduced in Chapter 5.

Additionally, Bezuijen et al. (2004) presented the field measurements of grouting pressure of the Sophia Railway tunnel, which is shown in Fig. 2.10. The tunnel crown is located at a depth of 14.77 m where the overburden pressure is approximately 200 kPa. A single component grout was used in this project. The sensors monitored from the moment of the rings were placed to about 11 hours after leaving the shield. As seen in Fig. 2.10, the most relevant grouting pressure and vertical gradient are shown. During tunnel excavation, the grout was constantly injected in the annular gap, this results in increase of grout pressure during drilling. In contrast, during stand still, the grouting pressure decreases. For the first two cycles, one can see a considerable decrease in the grouting pressure. Dias & Bezuijen (2015) gave the reason that TBM advanced a few seconds before the grout pumps were activated. After four cycles, the grout injection at TBM tail became not influencing while the pressure continuously decreased. Furthermore, when the grout was injected, the gradient was equivalent to the grout weight for the first four cycles. During the stand still, there was a sharp decrease. Finally the gradient reduced with time to the weight of water. Within this framework, when the grout material is modeled as a fluid in the numerical simulation of mechanized tunnel excavation, it is necessary and valuable to take into account the variation of grouting pressure and grout gradient with the advancement of the TBM.

Lining behavior

Since the concrete lining segments are the permanent structures used to support the tunnels, proper design of lining segments plays a pivotal technical and economical role in mechanized excavation for both shallow and deep tunnels. The behavior of lining is affected by the complex construction features, for example the progressive excavation process and backfill grouting. Therefore, developing a framework to accurately predict the lining forces and deformations before tunnel construction is essential for the purpose of structural safety and optimum design. Additionally, the cost of tunnel construction depends to a large extent on the cost of lining, this also contributes to the importance of structural design of linings in short- and long-terms stability of the tunnel.

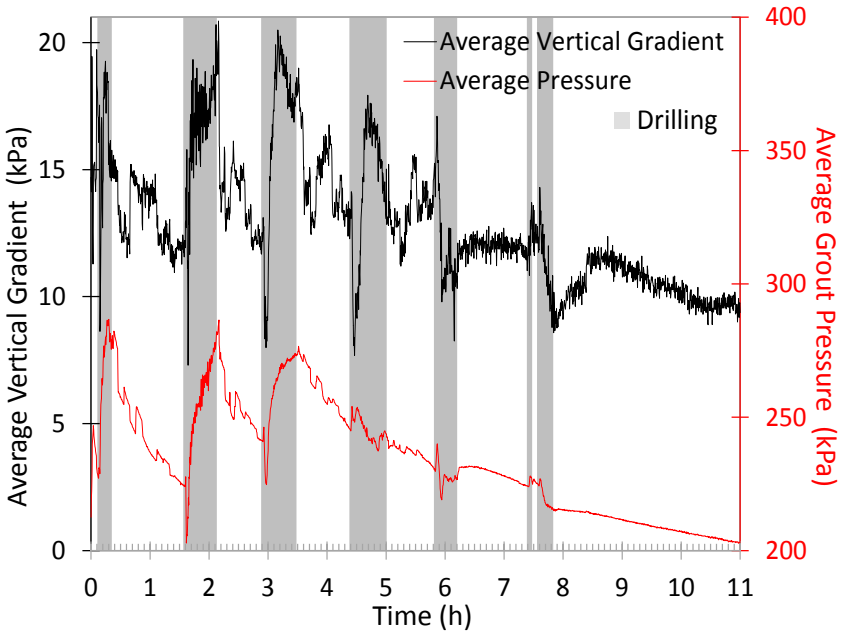

Figure 2.10: Measurement of average grouting pressures and vertical gradients with time, after Bezuijen et al. (2004)

Axial forces, bending moments and radial displacements are the most significant responses of lining segments during construction, which strongly depend on the confining pressure due to the surrounding soil stresses. As soil deformation and soil-lining interaction induce the variation of soil stresses applied on lining, analysis of tunnel lining and its interaction with soil becomes even more complex because of the dependence of such interaction on the construction technology and schemes (El-Nahhas et al. 1992).

- Analytical solutions of lining behavior

For the preliminary design of lining segments, analytical solutions can be used to give a good insight into the dominant processes. The analytical solutions are developed on the basis of 2D idealization of tunnel construction. There are two main categories of structural models for mechanized tunneling have been proven and established for usual applications: the continuum models (see Figs. 2.11(a) and 2.11(b)) preferred for deep tunnels and the bedding models (see Fig. 2.11(c)) preferred for shallow tunnels.

An overview of the contributions to analytical solutions is given in Table 2.5. The list and the following brief discussion are, of necessity, incomplete. Schmid (1926) was probably the first who proposed an analytical solution for thick lining segments in contact with elastic soil. A thinner lining is assumed by Voellmy (1937), however, his results do not comply with the equilibrium of forces since the tangential components of soil pressure are

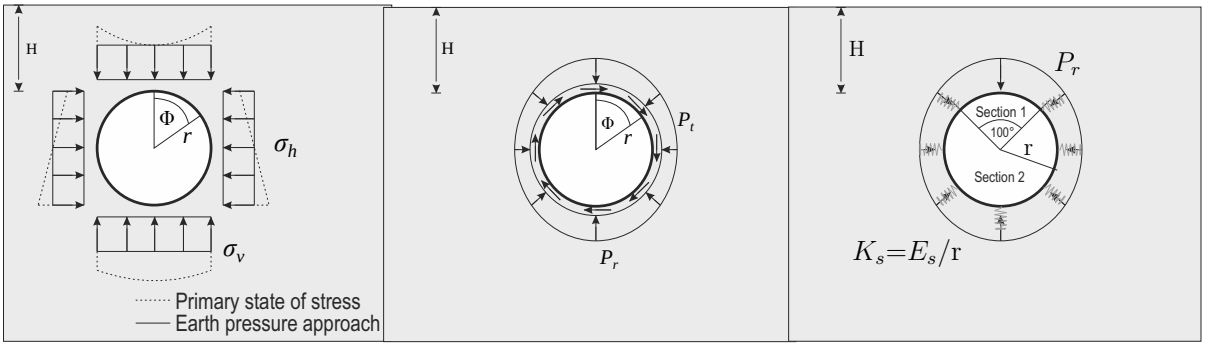

(a) (b) (c)

Figure 2.11: Schematic illustration of different analytical solutions: (a) the continuum model with Cartesian coordinates, (b) the continuum model with polar coordinates and (c) the bedding model

neglected. Morgan (1961) proposed an analytical solution using continuum model, which takes into account the elliptical deformation of the lining. Schulze & Duddeck (1964) published a complete and closed solution using bedding model, which was applicable for shallow tunnels. After that, Windels (1967) proposed a complete solution on the circular tunnel in an elastic soil domain by also taking into account the geometric non-linearity and an approximation for the lining deformations. Wood (1976) corrected the solution of Morgan (1961) by including the tangential stresses on the model and the radial deformations due to these stresses are considered as well. In 1982, an exhaustive and theoretically complete solution was finally achieved by Ahrens et al. (1982). Additionally, Molins & Arnau (2011); Arnau & Molins (2011) conducted experimental and analytical study of the structural response of segmental lining based on an in situ loading test. Their approach is able to asses a realistic consideration of the soil-structure interaction. Vu et al. (2017) considered the difference of loadings at the crown and the invert of the shallow tunnel, they developed a new model by calculating the soil pressures at particular points on the cross section of the tunnel combined with the FEM for tunnel structural analysis. In their approach, the longitudinal joints of the lining segments were considered, and the proposed model was validated based on the real measurements.

To be specific, the analytical continuum model consists of a homogenous elastic circular ring embedded in a plane 2D-continuum (see Fig. 2.11(a)). Herein, the idealized primary stress state is obtained from equilibrium of vertical and horizontal forces induced by earth pressures. The vertical component of lining load (σ_v) is modeled as an uniformly distributed load on top and bottom of the tunnel. This lining load is depth independent

Table 2.5: Brief overview of the contributions to structural design models of linings

Reference	**Description**
Schmid (1926)	First to analyze the elastic continuum with considering the soil-lining interaction
Voellmy (1937)	The continuum model, omission of the tangential components of soil pressure
Bull (1946)	The bedding model for shallow tunnel, tedious calculation
Engelbreth (1961)	The continuum model with closed form
Schulze & Duddeck (1964)	The bedding model with complete and closed solution
Windels (1967)	The continuum model with complete solution
Ahrens et al. (1982)	The exhaustive and theoretically complete solution
Bakker (2003)	Unidimensional model without considering the soil-lining interaction
Kim & Eisenstein (2006)	Using correction factors considering the non-linear ground behavior
Vu et al. (2017)	The bedding model consider the depth dependent loading pressure and longitudinal joints

and determined based on the soil stress at the depth of tunnel axis. The horizontal load (σ_h) is also applied as a constant pressure, its magnitude is defined as the vertical earth pressure multiplied by the coefficient of lateral earth pressure at rest (K_0), namely $\sigma_h = K_0\sigma_v$. To compute the internal forces on lining, it is necessary to transform the vertical and horizontal earth pressures into radial and tangential load components (see Fig. 2.11(b)). Therefore, the Fourier transformation can be employed to respectively split the radial and tangential forces acting on the circular ring and the continuum. Generally, two different analytical solutions can be distinguished: (a) full bond takes into account both, radial and tangential bond between the soil and lining; (b) tangential slip assumes only the radial bond between soil and lining, and the tangential load component does not affect the lining behavior. In concrete lining design the model of the circular ring embedded in an elastic continuum serves as an adequate analytical model for deep tunnels. It takes into account the arching effect due to a fully embedded ring and allows for tensile forces in springs to minimize loads on the lining. Consequently lower deformations and lining forces occur which constitute the minimum level of lining forces at all. In case of shallow tunnels the idealizations, more or less simplifications, of the continuum model

(e.g. soil-structure interaction) strongly underestimate deformations and lining forces (Ahrens et al. 1982), so that this model might be inappropriate.

The bedding beam model employes linear or nonlinear springs whose stiffnesses are assumed to be equal to the predefined subgrade moduli ($K_s = E_s/r$, where E_s is the constrained modulus of the surrounding soil and r is the radius of the tunnel). These moduli are specifically obtained with respect to the alternative modeling approach. For instance, in case of deep tunnels a reasonable mechanical model assumes fully embedded circular rings and elastic springs. Generally, the bedding model is derived from a circular ring embedded in an elastic domain assuming tangential slip for soil-structure interaction. Accordingly, fully embedded crowns lead to tensile stresses in the elastic springs (crown of the tunnel). Consequently, the lining is locally unloaded. In practice this is related to the soil arching effect that results in lower bending moments. However, the arching effect is normally neglected in case of shallow tunnel (the overburden is less than twice the diameter of the tunnel). To ensure appropriate bending moments the crown is modeled to be unbedded in the analytical method (see Fig. 2.11(c)). In mechanized tunneling, the unbedded crown happens when the ring leaves the TBM or due to loosening of the surrounding soil during excavation (Schulze & Duddeck 1964; Kämper et al. 2016). After that, the crown, due to inward deflections, is subjected to the soil's total weight but not embedded anymore. This results in larger bending moments in the crown. Hereby, the size of the unbedded zone (about 100°) is characterized by transition of inwards to outwards radial deformations and the positions of longitudinal joints of a segmental lining.

It should be noted that the above mentioned analytical models are conducted based on the following assumptions: (1) the analytical solutions are sufficient to consider only a cross-section, which means plane strain condition is assumed; (2) the cross section of the tunnel is assumed to be circular; (3) the soil stresses on the lining segments are assumed to be equal to the primary stresses in the undistributed ground; (4) there is a bond between the lining and the ground, it takes into account the soil-lining interaction; and (5) the material behavior of soil and lining is generally assumed to be elastic. Therefore, the important features of tunneling process (e.g., soil plasticity, progressive excavation, volume loss around the tunnel, tail void grouting, etc.) cannot be captured by the analytical solutions.

- Numerical analysis of lining behavior

In order to reliably predict the lining forces and deformations, finite element method (FEM) analysis has become a popular tool which can simulate staged construction procedures and reproduce the soil and structure behavior by using appropriate constitutive models (Zhao et al. 2017). In engineering practice, the numerical modeling often relies

on the two dimensional (2D) analysis, since it is straightforward and cost-effective. For the numerical simulation of mechanized tunneling process in plane strain condition, it normally takes into account the tunnel construction process including TBM excavation, backfill grouting and lining installation as well as the soil-lining interaction. Oreste (2007) developed a special code within the FEM framework using hyperstatic reaction method to consider the actual geometry of the lining support and the horizontal loads that are different from the vertical ones, it is therefore able to analyze the mass-structure interaction in detail. Möller & Vermeer (2008) applied FEM to simulate the conventionally driven Steinhaldenfeld tunnel and Heinenoord slurry shield tunnel, and studied the influences of constitutive model and applied construction method on lining forces and ground deformation. Zhang et al. (2015) analyzed the influence of multi-layered soil formation on tunnel lining behavior by employing FEM, and the results show a good agreement between the numerical model responses and the real measurements. In all these studies, the joints between the lining segments are not explicitly modeled. As an alternative, the reduced lining stiffness are used in their numerical simulation (Wood 1975). Blom (2002) pointed out that in many analyses there may be great interest in the macro deformations of the lining or soil domain that are not suitable to explicitly implement the longitudinal joints and couplings of lining. While these analyses very often use the homogeneous ring with a reduced bending stiffness to involve the global influence of the longitudinal joints on the bending stiffness. He also investigated the variation of reduction factor for the bending stiffness with respect to lining and joint properties, this can be seen in Fig. 2.12. For example, by assuming that the contact area (l_t) in the longitudinal joint is 200 mm, lining radius (r) is 4250 mm, the lining thickness (d) is 400 mm and each ring has 7 segments, it can be derived that the reduction factor is about 0.75. If the assumed Young's modulus of reinforced concrete is 40 GPa, 30 GPa is used in the numerical model to represent the reduced bending stiffness of lining.

In order to study the influence of joints between lining segments on the lining behavior, Do et al. (2013) modeled the longitudinal joint by six springs with double node connections and six degrees of freedom using a 2D finite difference element method. Their model allows the effect of not only the rotational stiffness but also the radial and axial stiffnesses of the joints. Numerical results show that the maximum bending moments reduce with increasing number of the joints, which is consistent with the results of Blom (2002). While the influence of axial and radial stiffness of the joints on the lining behavior is insignificant. Klappers et al. (2006) studied the effects of both longitudinal and circumferential joints by using a 2D spring coupled beam model and a 3D shell elements FE model. They found that for uniform design loads, it is not necessary to employ a 3D model due to

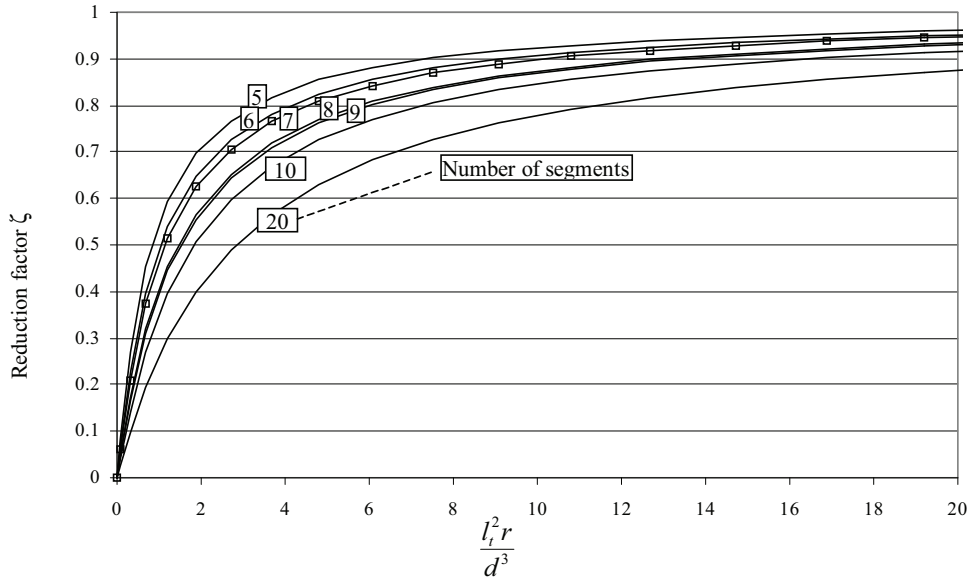

Figure 2.12: The reduction factor for the lining stiffness as function of the contact area (l_t in the longitudinal joints, the segmental thickness (d) and the lining radius (r), after Blom (2002)

the similar results provided by the simplest beam spring model with coupled rings. This is consistent with the findings of Arnau & Molins (2012). They investigated the 3D structural responses of lining segments and concluded that the staggered configuration of the lining joints increase the lining stiffness in respect to the isolated ring consideration. While this does not significantly influence the structural responses out of the combination of really soft grounds and high unbalanced loads.

In the realistic tunneling process, the excavation procedure changes the primary stress field at the tunneling face (ITA 1988). Furthermore, the soil stresses on lining segments are influenced by the progressive excavation process and 3D arching effect of the soil towards the end of tunnel. Despite of the popularity of 2D numerical analysis, its deficiencies, that face support in front of TBM, the sequential excavation process and the inclination of the tunnel cannot be modeled, are inevitable. Within this framework, the use of 3D FEM analysis is essential if one wants to correctly evaluate the influence of staged excavation process on lining structure responses. Hudoba (1997) studied how the lining structures react under static loading of the surrounding soil during tunneling process using both 2D and 3D computing models. Galli et al. (2004) modeled tunnel excavation and lining installation in both 2D and 3D models, they showed that 3D discretization of soil-tunnel system is essential to analyze the soil deformation and stresses in the lining elements.

Although FEM analysis is a powerful tool in simulations of engineering problems, uncertainty in model responses is unavoidable due to the complex tunnel construction procedures, limitations of employed FEM techniques and the insufficiency of constitutive models themselves. Additionally, it costs many resources to obtain the input parameters to be used in numerical model, while running the sophisticated model is time-consuming, especially for complex 3D tunneling model.

2.2.3 Hydro-mechanical interactions around the tunnel

The tunneling process predominantly changes the initial stress state due to soil excavation, face support and grout injection. In case of tunneling under ground water level, the excavation process will generate not only a mechanical response through stress changes and displacements in the soil but also a hydraulic response through pore water pressure changes. In other words, generation and dissipation of excess pore water pressure in the soil due to mechanized tunneling affect the soil effective stresses and the subsequent system responses (e.g. soil deformation, stress path, lining forces, etc.). Therefore, it is valuable and necessary to study the Hydro-mechanical interaction in the tunneling process. Considering the specific type of the soil and its permeability, time dependent variation of the pore pressure can be reliably investigated by finite element analysis (Zienkiewicz et al. 1974, 1999; Finno & Clough 1985).

In geotechnical applications, the undrained analysis in conjunction with constant volume is usually adopted to study the short-term construction stage (Franzius et al. 2005*b*; Schuerch & Anagnostou 2013*b*), while the drained analysis assuming no excess pore pressure evolution is popular method to address the long-term performance of the projects (Vermeer et al. 2002; Dias et al. 1999). However, it is not always obvious which calculation is applicable for a particular tunneling problem (Atkinson & Mair 1981). In contrast to these extreme assumptions, it is most likely that the excess pore pressure generates and dissipates in the soil deposit in both short- and long-term loadings while this process may result in the change of hydraulic boundary conditions close to the tunnel boundary. This hydraulic incidents around the excavation zone can significantly affect the system behavior (Lavasan, Zhao, Barciaga, Schaufler, Steeb & Schanz 2018).

In the second Heinenoord tunnel (under the river Oude Maas in the Netherlands), the tunneling process was conducted in soft to very soft fine sand and clay with high water pressure. The field measurements indicated that the ground water flow reached the stationary condition after approximately 5 minutes and the entire excess pressure was

dissipated in about 30 minutes after the TBM was stopped (Broere 2003). Such abrupt generation and dissipation of excess pore pressure is often ignored within a drained analysis considering stationary ground water flow. Nevertheless, neglecting the variation of excess pore pressure may affect the other model responses due to fluctuations in flow regime around the tunnel. When the dissipation of the pore pressure takes longer, the hydro-mechanical interactions should be modeled by a consolidation analysis to address transient groundwater flow. Schuerch & Anagnostou (2013*a*) investigated the time dependent stability of the tunnel face during consolidation process of the ground under the transient conditions. Holt & Griffiths (1992) applied finite element approach to assess the effects of excavation rate, soil permeability and drainage length on the transient stability of tunnel excavation in elasto-plastic soil. In reality, different steps of loading, unloading and reloading in tunneling process induces frequent generation and dissipation of excess pore pressure during excavation and standstill periods (Dias & Bezuijen 2015). Besides a fully coupled hydro-mechanical analysis (Adachi et al. 2006; Kasper & Meschke 2004), some studies attempted to assess the time-dependent behavior of tunnels in rock and soils by the use of single-phase elasto-viscoplastic models (Zienkiewicz et al. 1974; Sakurai 1978; Pan & Hudson 1988; Hawlader et al. 2006). Adachi et al. (2006) and Swoboda & Abu-Krisha (1999) numerically investigated mechanized tunneling process in saturated soil considering coupled linear flow. Results of these studies revealed that the excess pore pressure and deformations can be realistically predicted by FE simulations.

In the numerical analysis conducted in this research, the consolidation analysis is carried out on the basis of a so-called hybrid consolidation model. The hybrid consolidation concept is proposed to avoid the ill-conditioning and instability in Biot (1941) consolidation equations which can significantly affect the pore pressure solution (Ferronato et al. 2010). This theory takes into account a material compressible pore fluid ρ^{f} while the solid grains composing the soil skeleton ρ^{s} are assumed to be incompressible. In consolidation calculations, the hydraulic analysis is fully coupled with the constitutive behavior of extra stress whilst the total stress is divided into the effective stress and the pore pressure. In the present FE approach, primary variables are the solid displacements and the excess pore pressures. To be specific, the increment of nodal displacement is governed by the mechanical analysis on the basis of effective constitutive model and the consolidation analysis deals with the excess pore pressure increment due to the soil deformation.

In the general form, the water outflow from a solid element should be equal to the mass exchange in the volume based on the continuity law. Accordingly the water outflow can

be written as divergence of the discharge as follows (Renner & Steeb 2015):

$$\frac{1}{M}\partial_t(p) - \operatorname{div}\left[\frac{k^{\mathfrak{f}}}{\gamma^{\mathfrak{f}R}}\operatorname{grad} p\right] + \operatorname{div}\mathbf{v}_{\mathfrak{s}} = 0 \tag{2.13}$$

where p is a scalar representing the fluid pore pressure ($\operatorname{grad} p$ is the gradient of pore pressure which leads to fluid flow), M is a storage modulus or $1/M$ is a specific storage capacity, i.e., a measure of change in fluid volume in a bulk volume upon a change in fluid pressure for fixed mean stress. $k^{\mathfrak{f}}$ represents permeability, $\gamma^{\mathfrak{f}R}$ is the effective weight of the fluid and $\mathbf{v}_{\mathfrak{s}}$ denotes the velocity of solid.

The balance of momentum for the mixture is given as (Renner & Steeb 2015):

$$-\operatorname{div}(\mathbf{T}_E^{\mathfrak{s}} - p\mathbf{I}) = \rho\,\vec{b} \tag{2.14}$$

where $\mathbf{T}_E^{\mathfrak{s}}$ represents the effective stress for which constitutive model is developed, $\mathbf{I}$ is the second order unity tensor, $\rho\,\vec{b}$ are the body forces and ρ denotes the mixture's density which is defined as:

$$\rho = (1-\phi)\rho^{\mathfrak{s}R} + \phi\rho^{\mathfrak{f}R} \tag{2.15}$$

where ϕ denotes the porosity, $\rho^{\mathfrak{s}R}$ and $\rho^{\mathfrak{f}R}$ are the effective density of soil and fluid, respectively.

Based on these equations, a coupled hydro-mechanical (consolidation) analysis has been conducted within the employed constitutive model. Thereafter, the obtained results are coupled with a hydraulic fluid flow model to estimate the corresponding excess pore pressure and its time dependent dissipation.

2.3 Introduction of tunneling induced ground movements

2.3.1 Greenfield ground movements due to tunneling

Empirical methods

Tunnel excavation inevitably induces deformations in the soil domain around the tunnel and changes the stress distribution. As a result, the stress redistribution induces deformations in soil that propagates up to the ground surface and form a settlement trough which may consequently endanger the existing buildings. Therefore, it is essential to develop a platform to accurately predict the ground movements due to tunnel excavation, and to

evaluate a relation between ground deformations and factors that affect the magnitude, orientation and location of the surface displacement profile. The substantial hazardous damages in the infrastructures due to development of deformations and forces induced by tunneling calls for great interest to the engineers and researchers (Fu 2014). Since it is extremely difficult to formulate a relationship to predict the ground movements by incorporating all the influencing factors, it is necessary to figure out the most important variables. According to Tan & Ranjith (2003); Potts (2008), the important factors are summarized as: (1) field condition, such as the initial and boundary conditions, soil properties, hydraulic properties, etc; (2) tunnel design requirements, such as the tunnel diameter, overburden depth, TBM and lining properties, etc; (3) tunneling techniques that include the construction method, applied support pressures, interaction between the tunnel and surrounding soil, etc.

Empirical methods for predicting the tunneling induced ground movements were firstly introduced by Peck (1969) who suggested to use invert Gaussian normal distribution curve to predict the tunneling induced surface settlement profile in transverse direction of tunnel axis. O'Reilly & New (1982); Mair et al. (1993) modified the transverse settlement trough as:

$$S_{y,z} = S_{max} \exp\left(\frac{-y^2}{2\, i_z^2}\right) \tag{2.16}$$

where $S_{y,z}$ is the settlement at the distance of y from the tunnel center line and depth of z from the ground surface in the transverse direction, S_{max} is the maximum settlement, i_z is the horizontal distance from the tunnel center line to the inflection point (see Fig. 2.13) at the depth of z. According to this equation, the settlement trough at the ground surface is dominated by two parameters. S_{max} can be directly measured during the excavation. For i_z, O'Reilly & New (1982) found that there is a linear correlation between i_z and tunnel depth. They stated that if all the movement of the soil is assumed to occur along radial paths towards the tunnel axis, i_z at the surface is approximately a linear function of the tunnel axis depth (Z_0), given as:

$$i_z = K_z \cdot Z_0 \tag{2.17}$$

where K_z is model parameter that depends on the soil type and varies between 0.25-0.6 for gravel/sand and 0.3-0.9 for clay/silt (Fillibeck & Vogt 2012).

The empirical method does not identify the contribution of each component that induces soil volume loss, while it interrelates the settlement trough to a rather curve fitting model parameters (K_z) when the maximum surface settlement is known. It is worth to be noted that the value of S_{max} can be estimated based on the surface volume loss. To be specific,

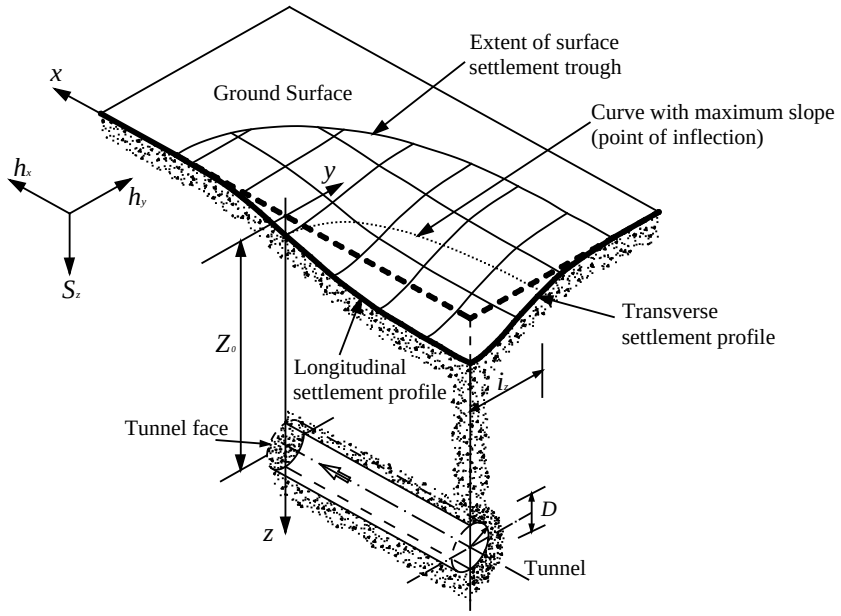

Figure 2.13: Tunneling induced surface settlement profile, after Attewell et al. (1986)

the ground deformation caused by tunneling is characterized by the term of "surface volume loss" (see Fig. 2.8). The volume loss per unit length at ground surface (V_s) can be obtained by integration of the settlement curve:

$$V_s = \int S_{y,z}\,\mathrm{d}y = \sqrt{2\pi} i_z S_{max} \tag{2.18}$$

According to the aforementioned definition of surface volume loss ratio R_s (see section 2.2.2), the maximum vertical settlement S_{max} can be represented as the function of R_s and the width parameter of the settlement trough i_z as:

$$S_{max} = \frac{\sqrt{\pi} D^2 R_s}{4\sqrt{2} i_z} \tag{2.19}$$

In addition to the widely applied Gaussian distribution curve, alternative curves can be used to describe the tunneling induced surface settlement profile in the transverse direction. Jacobsz et al. (2004) suggested a slightly different version of the Gaussian curve which has also two degrees of freedom:

$$S_{y,z} = S_{max} \exp\left[-\frac{1}{3}\left(\frac{|y|}{i_z}\right)^{1.5}\right] \tag{2.20}$$

Celestino et al. (2000) used curves with one additional degree of freedom compared with the Gaussian distribution curve:

$$S_{y,z} = \frac{S_{max}}{1 + (|y|/a)^b}, \tag{2.21}$$

where $i_z = aB$, $B = (\frac{b-1}{b+1})^{(1/b)}$. Vorster et al. (2005) used three degrees of freedom curve to describe the transverse surface settlement profile as well, thus more flexibility to the shape of the curve can be obtained:

$$S_{y,z} = \frac{nS_{max}}{(n-1) + \exp[\alpha(y^2/i_z^2)]}, \tag{2.22}$$

where $n = \exp(\alpha)\frac{2\alpha-1}{2\alpha+1} + 1$.

According to these distribution curves, the transverse surface settlement profile can be determined by two or three fitting parameters that are affected by the soil properties, size, depth and volume loss of the tunnel. Marshall et al. (2012) conducted centrifuge tests for tunnels in sands and examined the effects of size, depth and volume loss on the greenfield displacements. A set of complex equations is developed to correlate the trough width parameter with tunnel size, depth and volume loss. While the determination of the maximum surface settlement S_{max} (or equivalent R_s) is based on the engineering experience. There is no quantitative relation between R_s and soil/tunnel properties. Fillibeck & Vogt (2012) proposed a method to specify the surface volume loss ratio as a function of the probability of occurrence considering the tunnel depth and soil stiffness. However, it is still not possible to calculate a "true" settlement trough in advance.

According to the aforementioned discussion, the surface settlement profile can be attributed to both tunnel volume loss and tunnel construction induced variation of stress/strain state in the soil domain. The difference between V_s and V_t can be defined as contribution of the volume change of ground domain V_g (see Fig. 2.8) due to soil's deformability characteristic. Thus, the influence of tunnel volume loss (V_t) on the surface volume loss (V_s) cannot be explicitly captured by the empirical solutions.

Analytical solutions

The analytical solutions offer a rapid analysis of the stress and strain fields around the tunnel. They can be used to evaluate the influence of tunnel volume loss on surface volume loss. The main analytical methods can be categorized into four groups, namely (1): the general solution in the form of Airy function in polar coordinate (Bobet 2001; Park 2005); (2) the stochastic medium theory (Liu 1992; Yang et al. 2004); (3) the virtual image technique (Sagaseta 1987; Verruijt & Booker 1996); (4) the complex variable method (Verruijt & Booker 1997; Wang et al. 2009). Among these solutions, the deformations of the tunnel cavity can be decomposed into three basic modes, namely uniform convergence, ovalization and vertical translation. The closed form solutions of the analytical methods

are able to derive the relation between each of these components on the surface settlements. However, the deficiencies of the analytical methods are inevitable. On the one hand, assumptions about geometry and boundary conditions should be made when modeling the real engineering problem into an equivalent mathematical form. On the other hand, soil behavior is highly complex, it behaves non-linearly in both elastic and plastic deformation ranges. While the soil is normally assumed as an elastic material or the plastic behavior is simplified in the analytical methods. Moreover, the inherent complexities of tunnel construction cannot be captured in the analytical solutions. Therefore, these analytical methods are not applicable for realistic tunneling problems. Nevertheless, they can provide a straightforward engineering judgment during construction, and the results can be served as a preliminary evaluation for the advanced numerical simulation (Pinto & Whittle 2013; Pinto et al. 2013).

Numerical investigation

Nowadays, FEM has become a powerful tool for studying the tunneling induced ground movements. In the early works, most of the simulations were based on plane strain assumption due to the limited computer resources, complex three-dimensional (3D) geotechnical systems and lack of information to validate the numerical model. In 2D simulations, the support at tunnel face and staged excavation process are idealized, and the variation of 3D arching effect due to progressive excavation can not be adequately captured. Therefore, 3D model is essential to accurately simulate the tunneling process and its corresponding construction features (Zhao et al. 2015). However, 3D model of tunneling process is often complex and requires excessive computational efforts and time. In contrast, the 2D model is efficient and computational cost-saving, thus it is a powerful tool to conduct parametric study (Zhao, Lavasan & Schanz 2014). Franzius & Potts (2005) summarized a number of FE studies for tunneling problems, the modified summary is given in Table 2.6. For each study, the table describes the soil model used, the diameter D, depth Y of the tunnel and the name of the FE code.

These numerical analyses focus on different aspects, such as tunneling technique, initial stress conditions, size, depth of tunnel and soil-structure interaction. In the work by Katzenbach & Breth (1981), tunnel excavation (New Austrian Tunneling Method) was simulated by a step-wise approach. Although the authors pointed out that this a first step in 3D simulation of tunneling process, the numerical results captured the typical 3D behavior such as arching effect. After that, this step-wise approach has been adopted by various authors to model the tunnel excavation. Franzius et al. (2005*a*) demonstrated

Table 2.6: Summary of FE analyses for tunneling, modified after Franzius & Potts (2005)

Authors	Material	D[m]	Y[m]	FE code
Katzenbach & Breth (1981)	Nonlinear elastic	6.7	15.2	-
Lee & Rowe (1991)	Elastic perfectly plastic	2.5	8.0	FEM3D
Desari et al. (1996)	Nonlinear elastic perfectly plastic	8.0	25.0	CRISP
Tang et al. (2000)	Elastic perfectly plastic	8.6	25.0	ABAQUS
Dias et al. (1999)	Elastic perfectly plastic	9.8	25.0	FLAC3D
Vermeer et al. (2002)	Linear elasti perfectly plastic	8.0	2.0	PLAXIS
Shin et al. (2002)	Elastic perfectly plastic	9.2	20.0	ICFEP
Galli et al. (2004)	Elastic perfectly plastic	11.0	11.0	LUSAS
Franzius et al. (2005a)	Nonlinear elasto-plastic	4.15	20.0	ICFEM
Möller & Vermeer (2008)	Nonlinear elasto-plastic	8.3	11.25	PLAXIS
Vakili et al. (2014)	Nonlinear elasto-plastic	8.5	8.5,42.5	PLAXIS

the influence of K_0 on ground surface movements resulting from tunnel excavation, and they found that maximum surface settlement increases with lower value of K_0. This coincides with the research of Rott et al. (2015) where they found that the ratio of horizontal and vertical displacements are highly influenced by the values of K_0. Möller & Vermeer (2008) highlighted the importance of modeling soil-structure interaction in tunneling simulation, which affects the stress distribution around the tunnel and induces effects to the ground surface. Vakili et al. (2014) studied the tunneling induced ground movement using different constitutive models, by doing so, the effect of elasto-plastic deformation of soil domain on the surface settlement is evaluated.

According to these researches, the components that contribute to surface volume loss during tunneling process are not explicitly elaborated, and there are rare studies to evaluate the influence of tunnel volume loss on the surface volume loss by taking into account both compressibility, elasticity and plasticity of soil. Within this framework, this research aims to investigate the quantitative relation between tunnel volume loss and surface volume loss by considering the tunnel depth, volume loss and soil/tunnel properties using different soil constitutive models. Furthermore, the obtained correlation between tunnel volume loss and surface volume loss will be applied in the empirical method, which makes the empirical method capable to predict the tunneling induced surface settlement profiles before

excavation. The detailed simulation process and results interpretation will be described in Chapter 4.

2.3.2 Adjacent building responses due to tunneling

In the urban environment, many buildings supported by shallow or deep foundations might be affected by underground tunneling. Tunnel excavation inevitably induces unloading due to soil mass removal and stress relaxation in the soil domain around the tunnel that leads to stress redistribution in the soil system. Consequently, the induced deformations can jeopardize the integrity of foundations themselves. Thus, the effects on buildings in the vicinity of the tunnels should be evaluated to ensure that their influences do not exceed the allowable capacity of the structure.

The process of building damage assessment is usually conducted from preliminary evaluations to simple conservative approaches, and eventually to detailed procedures as introduced by Mair et al. (1996). In the preliminary stage, the zone where the ground surface settlement is induced by tunneling is determined. In the second stage, empirical-analytical methods, namely limiting tensile strain method and relative stiffness method, are utilized to calculate the strains and distortions in the buildings to determine the possible structural damages. The third step of a detailed assessment is necessary if there are buildings in the second step being classified in the damage category. Accordingly, an accurate analytical or complex numerical analysis that accounts for details of the building and soil-structure interaction should be conducted (Fu 2014).

Analytical methods for predicting soil-structure interaction

The Limiting Tensile Strain Method (LTSM) was originally developed by Burland et al. (1977) and further modified by Boscardin & Cording (1989). In this approach, the green-field displacements are imposed to a simplified beam model of the building. The maximum bending strain ($\varepsilon_{b,\max}$) and diagonal strain ($\varepsilon_{d,\max}$) are derived on the basis of Timoshenko (1955) beam theory as:

$$\varepsilon_{b,\max} = \frac{\Delta/B}{\frac{B}{12t} + \frac{3EI}{12GBHt}} \tag{2.23}$$

$$\varepsilon_{d,\max} = \frac{\Delta/B}{1 + \frac{GBH^2}{18EI}} \tag{2.24}$$

where B, H, I, E, G are the width, height, second moment of area of the building cross-section, the Young's modulus and shear modulus of the equivalent beam, respectively. t is

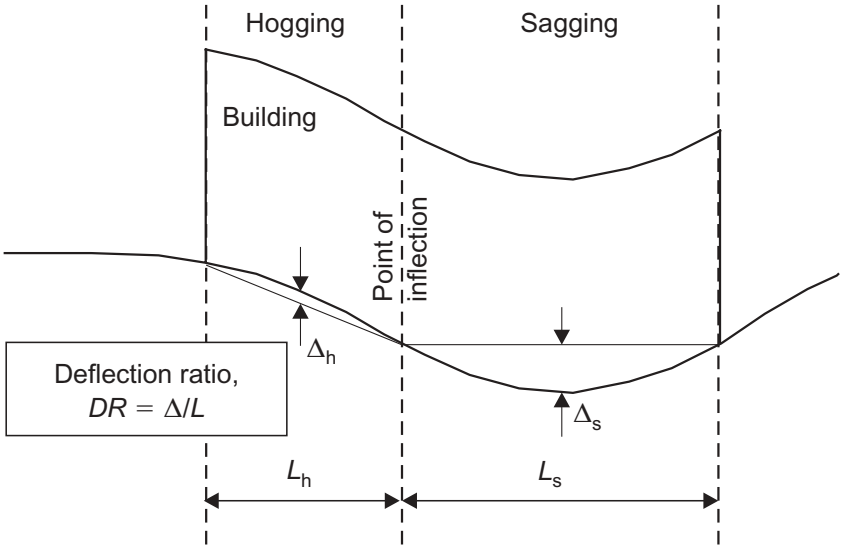

Figure 2.14: Definition of deflection ratio, after Franzius et al. (2005*b*)

the distance between the neutral axis and the edge of the beam in tension. The deflection ratio is illustrated in Fig. 2.14, and therefore it is separately calculated for hogging and sagging portions of the settlement profile.

The beam horizontal strain is calculated as $\varepsilon_h = \delta/L$, where δ is the difference between the horizontal displacements of the greenfield profile at the two ends of the beam. After that, the total bending (ε_{bt}) and shear (ε_{dt}) strains can be calculated using the following equation before to be compared to the limit values for determination of the damage class.

$$\varepsilon_{bt} = \varepsilon_{d,\max} + \varepsilon_h \tag{2.25}$$

$$\varepsilon_{dt} = \varepsilon_h/2 + \sqrt{(\varepsilon_h/2)^2 + \varepsilon_{d,\max}^2} \tag{2.26}$$

It should be noted that in this approach, the soil-structure interaction is not considered. Due to this reason, Potts & Addenbrooke (1997) proposed the Relative Stiffness Method (RSM) for improving the LTSM beam deflection ratio using the following modification factors:

$$M^{DR,\text{sag}} = \frac{(\Delta_s/L_s)}{(\Delta_s/L_s)_{gr}} \tag{2.27}$$

$$M^{DR,\text{hog}} = \frac{(\Delta_h/L_h)}{(\Delta_h/L_h)_{gr}} \tag{2.28}$$

where Δ_s/L_s and Δ_h/L_h are the actual building deflection ratios, while $(\Delta_s/L_s)_{gr}$ and $(\Delta_h/L_h)_{gr}$ are the green field deflection ratios. In their approach, the relative bending

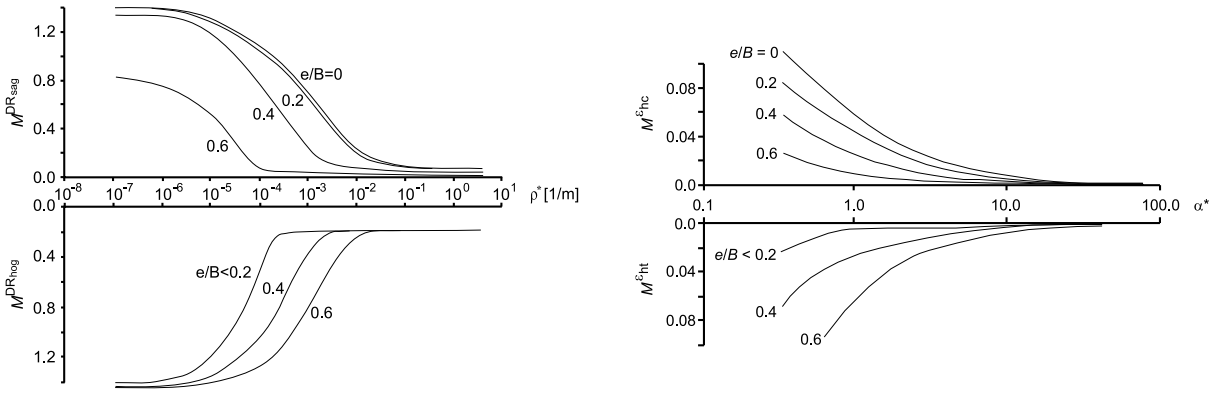

Figure 2.15: Design curves for modification factors of deflection ratio (left) and maximum horizontal strain (right), after Potts & Addenbrooke (1997)

($\rho*$) and axial ($\alpha*$) stiffnesses of the building compared to the soil are evaluated using the following equations:

$$\rho^* = \frac{EI}{E_s(B/2)^4} \tag{2.29}$$

$$\alpha^* = \frac{EA}{E_s(B/2)} \tag{2.30}$$

where A is the cross-section area and E_s is the soil secant stiffness obtained at 0.01% axial strain in a triaxial compression test performed on a sample retrieved from a depth of $Z_0/2$. Thereafter, the modification factors can be obtained on the basis of the specific features of the building and soil using the design curves. This is can be seen in Fig. 2.15. This method was further improved by Franzius et al. (2005*b*), the following equations show that the relative stiffnesses are modified to be dimensionless:

$$\rho^*_{\mathrm{mod}} = \frac{EI}{E_s B^2 Z_0 L} \tag{2.31}$$

$$\alpha^*_{\mathrm{mod}} = \frac{EA}{E_s B L} \tag{2.32}$$

where L is the building length.

Determination of building stiffness

One of the most difficult tasks in the application of the aforementioned RSM is the determination of the overall bending stiffness of the building. An accurate calculation would require a detailed knowledge on the structure type, material properties, construction techniques, current status, etc. It is tough to obtain all this information at the

time of assessment. Furthermore, the building bending stiffness is essential for numerical simulation of soil-structure interaction as well.

Potts & Addenbrooke (1997) referred to two possible methods for the calculation of the building bending stiffness. For a building with n stories the model parameters can be calculated assuming that the building consists of n+1 slabs. The axial and bending stiffnesses of the structure can be calculated as:

$$EA = E\sum_{i=1}^{n+1}(A_{\text{slab},i}) \tag{2.33}$$

$$EI = E\sum_{i=1}^{n+1}(I_{\text{slab},i} + A_{\text{slab},i}H_i^2) \tag{2.34}$$

where E is the Young's modulus of the slab, $A_{\text{slab},i}$ is the cross sectional area of each slab, i is the number of floor slabs, $I_{\text{slab},i}$ is the second moment of area of each slab, H_i is the distance between the structure's neutral axis and the slab's neutral axis. It is worth mentioning that the second moment of area for the equivalent single beam in Eq. 2.34 is calculated using the parallel axis theorem Timoshenko (1955), this may overestimate the bending stiffness of framed structure. Therefore, they suggested the following alternative by ignoring the shear transfer between the slabs:

$$EI = E\sum_{i=1}^{n+1}(I_{\text{slab},i}) \tag{2.35}$$

It should be noted that Eq. 2.35 is based on the formulation proposed by Meyerhof (1953) for a multi-story building frame: $EI = E\Sigma_{i=1}^{n}(I_i)$, here I_i is the second moment of area of each story:

$$I_i = I_b\left[1 + \frac{(K_l + K_u)B^2}{(K_b + K_l + K_u)l^2}\right] \tag{2.36}$$

where $K_b = I_b/l_b$ is the average stiffness of beams, $K_l = I_l/h_l$ is the average stiffness of lower columns, $K_u = I_u/h_u$ is the average stiffness of upper columns, l_b is beam length, h_l and h_u are height of lower and upper columns, respectively.

Melis & Ortiz (2014) developed an unified approach for different structural typologies:

$$EI = \sum(EI)_{\text{floors}} + \sum(EI)_{\text{walls}} + \sum(EI)_{\text{basements}} \tag{2.37}$$

where $(EI)_{\text{floors}} = E(Lb_s^3/12 + Lb_sd_s^2)/L$ is the contribution of each floor slab, $(EI)_{\text{walls}} = E(b_wH^3/12 + b_wHd_s^2)/L$ is the contribution of each wall, $(EI)_{\text{basements}} = E(Lb_b^3/12 + Lb_bd_s^2)/L$ is the contribution of each foundation slab rigidly connected to the building and

$(EI)_{\text{basements}} = E(Lb_b^3/12 + Lb_b c_b^2)/L$ is the contribution of the foundation slab hinged to the building. Here b_s and b_b are the thicknesses of slab and basement, respectively. d_s is the distance from the slab to the neutral axis of the structure, c_b is the distance from the assumed hinge between the building and the basement. Furthermore, they introduced reduction factors to consider the effect of door and window openings. Here the reduction factor is dependent on the percentage of openings and the aspect ratio of the building.

Numerical simulation of soil-structure interaction

In order to investigate the realistic ground behavior during tunneling, Shahin et al. (2016) conducted 2D model tests on tunnel excavation beneath an existing building. They also applied non-linear finite element analyses in accordance with their model tests. They revealed that surface settlement was highly dependent on the distance between tunnel and building where the building might be significantly affected even by deep tunneling. Elsaied (2014) studied the influence of tunneling on settlements induced in adjacent building by considering variable tunnel diameters, overburden depths and horizontal distances between the tunnel and building in a 2D numerical model. However, the interaction between the building and soil was not taken into account. A critical review on idealization and modeling of soil-structure interaction conducted by Dutta & Roy (2002) indicated the crucial role of such interaction under the influence of both static and dynamic loading in order to accurately estimate the design force quantities. Franzius et al. (2004) modeled the concrete frames, Eqs. 2.33 and 2.34 were used to determine the building stiffness for evaluation of the effects of building weight on tunneling induced building deformation. Farrell et al. (2012) applied Eq. 2.37 to calculate the building stiffness for assessment of the risk damage to the building, and the numerical results well match the real measurements. Generally, these researches investigate the influence of one or several important factors on the model responses individually whilst the coupling effects between these factors were not taken into consideration. Therefore, it is valuable to study these influencing factors which may affect the building behavior simultaneously by employing an adequate numerical model, and to evaluate the relative importance of these influencing factors by using global sensitivity analysis method. To be specific, the possible influential factors (e.g. inherent material properties, geometrical and tunneling parameters), such as soil stiffness and shear strength, tunnel overburden depth, distance between the tunnel axis and the building, soil-structure contact properties, volume loss around the tunnel due to excavation, stiffness of the building, and structural loads acting on the building are

considered to study their effects on the building behavior by the use of an adequate FE numerical model.

In spite of the fact that numerical simulation method is capable to predict the building behavior by considering all the details, the uncertainty embedded in soil and tunneling parameters cannot be captured by FE-model in a deterministic approach. Due to the natural variability of soil characteristics, the measurement error in quantifying the soil properties and diminutive fraction of the investigated soil volume in comparison with the whole affected soil domain (Journel & Alabert 1989), the soil parameters are associated with inevitable uncertainties. Furthermore, some constitutive parameters have no physical meaning and they are difficult or even not possible to be determined by laboratory tests or in-situ investigations that significantly enhance the uncertainty of system responses as well. In numerical simulation, the uncertain parameters are normally assumed in a preliminary study. Afterwards, back analysis is widely applied to identify the model parameters and to update the values of uncertain parameters on the basis of the real measurements (Khaledi, Mahmoudi, Datcheva, König & Schanz 2016). During this process, reliable field measurements are essential for parameter identification/update. In addition to reliable measurement data, the quality of the parameter identification process can be increased by employing appropriate field data from expedient locations depending on the physical and hydro-mechanical incidents that take place in the soil domain. Therefore, an optimum design for the sensor locations is necessary and can be decisive to enhance the quality of identified parameters. However, the methodology of Design of Experimental (DoE) is not well established in the field of geotechnical engineering yet. Hölter et al. (2015) conducted a research on an optimal design of monitoring strategy for appropriate parameter identification in soft clays using global sensitivity analysis. They concluded that an optimal arrangement in terms of the type and position of the sensors can be determined by evaluating the sensitivity field in the relevant geometrical area. Within this framework, the concept of optimal sensor locations based on sensitivity field is applied in this research for tunnel excavation under existing buildings. The optimal sensor locations to measure the soil deformations for the purpose of constitutive parameter identification and model update can be evaluated. The detailed description will be given in Chapter 4.

2.4 Introduction of advanced process simulation

Numerical investigation of mechanized tunneling via FEM is popular in both research activities and engineering practice. However, it is time-consuming to obtain the accurate

and detailed model responses using the finely meshed tunnel model. Especially in case of 3D tunneling, the numerical model is created to be large enough to avoid the influence of boundary effect. Furthermore, as the sequential excavation method is employed to simulate the tunneling process, the steady-state solution with a constant shape of the settlement trough is only reached after many steps of excavation (Franzius et al. 2005*a*). Consequently, the simulation of the FE-model is extremely computational cost consuming. Additionally, when a sophisticated constitutive model is applied to describe the soil behavior, it may need smaller time steps and elements that will make the convergence difficult, especially in the hydro-mechanical coupling analysis.

In the tunneling design phase, complexity arises from simulating the TBM progressive excavation considering all construction details and interactions by dedicating an appropriate constitutive model to assess the mechanical behavior of the soil deposit. Generally, an adequate constitutive model should address soil's fundamental behavior under the stress paths that take place in the domain. While in the numerical simulation, the resulting stress path also depends on the applied constitutive model. Therefore, it should be careful to choose the appropriate constitutive model in the corresponding domain. As mentioned before, the mechanized shield tunneling comprises several sub-systems that should be addressed in the numerical simulations. The contribution of the sub-systems and tunneling induced hydro-mechanical interactions impose complex load patterns in the vicinity of tunnel whilst the rest of the model remains significantly uninfluenced. The highly affected region around the TBM is called near-field zone. In many academic and practical attempts, not only the contribution of certain sub-systems is neglected but also a basic constitutive soil model such as conventional Mohr-Coulomb model is uniformly assigned to entire soil domain (Shin et al. 2002; Mollon et al. 2013*b*). The basic constitutive models are usually inappropriate for complex stress paths; however, their limited number of parameters can be simply measured in laboratory (e.g., direct shear and triaxial tests). For instance, conventional Mohr-Coulomb model provides questionable results for non-monotonic loading due to its unique stiffness for loading, unloading and reloading (Vakili et al. 2014, 2013; Brinkgreve 1994; Molenkamp 1998) where mechanized tunneling mainly imposes loading-unloading-reloading cycles specially to near-field subdomain. Thus, on the one hand, employing advanced soil models is essential to enable accurate prediction of the system responses due to non-monotonic loading. On the other hand, Zhao et al. (2015) revealed that simulation of a real supported tunnel excavation (Western Scheldt tunnel in the Netherlands) in layered soil by using sophisticated constitutive models may entail exact knowledge about large number of constitutive parameters where some parameters are difficult to obtain due to the complex and costly in-situ or laboratory tests.

It was therefore noticed that although advanced models can enhance the quality of the numerical predictions, the uncertainties in the predictions due to embedded uncertainty in advanced constitutive parameters will be notably increased. In addition, identifying the constitutive parameters based on the data from monitoring and observations in such cases incorporates with tremendous efforts. In the case of Western Scheldt tunnel, Zhao et al. (2015) conducted an extensive sensitivity analysis and pointed out that the soil parameters of just one layer in the vicinity of the tunneling zone have the most dominant influence on the prediction of the deformations in the system.

2.4.1 Adaptive constitutive modeling

In past decade, several numerical techniques have been developed to pay more attentions to a given zone within the model where the stress and/or strain is applied or the boundary conditions have changed during analysis. Heaney et al. (2013) applied a recovery-based algorithm in the adaptive mesh refinement approach that aims to reduce the discretization error during analysis. In this approach, the mesh refinement takes place once the incremental deviatoric strain in the observation domain exceeds the allowable error. Elias (2016) developed an adaptive technique to investigate the development of fracture in the discrete model. Their simulations started with coarse mesh discretization in the elastic material, then the mesh was adaptively refined in the regions that suffer high stresses which may induce cracking and strain localization. All these approaches aim at enhancing the quality of the numerical predictions (decreasing the global error) without inducing excess computational costs. It is worth mentioning that the constitutive model used to describe the material behavior is not adaptive with the variation of the stress or strain. Therefore, it is of interest to develop an innovative concept of adaptive constitutive modeling in the numerical simulation of mechanized tunneling. To be specific, appropriate constitutive models can be assigned to different subdomains (near- and far-fields) with respect to time (excavation step) and space in accordance with the actual location of TBM and its corresponding stress path. For instance, the advanced constitutive model is applied in the near-field around the tunnel to describe the most complex system behavior, while the rest of the tunneling model can be simulated using the basic constitutive model. By doing so, the accuracy of the numerical results is achieved. At the same time, in comparison with the model where advanced constitutive model is applied in the entire domain, the uncertainty of the model responses is reduced by using basic model where less uncertain model parameters are involved. Additionally, the computational cost decreases as well. The detailed explanation of this methodology will be given in Chapter 6.

2.4.2 Submodeling

During numerical simulation of engineering problems, in order to provide a model that is robust, representative and cost-economy for explaining the complex behavior in the region of interest, one of the possibilities is to reduce the problem to a smaller scale, by means of cutting out a local part of the large scale model. This approach is called submodeling (also known as multi-scale modeling) which is widely applied in structural engineering. Bogdanovich & Kizhakkethara (1999) conducted 3D finite element analysis of doubled-lap composite adhesive bonded joint using submodeling approach and found that submodeling provides much smoother stress variations and higher stress peaks in a narrow region near the end of the overlap of the structure. In the research of Liu et al. (2006), submodeling technique was applied to study the fatigue damage in the railroad wheels, both computational efficiency and model accuracy are achieved. Li et al. (2009) developed a methodology for concurrent finite element modeling in the framework of submodeling. In their approach, the linear global structural behavior and non-linear damage features of local details in a large complicated structure could be concurrently analyzed. Ciptokusumo et al. (2009) applied the submodeling technique to investigate the stress distribution of a structure with different boundary conditions and model geometry sizes, and they concluded that submodeling is a powerful tool for reduction of simulation time and precise results. Nevertheless, there is limited numbers of research on geotechnical problems using submodeling technique. Spickermann et al. (2005) conducted numerical modeling of primary stress states in deep seated slope problems using submodeling approach. Shen et al. (2009) applied submodeling method to conduct dynamic numerical simulation of cutterhead and soil interaction in slurry shield tunneling, and their approach was validated based on the monitored data from the model test for Yangtze River tunneling project. According to these studies, submodeling is a powerful tool to study in details for parts of the large scale engineering problems and the challenge is to find an optimal constitutive model that adequately reflects the reality and the needs of details. However, rare studies are reported on submodeling technique in the tunneling problems. As mentioned before, complex load patterns occur in the near-field around the tunnel and this domain progressively moves with the advancement of TBM, it is of interest to apply the submodeling technique in numerical simulation of mechanized tunnel excavation. By doing so, the FE model has smaller size and mainly focuses on the near-field around the tunnel and region of interest. Furthermore, in case of parametric study of engineering problems (e.g., sensitivity, inverse and probabilistic analyses, etc.), intensive evaluation of the numerical model might be needed (Sert & Kılıç 2016; Hölter et al. 2017).

Hence, the computational cost of FE simulation can be significantly reduced by applying submodeling technique. Within this framework, the submodeling approach for tunneling simulation will be introduced in this thesis.

2.4.3 Hybrid modeling

One of the main objectives of tunnel excavation is to control the tunneling induced ground movement especially when there is buildings on the ground surface. In this process, there are two categories of model parameters that play the significant role. First is the soil parameters that govern the soil behavior under different load patterns. Second is the tunneling process parameters (face pressure, grouting pressure, etc.) that highly affects the model boundary conditions. Therefore, it is necessary to have adequate knowledge on these model parameters for the reliable prediction of the tunneling induced system responses, such as surface settlements. For the soil parameters, parameter identification is widely applied when the soil deformations at surface or sub-surface level are well documented. While the tunneling process parameters can be controlled to fulfill the design criteria when the soil parameters have been identified. In the tunnel design stage using numerical simulation, the parametric study for these model parameters are inevitable, intensive evaluation of the FE model is required. Therefore, the aforementioned submodeling technique can be applied. It is worth mentioning that the submodel boundary conditions should not be constant when the soil parameters vary. It is time-consuming to derive the corresponding boundary conditions from the global model each time. Therefore, this research proposes an innovative hybrid modeling approach to address this problem. In this hybrid modeling approach, the process-oriented submodeling approach (detailed FE simulation) is combined with the efficiency of metamodel (or surrogate model) which can provide a data base for the boundary conditions of the submodel. Furthermore, this approach is extended by involving the tunneling process parameter optimization in the submodel. When the soil parameters have been identified, the tunneling parameters can be optimized to control the tunneling induced soil deformations in the following excavation steps. The detailed methodology and application for hybrid modeling approach will be introduced in Chapter 6.

3 Numerical modeling of mechanized tunnel excavation

3.1 Introduction

Nowadays the numerical methods have been widely applied in tunnel design, the modern user-friendly and pre- and post-processing tools are being developed to make the numerical modeling of tunnel excavation efficient and robust. On the one hand, the numerical model can take into account the complex material behavior and sophisticated boundary conditions, and the parametric study can be easily carried out. On the other hand, the proper use of numerical tools requires sufficient background knowledge on both geotechnical engineering and numerical method itself. Therefore, results of numerical analyses often need to be verified by the experienced engineers to ensure that the results are plausible (Möller 2006). The main numerical tools includes Finite Element Method (FEM), Finite Difference Method (FDM), Boundary Element Method (BEM), Discrete Element Method (DEM), etc. In this research, FEM is adopted to model the tunneling process, and the general description of the numerical model is given in this chapter. The model geometry, boundary conditions, tunnel staged excavation process, material constitutive model, soil-structure interaction are introduced in both 2D and 3D numerical models. All these features have been considered by using the commercially available FE-code *Plaxis*.

3.2 2D FE model

Fig. 3.1(a) shows the geometry and mesh discretization of the 2D tunneling model. The 15-node triangular elements are used to model the soil elements. Due to the symmetry of the model, only half of the model is simulated to optimize the computational cost of the numerical solution. The diameter of tunnel (D) is assumed to be equal to 8.5 m. The overburden depth (Y) of the tunnel is variable which depends on the detailed application,

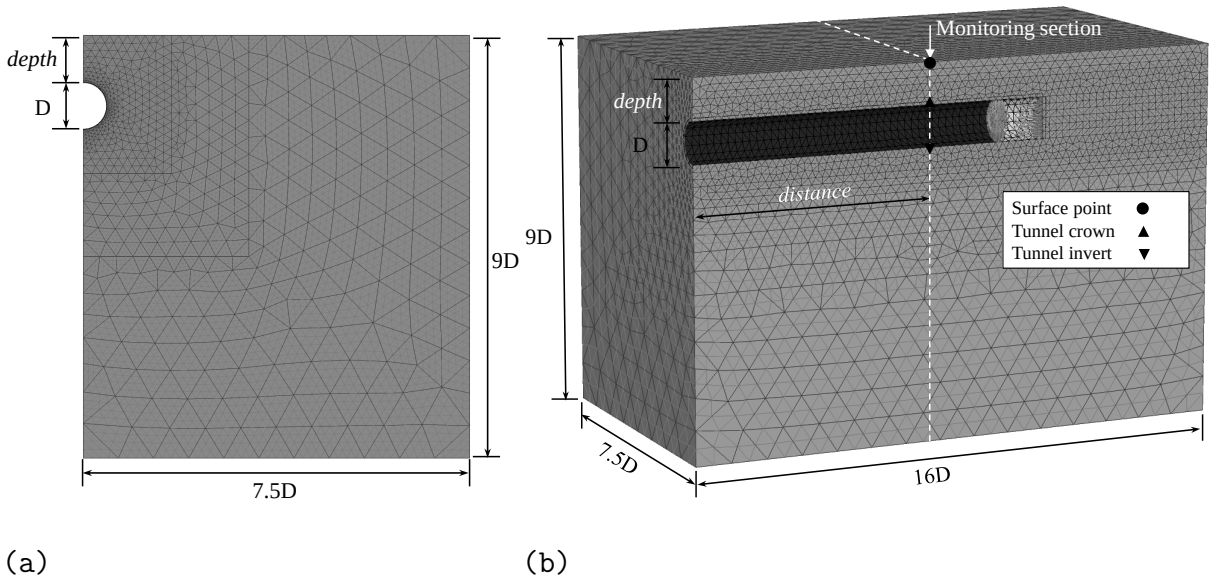

Figure 3.1: Geometry of tunnel for (a) 2D model (b) 3D model

this will be specified in the corresponding chapter. By conducting a series of trial analyses, the appropriate size of the model domain and appropriate mesh discretization were determined in a way that model responses are not influenced by boundary conditions and domain discretization. To be specific, in the first step, a reference model is generated by applying very fine finite element discretization and the solution in terms of ground settlements at the observation points was further considered as the "true" solution. In the next step, a model with coarser spacial finite element mesh was generated and the mesh coarseness factor in the area nearby the tunnel was varied until the maximum discrepancy between the current solution and the "true" solution became less than 0.5%. This last finite element mesh is further adopted in the presented hereafter analysis. Fig. 3.2 shows an example of determining the mesh discretization of a 2D tunneling model. The true value of maximum settlement is obtained via a fine mesh discretization, the discrepancy between current model result and true value decreases with increasing element numbers. When the element number is higher than about 2800, the model is considered to be accurate enough and will be used in the continuous analysis.

The TBM-shield and concrete lining segments are modeled by using shell elements that obey isotropic linear elastic constitutive behavior. The detailed material properties will be given later in the specific chapters. It should be noted that the most realistic numerical model should properly address the joints between the lining segments in the longitudinal direction. However, as mentioned in the previous chapter, Blom (2002) pointed out it is applicable to use the homogeneous ring with a reduced bending stiffness to involve

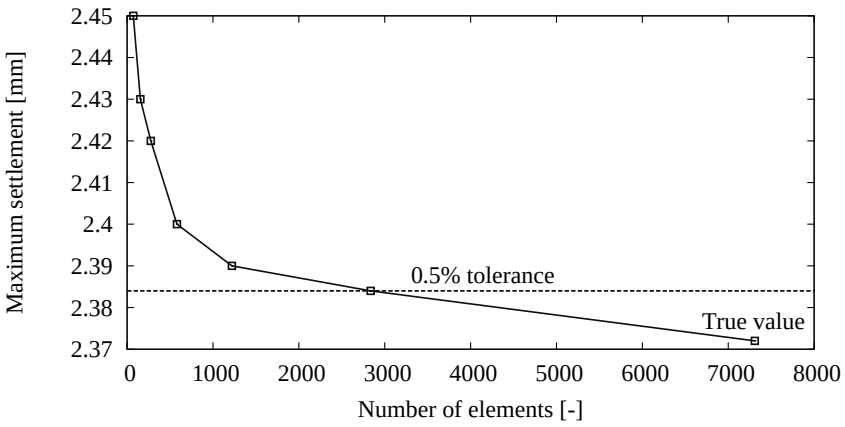

Figure 3.2: An example to determine the FE mesh discretization

the global influence of the longitudinal joints on the bending stiffness. Furthermore, the prior studies have shown that simulating the lining system by an isotropic shell element provides an adequate level of accuracy in comparison with field data (Möller & Vermeer 2008; Bakker 2003). Therefore, in the current study the lining is modeled as a single ring without considering segmental joints for the sake of simplicity.

The interaction between soil and structure elements is simulated with reference to in-built interface elements (Brinkgreve et al. 2014). In the numerical simulations, interface elements consist of pairs of nodes, compatible with both sides of soil element or shell element. By the use of interface elements, the relative deformation between the shell and surrounding soil elements is enabled. As the mechanical behavior of contact between tunnel and soil depends on the type of soil and volume loss around the tunnel, the contact properties may vary in a certain range. In most geotechnical applications, the reduction factor (R_{int}) for the contact between the concrete and the soil is taken in range of 0.7-0.75. However, during mechanized tunneling, the intermediate gap between the tunnel and the soil is filled with the mortar grout that hardens with time. Since the mortar has less short-term strength and stiffness than concrete lining element, the reduction factor in the numerical model can be reduced slightly. Therefore, a reduction factor of 0.6 has been assigned to the interface elements between the tunnel and surrounding soil. Additionally, the contact between shield skin and surrounding soil that is mixed with bentonite for slurry shield TBM might be slightly weaker than that of the contact between lining and surrounding soil. While for the sake of simplicity, a reduction factor of 0.6 is assigned to the interface elements between the shield and soil as well.

In the 2D plane strain condition, the simulation of staged excavation, face support pressure and backfill grouting are not straightforward. Since the soil/structure elements in

the direction of tunnel axis cannot be associated to the progressive excavation, the face pressure and progressive excavation process are not considered in the 2D model. Soil excavation is modeled by deactivating the soil elements inside the tunnel. The support of the TBM shield is simulated by assigning the shield material to the corresponding shell elements that represent the TBM. After that, contraction method is used to model the volume loss around the tunnel. In order to model the grout injection, a distributed mechanical load is used and applied on the surrounding soil elements. It should be noted the shell elements that represent the TBM are not activated when applying the grouting pressure. After grout injection, the lining material is assigned to the shell elements to model the final lining installation.

In this 2D tunneling model, the mechanical boundary conditions on the bottom and outer boundaries of the model as well as the symmetry surface is defined by restricting the normal deformations where the in plane displacements are allowed. There is no mechanical fixity on the model surface and the ground water level will be defined later in each chapter.

3.3 3D FE model

As mentioned before, the three dimensional excavation process and face support cannot be captured by the 2D model. Therefore, these factors have been taken into account in the 3D numerical model to study their influences on the model responses.

Fig. 3.1(b) shows that 3D model is generally the extrusion of 2D model in the direction of the tunnel axis. The 3D FE model is set up using 10-node tetrahedral elements and 6-node triangular elements for soil and shell elements, respectively. The width of single precast concrete lining segments is assumed to be equal to 1.5 m. Thus, TBM advances 1.5 m in each step of the staged excavation. To avoid the collapse of the soil body in front of TBM, face support pressure is applied. As described in section 2.2.2, this face support is numerically simulated through a depth dependent laterally distributed load on the front soil elements. The value of face pressure is determined with respect to the vertical stress arisen from the weight of soil deposit (ZTV 2012), and its gradient is 12 kPa/m related to the unit weight of bentonite suspension. The grouting pressure is applied at the tail of TBM and its value is recommended to be higher than the face pressure at the same depth (ZTV 2012), in this research the value of grouting pressure is defined by increasing the face pressure for 50 kPa at tunnel crown. The grouting pressure linearly increases from

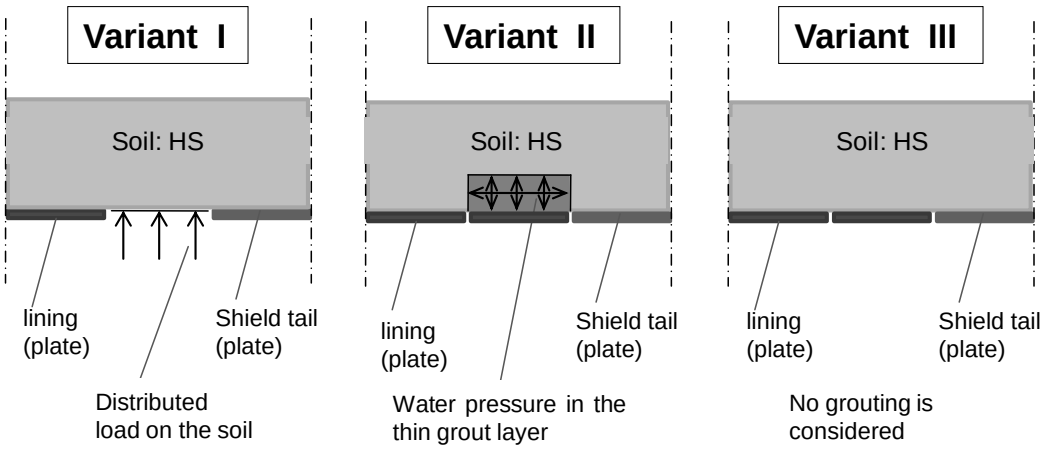

Figure 3.3: The schematic shape of different variants for the numerical simulation of the grouting pressure

tunnel crown to invert with gradient of 15 kPa/m which is determined based on the unit weight of the grout material.

The staged excavation process is modeled via a step-wise procedure, where the progressive advancement of TBM is achieved by a sequential of 1.5 m soil excavation in each step. In this sequence, the excavated soil is deactivcated and the support pressures as well as the newly installed lining segments are activated. By using the similar approach introduced in Zhao et al. (2015), the first six excavation steps represent the advancement of 9 m long TBM-shield, the shell elements are activated with assigned TBM material. Afterward, the installation of lining proceeds by assigning the lining material to the corresponding shell elements.

In mechanized tunneling process, the back-fill grouting is regularly conducted by injecting the suspension mortar at the TBM tail void, which can be numerically dealt with as a mechanical or hydro-mechanical process. To study these numerical approaches, three different variants for the numerical simulation of back-fill grouting are taken into consideration, namely distributed mechanical load (variant I), constant hydraulic total pressure (variant II), and no grouting pressure (variant III). The schematic shape of the variants for the numerical simulation of the grouting at the tail void of the TBM is shown in Fig. 3.3.

In variant I, the backfill grouting process is simplified as a distributed mechanical load (total pressure) which is applied on the soil elements (length of one lining ring). It should be noted that the lining elements are not activated in the grouting area. Furthermore, the hardening of the grout material is not considered in the preliminary study. This

means when the TBM advances in each step, the grout material injected in the last step is assumed to be solid and behaves same as the surrounding soil. Due to these reasons, in variant I the load is not applied to the lining extrados. Additionally, the influence of different methods of simulating the hydro-mechanical grout pressure has been investigated by Lavasan & Schanz (2017). The outcome of this research also shows that despite the popularity of the mechanical pressure to simulate the grout pressure, this method does not adequately predict the bending moments in the lining. However, this numerical simulation approach is widely referred to simulate the grouting pressure both in academia and practice. Although simulating the grouting pressure as mechanical load at the excavation boundary (variant I) satisfies the equilibrium in the system, it does not reflect the hydraulic backfill grouting procedure. In real mechanized tunnel excavation, the lining erection is carried out inside the shield. Hence, the grouting process is conducted in the intermediate zone between the newly installed lining and surrounding soil. Therefore, in variant II, a thin layer around the lining (assumed to be 20 cm based on Talmon & Bezuijen (2009)) is assumed to represent the grouting zone. The grouting pressure is applied as a predefined isotropic hydrostatic pore pressure (total pore pressure) in this thin layer. This load will be transferred to both the surrounding soil and the lining extrados. The mechanical balance in this approach is ensured by the simultaneous installation of lining and grout injection. Variant III assumes no physical gap between the lining element and the surrounding soil where the construction is simulated by changing the stiffness and weight of the shell element from TBM shield to concrete lining. In addition, as the soil excavation and lining installation take place simultaneously in a single construction/calculation phase, there is no chance that the numerical model captures properly the stress release/redistribution around the tunnel due to tunnel construction. Accordingly, although this numerical simulation approach (Variant III) properly adopts neither the hydro-mechanical incidents nor the stress release/redistribution around the tunnel, it is presented to study the influence of simplifying assumptions on the model responses (e.g., surface settlement, pore water pressure, etc).

To observe the final lining forces and deformations after tunnel excavation, the synthetic monitoring section is defined as the vertical cross section which is far away from the boundary, the exact distance will be specified in the corresponding chapters. On the monitoring section, the measurement points are specified at tunnel's crown, invert and ground surface. Lining axial forces, bending moments and radial displacements are extracted with the advancement of TBM to study the influence of present excavation on the tunneling induced system behavior.

3.4 Hierarchical modeling strategy

In numerical simulations of tunneling construction, the ground deformations and structural forces are affected by large numbers of factors due to the complexity of ground behavior and excavation procedures. It is a challenge to choose an appropriate constitutive model to reproduce the soil behavior by considering the realistic heterogeneity, anisotropy, sensitivity and loading history (OCR) of soil deposit. Normally the soil is assumed to be homogeneous and isotropic material, and both elastic and plastic behaviors are taken into account. While the soil stiffnesses may vary due to different stress levels which are related to the confining pressure due to depth of the soil deposit. In the plastic domain around the excavation zone, considering the hardening/softening behavior is more crucial. Additionally, soils show different stiffnesses in unloading/reloading conditions compared to the primary loading (Schanz 1998). The non-linear elasto-plastic models were employed in Möller & Vermeer (2008), it was found that soil deformations are highly influenced by the constitutive model, while structural forces are less influenced by the choice of the constitutive model. Vakili et al. (2014) investigated the influences of soil constitutive model on the numerical results of mechanized tunneling and suggested to be careful in employing the appropriate constitutive model for reliable results.

In order to study the effects of soil's elasticity, plasticity and small strain stiffness on the lining forces and soil deformations, four hierarchical constitutive models are employed in this study. Namely (a) Linear elastic model (LE), (b) Mohr-Coulomb model (MC), (c) Hardening soil model (HS), and (d) Hardening soil model with small strain stiffness (HSS).

LE model is used in the numerical simulation to evaluate the applicability of the analytical methods in predicting the system behavior. In reality, however, the soil does not behave in such an ideal manner but in highly non-linear way (Potts & Zdravković 1999). O'Reilly & New (2000) pointed out that, by using simple linear elastic soil constitutive model rather than more sophisticated non-linear models, the maximum surface settlement could be reasonably predicted, however, the distortion and curvature of the surface settlement could not be well predicted. Additionally, the plastic irreversible deformation of soil body also should be taken into account. Schweiger (2008) summarized the various constitutive models for modeling soil behavior, and concluded that an advanced elasto-plastic model is more likely to accommodate the actual soil behavior around the excavation zone. Therefore, due to the important role of constitutive model in accurate

prediction of system deformability (Vakili et al. 2014), the sophisticated elasto-plastic Hardening Soil (HS) model is employed.

In order to show the influence of non-linearity and plasticity on system deformability, numerical scenarios are defined by employing LE and HS models. In HS model, the soil stiffnesses (E_{oed}, E_{50}, E_{ur}) are defined to be stress dependent. Accordingly, the stiffness increases with depth where the confining stress is higher. Several studies have indicated that the tunneling problems mainly deal with unloading-reloading stiffness (E_{ur}) as the main deformations are imposed to the system due to soil excavation (unloading) or the grout injection and face stabilizing process (reloading). Within this framework, the elastic modulus in LE model is assumed to be correlated to E_{ur} in hardening soil at each depth. Accordingly, the profile of stiffness (E_{ur}) over depth (z) is retrieved at geostatic stress condition (before the excavation) for HS model and assigned to the elastic soil stiffness (E) as a linear function of depth (z), namely $E = f(z)$. After that, this depth dependent soil elastic stiffness is defined in the LE model.

Since it is difficult to study the effect of non-linear stiffness and hardening plasticity individually for HS model. Due to this reason, the linear elastic perfectly plastic Mohr-Coulomb (MC) model is selected as an intermediate constitutive model to describe this class of soil behavior. When same elasticity parameters are used in LE and MC model, the influence of material plasticity on surface volume loss can be evaluated. Therefore, depth dependent elastic modulus distribution is defined in MC model, and shear parameters defined in MC model are same as those used in HS model.

Finally, in order to capture the realistic behavior of soil in small strain range, the most sophisticated Hardening soil model with small strain stiffness is adopted.

It is worth mentioning that the soil deformations and structural forces are also highly influenced by the construction procedures and the soil-structure interaction. TBM excavation may change the ground pressure distribution before lining installation, and the grouting injection keeps the support firm and reduces the soil deformations. This plays an important role in the accurate prediction of system behavior. In this study, applying the hierarchical modeling strategy aims to evaluate the effects of constitutive models, construction procedures and the soil-structure interaction.

4 Ground movements and associated building responses due to tunneling

4.1 Introduction

Tunnel excavation inevitably induces unloading due to soil mass removal and stress relaxation in the soil domain around the tunnel that leads to stress redistribution and ground movements. In order to evaluate the components of surface volume loss and to obtain a general correlation between them, a series of numerical simulations are conducted in this chapter using different constitutive models. The numerical results are compared to those obtained by empirical solutions, modification of the empirical method is proposed. The proposed equations are validated on typical types of clay/sand and a case study of centrifuge tests from the literature. Furthermore, since many buildings in the urban environment are supported by shallow or deep foundations, the tunneling induced deformations can jeopardize the integrity of foundations themselves. Thus, the effects on buildings in the vicinity of the tunnels is evaluated to ensure that their influences do no exceed the allowable capacity of the structure. Additionally, sensitive analysis is conducted to distinguish the relative importance of model parameters in determining the ground movements and building behavior due to tunnel excavation. After that, the sensitivity field is utilized to indicate the proper monitoring regions to install the relevant sensors.

4.2 Mechanized tunneling induced ground movements

4.2.1 Numerical simulation of tunnel excavation

To numerically simulate the mechanized excavation process, a 2D numerical model is generated to save time and computational efforts, due to the fact that intensive evaluation

of the FE-model is required during the parametric study. The 2D FE model has been introduced in Chapter 3 (see Fig. 3.1(a) and section 3.2).

It should be noted that in this part of the study, the tunnel volume loss due to lining deformation in short- and long-term periods (see Fig. 2.7) is not considered. In other words, only the effect of different diameters of tunnel head and lining induced by overcut zone and conicity of TBM is taken into account. In order to model this kind of tunnel volume loss, contraction factor method is employed (Brinkgreve et al. 2014) which has been described in section 2.2.2. It should be noted that the contraction factor is isotropic and applied stepwise in the numerical simulation. In each iteration of applying the contraction factor, the different stress paths, stress states around the tunnel are not considered. While after applying the contraction factor in each step, the stress distribution around the tunnel varies and the position of tunnel may change to reach a new equilibrium. The contraction factor technically aims at simulation of local soil deformations due to the partial collapse of soil in the overcut zone to fill the intermediate gap between the lining and excavation boundaries. Since this section mainly focuses on the relation between tunnel volume loss and surface volume loss, compensation grouting process at tail of shield TBM is not considered. The ground water level is not considered in the current model for the sake of simplicity.

In the present study, the maximum tunnel volume loss is assumed to be 3%. To the best knowledge of the authors, in the early time, the tunnel volume loss is quite large. For instance, Line No.2 of San Francisco (1983) had about 6% volume loss. With the development of tunneling techniques, nowadays, tunneling induced volume loss can be well controlled. Heathrow express trial tunnel (1995) had about 2% volume loss, Madrid metro extension line No.1 (1999) has about 0.8% volume loss, Wehrhahn-line metro project (2010) had about 0.5% volume loss. Therefore, in this study, the author has assumed the range of tunnel volume loss as 0-3% that represent a wide range of projects worldwide.

Fig. 4.1 shows the schematic illustration of tunneling simulation process. The first step in 2D simulation is to generate the initial stress distribution via K_0 analysis (section A-A). To model the soil excavation, the corresponding soil elements inside the tunnel are deactivated and the TBM-shield material (see Table 4.1) is assigned to the shell elements in one calculation phase (section B-B). In the next calculation phase, lining segments are activated and tunnel contraction is applied to model the volume loss (section C-C). To this end, the transverse settlement trough can be evaluated, and the relation between the tunnel volume loss and surface volume loss can be investigated.

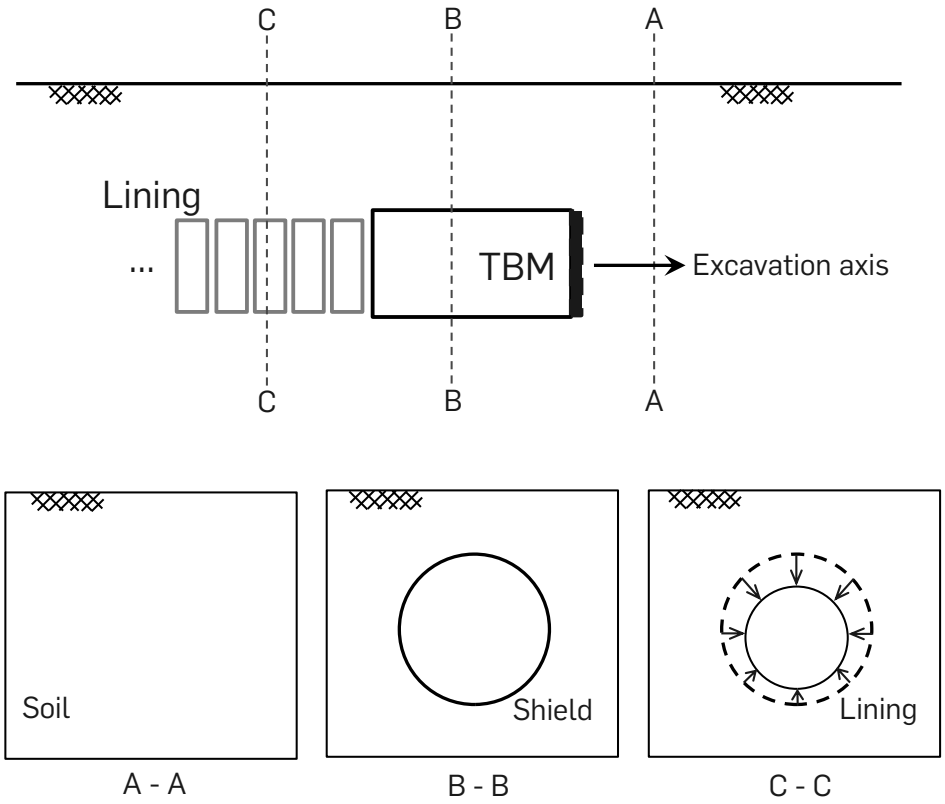

Figure 4.1: Schematic illustration of tunneling simulation process

Table 4.1: Input parameters of the used linear elastic constitutive model for TBM shield

Parameter	TBM shield	Unit
Axial stiffness (EA)	$4.2 \cdot 10^7$	[kN/m]
Bending stiffness (EI)	$1.4 \cdot 10^5$	[kNm^2/m]
Weight (w)	90	[kN/m^3]
Poisson's ratio (ν)	0.3	[-]

Table 4.2: Input parameters of the used soil constitutive model − the Hardening Soil model

φ'	ψ'	c'	E_{50}^{ref}	E_{oed}^{ref}	E_{ur}^{ref}	p^{ref}	m	K_0	ν	γ
25°	0	0	10 MPa	10 MPa	30 MPa	0.1 MPa	1.0	0.57	0.2	17 kN/m^3

Verruijt & Strack (2008) pointed out that the surface deformations above a bored tunnel are influenced by the buoyancy effect of a tunnel that is lighter than the excavated soil. They concluded that although other effects may play a role in determining the shape of the settlement trough, the buoyancy effect is large enough in relation to the settlements due to ground loss during tunnel excavation. Since this research aims to investigate the effect of tunnel volume loss on the surface volume loss, the weight of the TBM shield is assumed to be equivalent as the weight of the excavated soil, and lining is assumed to have identical properties as the shield. By doing so, the surface settlement profiles obtained by numerical simulation exclude the buoyancy effect. It is worth mentioning that due to the high stiffness of shield and lining, the ovalization deformation of the tunnel can be neglected.

In order to study the influence of soil elastic/plastic deformation on the tunneling induced surface volume loss, three constitutive models are applied in this part of the study. Namely LE model, MC model and HS model. As mentioned before, in incompressible soil the soil cannot contribute to system's volumetric deformability, the volume of surface settlement trough is equivalent to the volume of soil on the tunnel boundary converging into the tunnel. To reproduce such soil behavior in numerical simulation, Linear Elastic (LE) model is employed with elastic Poisson's ratio (ν) equals 0.5. Consider the effect of soil compressibility, different values of Poisson's ratio are used in LE model. To evaluate the effect of soil plasticity, linear-elastic perfect-plastic MC model is applied. Here MC has same elasticity parameters as the LE model. Finally, the elasto-plastic Hardening Soil (HS) model is employed to account for the fact the soil behaves in a highly non-linear way during tunneling process. The synthetic HS parameters set used in this study is given in Table 4.2, HS model and MC model have identical plasticity parameters. Furthermore, it is worth mentioning that the elastic stiffness distribution in LE/MC model is same as the unloading-reloading stiffness (E_{ur}) over depth in HS model, this has been introduced in section 3.4.

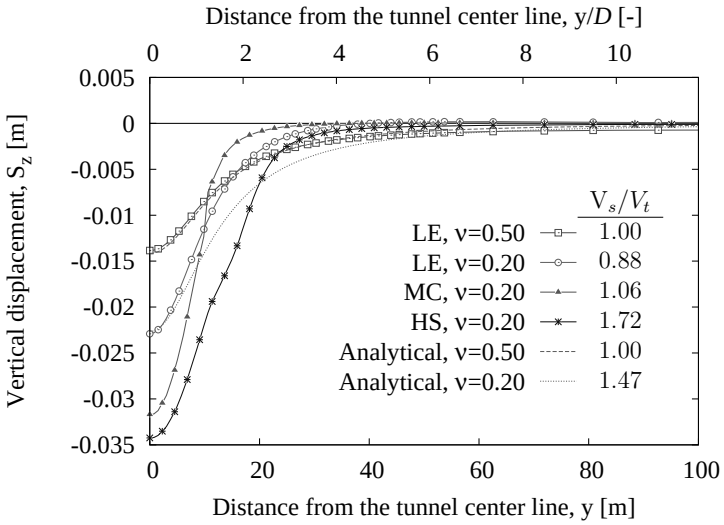

Figure 4.2: Transverse surface settlement profiles obtained from numerical solution using different constitutive models and analytical solution (Verruijt & Booker 1996) with R_t=1%

4.2.2 Components of the surface volume loss

The transverse surface settlement profiles obtained by numerical approaches are shown in Fig. 4.2. Contraction factor (tunnel volume loss ratio) of 1% is used for all these numerical analyses and the tunnel has an overburden of Y=D (D is the diameter of tunnel). Furthermore, the analytical solution proposed by Verruijt & Booker (1996) is employed to derive the tunneling induced surface settlement profile using different values of Poisson ratio. Additionally, the ratios between surface volume loss and tunnel volume loss are presented for the numerical simulation using different constitutive models.

According to Fig. 4.2, in both analytical and numerical solutions using LE model along with ν=0.5, the ratio of V_s and V_t tends to unity as 1, the Poisson's ratio induces incompressible soil behavior. When ν decreases to 0.2, the analytical solution provides larger settlements in the entire domain. However, the numerical results differ from the analytical results. To be specific, in the region closes to the tunnel center line, surface settlements increase and this coincides with the analytical result. While for the region $2D$ away from the tunnel center line, the surface settlements decrease. This can be attributed to the coupled correlation of strain (displacement) variations to the stress variations. When contraction factor is applied, the strain variations result in a different stress distribution. Subsequently, further deformations are generated in order to reach a new equilibrium. While this not considered in the analytical solution. Additionally, the arching effect also contributes to the discrepancy between analytical and numerical solutions. After applying

tunnel volume loss, the direction of principal stress changes in the near field around the tunnel. Subsequently, the mean stress may increase and affects the volume change of the soil domain. This deformation mechanism cannot be captured by the analytical solution.

As seen in Fig. 4.2, compared to the settlement trough calculated by LE model (ν=0.2), larger surface volume loss is observed when MC model (ν=0.2) is used to describe the soil behavior. This reveals the contribution of plasticity to enlarge the settlement trough. The relation between surface volume loss (V_s) and tunnel volume loss (V_t) for different constitutive models and Poisson's ratios is shown in Fig. 4.3(a). The correlation between V_s/V_t and R_t is illustrated in Fig. 4.3(b). As seen, surface volume loss increases with increasing of tunnel volume loss. The relation between surface volume loss and tunnel volume loss is linear in case that soil is assumed to be an elastic material. When the linear-elastic perfectly-plastic MC model is used to describe the soil behavior, the relation between V_s and V_t is non-linear. Soil plasticity induced ground deformation in accordance with MC model significantly affects the ratio of V_s/V_t (see Fig. 4.3(b)). Within this framework, soil volume change V_g consists of the contributions of Poisson's ratio V_ν and perfect plasticity V_p, namely $V_g = V_\nu + V_p$. Within this framework, Figs. 4.3(c) and 4.3(d) present the relation between V_ν/V_t and V_p/V_t versus R_t. Since same elastic stiffness and Poisson's ratio are used in MC and LE (ν=0.2) models, the proportion of ground volume induced by the Poisson's ratio (V_ν) to the tunnel volume loss is identical. When a small tunnel volume loss ratio (contraction factor) is applied, soil plastic deformation is negligible using MC model. By increasing tunnel contraction factor, plasticity contributed soil volume change increases. This can be seen from Fig. 4.4 which shows the distribution of relative shear stress (ratio of mobilized shear stress and ultimate shear stress) using different contraction factors. Furthermore, Fig. 4.5 presents the distribution of relative shear stress using HS model. As seen, the differences compared to that of MC model highlight the effect of stress dependent stiffness and hardening law of HS model.

According to Fig. 4.3, by applying hardening soil model (HS) that accounts for stress dependency of soil stiffness and isotropic plastic hardening, larger ground movements are generated. Even when tunnel volume loss ratio (contraction factor) is at low level, on the one hand, stress redistribution during tunneling process results in the variation of non-linear soil stiffness; on the other hand, shear strength mobilization of the soil around the tunnel lead to high plastic deformations. Subsequently the surface volume loss is larger than that of MC model. However, with the increase of contraction factor, the ratio of V_s and V_t decreases. This is due to variation of stiffness and hardening of soil. To be more specific, arching effect around the tunnel increases the soil stiffness, which results

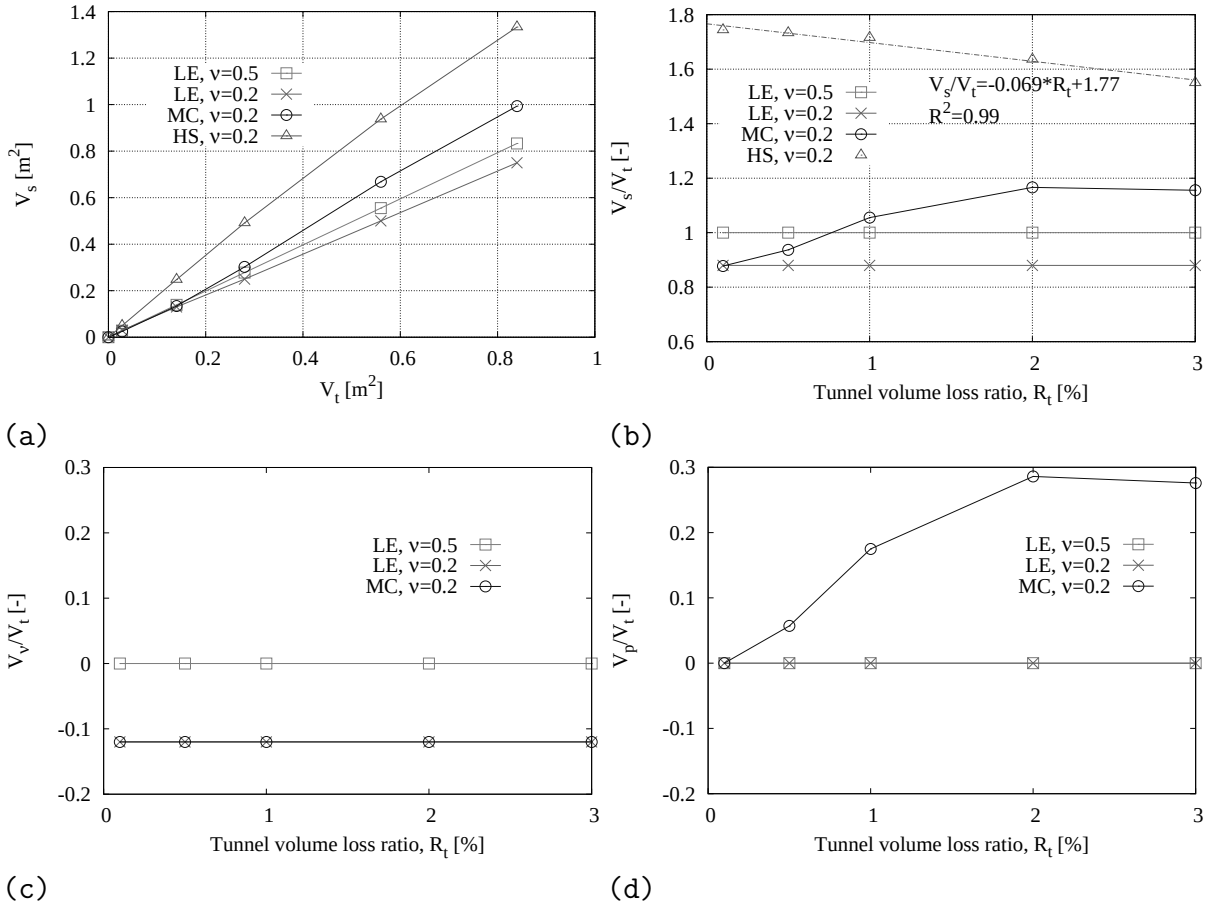

Figure 4.3: The relation between (a) V_s and V_t, (b) V_s/V_t and R_t, (c) V_ν/V_t and R_t, (d) V_p/V_t and R_t

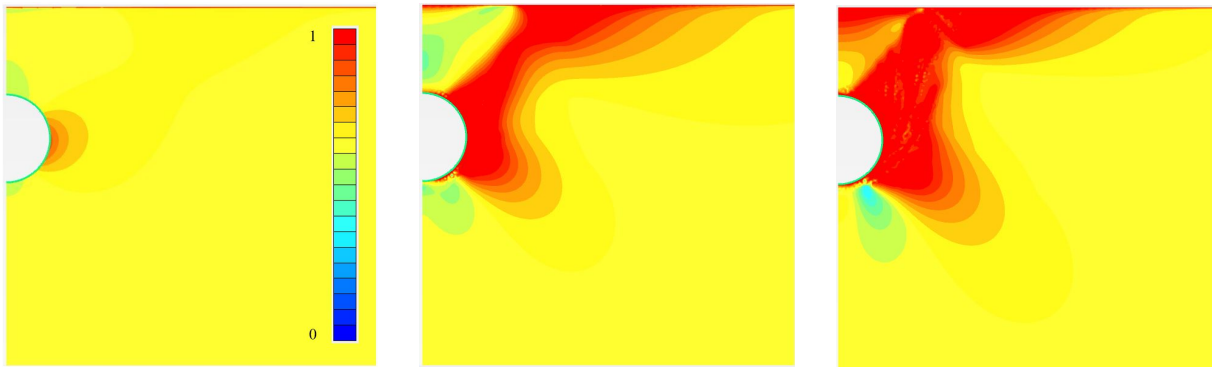

Figure 4.4: Distribution of relative shear stress using MC model with: (a) R_t=0.1%; (b) R_t=1%; (c) R_t=3%

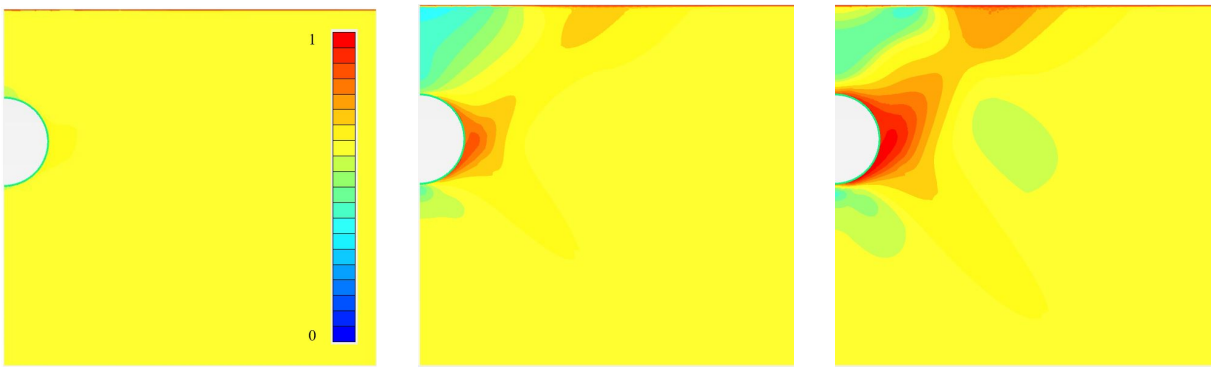

Figure 4.5: Distribution of relative shear stress using HS model with: (a) R_t=0.1%; (b) R_t=1%; (c) R_t=3%

in the reduction of V_ν/V_t with increasing R_t. At the same time, plastic deformation in HS model entails evolution of yield surface due to shear and volumetric hardening rules. Such densification in accordance with plastic deformations is also justified by experimental evidences. With the increase of tunnel volume loss ratio (contraction factor), the yield surface of soil expands and the soil becomes less deformable. Subsequently, same variation of contraction factor results in smaller soil volume change when tunnel contraction factor is at higher level. In other words, the incremental volume change of soil domain gradually decreases by an increase in the tunnel contraction factor. In contrast, for MC model, higher tunnel volume loss ratio (contraction factor) simply means contribution of plasticity to a larger extent. The ratio of V_s and V_t increases with increasing tunnel volume loss ratio (contraction factor). Furthermore, when HS model is used to describe the soil behavior, the relation between V_s/V_t and R_t can be approximated by using a linear function as shown in Fig. 4.3(b). Subsequently, the surface volume loss ratio can be expressed by the tunnel volume loss ratio as:

$$R_s = (1.77 - 0.069R_t)R_t,\ R_t \leq 3\% \tag{4.1}$$

It should be noted that this regression equation is only valid for the case considered in the present study. According to Eq. 4.1, the surface volume loss ratio can be expressed as a quadratic function of tunnel volume loss ratio. Therefore, this relation is applied in the following section to assess the possibility of improving the empirical solution.

Additionally, since stress reduction method (β method) is popular in modeling the volume loss during tunnel excavation, this method is employed in the present study to evaluate whether the findings from contraction factor method still hold true. Fig. 4.6(a) shows the variation of V_s/V_t with increasing R_t using both methods. It should be noted that the

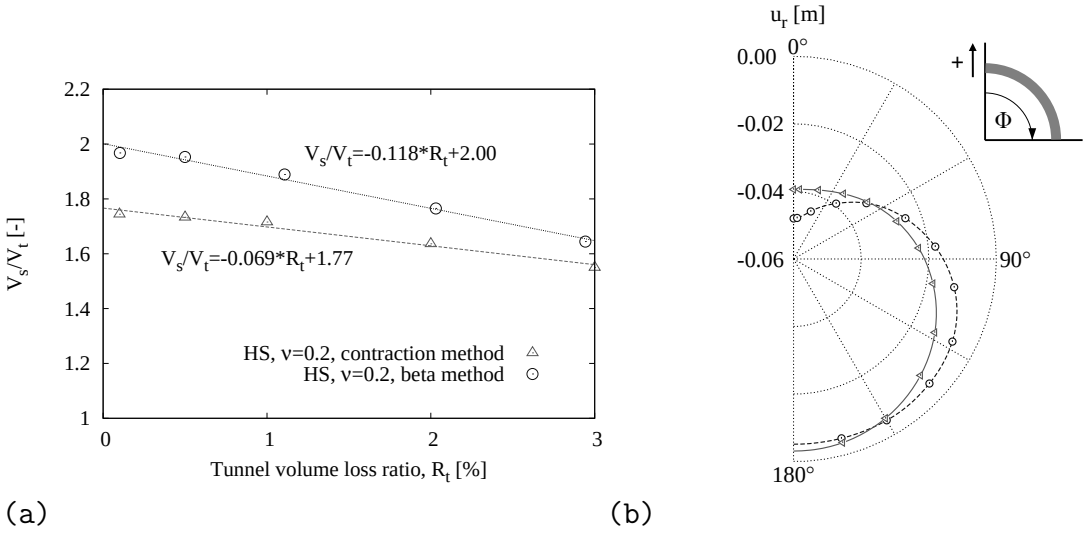

Figure 4.6: Model responses using contraction factor method and β method for (a) V_s/V_t versus R_t, (b) tunnel radial displacements under 1% tunnel volume loss

stress release factor in β method is manually modified to derive the corresponding volume loss due to tunnel excavation. As seen, the relation between V_s/V_t and R_t is approximately linear using β method as well. While the exact values differ. This is due to the different deformation mode of soil around the tunnel which is shown in Fig. 4.6(b). For β method, the soil are free to deform before activating the tunnel elements, while for the contraction factor method, the soil elements are forced to deformed to have consistent deformation with the tunnel elements. In the present study, since the shield has high stiffness and considered as rigid material, the contraction factor method is employed in the following simulations. However, for the real tunneling projects, both methods are applicable and model validation is essential to obtain the appropriate model parameters.

4.2.3 Modification of the empirical solution

In the traditional empirical method, the Gaussian distribution curve needs two parameters (R_s and K_z) to determine the surface settlement trough with certain tunnel overburden. Generally R_s is assumed based on practical experience and K_z is qualitatively assumed to be constant according to soil type. Therefore, it is valuable to find an appropriate way to determine the values of R_s and K_z on the basis of soil/tunnel properties.

According to the above discussion, when identical tunnel contraction factor (R_t) is applied, the surface volume loss ratio (R_s) is controlled by the applied constitutive model. In order to evaluate the corresponding values of K_z, the empirical Gaussian distribution

curve is employed to predict the transverse surface settlement profiles in comparison with the numerically obtained tunneling induced ground movements shown in Fig. 4.2. The comparison of the empirical and numerical results is given in Fig. 4.7. The surface volume loss ratios obtained from FE-model are adopted in the empirical solution. Furthermore, the values of K_z are manually modified to make the empirical results fit the numerical ones. As seen in Fig. 4.7, the empirical results well match the numerical predictions in conjunction with appropriate values of model parameters. Whereas for incompressible soil case (LE model with ν=0.5), the entire soil domain above the tunnel settles due to its incompressiblity in the numerical simulation. This leads to the discrepancy between empirical and numerical solutions. According to these comparisons, under certain value of R_t, the values of R_s and K_z depend on the used constitutive models that describe the soil behavior in different ways. By taking into account the stress dependent stiffnesses and elasto-plastic hardening behavior of soil, the author believes that HS model is able to better describe the soil behavior than LE and MC models. Therefore, the numerical results obtained by using HS model are adopted for the following modification of empirical solution with respect to variable R_t.

In case of $1D$ tunnel overburden and HS model is applied to describe the soil behavior, the surface volume loss ratio R_s can be expressed as a quadratic function of tunnel volume loss ratio R_t (see Eq. 4.1). Here R_t can be identified according to the diameter difference of lining segment and tunnel head. In order to determine the corresponding values of K_z, the surface settlement profiles of numerical model with respect to different values of tunnel contraction factor (R_t) are evaluated and shown in Fig. 4.8(a), and empirical solution is employed to be compared with numerical results. In this process, R_s is calculated based on Eq. 4.1. K_z is is optimized via trial and error to ensure that the discrepancy between empirical and numerical results is minimum. The obtained values of K_z are presented in Fig. 4.8(b). It is found that the correlation between K_z and R_t can be assigned through a linear function. Accordingly, the assumption in traditional empirical solution that K_z is a model parameter which depends on the soil type only might be inadequate.

Based on the above discussion, the model parameters R_s and K_z of the empirical method both can be expressed as function of the tunnel volume loss ratio (R_t) as:

$$R_s = (A_1 R_t + B_1) R_t \tag{4.2a}$$

$$K_z = A_2 R_t + B_2 \tag{4.2b}$$

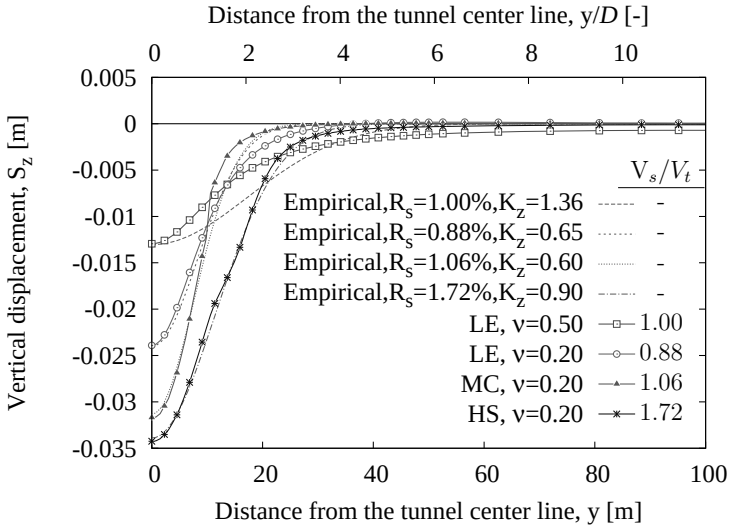

Figure 4.7: Comparison of empirical and numerical solutions for transverse surface settlement profiles with R_t=1%

This equation gives a quantitative relation between the model parameters and tunnel/soil properties by using four fitting parameters A_1, B_1, A_2 and B_2.

In order to obtain the typical ranges of the fitting parameters, 10 typical types of normally consolidated clay and sand were chosen from the literature and applied in the numerical simulation of shallow tunnel excavation ($1D$ overburden). The Hardening Soil parameters are given in Tables 4.3 and 4.4. The numerical simulation of tunneling procedure has been conducted on the basis of the model introduced in section 4.2.1 in conjunction with using different tunnel contraction factors ($R_t \leq 3\%$). Table 4.3 presents the values of fitting parameters and corresponding coefficients of determination for all clays. As seen, the proposed Eq. 4.2 can well capture the relation between R_s and R_t as well as K_z and R_t for all types of clay, and the values of A_1 and A_2 decreases with higher stiffnesses of soil. Likewise, the fitting parameters and coefficients of determination for different types of sand are given in Table 4.4. The relation between R_s, K_z and R_t can be captured by Eq. 4.2 in a good manner. However, the soil stiffness becomes less dominant in determining the fitting parameters due to the dilation behavior of soil which reduces the surface volume loss.

Additionally, it is observed that sand has higher values of A_1 and A_2 than that of clay. To be specific, for the selected clays, A_1 varies between -0.03 and -0.1, A_2 ranges between -0.035 and -0.08. While for the selected sands, A_1 is between -0.1 and -0.25, A_2 ranges between -0.05 and -0.1. Furthermore, the values of B_1 and B_2 for different types of clay and sand are in the same range. Therefore, it can be concluded that the proposed

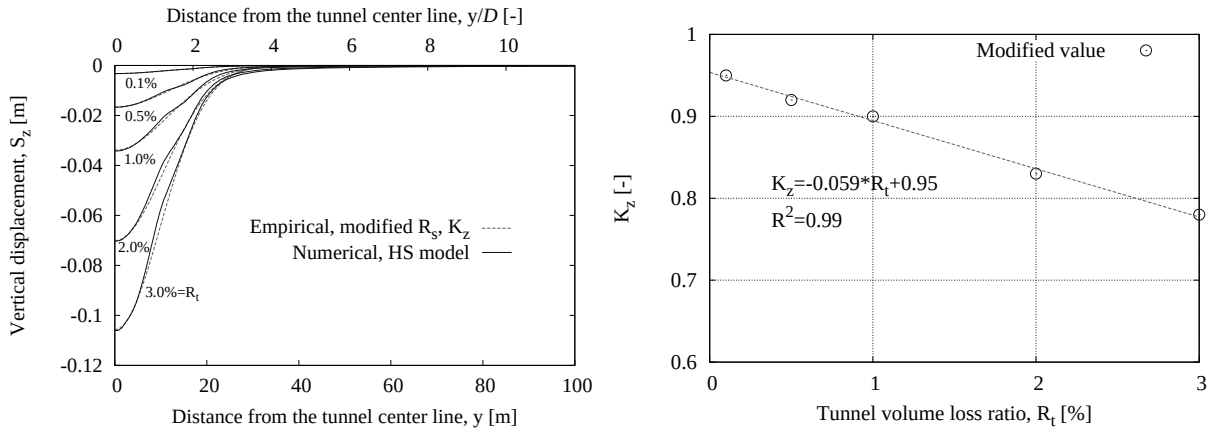

Figure 4.8: Comparison between improved empirical method and numerical solution using HS model: (a) transverse surface settlement profiles, (b) tunnel volume loss ratio dependent K_z

modification in accordance with Eq. 4.2 enhances the empirical solution by having more knowledge on the model parameters R_s and K_z.

4.2.4 Case study of centrifuge tests

In the work of Marshall et al. (2012), tunneling induced ground movements during centrifuge tests were reported. Fig. 4.9(a) shows the relation between tunnel volume loss and surface volume loss. The test were performed on the University of Cambridge 10 m diameter geotechnical centrifuge (Schofield 1980). A dry silica sand known as Leighton Buzzard Fraction E, with a typical D_{50} of 122 μm, a special gravity of 2.67, maximum and minimum void ratios of 0.97 and 0.64 respectively, was used. During the tests, a relative density of 90% was applied. The tunneling process was modeled by reducing the tunnel diameter to simulate schematically a ground loss. The cavity between the brass cylinder and the membrane was filled with water. The tunnel diameter was reduced by withdrawing water from this cavity. An image-based displacement measurement technique geoPIV was used to measure surface and subsurface soil displacements. For more details on the experimental design, one is referred to Farrell (2010); Marshall et al. (2012); Ritter et al. (2017).

According to Fig. 4.9(a), tunneling induced surface volume loss increases with increasing tunnel volume loss and this correlation is non-linear. It is worth mentioning that the diameter of tunnel D is different for these three scenarios (Marshall et al. 2012), subse-

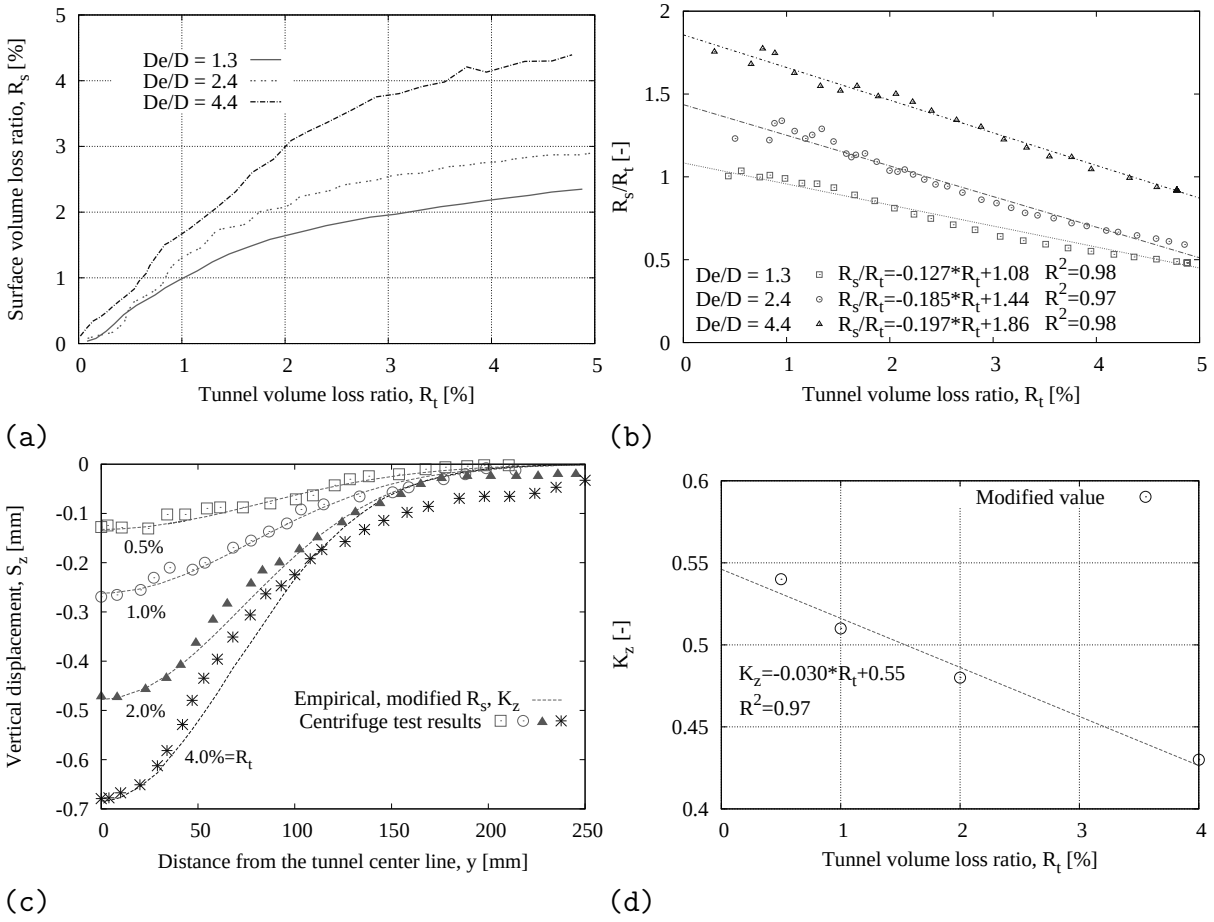

Figure 4.9: Case study: (a) relation between R_s and R_t from the centrifuge test (after Marshall et al. (2012), D_e/D represents cover-to-diameter ratio, while the tunnel diameter is different for these three scenarios), (b) relation between R_s/R_t and R_t derived based on the centrifuge test results, (c) comparison of the surface settlement profiles using modified empirical method and experimental results under D_e/D=1.3 (Farrell 2010), (d) tunnel volume loss ratio dependent K_z

Table 4.3: Hardening Soil model parameters for different types of clay and corresponding fitting parameters for Eq. 4.2

	Clay				
Parameter	Taipei[1]	Shanghai[2]	Bangkok[3]	Cairo[4]	Sweden[5]
φ'[°]	29	30	28	25	32
ψ'[°]	0	0	0	0	0
c'[kN/m^2]	0	17	11.5	10	3
E_{50}^{ref}[MPa]	6.55	8.37	9.5	10	33
E_{oed}^{ref}[MPa]	6.55	8.37	12	15	17.7
E_{ur}^{ref}[MPa]	19.65	25	30	30	66.3
p^{ref}[MPa]	0.1	0.1	0.1	0.1	0.1
m[-]	1	1	1	1	1
K_0[-]	0.55	0.5	0.5	0.5	0.53
A_1[-]	-0.031	-0.032	-0.046	-0.068	-0.106
B_1[-]	1.72	1.64	1.62	1.70	1.73
$R^2(R_s)$	0.95	0.94	0.94	0.98	0.99
A_2[-]	-0.035	-0.038	-0.043	-0.052	-0.076
B_2[-]	0.94	0.96	0.95	0.98	0.92
$R^2(K_z)$	0.99	0.99	0.99	0.99	0.99

Note: 1:Goh et al. (2017), 2:Xue et al. (2014), 3:Surarak et al. (2012), 4:Ahmad et al. (2015), 5:Wood (2016).

quently, the overburden depth differs. On the basis of Fig. 4.9(a), the correlation between R_s/R_t and R_t can be derived and shown in Fig. 4.9(b). As seen, the ratio of R_s and R_t can be expressed as a linear function of R_t for all scenarios, which proves the applicability of the proposed Eq. 4.2 for tunnel with variable diameters and overburden depths.

By analogy to Fig. 2.13, the comparison of surface settlement profiles using modified empirical equation and centrifuge tests is presented in Fig. 4.9(c). In this figure, the measured surface settlements were obtained using cover-to-depth of 1.3. Therefore, the correlation of $R_s = (-0.127R_t + 1.08)R_t$ derived in Fig. 4.9(b) is employed to modify the empirical equation. The value of K_z is manually optimized by trial and error to have the minimum discrepancy between the prediction and measurements. Within this framework, the modified values of K_z can be expressed as a linear function of R_t as $K_z = -0.030R_t + 0.55$ presented in Fig. 4.9(d).

Table 4.4: Hardening Soil model parameters for different types of sand and corresponding fitting parameters for Eq. 4.2

	Sand				
Parameter	Hostun[1]	Hokksund[2]	Toyoura[3]	Monterey[2]	Blessington[2]
$\varphi'[^\circ]$	34	34	37	36.7	42.4
$\psi'[^\circ]$	0	2.5	7	3.7	6.6
$c'[\mathrm{kN/m^2}]$	0	0	1	0	0
$E_{50}^{\mathrm{ref}}[\mathrm{MPa}]$	20	20	27	35	44
$E_{oed}^{\mathrm{ref}}[\mathrm{MPa}]$	20	25	27	35	25
$E_{ur}^{\mathrm{ref}}[\mathrm{MPa}]$	60	100	81	105	155
$p^{\mathrm{ref}}[\mathrm{MPa}]$	0.1	0.1	0.1	0.1	0.1
m[-]	0.65	0.5	0.5	0.5	0.4
K_0[-]	0.44	0.5	0.5	0.41	0.5
A_1[-]	-0.117	-0.121	-0.103	-0.249	-0.247
B_1[-]	1.94	1.66	1.45	2.07	1.64
$R^2(R_s)$	0.98	0.99	0.99	0.99	0.95
A_2[-]	-0.072	-0.062	-0.057	-0.122	-0.109
B_2[-]	1.00	0.82	0.77	1.04	0.78
$R^2(K_z)$	0.99	0.99	0.99	0.99	0.98

Note: 1:Schanz et al. (1999), 2:Gavin & Tolooiyan (2012), 3:Wong et al. (2012).

Additionally, it should be noted that Eq. 4.2 was proposed for the case in which tunnel volume loss ratio is less than 3%. Nevertheless, it is found that this equation is also valid in the cases where R_t increases up to 5%. According to this case study, it can be deduced that the proposed Eq. 4.2 is applicable to provide better knowledge on the model parameters of the empirical method for the real tunneling problems.

4.2.5 Important factors affecting the tunneling induced ground movements

In the previous numerical simulation, the tunnel overburden is assumed constant as $1D$, since in reality the tunnel overburden is variable, the influence of tunnel overburden depth on the surface settlements should be studied. Furthermore, initial effective stress distribution over the soil domain is dominated by the coefficient of lateral earth pressure K_0, soil

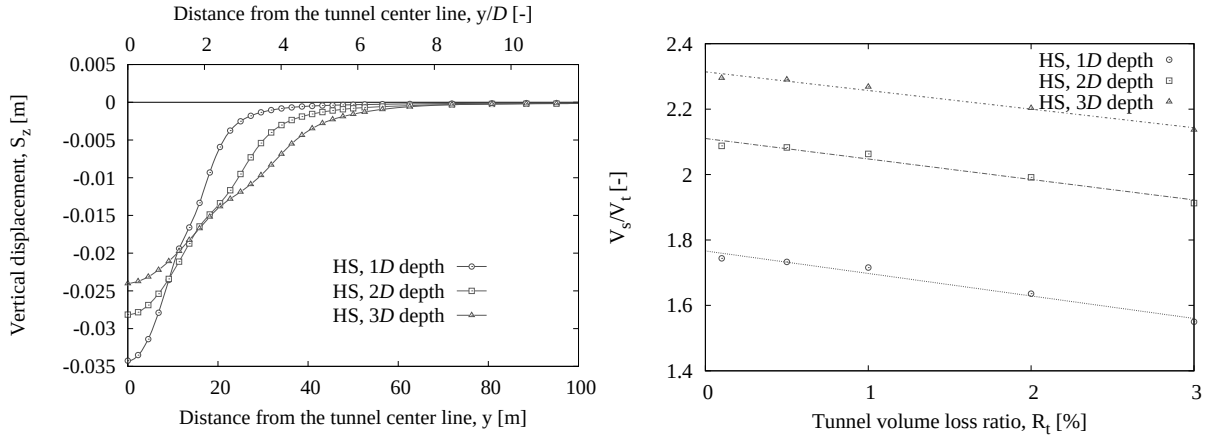

Figure 4.10: Influence of tunnel overburden depth on (a) transverse surface settlement profiles when 1% tunnel volume loss ratio (contraction factor) is applied, (b) volume loss

deformations around the tunnel are significantly affected by the initial horizontal/vertical stresses and this kind of deformation around the tunnel propagates up to the ground surface to form the surface settlement trough. Due to this reason, it is necessary to study the influence of K_0 on the ground movements as well.

Effect of tunnel overburden depth

Fig. 4.10(a) demonstrates the transverse surface settlement profiles for different embedment depths of tunnel. The distance from tunnel crown to ground surface varies from $1D$ to $3D$. It is obvious that the depth of tunnel increases the width of ground settlement trough. However, the maximum settlements at the ground surface induced by tunneling is larger for shallower tunnels. This can be proved by Eqs. 2.19 and 2.17, for a given surface volume loss, tunnel diameter and constant value of K_z, the settlement trough width parameter i linearly increase with higher tunnel depth and the maximum surface settlement is inversely proportional to the depth of tunnel. Moreover, as seen in Fig. 4.10(a), the slope of the settlement profile is flatter in case of deeper tunnel. This means deeper tunnel excavation induces less displacements to the adjacent buildings while the width of influence is wider.

The influence of overburden depth on the tunneling induced volume loss is shown in Fig. 4.10(b). As seen, under the same tunnel volume loss ratio (contraction factor), larger surface volume loss is observed by increasing the depth. However, the increment of the volume change of soil domain gradually reduces with increasing the depth. It can be

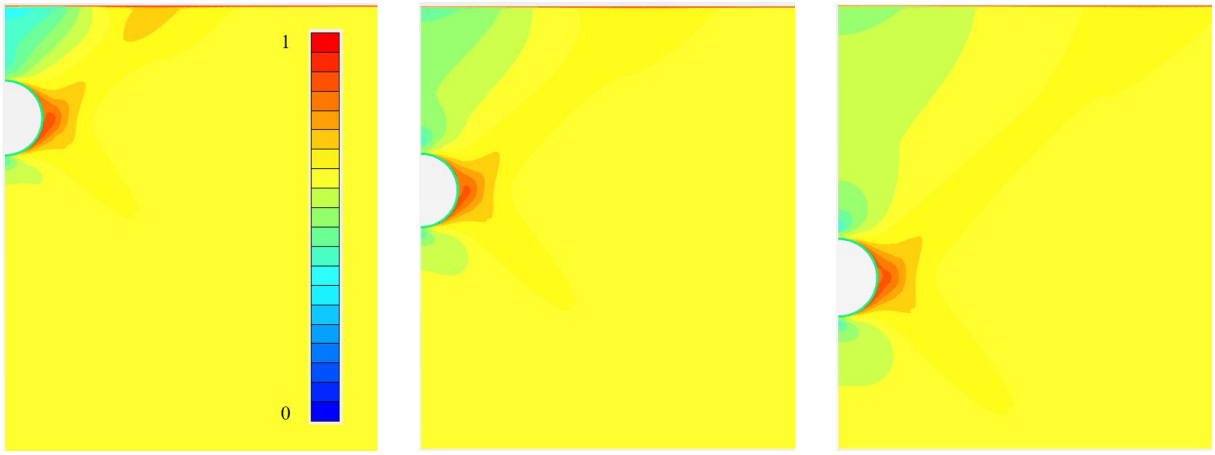

Figure 4.11: Distribution of relative shear stress using HS model and R_t=1% for : (a)1D depth; (b) 2D depth; (c) 3D depth

deduced that volume change of soil domain will be constant when the overburden depth reaches a certain level. In other words, almost identical surface settlement trough will be obtained when the vertical distance between the ground surface and the tunnel boundary is large enough. Moreover, as seen in Fig. 4.10(b), the slope of the regression line between V_s/V_t and R_t remains unchanged in accordance with the tunnel depth. In case of deeper tunnel, the plastic deformations around the tunnel induced by excavation is less influential on the ground surface. This consistent with the distribution of relative shear stress shown in Fig. 4.11.

Based on Fig. 4.10 which shows the effect of tunnel depth on the surface volume loss, it can be deduced that V_s/V_t is a function of tunnel volume loss ratio (R_t) and overburden depth (Y). By conducting more numerical simulations using different depths of tunnel, a nonlinear polynomial is derived to represent this relation as:

$$\frac{V_s}{V_t} = 1.39 - 0.066R_t + 0.42Y - 0.0016R_tY - 0.038Y^2, \text{for } R_t \leq 3\%, Y \leq 6D \ (R^2 = 0.99) \tag{4.3}$$

Fig. 4.12 illustrates the numerical results in a 3D (V_s/V_t, R_t, Y) space, and the corresponding nonlinear polynomial surface provides a good approximation of the surface volume loss. By increasing the depth, the ratio between surface volume loss and tunnel volume loss gradually reaches a constant value, which means the surface volume loss is less affected by tunneling. It should be noted that this nonlinear polynomial equation is valid only for the cases considered in this study, for other cases, the fitting parameters should be calibrated before application. According to the above analyses, the overburden

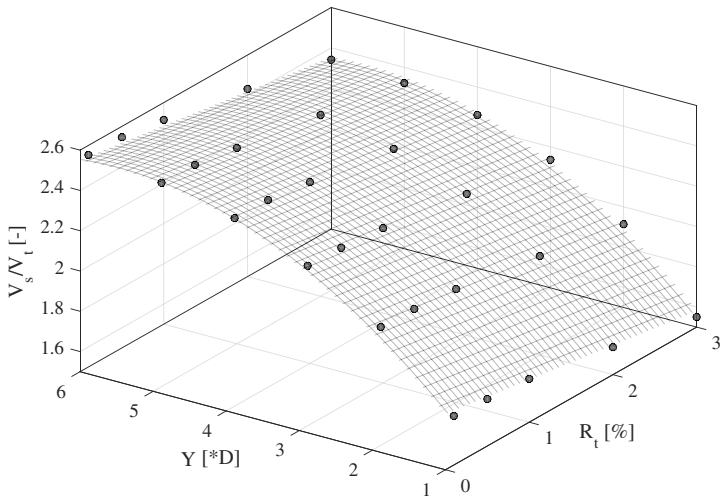

Figure 4.12: Influence of tunnel overburden depth on the surface volume loss

depth has significant influence on maximum vertical displacement, shape of settlement profile and ratio of V_s and V_t.

Effect of K_0

According to the literature study on different clays, it is found that the realistic range of K_0 is between 0.4 and 2.5. Franzius et al. (2005*a*) investigated the influence of K_0 on ground movements resulting from tunnel excavation, and they found that a lower K_0 leads to a higher surface volume loss owing to smaller horizontal earth pressure at tunnel depth. In this section, the influence of K_0 on the surface settlement profiles is evaluated and the results are shown in Fig. 4.13. Here the tunnel overburden depth Y is assumed to be D. As seen, by increasing the value of K_0 in the range of K_0=0.57 (=1-sinφ') to K_0=2.0, less surface volume loss is observed. To be specific, decreasing K_0 reduces the horizontal earth pressure around the tunnel. Since the soil stiffnesses (except E_{oed}) in HS model depend on the minor principle stress, a lower K_0 results in a smaller minor principle stress (direction of minor principle stress may change when K_0 is larger than 1) and therefore lower soil stiffness of soil compared with higher K_0 situations. Subsequently, this reduction of soil stiffness around the tunnel results in an increase of surface volume loss. This is consistent with the findings of Dias & Bezuijen (2014). They pointed out that for the isotropic state (K_0=1) the increment stress is predominantly of deviatoric stress during tunneling process. For the other states, the responses is distinguishable on whether the normal stress is the initial major (σ_1) or minor (σ_3) principle stress. The initial normal stress is σ_3 at tunnel crown for high value of K_0 and at tunnel side for

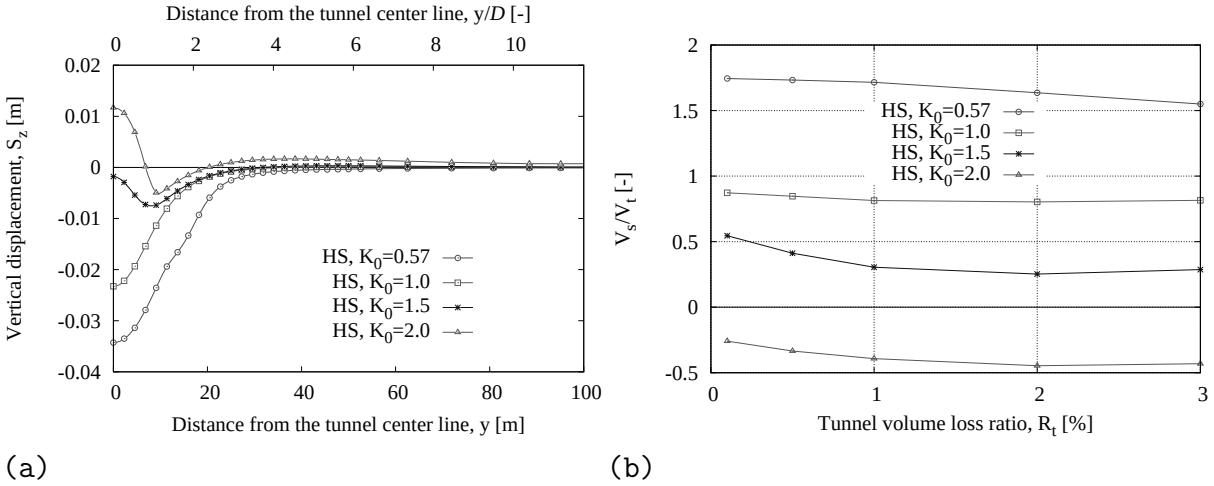

Figure 4.13: Influence of K_0 on (a) transverse surface settlement profiles when 1% tunnel volume loss ratio (contraction factor) is applied, (b) volume loss

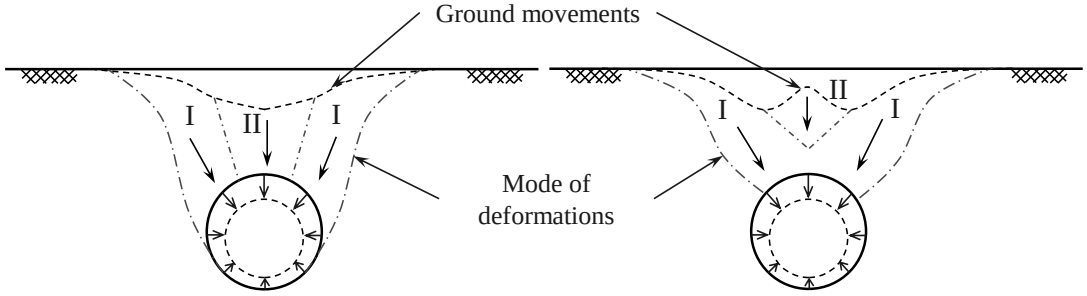

Figure 4.14: Schematic sketch of soil deformation for lower values of K_0 (left) and higher values of K_0 (right)

low value of K_0. During tunnel excavation, the normal stress decreases, which results in a decrease of σ_3 and an increase of σ_1. Finally, both deviatoric stress and mean stress increase.

Fig. 4.13(b) presents the relation between V_s/V_t and tunnel volume loss ratio (R_t) for various K_0. As seen, for higher values of K_0, the relation between V_s/V_t and tunnel volume loss ratio R_t (contraction factor) can not be expressed by a linear relationship. This non-linearity can be explained by the variation of the system behavior for small and large strain in which the contribution of the plastic deformation of the soil is different. Accordingly, the empirical estimation is not appropriate to address the ground movements in this case. Here the surface volume loss can be divided into two parts. First is the downward deformations of soil domain due to tunnel contraction (positive volume loss), second is the larger horizontal stress induced upward deformations (negative volume loss which represents volume expansion) that counteracts the total volume loss in the system.

When the tunnel volume loss ratio is less than 2%, the change of upward deformation is more influential on the surface volume loss. In contrast, when the tunnel volume loss is larger than 2%, the variation of downward settlement induced surface volume loss becomes dominant, which leads to the increase of V_s/V_t with respect to increasing R_t.

To better explain the ground displacements shown in Fig. 4.13(a), the schematic illustration of the mode of deformation with respect to different values of K_0 is presented in Fig. 4.14. Apparently, by volume loss around the tunnel, the soil blocks in the vicinity of the tunnel are forced to convergence to the updated tunnel boundary conditions (contraction). The deformed soil body can be divided into two kinds of blocks. Block I that moves downward due to the variation of tunnel boundary conditions by imposing contraction. However, the deformation mode of block II depends on the value of K_0. Since the horizontal stresses are lower for smaller values of K_0, the lateral stresses acting on the walls of the block II can trigger vertical downward deformations. Nevertheless, for higher K_0 cases, the horizontal stresses are dominant and the kinematics of deformation at high lateral earth pressures coincides with squeezing the soil block II in horizontal directions. Thus, block II experiences less settlement compared to block I. This phenomena was observed by Möller (2006) as well. In his research, tunnel overburden depth was $2D$ and stress reduction method (β-method) was adopted to simulate the tunneling induced volume loss. He firstly applied HS model to model the soil behavior and found that high K_0 leads to heave at the ground surface, and this phenomena is observed in both 2D and 3D FE simulations (see Fig. 4.15). In his second calculation, he applied HSS model to describe the small strain behavior as the elastic stiffness plays the dominant role in tunneling problem. His numerical results confirmed the phenomenon (even heave at ground surface), while this time the magnitude of heave was significantly reduced.

In the present analyses, OCR=1 for normally consolidated soil is considered, however, it should be mentioned that in reality the soil with high value of K_0 corresponds to overconsolidated soil (i.e., London clay). The loading history (OCR) makes the soil stiffer and affect the deformation mode of soil block II as well. Additionally, in reality high values of K_0 are normally observed in the soil domain close to the ground surface. With increasing depth, K_0 decreases and the horizontal stress may not able to form upward effect. This also explains that heave during tunnel excavation related with high value of K_0 of soil is rarely observed in practice. To the best knowledge of the author, tunnel excavation in grounds with high values of K_0 and the effect of ground deformation is a topic for further research.

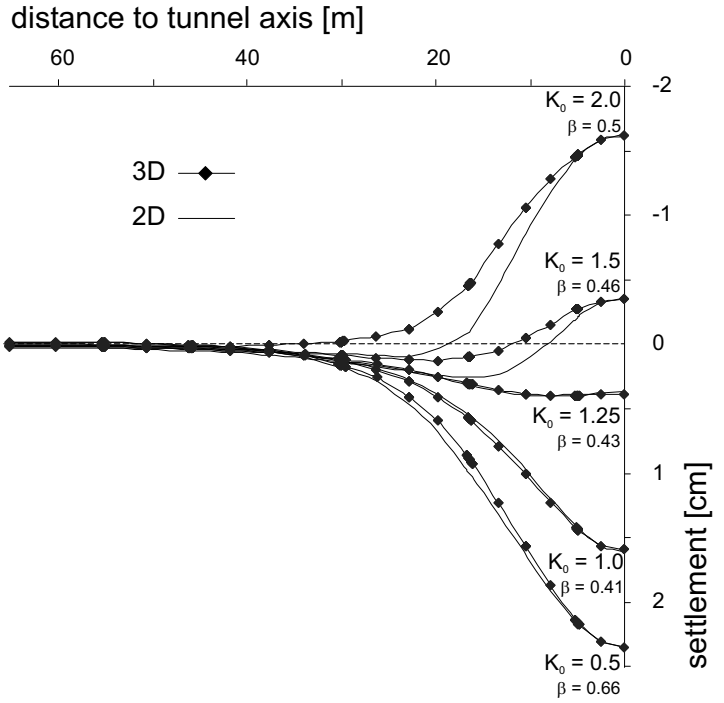

Figure 4.15: Transverse surface settlement profiles from 2D and 3D FE analysis for different values of K_0 (Möller 2006)

4.2.6 Sensitivity analysis

In the previous sections, tunnel overburden and coefficient of lateral earth pressure at rest are considered to study their influence on the tunneling induced surface settlements under identical soil properties. This section takes into account the variation of soil stiffness, shear strength and soil-tunnel contact properties, to evaluate the relative importance of these model parameters in determining the settlement trough. In order to distinguish the relative importance of the model parameters in predicting the surface settlement profiles, sensitivity analysis is conducted. There are two main concepts for sensitivity analysis, namely Local Sensitivity Analysis (LSA) and Global Sensitivity Analysis (GSA). For LSA, the partial derivatives of the model response with respect to related model parameters are evaluated at a given point in the parameter space. It should be noted that if the relation between input and output values is non-linear, sensitivity information obtained by this way is highly dependent on the given local point and step size in numerical calculation of the derivatives (Iott et al. 1985; Rohmer 2014). Hence, it is questionable to apply the LSA result obtained at a given point in the parameter space to the whole parameter space under consideration. Additionally, only one parameter is varied in each evaluation, coupled effect between different parameters is not considered. In contrast,

GSA explores the whole input space of related parameters, the reliability of result is not affected by the nature of model. Moreover, it evaluates the uncertainty contribution not only from the variation of a specific parameter itself, but also from the correlated variations of other parameters. Therefore, GSA can be applied to accurately estimate the sensitivity of model responses to input parameters within the whole input space. In this section, Variance-Based (VB) (Sobol' 1993) method of GSA is applied to study the model response uncertainty due to input parameters uncertainty. This method has been applied to mechanized tunneling problems by Miro et al. (2014); Zhao et al. (2015); Hölter et al. (2017). In the current study, Latin Hypercube Sampling (LHS) procedure is applied to generate a well distributed sample points in the entire input space. According to Saltelli et al. (2008), the number of random samples should be gradually increase to ensure that no significant change in coefficient of variation of the sensitivity index. The first order index S_i (Saltelli et al. 2008) and the total effect index S_{Ti} (Jansen 1999) are calculated to show the relative importance of model input parameters. The equations are given as:

$$S_i = \frac{\mathbf{y_A}^T \mathbf{y_{Ci}} - n\left(\bar{y}_A\right)^2}{\mathbf{y_A}^T \mathbf{y_A} - n\left(\bar{y}_A\right)^2}, S_{Ti} = \frac{\left(\mathbf{y_B} - \mathbf{y_{Ci}}\right)^T \left(\mathbf{y_B} - \mathbf{y_{Ci}}\right)}{2\mathbf{y_B}^T \mathbf{y_B} - 2n\left(\bar{y}_B\right)^2}, \tag{4.4}$$

where $\mathbf{A}$ and $\mathbf{B}$ are two independent (n, k) matrices, each contains n random samples of the input parameters vector $\mathbf{Z}$=$Z_1, Z_2, ..., Z_k$. For matrix $\mathbf{Ci}$, its columns are copied from matrix $\mathbf{B}$ except the i-th column copied from the corresponding column in $\mathbf{A}$. $\mathbf{y_A}$, $\mathbf{y_B}$ and $\mathbf{y_{Ci}}$ are vectors containing model evaluations for matrices $\mathbf{A}$, $\mathbf{B}$ and $\mathbf{Ci}$, respectively. $\bar{y}_A$ and $\bar{y}_B$ are the mean value estimated from components of $\mathbf{y_A}$ and $\mathbf{y_B}$, respectively.

Table 4.5 represent parameters and their corresponding ranges of variation that are chosen according to the experience of the author. It should be noted K_0 is not considered in the sensitivity analysis. This is due to the fact that variation of K_0 changes the mode of deformation around the excavation zone, this cannot be introduced by variation of any other model parameters.

Fig. 4.16 shows the relative sensitivity of ground movements to the model parameters. As seen, the surface volume loss (V_s), maximum surface settlement and maximum slope of the settlement profile are most sensitive to R_t, this is due to the fact that tunnel volume loss triggers the soil deformations by updating the tunnel boundary condition as predefined tunnel contraction factor in the system. Furthermore, soil's friction angle plays an important role in determining the surface volume loss since the plasticity induced volume loss (V_p) is dominated by φ'. Subsequently, the friction angle contributes to both the maximum settlement and slope of settlement profile. However, it is less influential compared to the tunnel depth in the given parameter ranges. This can be explained

Table 4.5: Lower and upper bounds of input parameters for global sensitivity analysis

Parameter	Lower bound	Upper bound	Unit
E_{50}^{ref}*	5	15	[MPa]
E_{ur}^{ref}	15	45	[MPa]
φ'	15	30	[°]
R_{int}	0.4	1.0	[-]
$depth$	$4.25(0.5D)$	$42.5(5D)$	[m]
R_t	0	3	[%]

*$E_{50}^{\text{ref}} = E_{oed}^{\text{ref}} \leq 0.5E_{ur}^{\text{ref}}$

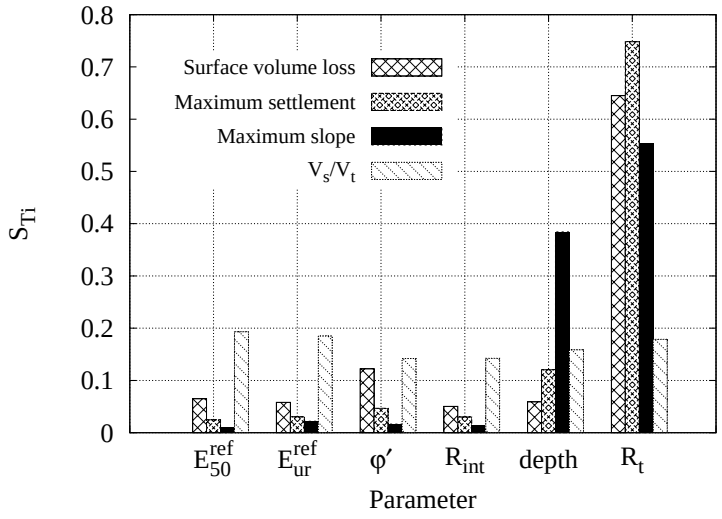

Figure 4.16: Global sensitivity analysis for 2D numerical model responses to soil constitutive parameters and tunneling parameters

by Eq. 2.17 which reflects the position of inflection point of the settlement profile, the variation of stiffness and friction angle in the given range has a little influence on the position of inflection point. However, the position of the inflection point is highly affected by the tunnel depth in this study. This leads to the fact that the maximum slope of surface settlement profile is secondarily sensitive to the tunnel depth.

Since the ratio of V_s and V_t is dominated by the volume change of ground domain V_g, V_s/V_t is sensitive to all parameters that affect the soil deformation around the tunnel. On the one hand, the soil stiffness and shear strength parameters are significant to describe the soil behavior, and they contribute to the magnitude of ground volume loss. The soil-tunnel interaction influences the transition of tunnel boundary conditions on the surrounding soil. On the other hand, the tunneling parameters, such as tunnel depth and contraction factor affects the tunnel boundary conditions. As a result, there is no dominating parameters in the assumed parameter ranges for obtaining the ratio between surface volume loss and tunnel volume loss. All these parameters are important to determine V_s/V_t.

According to sensitivity analysis study, for the purpose of accurate prediction of tunneling induced settlement trough, it is most valuable to obtain adequate knowledge of tunnel volume loss, tunnel overburden depth and shear strength of soil.

4.2.7 Conclusion

This section introduces several factors that may induce volume loss during mechanized tunneling process. The relation between the tunnel volume loss and the surface volume loss is investigated by using a 2D FE model. Modification of the empirical solution is proposed to make it capable to predict the surface settlement trough. Furthermore, global sensitivity analysis is conducted to evaluate the relative importance of overburden depth, K_0, soil-tunnel interaction and soil properties in determining the volume change of soil domain. The main findings are summarized as follows:

1. When the soil is modeled as an incompressible elastic material, surface volume loss and tunnel volume loss are identical. When the soil is modeled via Mohr-Coulomb model, the relation between plasticity induced soil volume change and tunnel volume loss is non-linear. In case of applying Hardening Soil model, the ratio of surface volume loss and tunnel volume loss has a linear relationship with the tunnel volume loss ratio (contraction factor).
2. Surface volume loss ratio and settlement trough width parameter in the empirical solution can be respectively expressed as quadratic and linear equations of tunnel

volume loss ratio. The proposed equations have been validated on different types of clay/sand and a case study of centrifuge tests.

3. By increasing tunnel depth, maximum surface settlement reduces, the slope of settlement trough becomes flatter. The ratio of surface volume loss and tunnel volume loss can be expressed a linear polynomial of tunnel volume loss ratio and overburden depth.

4. For higher K_0 cases, the kinematics of deformation at high lateral earth pressures coincides with squeezing the soil block above the the tunnel crown in horizontal directions, which results in heave at the ground surface. In contrast, only vertical downward deformations are observed in cases that lower K_0 is applied.

5. Global sensitivity analysis shows that surface volume loss, maximum surface settlement and maximum slope of the settlement profile are most sensitive to tunnel volume loss ratio. For the purpose of providing accurate prediction of surface settlement profiles, it is most valuable to obtain adequate knowledge of tunnel volume loss, overburden depth and shear strength of soil.

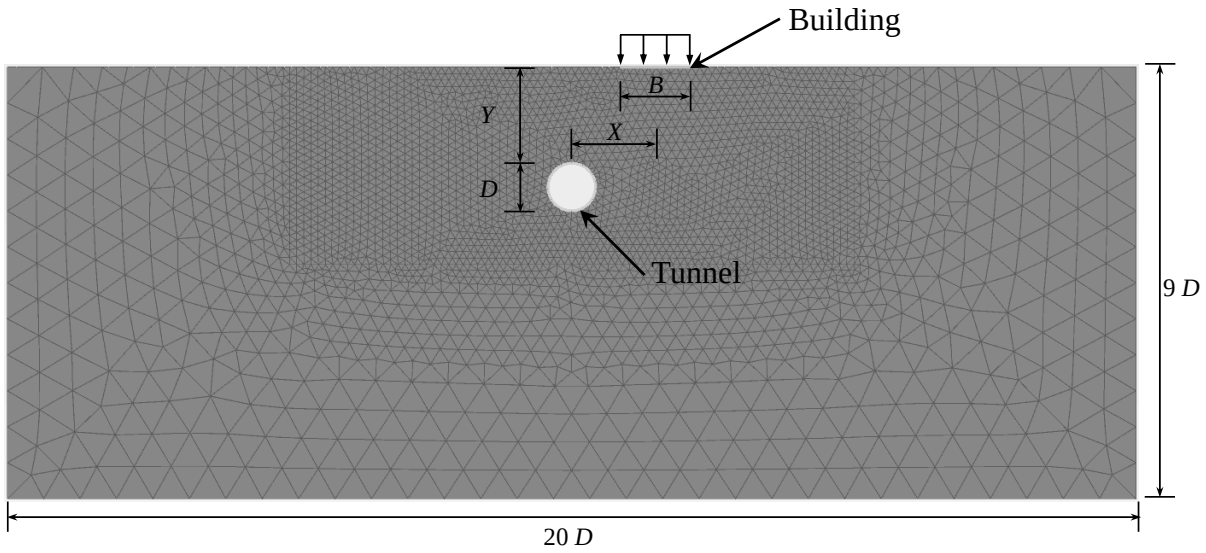

Figure 4.17: Geometry and mesh discretization of the tunneling model (where D= 8.5m is tunnel diameter, B=1.5D is building width, X is horizontal distance between the centers of the tunnel and building, Y is the overburden depth)

4.3 Mechanized tunneling induced building settlements and tilt

4.3.1 Model description

In this section, 2D numerical analyses are conducted to study the building behavior induced by tunnel excavation. The parametric study is conducted to determine the suitable dimensions beyond which no changes, in both soil stress and displacements, occurr. The model geometry to be analyzed in this research is shown in Fig. 4.17. The mechanical boundary conditions on the bottom and outer boundaries of the model is defined by restricting the normal deformations where the in plane displacements are allowed. There is no mechanical fixity on the model top surface and the ground water level is not considered.

In the numerical simulation, the existing building on the ground surface is modeled by using beam elements that are based on the Mindlin beam theory (Bathe 1982). This means that, in addition to bending, shear deformation is considered as well. The axial stiffness and bending stiffness are calculated using the aforementioned Eqs. 2.33 and 2.35, respectively. Here the slab properties are assumed as E=2.3·10^7 kN/m^2, A_{slab}=0.15 m^2/m, I_{slab}=2.8·10^{-4} m^4/m on the basis of Franzius et al. (2004). Furthermore, the beam

elements are assumed to be weightless and the corresponding load of the entire structure is modeled as a vertical uniform load applied on the beam elements.

In order to study the effect of tunneling on the building behavior, staged construction process is considered in numerical simulation. First, the initial stress distribution is computed in the absence of tunnel (K_0 analysis). It is assumed that tunnel excavation carries out long after the construction of the building. Second, the tunnel excavation and lining installation take place. Third, the soil volume loss due to overcut zone and conicity of tunnel are modeled. Lavasan & Schanz (2017) studied the influence of the method that is selected to model the volume loss on the model responses. They found that each of these methodologies has their specific limitations and advantages, the decision on the numerical simulation method should be taken with a careful attention to the desired output of the numerical model. In the current study, contraction factor method (Brinkgreve et al. 2014) is utilized. The value of contraction factor is expressed as a percentage, representing the ratio of the volume reduction and the notional excavated area (per unit length). In practice, the volume loss ratio due to over-excavation varies between 0.1% to 3% depending on the geometry of the TBM, depth of the tunnel, and the intensity of the prohibiting measures to reduce the tunneling induced settlements (i.e. backfill grouting in tail void). Taking into account, the influence of stress release in the proximity of the tunnel, the possible range for the variation of the contraction factor can be slightly higher. Finally the interaction between the tunnel and surrounding soil incrementally reaches an equilibrium condition where the support pressure of lining itself balances the released earth pressure. It is significant to note that system deformations before tunnel excavation ought to be set at zero, since this analysis is for the purpose of evaluating the reactions of the building solely due to tunnel construction.

In this study, the soil behavior is described by using elasto-plastic Hardening Soil (HS) model. The synthetic parameters set used in this study are given in Table 4.2. The effect of ground water is not considered for the sake of simplicity.

Farrell et al. (2012) used beam theory to assess the risk of damage to buildings during tunnel excavation. Their study showed clear regions where hogging and sagging were observed for the relatively flexible buildings. In contrast, for the rigid buildings, an apparent tilt towards the tunnel centerline with no distinct hogging or sagging regions was observed. Due to this reason, two types of building with different stiffnesses are considered in this study. The corresponding material parameters are given in Table 4.6. Buildings I and II represent a 1-story and 10-story buildings, respectively. Accordingly,

Table 4.6: Input parameters of the used linear elastic constitutive model for tunnel lining and building

Parameter	Lining	Building I	Building II	Unit
Bending stiffness (EI)	$2.18 \cdot 10^5$	$1.30 \cdot 10^4$	$7.12 \cdot 10^4$	[kNm^2/m]
Axial stiffness (EA)	$1.05 \cdot 10^7$	$6.90 \cdot 10^6$	$3.80 \cdot 10^7$	[kN/m]
Weight	25	-	-	[kN/m^3]
Load	-	10	100	[kN/m^2]

building I is relatively flexible while building II is relatively rigid. The corresponding load of the entire structure is determined based on Franzius et al. (2004).

To simulate the interaction between the structures (i.e. tunnel and building) and adjacent soil, interface elements are employed and the reduction factor R_{int} is assumed to be 0.6 for both soil-lining and soil-building interaction in the preliminary study.

4.3.2 Effect of stiffness and load of the building

In this section, numerically calculated model responses are discussed to examine the effects of stiffness and load of the building on the tunneling induced building settlements. Firstly, the free-field surface settlement troughs are compared with that when building and load are applied. Fig. 4.18(a) shows the transverse ground settlement profiles for different surface scenarios when 1% tunnel contraction factor is applied. In these scenarios, the tunnel is located at the center of the building and the vertical distance between tunnel crown and building is $1D$ (D=8.5m is the tunnel diameter). As seen, larger maximum surface settlement is observed when building exists on the ground surface. By increasing the load and stiffness of the building, the corresponding surface settlements beneath the building increase. Furthermore, it is apparent that building II responds rigidly and there is no tilt due to symmetrical location of the tunnel. In contrast, the response of building I is seen to be relatively flexible with obvious regions of sagging and hogging. This is due to the effect of stiffness and load of the building, and it is consistent with the finding of Farrell et al. (2012).

Figs. 4.19 and 4.20 show the directions of the principle stresses before and after tunnel excavation for the cases mentioned above. Due to the load of the building II, stresses of the soil bearing the building are enlarged and the directions of principle stresses rotate towards

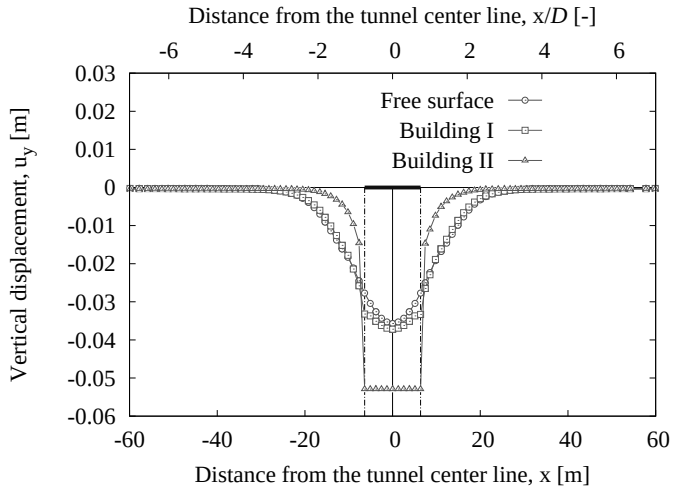

Figure 4.18: Comparison of surface settlement profiles using 1% tunnel contraction factor with respect to different values of contraction factor (X=0, Y=1D)

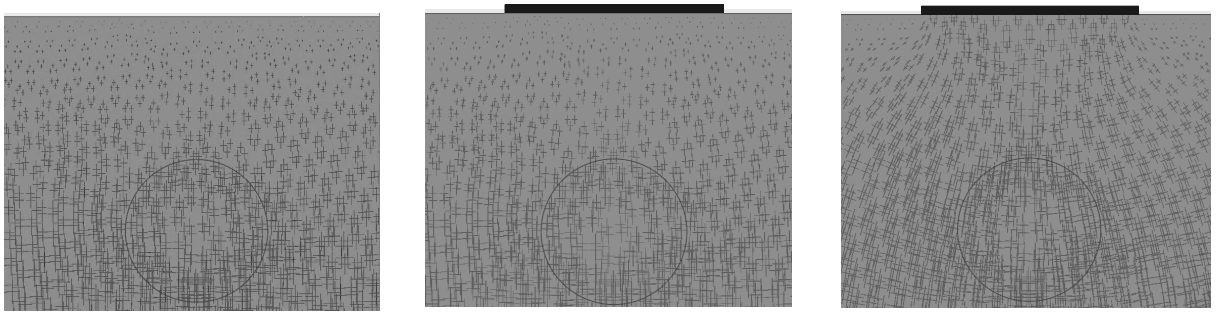

Figure 4.19: Direction of principle stress in the system using 1% contraction factor before tunnel excavation; (a) free surface; (b) building I; (c) building II (X=0, Y=1D)

the building. For building I, since the load of the building is relatively small, the stresses beneath the building are slightly increased and there is no distinct difference of principle stresses direction compared to that of free surface case. After tunnel excavation, arching occurs around the tunnel. In case of free-field surface, this process significantly changes the direction of principle stresses. However, the arching effect gradually disappears when there is building on the ground the surface and with higher load. This is consistent with what is reported by Lavasan et al. (2016).

4.3.3 Effect of overburden depth of the tunnel

The building settlement changes as a result of increasing the overburden depth of the tunnel, and the result is plotted in Fig. 4.21(a). The average settlement of the building

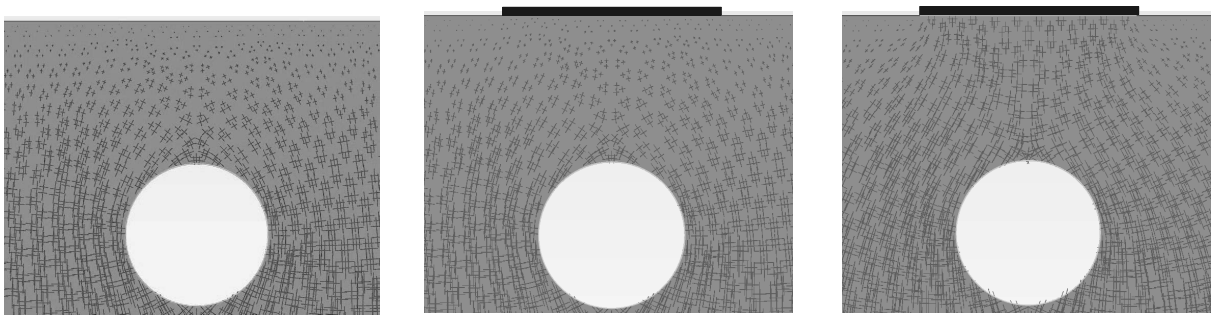

Figure 4.20: Direction of principle stress in the system using 1% contraction factor after tunnel excavation; (a) free surface; (b) building I; (c) building II (X=0, Y=1D)

(S) is calculated as:

$$S = \frac{1}{B}\int_0^B u_y \mathrm{d}x \tag{4.5}$$

where u_y represents the vertical displacements of the building along the x direction, B is the width of the building. For the free surface scenario, soil surface settlement at the same position of the building is derived for the comparison with average building settlement. As seen in Fig. 4.21(a), with increasing tunnel depth, the settlement induced in the building due to tunneling reduces. This is because that greater tunnel depth induces wider influence zone, regardless of the existence of the building. Furthermore, it is found that increasing the tunnel depth to 3-4D, the average settlement of building II reduces dramatically. This is attributed to the degree of shear strength mobilization of soil domain beneath the building. In the current study, after the building loading stage, there are larger shear strength mobilization beneath building II compared to that of building I. Consequently, the effect of tunnel depth on the average settlement of the building is more influencing for building II in comparison to building I. Elsaied (2014) conducted similar simulation and concluded that the influence of tunnel excavation on the tunneling induced settlements in adjacent building becomes negligible beyond a vertical depth equal to twice the building width that corresponds to 2.2 times the tunnel's diameter in their research (tunnel diameter D=9 m and building width B=10 m). The possible reason to have different conclusions may be attributed to the different soil profiles. In their study, multi soil layers are considered, and the effect of tunnel overburden depth on the building's settlement is significantly influenced by soil properties in each layer. Furthermore, the load of building is influential only when the overburden depth is less than 4 times the tunnel's diameter. For deeper tunnels, the load of building has less influence on the

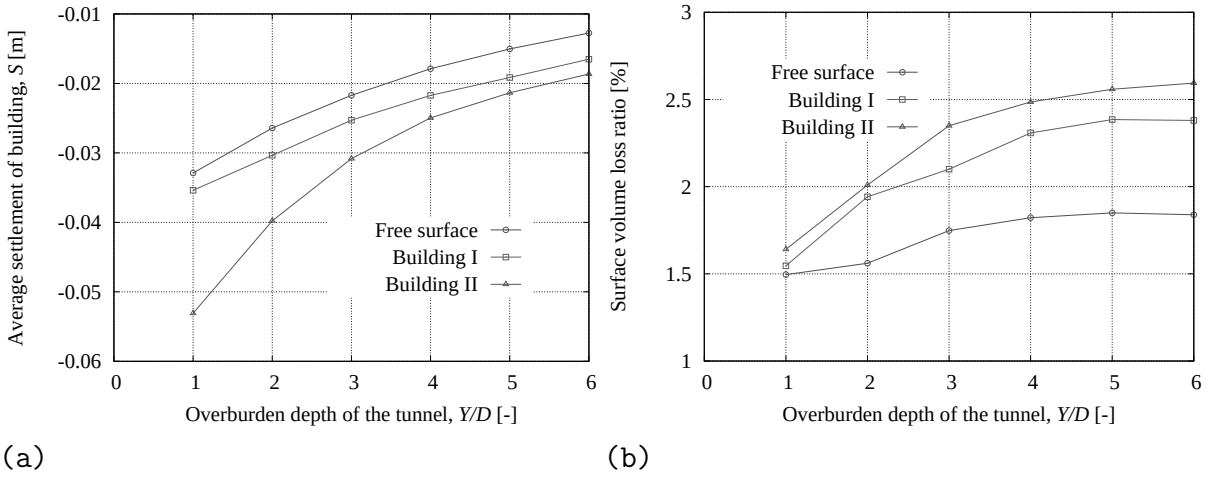

Figure 4.21: Influence of tunnel overburden depth on (a) average settlement of the building, (b) surface volume loss ratio using 1% tunnel contraction factor (X=0)

stresses distribution in soil domain around the tunnel. Subsequently tunnel volume loss results in comparable stress redistribution for the scenarios with and without buildings.

The effect of tunnel depth on the ground surface settlement is depicted in Fig. 4.21(b). As seen, in case of shallow tunnels (Y =1D), volume loss at ground surface is almost identical with or without building on the ground surface. With an increase in tunnel overburden depth, surface volume loss increases and larger volume loss is obtained when building exists. When the tunnel depth increases to more than 4D, the surface volume loss remains unchanged. This means stresses redistribution around the tunnel induces no more incremental plastic deformations in the soil domain close to the ground surface. This is consistent with that building and its corresponding load distribution area stay isolated considering the deep tunneling process (see Fig. 4.21(a)).

4.3.4 Effect of horizontal distance between the tunnel and building

Fig. 4.22(a) shows the variation of building settlements with respect to variable horizontal distance between the building and tunnel (see Fig. 4.17). It is observed that building settlement gradually decreases with increasing the horizontal center to center distance between of building and tunnel. In case of shallow tunnel (Y=1D), beyond a horizontal distance of about 3D, tunnel excavation induces no more significant effect on the building settlement. This coincides with that the size of influence zone in transverse direction due to tunneling is about 3D which can be seen in Fig. 4.23(a). In case of deep tunnel (Y = 4D), Fig. 4.23(b) shows that the size of influence zone due to tunneling is larger

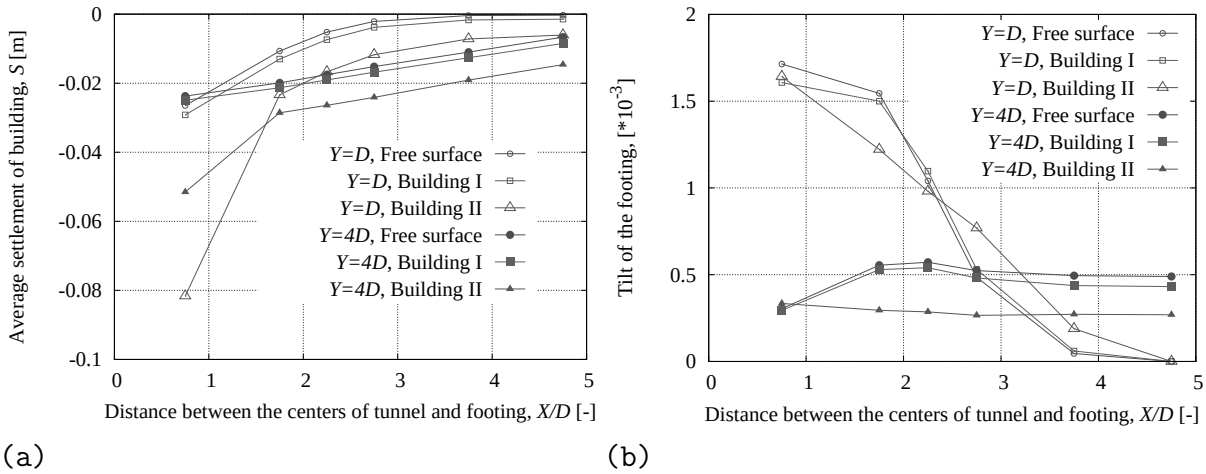

Figure 4.22: Influence of building position on (a) building settlements, (b) tilt of the building using 1% tunnel contraction factor

than $7D$ in transverse direction. Accordingly, the tunneling induced building settlements cannot reach steady state condition when $X/D < 7D$ as can be seen in Fig. 4.22(a). Furthermore, in case of building with higher loads, larger settlements are observed; however, the difference between the building settlements obtained from different buildings scenarios are gradually negligible with increasing horizontal distance between tunnel and building.

In addition to the average building settlements, the tilt of building, which is expressed as the ratio of the relative vertical displacement at building sides and the width of the building (B), is plotted in Fig. 4.22(b). As seen, for the shallow tunnel, the tilt of building decreases with an increase in the distance between the horizontal building and tunnel. However, for the deep tunnel, the tilt of building increases to a certain level before decreasing. This is due to the position of inflection point of the transverse settlement profile. The inflection point is much closer to the tunnel centerline in case of shallow tunnel (about $1D$ for free surface scenario), this results in the maximum tilt of building when $X/D = 0.75$. In contrast, the distance between the inflection point and deep tunnel centerline is about $2.5D$, this coincides with that building's tilt reaches maximum value for $X = 2.25D$ as seen in Fig. 4.22(b).

According to Fig. 4.23, it can be seen that the tunneling induced surface settlement may not be maximum just above the tunnel axis when superstructure exists in the vicinity of the tunnel. Apparently for deep tunnel, the maximum settlement of the building is about 1.2 times larger than the surface settlement above the tunnel axis. This emphasizes the importance of proper prediction of the surface settlement profile to prevent excess damage of adjacent buildings.

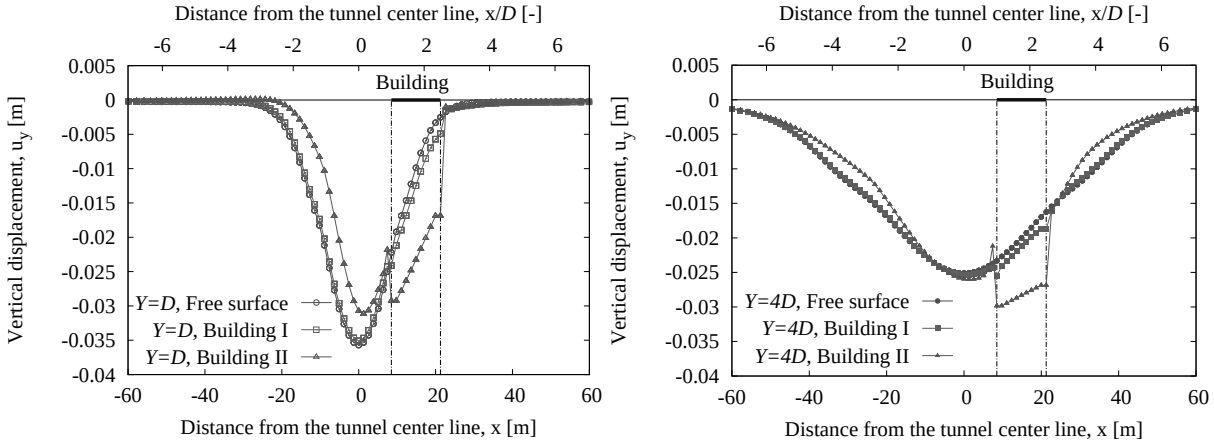

Figure 4.23: Comparison of the surface settlement profile for free surface and with building using 1% tunnel contraction factor: (a) X=1.75D, Y=1D, (b)X=1.75D, Y=4D

4.3.5 Effect of the soil-building interaction

As mentioned before, the soil-building interaction is considered in the present study by incorporating the interface element beneath the building that obeys the same constitutive law in accordance with 60% of the stiffness and shear strength of the adjacent soil. This section aims to evaluate the influence of soil-building contact properties on the tunneling induced settlements in the building. In general, it can be expected that introducing interface between the building and soil can lead to an increase in the building's settlement and tilt due to higher degrees of freedom in the soil-building contact that permits relative deformations between building and the bearing soil due to tunneling. However, when no interface is assigned, the full contact between the soil and building trough common nodes can impose an excessive restriction to the building-soil contact surface. Depending on the properties of the soil and the geometry and load of the building, assuming a full contact between the soil and building can lead to a slight underestimation of average building settlement and tilt. This aspect has been studied and the results for different combinations of the soil properties and the model geometry are illustrated in Fig. 4.24. According to Fig. 4.24(a), adopting interface element at the contact between the superstructure and soil has an insignificant influence on the settlement and tilt of the footing for both buildings assumed in the present study. This may be attributed to the current combination of system geometry (e.g. shallow tunnel)and model parameters (e.g. soil friction angle and large contraction factor). However, Fig. 4.24(b) reveals that the effect of interface properties for another set of soil parameters and model geometry can be significant. As seen, the behavior of building II is highly affected by the interface elements. Especially

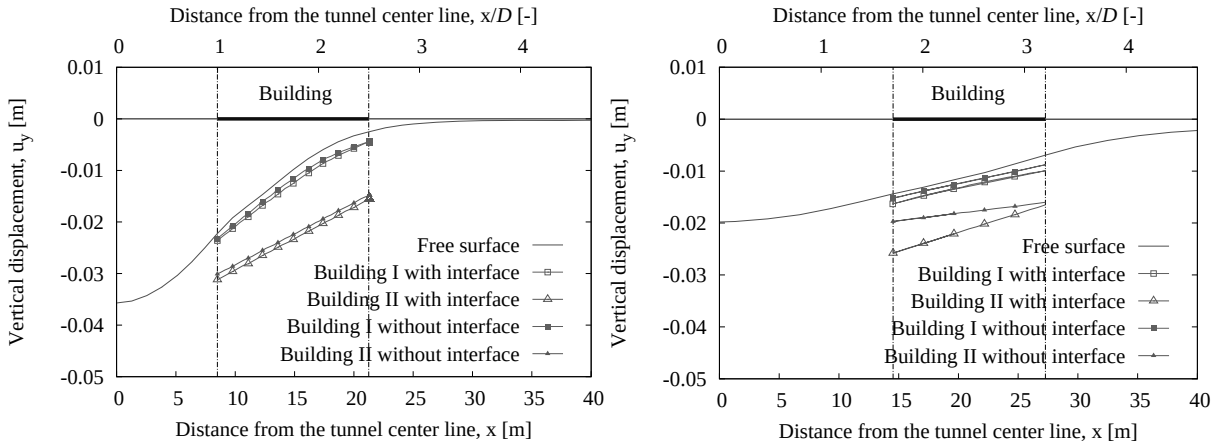

Figure 4.24: Effect of soil-building interface on the displacement of building [R_{int}=0.6 in the model with interface]: (a) E_{50}^{ref}=10MPa, E_{ur}^{ref}=30MPa, φ=25°, R_t=1%, X=1.75D and Y=1D; (b) E_{50}^{ref}=7.6MPa, E_{ur}^{ref}=34.6MPa, φ=19.5°, R_t=0.42%, X=2.47D and Y=2.59D

the tilt of building II is about 60% underestimated without modeling the soil-building interaction. Accordingly, the effect of soil/-building interface on the tunneling-induced settlement and tilt of building depends on the soil parameters, building load and model geometry. Considering the significant influence of these items on the model response, a comprehensive sensitivity analysis is carried out in the following section to assess the sensitivity of the building's behavior to these influencing parameters for different soil conditions and geometrical configurations.

4.3.6 Sensitivity analysis

According to the above discussions, building's position plays a significant role in determining the building's responses to tunneling. As the soil constitutive parameters dominate the soil behavior and tunnel contraction triggers the surface volume loss, settlements and tilt of building highly affected by these parameters as well. In reality, uncertainty is inevitably involved in these model parameters due to inadequate knowledge of in-situ measurements and laboratory tests. Therefore, it is necessary and valuable to investigate how the building response uncertainty is affected by the model parameter uncertainty. Within this framework, global sensitivity analysis is conducted in this section to distinguish the relative importance of these model parameters for the purpose of optimal design of tunnel construction and prediction the building's behavior. The selected parameters and their corresponding ranges of variation are given in Table 4.7 which are determined based on

the experience of the author. It should be noted that in the synthetic tunnel model of current study, in order to evaluate the effect of different combination of soil/tunneling parameters on the tunneling induced building deformations, on the one hand, the bounds of these soil parameters are defined with a wide range to cover different types of soil. On the other hand, the tunneling design parameters are defined in a wide range to check their influence on the system behavior that can later benefit the tunnel design. Nevertheless, for a particular case study, when the soil properties ranges and tunneling parameters are well known, it is recommended to conducted sensitivity analysis within these explicit ranges.

Table 4.7: Lower and upper bounds of input parameters for global sensitivity analysis

Parameter	Lower bound	Upper bound	Unit
φ'	15	30	[°]
E_{50}^{ref}*	5	15	[MPa]
E_{ur}^{ref}	15	45	[MPa]
R_{int}	0.4	1.0	[-]
Overburden depth Y	$4.25(0.5D)$	$42.5(5D)$	[m]
Horizontal distance X	$6.375(0.75D)$	$40.375(4.75D)$	[m]
Contraction factor R_t	0	1.5	[%]

*$E_{50}^{\text{ref}} = E_{oed}^{\text{ref}} \leq 0.5E_{ur}^{\text{ref}}$

Fig. 4.25 presents the sensitivity of building behavior to the model parameters in the whole parameter space. φ', R_t, X, Y are the key parameters that govern the building settlement. This is due to the fact that contraction factor triggers the volume loss around the tunnel and subsequently the stress redistribution. As a result, the change of stress and deformation propagates up to the ground surface and induces settlements in the superstructure. In this process, X and Y are important geometrical parameters that control the horizontal and vertical distances between the tunnel and building, respectively. Moreover, since the plastic deformation is the dominating part of the soil deformation in the region around the tunnel, the influence of friction angle on the building settlements is significant.

Likewise, for the tilt of the building, the GSA results show that the most important model parameters are $Y, \varphi', R_{\text{int}}, R_t$ in the whole space of variable parameters. For deeper tunnels, the tunneling induces less surface settlements and subsequent building deformations.

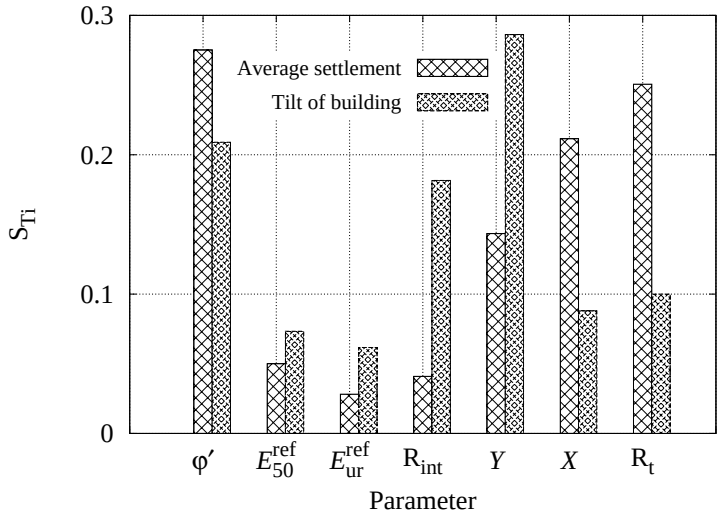

Figure 4.25: Global sensitivity analysis of 2D numerical model responses of building II to soil constitutive parameters and tunneling parameters

Accordingly, tunnel overburden depth becomes the dominant parameter that governs the tilt of building. Since the friction angle controls the plastic zone around the tunnel, it highly affects the tilt of building as well. Furthermore, the soil-building contact properties plays an important role in describing the tilt of superstructure and slightly affects the building's settlement. This is due to the fact that shear deformation pattern is generated from the tunnel side to the building (see Fig. 4.28 and the corresponding interpretation is given in section 4.3.7), the differential settlements along the building are significantly influenced by the properties of contact between the building and soil. Apparently, contact shear strength is more influential on the tilt of the building when it is much lower than that of soil body.

According to the sensitivity analysis results, since tunnel volume loss triggers the soil and building deformations, it plays a significant role in determining the settlement and tilt of the building. Friction angle is the most dominant soil parameter that governs the soil behavior and subsequent building deformation. The overburden depth of tunnel as well as the building-soil contact properties highly affect the tilt of building. The sensitivity analyses reveal that geometrical characteristics of the system (X and Y) are dominant parameters where the depth of the tunnel mainly governs the tilt of building while the horizontal distance between the tunnel and building regulates the average settlement of building. Apparently, a reliable prediction of the building behavior demands an appropriate identification of these parameters.

4.3.7 Optimal sensor location based on sensitivity distribution

As mentioned before, the soil properties are associated with inevitable uncertainties that result from the natural variability of soils. In addition, the measurement errors in process of quantifying the soil properties by in-situ or laboratory tests in diminutive fraction of the investigated soil volume in comparison with whole influenced soil domain can lead to further uncertainty in the system investigation. Therefore, parameter identification/update for the purpose of model calibration is essential to decrease the input parameters' uncertainty. During this process, a well considered position of sensors with respect to the mechanical incidents in the domain can increase the quality of the measurement and/or reduce the number of monitoring points. In other words, more useful information related to the parameter of interest can be derived with less monitoring points. This concept is usually described as "Design of Experiment" (DoE) which has been applied in several manners and in different fields. Ucinski (2005) proposed the Fisher-Information matrix to identify optimal sensor positions for different applications of meteorology or mechanical engineering. Schenkendorf et al. (2009) employed the so-called bootstrap- and the point-estimate method to identify system parameters in a bio-reactor. Hölter et al. (2015) applied the sensitivity distribution in the entire domain of a loading device to obtain the knowledge where to arrange the sensors for the purpose of parameter identification/update. Later Hölter et al. (2018) applied this approach in a 3D tunneling problem. Within this framework, this section aims to examine the most relevant locations of sensors to properly identify the soil properties with less effort and with limited number of sensors (Zhao, Lavasan, Hölter & Schanz 2018).

To identify the regions in the system that are very promising for sensor locations, GSA is applied in the aforementioned way using synthetic measurements at different possible monitoring points as model responses. The assumed 386 monitoring points (possible sensor locations) in the entire domain are illustrated in Fig. 4.26, both horizontal and vertical displacements are derived as the measurements. In this part of the study, the soil stiffness and shear strength parameters $E_{50}^{\mathrm{ref}}, E_{ur}^{\mathrm{ref}}$ and φ' are assumed to be the most uncertain soil parameters that need to be identified. The range of the variation of parameter are assumed to be same as those used in Table 4.7. Subsequently, GSA is performed at each of the monitoring point for vertical displacement u_y and horizontal displacement u_x with respect to $E_{50}^{\mathrm{ref}}, E_{ur}^{\mathrm{ref}}$ and φ' to gain the sensitivity indices S_{Tj}. To be specific, the GSA is conducted for the soil deformations at different positions to the variable soil properties. For example, for the soil properties in the given range, 10,000 samples are firstly generated via Latin Hypercube Sampling (LHS) method, then the sensitivity index (S_{Tj})

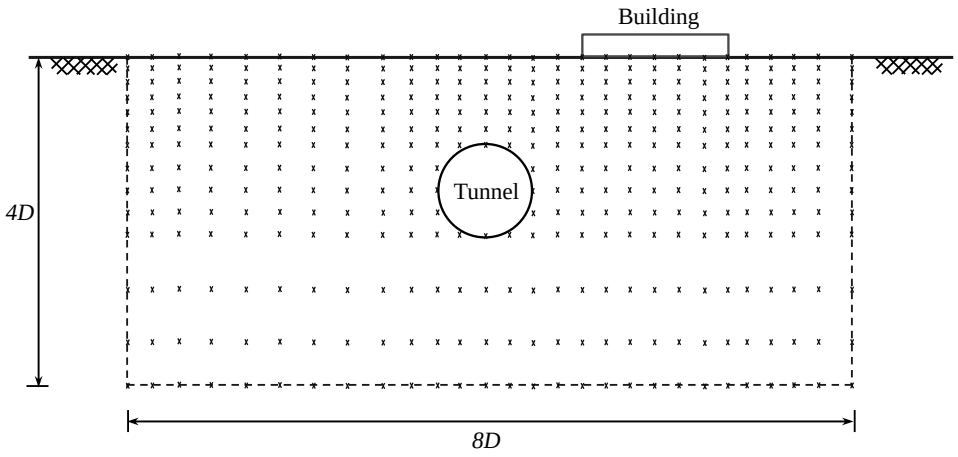

Figure 4.26: Distribution of synthetic measurement points (X=1.75D, Y=1D)

of vertical displacements (u_y) at the assumed 386 monitoring points to the friction angle is calculated. At the same time, due to the uncertainty involved in the measurements, it is reasonable to take into account the variance of measurement at each monitoring point. Therefore, the coefficient of variance of the vertical displacement at each of these 386 monitoring points is derived. Thereafter, the sensitivity information SA_i and β_i are obtained. It should be noted that in this process, the soil domain is assumed to be homogeneous and each set of variable soil parameters is applied to the entire model. Within this framework, the sensitivity information at each point SA_i are defined as:

$$SA_i = \mathrm{Var}_i \times S_{Tj}, \tag{4.6}$$

where Var_i is the variance of u_x or u_y at i-th monitoring point. In order to compare the sensitivity information of different outputs, the ratio β_i is used:

$$\beta_i = \frac{SA_i}{\max(SA)} \tag{4.7}$$

The contour plots of sensitivity distribution over the domain are shown in Fig. 4.27 where the red and blue colors respectively represent relative highest and lowest sensitivities of the model response towards the model parameters.

As seen in Figs. 4.27(a) and 4.27(c), only the deformations of the soil body (u_x, u_y) from the outer side of the building towards the tunnel wall in the vicinity of the building II is sensitive to the triaxial loading stiffness E_{50}^{ref}. It should be noted that the tunnel construction parameters (X, Y, R_t) keep constant in this part of the study. For the region beneath the building, due to the load of the building, the stress in soil within

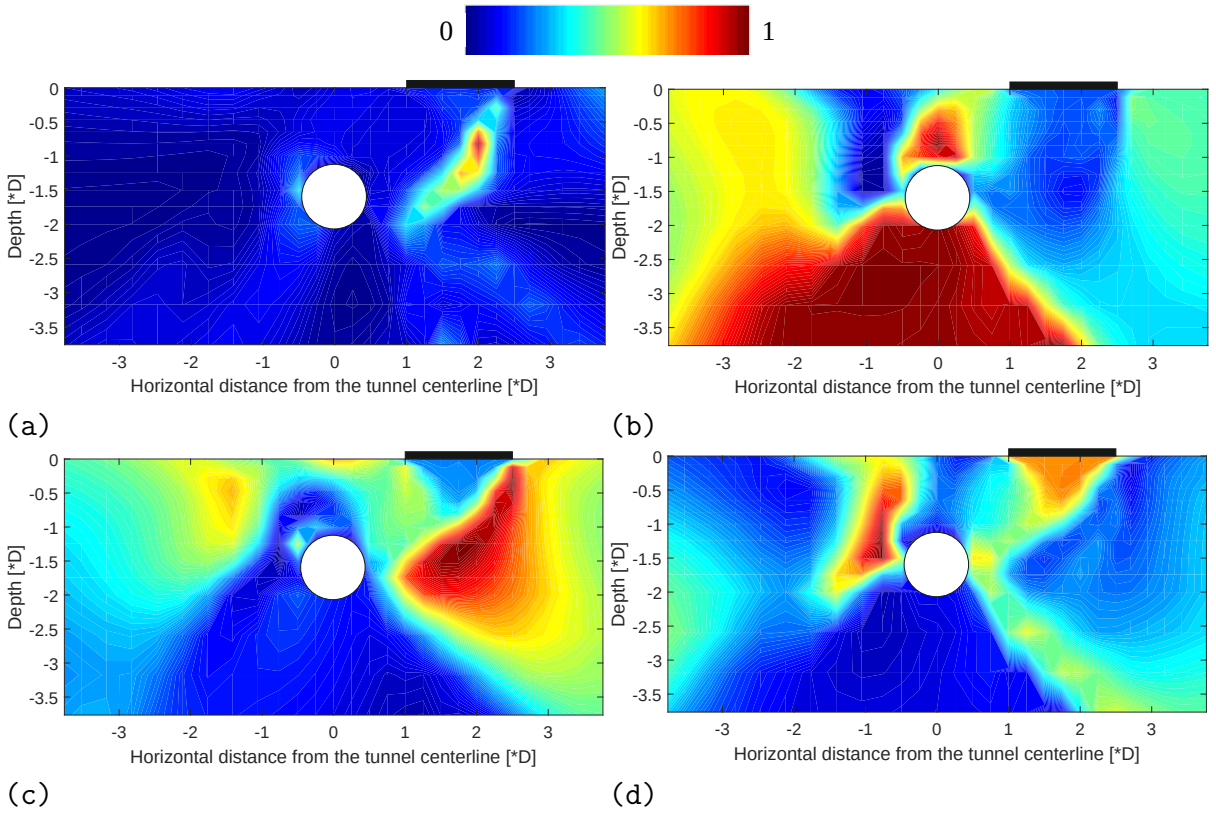

Figure 4.27: Sensitivity distribution for (a) u_x towards E_{50}^{ref}, (b) u_y towards E_{ur}^{ref}, (c) u_y towards E_{50}^{ref} and (d) u_y towards φ'

this region is higher, consequently higher stiffness makes the soil body less deformable compared to the adjacent soil body, as the E_{50}^{ref} is dependent on the stress level. Within this framework, the author assumes that soil underneath the foundation of building experiences compression. It is to be noted that the sensitivity information (SA_i in Eq. 4.6) takes into account the coefficient of variance of soil deformation. Stiffer soil beneath the building induces smaller soil deformation that corresponds to smaller variance of deformation and therefore less sensitivity. Furthermore, according to Fig. 4.28 that shows the incremental deviatoric strain distribution, the main shear deformation occurs from the right-hand side of the building towards the right-hand side of the tunnel. Therefore, the triaxial loading stiffness E_{50}^{ref} in this region is more influencing the model response due to larger variation of deviatoric stress.

Fig. 4.27(b) shows the sensitivity information of soil's vertical displacement to soil elastic unloading/reloading stiffness E_{ur}^{ref}. As seen, a high sensitivity area is observed below the tunnel invert. This is mainly attributed to the unloading at the bottom of the tunnel that is induced by tunnel excavation. This coincides with the GSA results (see Fig. 4.25(b))

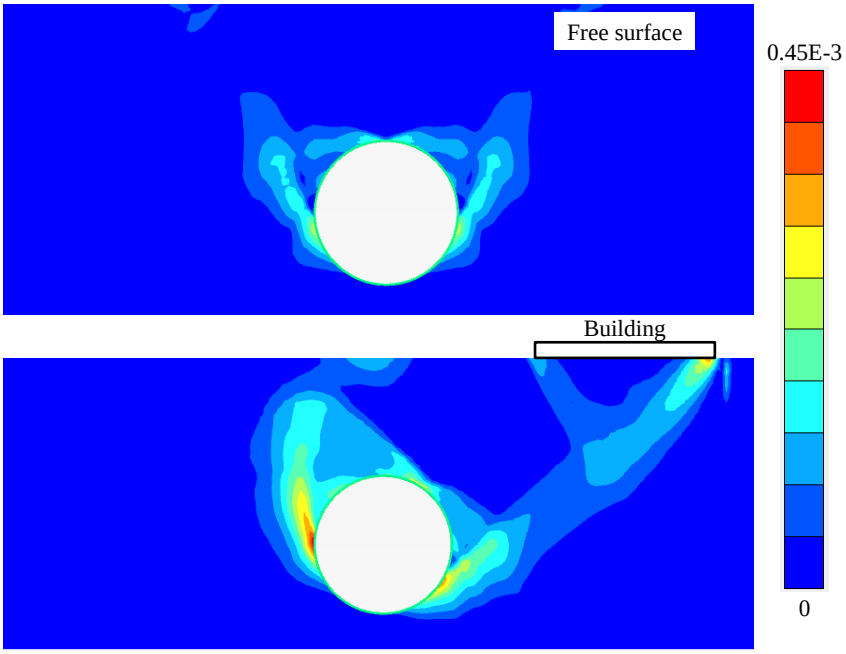

Figure 4.28: Incremental deviatoric strain distribution after tunnel excavation using 1% tunnel contraction factor (Y=1D and X=1.75D for the building position)

that settlements and tilt of the building are not sensitive to the elastic stiffness of the soil domain. Moreover, E_{ur}^{ref} is an important parameter in determining the vertical displacements of the soil right above the tunnel crown. This is due to the arching effect induced by the unloading (tunnel excavation) and reloading (lining installation) in the tunneling process.

To better interpret the sensitivity field in terms of mechanical incidents in the system, the distribution of incremental deviatoric strain after tunnel excavation for different scenarios are shown in Fig. 4.28. When there is no building on the ground surface, the tunneling induced shear formation pattern is symmetric and it develops from tunnel sides towards the ground surface. When the building is applied on the right side of the tunnel, the shear formation pattern of soil at left side of the tunnel is similar with the free surface case. This coincides with relative high sensitivity of vertical displacement to friction angle at left side of the tunnel towards the ground surface (see Fig. 4.27(d)). However, at the right side of the tunnel, shear formation pattern of soil is shifted from tunnel side towards the bottom of the building. This is due to the effect of the building's load, higher stress level leads to the fact that soil deformation is less sensitive to shear parameters compared to that at the left side of the tunnel. Furthermore, as seen in Fig. 4.28 that smaller incremental

deviatoric strain is observed at the intermediate zone between the tunnel and building, this coincides with the result of aforementioned sensitivity field (see Fig. 4.27(d)).

According to the above discussion, when there is limited number of sensors to measure the soil deformation, the optimal sensor location can be obtained based on the analysis of sensitivity fields. In order to identify the soil's stiffness (deformability parameter) and friction angle (shear strength parameter) for this tunnel-building arrangement, three optimal sensor location areas could be suggested to measure the horizontal and vertical displacements, namely (1) $D/2$ to outer side of the tunnel with respect to the position of the building, (2) below or above the tunnel, and (3) $1D$ below the building and $2D$ horizontal distance to the inner side of the tunnel towards the intermediate zone between the tunnel and building.

In the present study, the ground water is assumed to be significantly lower than the tunnel level. Apparently, the effective stress distribution and the effect of buoyancy in the domain would differ when the influence of ground water is taken into account. This can result in different effective stiffness and shear strength of soil which may change the tunneling-induced deformations in the subsoil and building. Expectedly, in the soils with high hydraulic conductivity (e.g. sand and gravel), it can be envisaged that the relative effect of model parameters remains nearly similar to the model with low ground water table. For the sensitivity analysis results, variation of effective stress varies the ranges of effective stiffness and shear strength of soil, then the relative sensitivity of subsoil/building deformations to these parameters becomes different, while an overall analogy between the sensitivity field of soil deformations to certain soil parameter is possible. For instance, the zones with the highest sensitivity towards effective friction angle, effective secant and unloading/reloading stiffness are likely to remain the same. Within this framework, the findings of optimal sensor location from present study can be qualitatively applied to the tunnels in saturated domain with high permeability. However, determination of the most optimized locations for sensors in soils with low permeability (e.g. silt and clay) with high groundwater table needs further assessment.

4.3.8 Conclusion

This section studies the influences of inherent soil properties (e.g. stiffness and shear strength), interaction parameters (e.g. soil-building contact properties), geometrical factors (e.g. tunnel and building relative position), and tunneling properties (e.g. tunnel volume loss) on the settlement and tilt of buildings at the ground surface during tunnel-

ing process. In order to evaluate the model response, a number of preliminary analyses have been conducted to elucidate the relation between the system parameters and model responses. Afterwards, global sensitivity analysis was conducted to evaluate the relative importance of system parameters in accordance with their influence on the model responses. Based on the sensitivity field in the entire domain, optimal sensor locations are suggested for the purpose of parameter identification. The following conclusions can be drawn:

1. When the building is centrally located on the axis of the tunnel, the building with high bending stiffness responds rigidly while no tilt is observed. In contrast, the response of building with low bending stiffness is relatively flexible with clear regions of sagging and hogging.

2. The higher load imposed by the building redistributes the stress around the tunnel and gradually eliminates the arching effect. For shallow tunnels (overburden depth less than $1D$) symmetrically excavated underneath the building, higher building pressure increases the maximum settlement.

3. Increasing the overburden depth of tunnel beyond $3D$, the tunneling induced settlement of building reduces dramatically, and the intensity of building pressure plays a significant role within this depth. For a constant building load, with increasing tunnel overburden depth, surface volume loss increases. For tunnels deeper than $4D$, the surface volume loss becomes independent of tunnel depth.

4. With increasing the horizontal distance between the building and tunnel, the tunneling induced settlement in the building gradually decreases. Beyond the influence width of tunnel, the tunneling induced settlements becomes negligible. The tunneling induced tilt in the building highly depends on the position of inflection point of the surface settlement profile (about $3D$ for shallow tunnel and $7D$ for deep tunnel). In case of deep tunnels, with increasing the distance between the tunnel and building, tilt of the building increases to a peak value before reaching the a steady state condition. However, the inflection point of settlement profile is much closer to the tunnel centerline for the shallow tunnels where the tilt of building gradually reduces with increasing the distance between the tunnel and building.

5. The global sensitivity analysis indicated that soil friction angle, tunnel volume loss and horizontal distance from the tunnel are dominant parameters in determining the building's settlement. The overburden depth of tunnel as well as the contact properties between the building and soil highly affect the tilt of building. The reliable

prediction of building behavior based on numerical solutions entails an adequate knowledge about these aspects.

6. According to the sensitivity field for the soil deformation with respect to soil stiffness and strength parameters ($E_{50}^{\text{ref}}, E_{ur}^{\text{ref}}, \varphi'$), the three optimal sensor locations to measure the vertical and horizontal displacements are (1) $D/2$ to outer side of the tunnel with respect to the position of the building, (2) below or above the tunnel, and (3) $1D$ below the building and $2D$ horizontal distance to the inner side of the tunnel towards the intermediate zone between the tunnel and building.

5 Numerical simulation of mechanized tunnel excavation in saturated soil

5.1 Introduction

This chapter investigates the slurry shield tunneling in the fully saturated soil deposits in short- and long-term periods. A fully coupled hydro-mechanical 3D model that accounts for main aspects of tunnel construction and the interactions between different domains due to tunneling process is developed. This chapter mainly focuses on assessing the influence of soil permeability and the method to simulate tail void grouting on the ground movements, pore water pressures and lining forces. By taking into account the soil permeability and TBM advance speed, different types of numerical analysis have been conducted to computationally address the tunnel construction. In addition, three distinct numerical techniques are employed to apply the grouting pressure at the TBM tail void and their effects on the model responses are assessed. Finally, the effects of grouting suspension infiltration induced time/space permeability evolution and grout hardening induced time dependent stiffness evolution in the vicinity of the tunnel are investigated.

5.2 Numerical simulation of tunneling process

As mentioned in the previous chapters, the three dimensional model can accommodate the face support, grouting pressure, progressive excavation as well as geometry of underground (e.g. tunnel inclination or curvature), albeit generating appropriate mesh in 3D model is more crucial (Franzius & Potts 2005). For the sake of simplicity in this research, the hydraulic jack pressure, the TBM conicity, overcut zone and time dependent evolution of shear strength in grouting material have not been explicitly simulated.

The geometry of 3D FE model can be seen in Fig. 3.1(b) and the model description has been introduced in section 3.2. In this chapter, the tunnel is assumed to have an

Table 5.1: Input parameters of the applied constitutive model for the soil − the Hardening Soil (HS) model

φ'	ψ'	c'	E_{50}^{ref}	E_{oed}^{ref}	E_{ur}^{ref}	p^{ref}	m	R_{int}	ν_{ur}	γ_{sat}
25°	0	0	35 MPa	35 MPa	100 MPa	0.1 MPa	0.7	0.6	0.2	20 kN/m^3

embedment depth of $1D$. The water level is set at the ground surface, the TBM (including the tunnel face where support pressure is applied) and the lining are assumed to be impermeable. Thus, the excess pore pressure cannot get dissipated through the water flow towards the excavation zone. The hydraulic flow through the outer and top surfaces of the model is permitted and therefore no excess pore pressure can be generated at the model outer surfaces. The bottom of the model and the symmetry surface are assumed to be impermeable in accordance with no flow hydraulic condition. The monitoring section is defined to be $4.5D$ away from the model boundary.

The isotropic Hardening Soil (HS) model has been applied in this chapter to describe the system behavior. The constitutive parameters of the soil chosen in this study are shown in Table 5.1. Considering Jacky (1944) equation ($K_0^{\mathrm{NC}} = 1-\sin\varphi'$), the initial stress in the domain is set in accordance with $K_0^{\mathrm{NC}} = 0.58$ (for φ'=25°).

As mentioned before, the TBM and the concrete lining are simulated by elastic shell elements where the high rigidity of the TBM shield is considered by assigning a high elastic stiffness to the shell element to avoid deformations in the TBM. The properties of lining elements are defined based on typical concrete lining elements with a thickness of 0.4 m. The mechanical parameters of the TBM and lining segment are presented in Table 5.2. It should be noted that homogeneous ring with a reduced bending stiffness is used in the present study to involve the global influence of the longitudinal joints on the bending stiffness (Blom 2002). This has been introduced in section 3.2.

The determination of face support and grouting pressure has been introduced in Chapter 2, section 2.2.2. Within this framework, the proper face pressure in this model is defined to be equal to 168 kPa and 270 kPa respectively at tunnel crown and invert. It is to be noted that the gradient of the face pressure is assumed to be equal to 12 kPa/m based on the unit weight of bentonite. The grouting pressures at the tunnel crown and invert are respectively 218 kPa and 320 kPa, the gradient of grouting pressure is 15 kPa/m according to the unit weight of grouting mortar.

Table 5.2: Input parameters of the used linear elastic constitutive model of the shell elements for representing the tunnel lining and TBM

Parameter	Lining	TBM	Unit
Thickness (d_t)	0.40	0.35	[m]
Elastic Modulus (E)	30	210	[GPa]
Unit weight (γ)	24	38	[kN/m^3]
Poisson's ratio (ν)	0.1	0.3	[-]

5.2.1 Numerical scenarios

Considering different construction strategies and speeds of TBM advance in accordance with the type of soil, fully drained, undrained or transient consolidation analyses can be carried out. In general, the excavation process can be divided into two construction steps namely, drilling and lining installation. According to Bezuijen et al. 2004, in the Botlek Railway tunnel and the Sophia Railway tunnel, the drilling process takes about 0.25-0.5 h, and stand still takes approximately 0.5-1 h, respectively. Therefore, it is reasonable to assume that one excavation process takes 1 h in this chapter. Considering the time needed for each step, different computational scenarios can be defined for the consolidation analysis. For the consecutive consolidation scheme A.1, each advance step of tunneling is divided into two calculation phases namely undrained excavation step (it is assumed to take place in an undrained calculation phase) that is followed by a consolidation phase within a certain time interval (1 hour) where no boundary conditions and mechanical load change. Apparently, these calculation phases separately represent the excess pore pressure generation (undrained calculation phase) and dissipation (consolidation phase) during drilling and standstill. For the simultaneous consolidation scheme A.2, the drilling and standstill steps have been simulated in an individual hydro-mechanical coupled analysis phase. In other words, the excess pore pressure generation and dissipation take place in a single calculation phase where the duration of this phase is identical to the time of the consolidation stage in the consecutive scheme (1 hour). Therefore, two scenarios can be interpreted with respect to TBM advance speed and soil permeability. The consecutive scheme allows full generation of the excess pore pressure during drilling, whilst the simultaneous scheme may result in less excess pore pressure due to the fact that consolidation and drilling coincide in each excavation step (length of one lining ring). It should be noted that the speed of excavation and tunnel advance are not absolute terms

but significantly depend on the permeability of the subsoil. In reality, the consolidation highly depends on the rate of generation and dissipation of excess pore pressure that is governed by the coefficient of consolidation, soil permeability, drainage length, model boundary conditions and TBM advance speed. In tunneling design, the numerical calculation is often conducted as extremely simplified drained (i.e. long construction time in high permeable soil) and undrained analyses (i.e. fast construction in low permeable soil). To study the influence of the type of analysis on the model response, the drained and undrained analyses as well as the simultaneous and consecutive consolidation schemes have been taken into consideration in this research.

To assess the effect of soil permeability on the model responses (e.g. deformation, excess pore pressure, lining forces), two soils with identical mechanical characteristics having different permeabilities, namely k^{f}=1 $\times$ 10^{-9}m/s (low permeable case) and k^{f}=1 $\times$ 10^{-5}m/s (high permeable case) are assessed in each scenario. It should be mentioned that undrained analysis in high permeability case is unrealistic, therefore, the corresponding results are skipped in this part of the study.

Three methods for modeling the grouting pressure have been introduced in Chapter 2, section 3.3. In Variant I this pressure is applied as mechanical total stress and in Variant II it is simulated as hydraulic total pore pressure. Variant III assumes no physical gap between the lining element and the surrounding soil where the construction is simulated by changing the stiffness and weight of the shell element from TBM shield to concrete lining. It is to be noted that in all of these variants, although the lining elements are assumed to be impermeable and therefore hydraulic flow towards the tunnel is restricted, the pore pressure can dissipate or generate due to circumferential flows in the thin grouting zone around the tunnel.

5.2.2 Infiltration concept during backfill grouting

The evolution of the time dependent permeability in the region close to the annular void is simulated by introducing an additional small scale, i.e. mesoscopic model which interacts with the aforementioned macroscopic model for mechanized tunneling process only through the evolution of permeability. The numerical investigation of the mesoscopic approach, is performed within the framework of the Theory of Porous Media (TPM). The TPM is used to describe the ongoing physical processes of deposition of grouting mortar in the surrounding soil during the back-filling process at the tail void. It should be noted that the development of the infiltration model is beyond the scope of this research, the

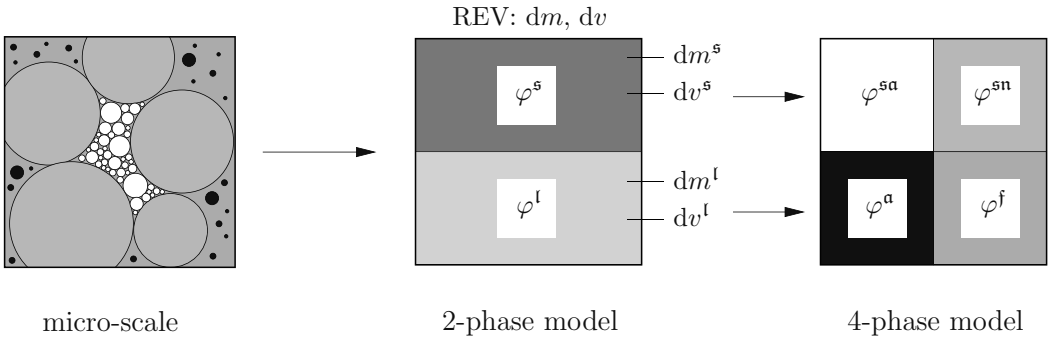

Figure 5.1: Micro-scale and REV of a fully-saturated soil and corresponding four-phase continuum model, after Schaufler et al. (2013*a*)

model developed by Schaufler et al. (2012, 2013*a*,*b*) is applied in this chapter and described as follows.

It is assumed that the mortar and the surrounding soil are represented by a more complex mixture of grains of different types and a pore fluid with evolving morphology and hydraulic properties. Therefore, the domain is described by four constituents φ^α with $\alpha = \{\mathfrak{f}, \mathfrak{a}, \mathfrak{sn}, \mathfrak{sa}\}$ (see Fig. 5.1) where the Representative Elementary Volume (REV) is divided into the volume fraction of the rigid skeleton $n^{\mathfrak{sn}}$, a volume fraction of the pore fluid $n^{\mathfrak{f}}$, a volume fraction of fines which are attached to the skeleton $n^{\mathfrak{sa}}$ and a volume fraction of fines being transported $n^{\mathfrak{a}}$. The volume fractions n^α are defined as:

$$n^\alpha = \mathrm{d}v^\alpha / \mathrm{d}v \tag{5.1}$$

where $\mathrm{d}v^\alpha$ is the partial volume of the constituent φ^α in the REV with volume $\mathrm{d}v$.

According to Steeb (2008) and de Boer (2000) the partial mass balance in local form reads:

$$\partial_t(n^\alpha \rho^{\alpha R}) + \mathrm{div}(n^\alpha \rho^{\alpha R} \mathbf{v}_\alpha) = \hat{\rho}^\alpha =: \hat{n}^\alpha \rho^{\alpha R} \tag{5.2}$$

where $\rho^{\alpha R}$ is the effective density which is defined as the ratio between $\mathrm{d}m^\alpha$ and the actual volume of the phase $\mathrm{d}v^\alpha$, $\mathbf{v}_\alpha$ is the velocity of the phase. Note that the partial mass balance equation 5.2 contains a density (mass) production term $\hat{\rho}^\alpha =: \hat{n}^\alpha \rho^{\alpha R}$ on the right hand side. The mass production term allow for local "phase change" from a liquid to a solid state (clogging) of fines. An extensive discussion of the model describing morphology evolution and clogging is out of the scope of the current contribution.

Following this, evolution of hydraulic properties during back-filling process of grouting mortar can be traced back to infiltration of fines. Whereas infiltration processes can be interpreted as phase transition from fluidized fines to fines attached to the rigid skeleton

($\varphi^{\mathfrak{a}} \rightarrow \varphi^{\mathfrak{s}\mathfrak{a}}$). Due to an increase of the solid volume fraction by infiltration, porosity and therefore also the permeability decreases. Numerically, infiltration is considered by the term on the right hand side of the general mass balance in Eq. 5.2, the so-called volume (mass) exchange term $\hat{n}^{\alpha}$. Considering phase transition only between two constituents the mass exchange term can be specified to $\hat{n}^{\mathfrak{a}} = -\hat{n}^{\mathfrak{s}\mathfrak{a}}$. Furthermore, we assume similar effective densities of the porous skeleton and the fine particles as well as material incompressibility $\rho^{\alpha R} = \rho_0^{\alpha R}$. Therefore, the mass balance collapses to a volume balance. Note that this incompressibility assumption is in contradiction to the assumption made in the consolidation model. As both models are only coupled via the permeabilities, this implies no further difficulties.

The mass exchange term can be understood as a constitutive assumption (Schaufler et al. 2013*a*), which for the case of infiltration, reads

$$\hat{n}^{\mathfrak{a}} = -\beta\, c\, \phi\ |\mathbf{q}|\,. \tag{5.3}$$

In Eq. 5.3 β is a material parameter, c is the local concentration of fines defined as $c = n^{\mathfrak{a}}/\phi$, $\mathbf{q}$ is the filter velocity following the Darcy-relationship (Ehlers & Bluhm 2002).

In addition, Eilers relation (Eilers 1941, 1943) is taken into account to model viscosity evolution:

$$\eta^{\mathfrak{f}R} = \eta^{\mathfrak{l}R}\left(1 + \frac{2.5\, c}{2\,(1-\kappa c)}\right)^2, \tag{5.4}$$

where the dynamic viscosity of the suspension $\eta^{\mathfrak{f}R}$ depends on the initial dynamic viscosity of the fluid phase without dissolved fine particles $\eta^{\mathfrak{l}R}$ and the concentration of fine particles c in the suspension and the material parameter κ.

The previously described equations can be summarized in the initial boundary value problem (IBVP) for the analysis of infiltration problems in porous materials as

$$\operatorname{div}\left[\frac{k^{\mathfrak{f}}(\phi)}{\eta^{\mathfrak{f}R}(c)}\operatorname{grad} p\right] = 0, \qquad \forall\, \mathbf{x} \in \mathcal{B} \times t, \tag{5.5}$$

$$\partial_t(c\,\phi) + \operatorname{div}\left[c\,\frac{k^{\mathfrak{f}}(\phi)}{\eta^{\mathfrak{f}R}(c)}\operatorname{grad} p\right] = \hat{n}^{\mathfrak{a}}, \qquad \forall\, \mathbf{x} \in \mathcal{B} \times t, \tag{5.6}$$

with boundary conditions for the flux $\mathbf{q}\cdot\mathbf{n} = \overline{q}$ at the Neumann boundary Γ_N and the pressure $\overline{p}$, concentration of fine particles c at the Dirichlet boundary Γ_D:

$$q = \mathbf{q}\cdot\mathbf{n} = \overline{q}, \quad \forall\, \mathbf{x} \in \Gamma_N \times t, \qquad \text{and} \qquad p = \overline{p}\,, c = \overline{c}, \quad \forall\, \mathbf{x} \in \Gamma_D \times t.$$

In addition, the evolution of porosity is solved with an ordinary differential equation of the form $\partial_t \phi = \hat{n}^{\mathfrak{a}}$. Again, mesoscopic Initial Boundary Value Problem (IBVP, see Fig. 5.2)

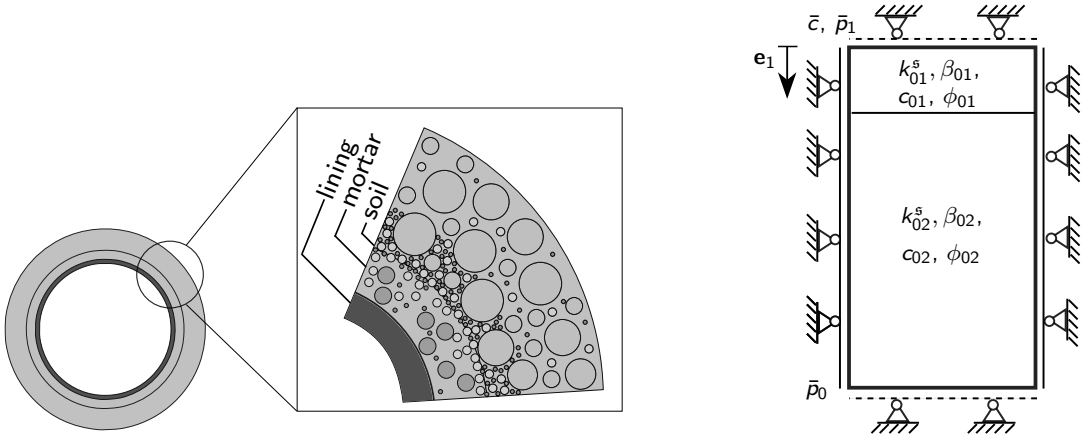

Figure 5.2: Tail void grouting: (a) illustration of the simulation of the grouting process, (b) schematic illustration of the considered IBVP

are numerically solved in weak form by Finite Element Methods (Schaufler et al. 2013*b*; Schaufler 2015).

The situation during the process of grouting at the TBM tail void is shown in Fig. 5.2(b). The injection of grouting mortar takes place at the TBM tail void in axial direction. As seen in Fig. 5.2, the dewatering process, which is responsible for the evolution of hydraulic and mechanical properties, is mainly oriented in radial direction of the tunnel axis. Thus, the simulation capturing infiltration phenomena is reduced to 2D domains. To investigate the effects of the infiltration modeling on the entire tunneling process, several calculations were carried out along one tunnel cross section.

Due to the homogeneous choice of boundary conditions and material properties, the evaluation of results reduces to 1D domain. Therefore, the evaluation of the hydraulic properties takes place along the coordinate $\mathbf{e}_1$. The calculated IBVP is graphically illustrated in Fig. 5.2(b). It consists of two domains, simulating the fully filled annular void and the surrounding soil. In consequence of the pressure boundary conditions, $\bar{p}_1$ at the upper and $\bar{p}_0$ at the lower edges, a pressure gradient arises which leads to a flux, resulting in a convective transport of fluidized particles. Further input parameter of the calculated examples can be found in Table 5.3.

To elucidate the physics related to infiltration phenomena, two different initial permeabilities ($k^{\mathrm{f}} = 10^{-5}, 10^{-9}$ m/s) were studied. The evolution of the permeability caused by infiltration strongly depends on its initial value. In the first case ($k^{\mathrm{f}} = 10^{-9}\,\mathrm{m/s}$) no significant change of permeability with respect to the overall mechanized tunneling process can be observed after infiltration time of 1 h. This effect can be explained by the

Table 5.3: Material properties and used boundary conditions

Length of domain 1	–	0.2	m
Length of whole domain	–	0.25	m
Pressure at boundary $e_1 = 0$	$\bar{p}_1$	146	kPa
Pressure at boundary $e_1 = L$	$\bar{p}_0$	0	kPa
Concentration of fines	c_{02}	0.01	
Concentration of fines	$c_{01} = \bar{c}$	0.08	
Effective dynamic viscosity	η^{lR}	1	mPa s
Initial porosity	$\phi_{01} = \phi_{02}$	0.33	
Material parameter	β_{01}	20	m
Material parameter	β_{02}	40	m
Material parameter	κ	1.3	
Calculation time	–	3600	s

lack of convective transport of the suspension of the mortar due to low permeability of the soil stratum. However, in the second case ($k^{\mathrm{f}} = 1 \times 10^{-5}$ m/s), a distinct evolution of the permeability in space and time is observed.

In Fig. 5.3, the space and time dependent evolution of the permeability of the surrounding soil is presented in a contour plot. The direction of the x axis represents the tunnel outward radial direction and origin of the x axis is located at the outer surface of the lining that extends in radial direction. It is worth to be noted that with increasing time of dewatering in the grouting zone, the permeability of the surrounding soil is reduced. This phenomenon occurs due to transport and infiltration of fine particles from the grout into the soil. Considering the heterogeneity between soil and mortar domain, the permeability is significantly decreased at grouting zone. Thus, the formation of a so-called internal filter cake occurred in the surrounding soil. Hence the surrounding soil acts as a filter in the case of backfill grouting. In the following sections the influence of the evolution of the permeability induced by infiltration on the consolidation of the subsoil will be investigated.

5.3 Results and discussions

In this section, the results of numerical simulations on the basis of different consolidation schemes to address the hydro-mechanical incidents around the tunnel (e.g. undrained,

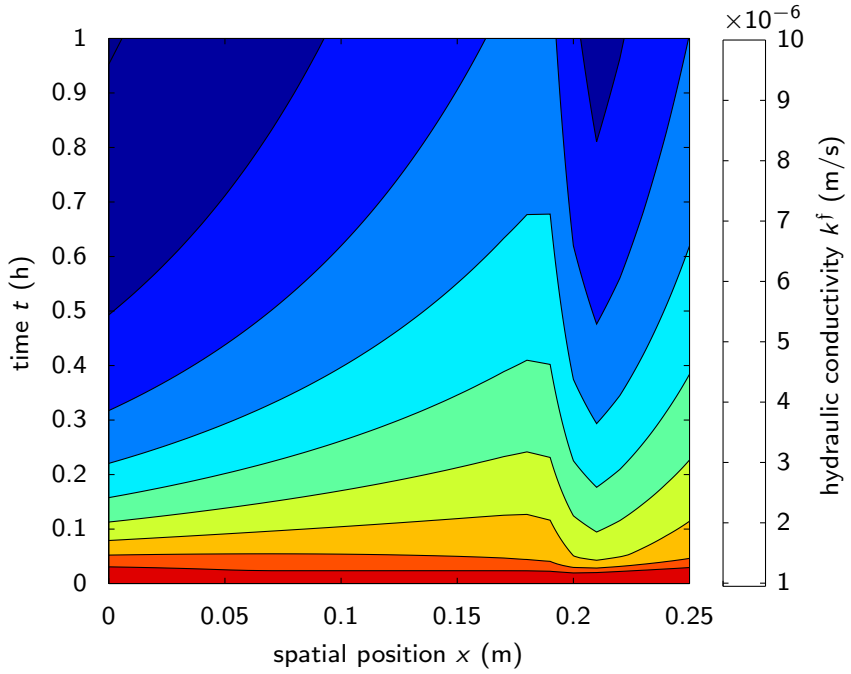

Figure 5.3: Evolution of the soil permeability in time and space around the tunnel with initial permeability of 1×10^{-5} m/s

drained, consecutive and simultaneous consolidation analyses) in accordance with different methods for the numerical simulation of backfill grouting are presented. In addition, the effect of infiltration and hardening of the grout material on the model responses (i.e. ground movements, excess pore water pressures and lining forces) is investigated.

5.3.1 Soil deformation

Soil deformation is typically distinguished as the most decisive criteria to evaluate the admissibility of construction and life design of tunnels due to its effects on the structures in the vicinity of the tunnel axes at the ground surface. The ground subsidence at the monitoring point for different numerical scenarios and various grouting variants are shown in Fig. 5.4.

As seen in Fig. 5.4, besides the type of analysis, the method employed to simulate the backfill grouting distinctly affects the displacements at the ground surface. When the grouting process is taken into account (variants I and II as shown in Fig. 3.3), the difference between drained and undrained analyses is remarkable. This difference highlights the significant contribution of the hydraulic interactions in the vicinity of the tunnel boundary to the model ground displacements. As expected in the simplified drained and

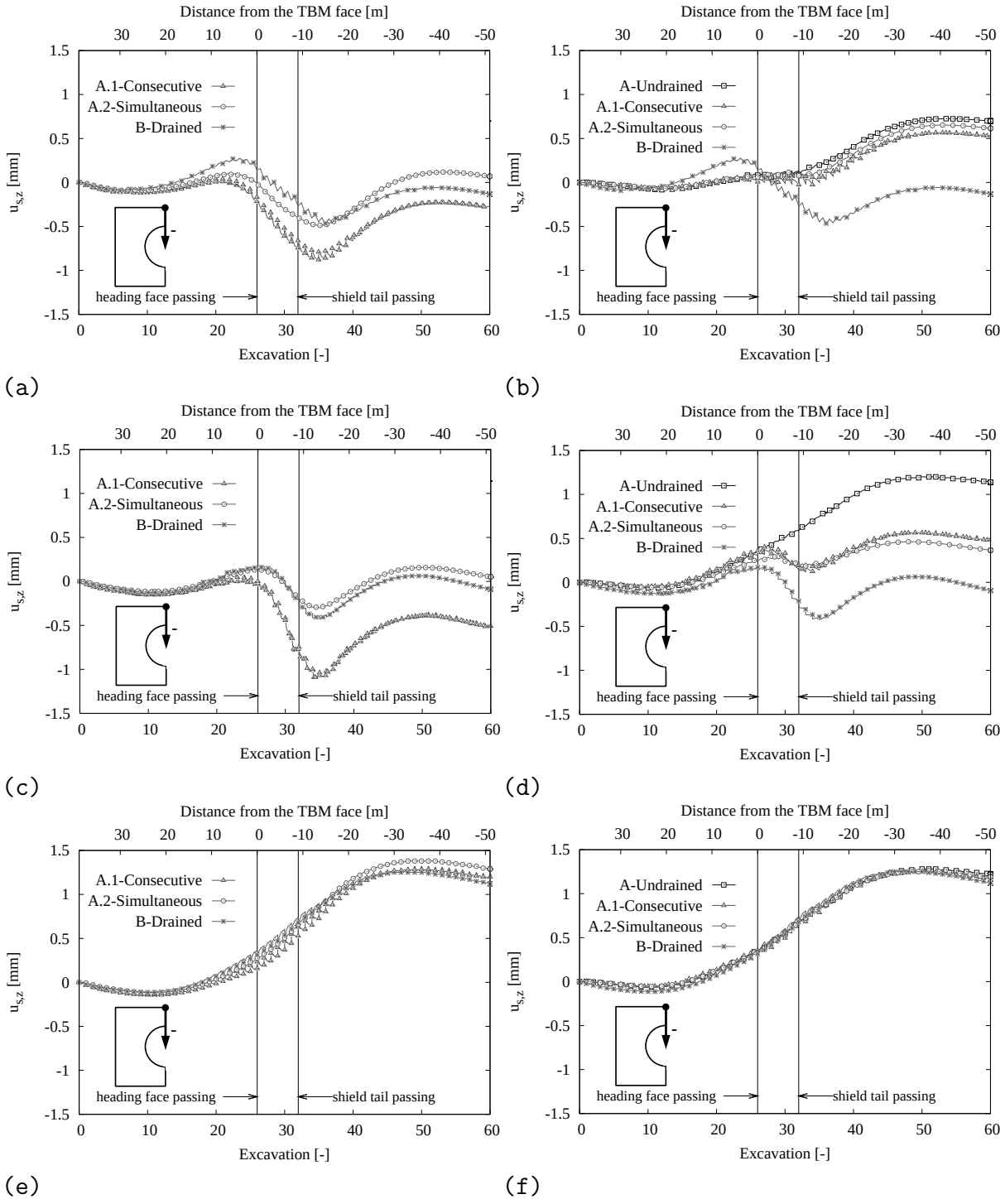

Figure 5.4: Ground subsidence due to tunneling in saturated soil with low and high permeabilities for different methods of grouting simulation; (a) $k^{\mathrm{f}} = 10^{-5}$ m/s (Variant I), (b) $k^{\mathrm{f}} = 10^{-9}$ m/s (Variant I), (c) $k^{\mathrm{f}} = 10^{-5}$ m/s (Variant II), (d) $k^{\mathrm{f}} = 10^{-9}$ m/s (Variant II), (e) $k^{\mathrm{f}} = 10^{-5}$ m/s (Variant III), (f) $k^{\mathrm{f}} = 10^{-9}$ m/s (Variant III)

undrained analyses, the permeability and type of analysis play no role and the only difference between the results obtained from drained (or undrained) for different variants is due to the method of backfill grout simulation. As shown in Figs. 5.4(e) and 5.4(f) for the most simplified case (variant III), the ground settlements from drained, consolidation, and undrained analyses coincide as the grouting pressure is omitted in the numerical simulations. In variant III, there is no particular gap between the lining elements and the surrounding soil; soil excavation and lining installation take place simultaneously in a single construction/calculation phase. In addition, no contraction has been assigned to the lining elements to trigger the volume loss due to tunneling. Therefore, the soil displacements (mainly uplift) in conjunction with variant III are dominantly governed by buoyancy effect and unloading due to tunnel excavation in this shallow tunnel with a surcharge depth of $1D$ (Verruijt & Strack 2008). Accordingly, the excess pore pressure is not significantly generated in the system and the results of different types of analysis coincide. Based on the comparison between the results obtained from Variants I and II for soils with low and high permeabilities (Figs. 5.4(a) to 5.4(d)), it can be concluded that the difference between different types of analysis is more significant when the grouting pressure is simulated as hydraulic total pore pressure (variant II). Regarding Figs. 5.4(a) and 5.4(b) for variant I, the consolidation analysis in soil with lower permeability results in ground settlement closer to the undrained condition. Distinguishably, the consolidation analysis in soil with higher permeability incorporates more settlements within the drained analysis. Based on Figs. 5.4(a) and 5.4(c), the model response for soil with higher permeability ($k^{\mathrm{f}} = 10^{-5}$m/s) is more sensitive to the consolidation scheme. In both cases the simultaneous consolidation scheme is nearly identical to drained results and consecutive consolidation scheme admits higher ground surface settlement. This can be attributed to the full generation of the excess pore pressure due to tunnel excavation and tail void grouting in the undrained excavation phase in the consecutive consolidation scheme. Although this excess pore pressure quickly dissipates in its following consolidation phase, it affects the hydraulic and mechanical characteristics of the subsoil.

The comparison of the drained and undrained solutions with the results of the consolidation analyses in Fig. 5.4 indicates that despite of different magnitudes of the surface deformation for different grouting variants, their patterns of variation with the advancement of the TBM are similar. Thus, to precisely identify the influence of the consolidation method on the system response, the deformation of the soil at tunnel crown and invert for variant II are shown in Figs. 5.5 and 5.6, respectively.

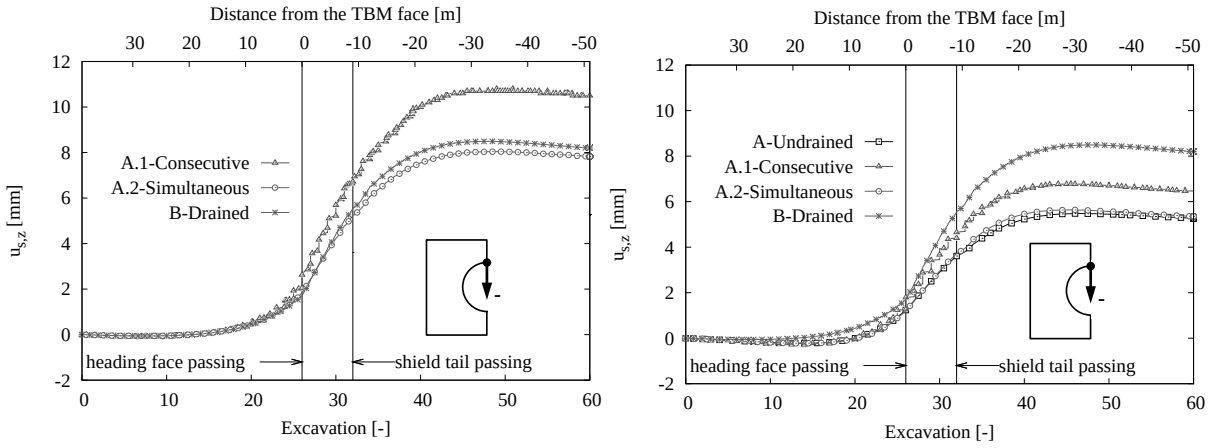

Figure 5.5: Soil displacements at the crown of the tunnel induced by tunneling in saturated soil with low and high permeabilities for variant II; (a) $k^{\mathrm{f}} = 10^{-5}$ m/s, (b) $k^{\mathrm{f}} = 10^{-9}$ m/s

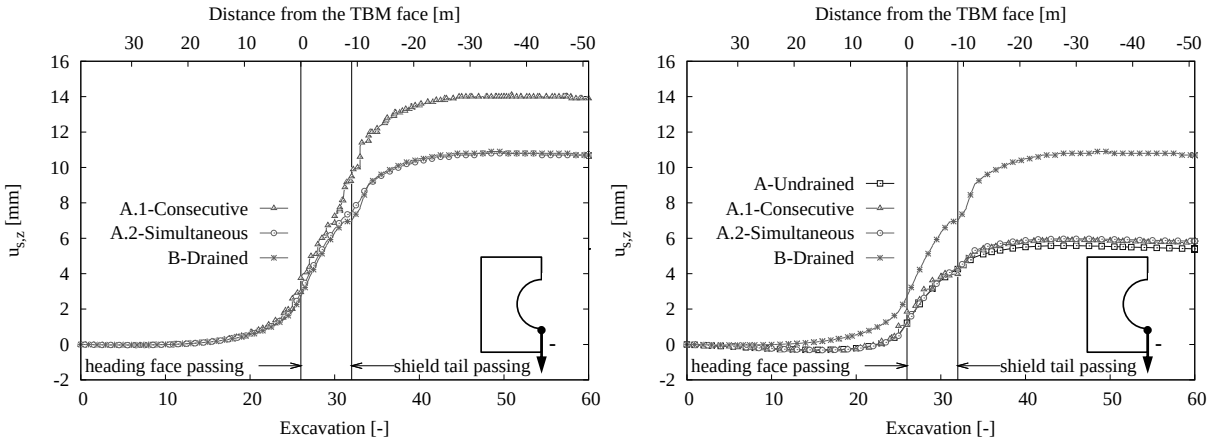

Figure 5.6: Soil displacements at the tunnel invert induced by tunneling in saturated soil with low and high permeabilities for variant II; (a) $k^{\mathrm{f}} = 10^{-5}$ m/s, (b) $k^{\mathrm{f}} = 10^{-9}$ m/s

According to Figs. 5.5 and 5.6, the crown and invert of the tunnel move upward for both high and low permeabilities. However, the magnitude of the displacement depends on the type of analysis. The undrained analysis represents the smallest lift at both the crown and the invert of the tunnel. This can be interpreted by the generation of pore suction underneath the tunnel that is induced by unloading due to tunnel excavation. As undrained analysis considers constant volume, the pore pressure/suction cannot be dissipated and that leads to significant accumulation with the TBM advance. In contrast, the drained analysis ignores the suction beneath the tunnel that results in higher upward displacements in the tunnel body.

In the drained analysis, the excess pore pressure is dissipated immediately and the grouting pressure is transferred to the soil skeleton which is assessed by the mechanical model. For the monitoring points at the crown and the invert of the tunnel, the results from the simultaneous consolidation scheme are identical to the drained analysis for higher permeability and to the undrained analysis for lower permeability, respectively. As seen in Figs. 5.5(a) and 5.6(a) for soil with higher permeability, the consecutive consolidation scheme predicts larger displacements at both the crown and the invert of the tunnel. As mentioned before, the consecutive consolidation scheme consists of two calculation phases namely the undrained excavation phase that is followed by a pure consolidation phase. In the first calculation phase, the excess pore pressure is generated but cannot be dissipated. As a principle in Hardening Soil model, the reference stiffness moduli for primary loading and unloading/reloading (E_{50}^{ref} and E_{ur}^{ref}) correspond to the reference mean stress p^{ref} (=100 kPa in this study). Nevertheless, the actual stiffness E_{50} and E_{ur} depend on the minor effective principal stress (σ_3'). Accordingly, the higher excess pore pressure results in lower the effective stress and lower actual stiffness moduli (E_{50} and E_{ur}) as the consequence. Thus, despite the insignificant direct influences of the hydraulic incidents due to the high inherent permeability of the soil ($k^{\mathrm{f}} = 10^{-5}$m/s), the stiffness variation due to the effective stress evolution indirectly affects the mechanical behavior of the system. Therefore, it can be deduced that the consecutive consolidation scheme leads to larger deformations around the tunnel due to higher pore pressures and lower effective stress as the consequence. This explanation can be better justified by the evaluation of generation and dissipation of excess pore pressure in the system due to mechanized tunneling.

5.3.2 Excess pore pressure

In addition to soil displacements, controlling the excess pore pressure due to tunneling is a crucial measure in mechanized tunneling. In addition, to interpret the mechanical behav-

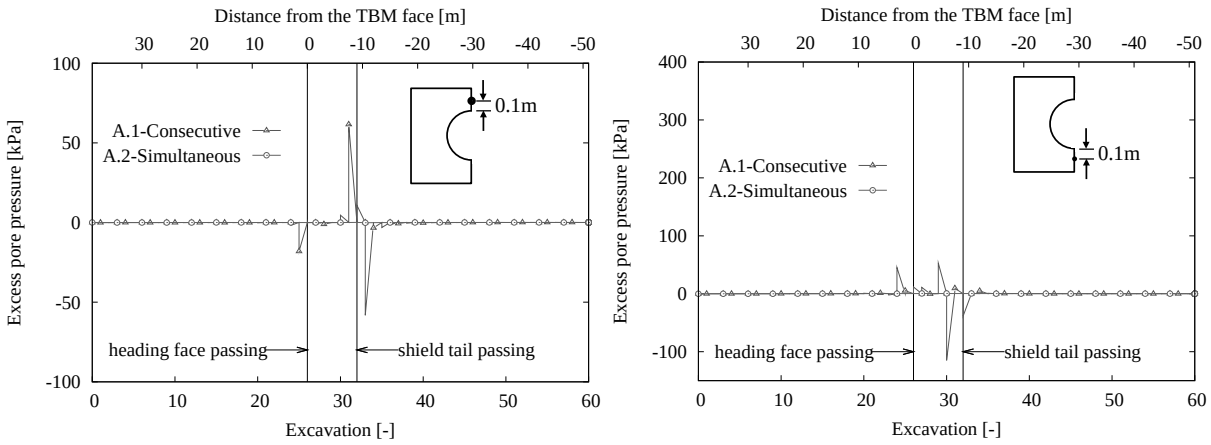

Figure 5.7: Variation of the excess pore pressure (suction is positive and compression is negative) due to backfill grouting simulated as pore pressure (variant II) in soil with high permeability ($k^{\mathrm{f}} = 10^{-5}$ m/s) ; (a) tunnel crown, (b) tunnel invert

ior of the system, one should know the hydraulic incident that take place in the domain with respect to mechanized tunneling. In this section, variation of excess pore pressure with excavation step is investigated for variant II (grouting as excess pore pressure).

To interpret the difference in the soil displacements from consecutive and simultaneous consolidation schemes in Figs. 5.5(a) and 5.6(a) for soil with higher permeability, the variation of the excess pore pressure at the tunnel crown and invert are shown in Fig. 5.7. As seen, the negative and positive pore pressures are generated at the tunnel crown and tunnel invert, respectively. The positive pore pressure (suction) can be explained by unloading due to mass loss in the excavation zone that results in a volume increase in the elements at the tunnel invert. The mass loss triggers the generation of suction that dissipates with time depending on the permeability of soil. In case of low permeable soil, higher negative pore water pressure and suction are generated during excavation and the dissipation of the excess pressure takes longer, which can be seen in Fig. 5.8. This interpretation also justifies the upward heave at the tunnel invert shown in Fig. 5.6. As seen, the accumulated excess pore pressure remains constant till the end of tunnel excavation in the soil with low permeability that compensates the buoyancy effect. Accordingly, the tunnel heaves larger when the pore suction can get dissipated.

As mentioned before, the simultaneous consolidation is the most realistic way of simulating a hydro-mechanical coupled process. However, on the one hand, when the time step is too large, it cannot capture the generation of excess pore pressure during excavation. On the other hand, when the time step is too small, the advance of the TBM has to be

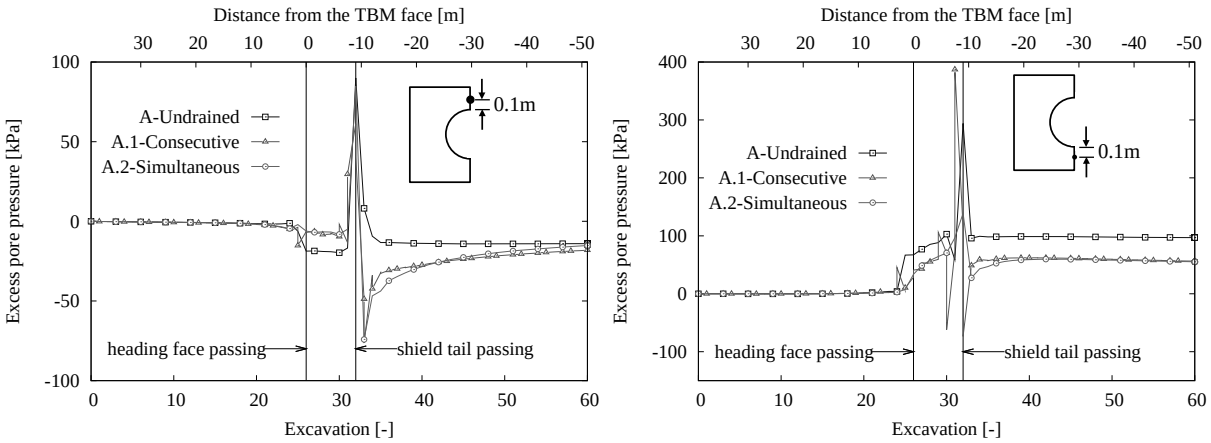

Figure 5.8: Variation of the excess pore pressure (suction is positive and compression is negative) due to backfill grouting simulated as pore pressure (Variant II) in soil with low permeability ($k^{\mathrm{f}} = 10^{-9}$ m/s) ; (a) tunnel crown, (b) tunnel invert

divided into very small sub steps. Subsequently the computational costs are extremely high. Due to these reasons, the alternative consecutive consolidation scheme is applied to model the excavation process. In the first excavation stage, fully undrained analysis is conducted under the assumption that the TBM advances at a high speed. This process is assumed to be very fast compared to the following standstill stage. In this consecutive consolidation scheme, the first stage is used to model the undrained removal of the soil, lining installation and the consequent generation of the excess pore pressure. The second stage deals with the time-dependent dissipation of the pore pressure. The combination of these two stages represents the completed mechanized tunneling process for the length of one lining ring. It should be noted that neither first nor second stage reflects the realistic tunneling process individually. In contrast, simultaneous consolidation scheme is adopted where excavation and the consolidation coincide in an individual phase. In this study, since TBM advances 1.5 m (e.g. length of one lining ring) in one hour, the rapid generation and dissipation of excess pore pressure is difficult to be captured in permeable soil through the simultaneous consolidation scheme.

As shown in Figs. 5.5(a) and 5.6(a), the variation of excess pore pressure due to grouting significantly affects the deformations in the system. As the deformations are numerically determined by a coupled hydro-mechanical analysis, the distinct hydraulic response can interactively induce different mechanical behavior in terms of stiffness evolution and plasticity. Thus, to trace the mechanical response of the model, the stress paths at the crown of tunnel in first and second invariants of effective stress space (I_1' and J_2) are presented

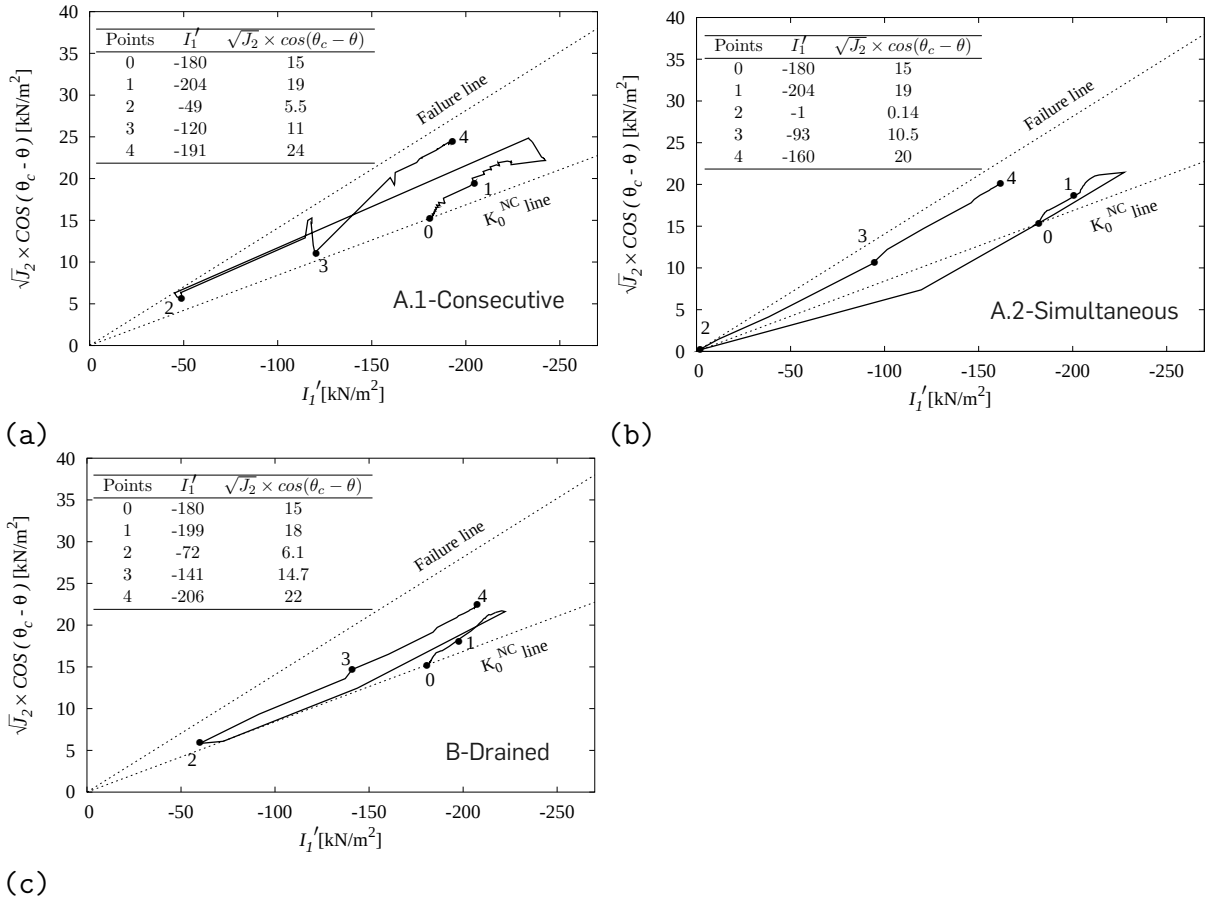

Figure 5.9: Effective stress path at the tunnel crown concerning different numerical analyses for $k^{\mathrm{f}} = 10^{-5}$ m/s (Variant II) [point 0: excavation starts, point 1: TBM arrives at the monitoring point, point 2: the TBM tail passes, point 3: grouting is finished, point 4: end of excavation]; (a) consecutive consolidation, (b) simultaneous consolidation, (c) drained analysis

in Fig. 5.9 for $k^{\mathrm{f}} = 10^{-5}$ m/s where the variation of the pore pressure plays a more substantial role. Here the vertical axis has been modified to ensure the MC failure line is Lode angle (θ) independent (see section 2.2.1), $\tan\theta_c$=$\sin\varphi'/\sqrt{3}$.

According to Fig. 5.9, regardless of the analysis type, the stress path begins from initial consolidation line K_0 (point 0) and it is subjected to loading due to the TBM advancement towards the monitoring point (points 0 to 1). When the TBM is passing underneath the monitoring section (points 1 to 2), unloading occurs due to mass loss arisen in accordance with the excavation. However, the monitoring point is re-loaded due to grouting (points 2 to 3). Afterward, the stress path slightly changes due to grouting in neighboring zones. As seen in Fig. 5.9, the effective stress is influenced by the type of analysis and scheme of

consolidation calculations. Thus, the mechanical responses of the model are also affected by the generation and dissipation of the excess pore pressure.

The stress path for the consecutive consolidation scheme (Fig. 5.9(a)) reveals that the stress path consists of several small cycles of loading and unloading that correspond to a sudden increase of the excess pore pressure in an undrained excavation step that is dissipated in its following consolidation phase. As shown in Fig. 5.7(a), the consecutive consolidation scheme allows generation and dissipation of the excess pore pressure in the system. Therefore, the effective stress decreases with an increase in the excess pore pressure. As mentioned before, the stress dependent soil stiffness in the Hardening Soil model depends on the effective minor principal stress (σ'_3). Eventually, the soil stiffness degrades with a decrease in the effective stress level.

5.3.3 Forces in the lining segments

Accurate determination of the forces in the tunnel lining is a challenging issue in reliable and economical tunnel design. Since the type of analysis, strategies to overcome numerical issues and the construction time periods remarkably affect the model responses, this section aims at investigating the influence of the type of numerical analysis (e.g. drained, undrained, consolidation analyses) and grouting simulation technique on the structural forces in the lining elements. The axial forces and bending moments of the lining are derived at the monitoring section at the end of the grouting stage. Accordingly, the scenario that accounts for tunneling without grouting is not considered and only the results for applying the grouting pressure as distributed load (variant I) and pore pressure (variant II) are presented in Fig. 5.10.

As seen in Fig. 5.10, the minimum and maximum axial forces and bending moments for both variants of grouting (I and II) mostly correspond to the undrained and drained analyses, respectively. This justifies the higher stress levels in the soil skeleton in the drained analysis that induce higher confining stresses on the lining and generate larger axial forces. In contrary, the undrained analysis accumulates the suction underneath the tunnel that carries the uplift forces and causes smaller axial forces in the lining. As seen, the results of the consolidation analysis in conjunction with the grouting modeled as mechanical total pressure (variant I) are very close to the forces corresponding to undrained analysis. This can be related to the unrealistic pore pressures and the effective stress distribution in case of applying the grouting pressure as the mechanical total pressure. However, the simulation of grouting as pore pressure represents logical results where the high and low

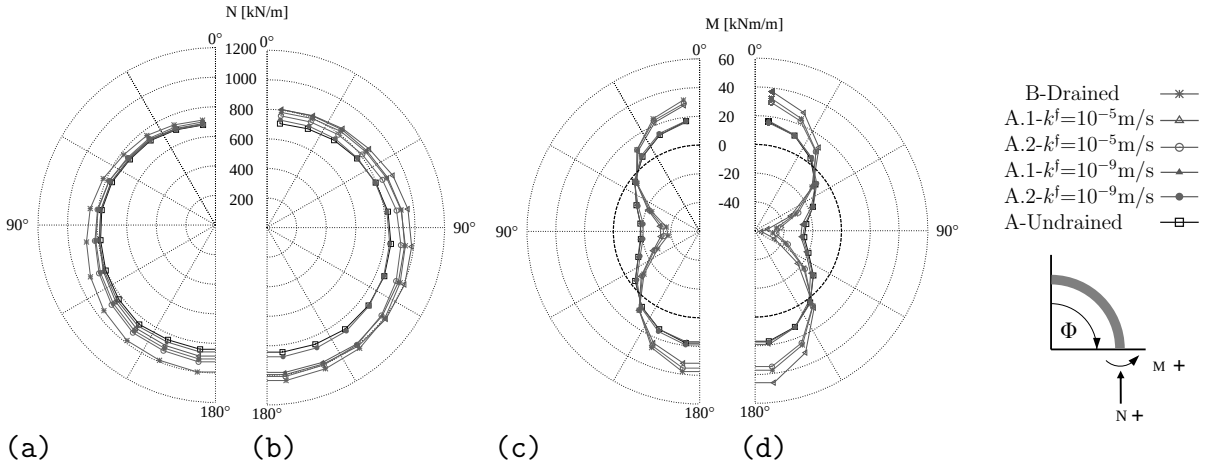

Figure 5.10: The variation of the lining forces for undrained and drained analyses of mechanized tunneling in saturated soil employing different variants of grouting pressure application schemes; (a) axial forces of variant I, (b) axial forces of variant II; (c) bending moments of variant I, (d) bending moments of variant II

permeabilities tend to drained and undrained analyses, respectively. As seen, the bending moments for both grouting scenarios for soil with high permeability is greater than the low permeable soil.

According to Fig. 5.9(a), the consecutive consolidation scheme permits the cyclic generation and dissipation of excess pore pressure around the tunnel in a limited periods of time. As mentioned before, this process induces changes in the effective stress distribution around the tunnel. Thus, the bending moments obtained from the consecutive consolidation scheme in the case of simulating the grouting as pore pressure is higher than bending moments in the drained analysis where the pore pressure plays no role.

Additionally, since time dependent consolidation analysis is considered in this study, the soil stresses around the tunnel vary with the advancement of TBM. Therefore, it is valuable to investigate the variation of lining forces during tunneling process, the results are presented in Fig. 5.11. In these analyses, both consecutive and simultaneous consolidation schemes are considered for soil with high permeability ($k^{\mathrm{f}} = 10^{-5}$ m/s). As seen, for the newly installed lining segments where grouting mortar is applied, largest axial forces and bending moments are observed. When the TBM advances, the distance between this lining and the grout injection area increases, therefore, less grouting pressure can be transferred to this lining. Subsequently the lining axial forces decreases. This phenomena is observed in both consecutive and simultaneous consolidation schemes. The

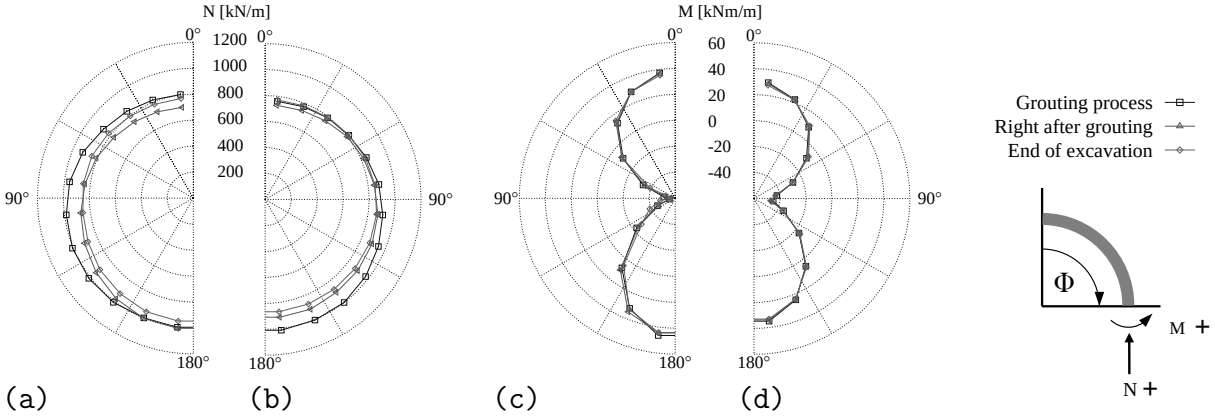

Figure 5.11: Time dependent lining forces employing variant II of grouting pressure and different consolidation schemes for soil with high permeability ($k^{\mathrm{f}} = 10^{-5}$ m/s); (a) axial forces of A.1, (b) axial forces of A.2; (c) bending moments of A.1, (d) bending moments of A.2

bending moments follow the similar pattern in comparison with the axial forces, while the magnitude of variation is neglectable.

5.4 Evolution of the permeability around TBM

To overcome the technical issues on using cement base grouting mortars (e.g. grouting pipes clogging in standstill periods), the application of grouting mortars with dewatering behavior has become more popular. The dewatering under a certain pressure gradient, which is justified by a consolidation process, induces the transport of fluidized fine particles of mortar into the surrounding soil under a constant grouting pressure at a certain period of time. Depending on the rate of deposition of fine particles of mortar suspension in the soil pore space (infiltration), the void ratio (and permeability) of the surrounding soil changes with time and a filter cake can form next to the grouting zone (see Fig. 5.3). Within this framework, the variation and distribution of permeability is firstly obtained from the one-dimensional infiltration model under the constant grouting pressure and soil/grout material properties (as described in section 5.2.2). After that, the permeability is updated in the numerical model of tunnel excavation in accordance with time and space. By doing so, the consolidation regime changes with time due to the evolution of permeability of the soil.

Since the infiltration of fine grout particles into the subsoil is unlikely in case of soil with low permeability, this section mainly deals with the evolution of permeability induced by

tail void grouting in soil with higher permeability ($k^{\mathrm{f}} = 10^{-5}$ m/s) as shown in Fig. 5.12. As mentioned before, the rapid generation and dissipation of excess pore pressure is difficult to be captured in the permeable soil through the simultaneous consolidation scheme without a need to dramatically decrease the length of time intervals. The consecutive consolidation scheme is used in the present study to address the permeability evolution due to grout infiltration.

As seen in Fig. 5.12(a), the ground settlement is not affected while the TBM face passes about $0.5D$ from the monitoring section. However, the ground surface settlement starts to differ beyond this distance. As seen, the evolution of permeability around the grouting zone results in a significant increase in the settlement. Since the evolution of the permeability causes lower permeability in the vicinity of the impermeably tunnel, the dissipation of the excess pore pressure due to flow in tunnel circumferential direction takes longer. Thus, a higher pore pressure at the tunnel crown decreases the effective stress above the tunnel which causes a lower stress dependent stiffness in Hardening Soil model and therefore larger surface settlements. In addition, the positive pore pressure (suction) beneath the tunnel remains longer in the system that slightly retards the buoyancy effect (due to unloading caused by soil excavation) that also leads to less lift of the tunnel body. The difference between the stress paths for the consecutive consolidation analysis based on constant and evolutionary permeability can be seen through a comparison between Figs. 5.12(b) and 5.9(a). As expected, the main difference between the stress paths are observed in the course of passing of the TBM tail till the end of the construction (points 2 to 4). In addition, it can be seen that the effective mean stress (I_1') after passing of the TBM till the end of the construction is smaller when the evolution of the permeability due to infiltration is taken into consideration. Therefore, the degradation of the soil stiffness at lower effective stresses results in larger settlements when the TBM passes. According to Fig. 5.12(c), the evolution of the permeability considerably influences the maximum axial force in the lining elements. The increase in the axial forces due to infiltration might be related to the lower permeability (due to grout filter cake formation in the surrounding soil) at the grouted zones. In other words, the longer resisting excess pore pressure (and pore suction) in the grout filter cake causes higher hydrostatic confining pressures acting on the lining. Fig. 5.12(d) shows lower bending moments in the lining when the infiltration process is taken into consideration. This can be attributed to the higher hydrostatic confining pressures in conjunction with suction at the invert of the tunnel that develops lower positive bending moments in the lining.

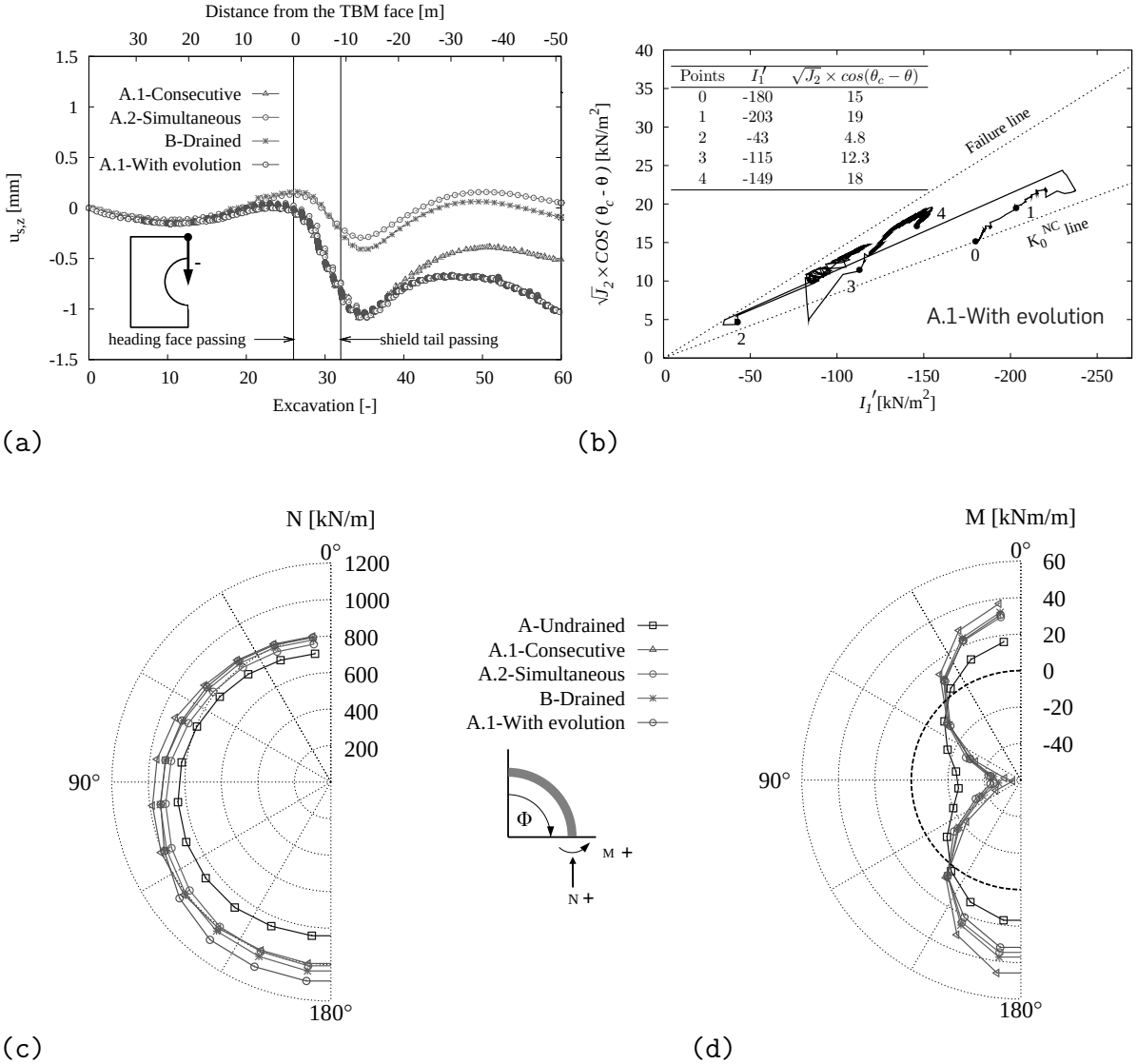

Figure 5.12: The effect of permeability evolution on model responses for grouting simulated as pore pressure (variant II) for soil with high permeability ($k^{\mathrm{f}} = 10^{-5}$ m/s); (a) soil displacement, (b) stress path at tunnel crown, (c) axial forces, (d) bending moments

5.5 Evolution of grout stiffness

In the previous section, the mechanical behavior of grout material is modeled by using HS model where grout hardening is not considered. To take into account the grout hardening induced evolution of stiffness, a constitutive model is developed to describe the time dependent elastic stiffness of grout mortar (TDE). To be specific, Eq. 2.11 (see Section 2.2.2) is modified and implemented in the framework of *Plaxis* user defined soil model (UDSM) as follows:

$$E(t) = \begin{cases} E_{28}\left[\exp\left(s_{\text{stiffness}}(1-\sqrt{\frac{t_{28}}{t_{0.042}}})\right)\right]^{0.5} & \text{for } t < 1\text{h} \\ E_{28}\left[\exp\left(s_{\text{stiffness}}(1-\sqrt{\frac{t_{28}}{t}})\right)\right]^{0.5} & \text{for } 1\text{h} \leq t \leq 28\text{d} \\ E_{28} \text{ for } t > 28\text{d} \end{cases}$$

In this expression, the stiffness of the grout is assumed to be constant after 28 days as hardening due to cement solidification is almost done after 28 days. Moreover, since in the early stage, the stiffness of grout material is very low, the huge difference of stiffness between grout and surrounding soil may result in convergence problem in the numerical algorithm. Therefore, the grout stiffness is assumed to be constant and equal to the stiffness after one hour (0.042 d). Model parameter $s_{\text{stiffness}}$ is the parameter governing stiffness evolution with time, it can be related to the stiffness ratio at 1 day and 28 days, as:

$$s_{\text{stiffness}} = \frac{\ln(E_1/E_{28})}{\sqrt{t_{28}/t_1} - 1} \tag{5.7}$$

In this study, the stiffness ratio at 1 day and 28 days is assumed to be 0.65 and the corresponding value of $s_{\text{stiffness}}$ is 0.2. The elastic stiffness of grout at 28 days is assumed to be 5250 kPa based on Ninić & Meschke (2017). The evolution of stiffness with time is shown in Fig. 5.13.

In section 5.4, consecutive consolidation scheme (A.1) using variant II to model the grouting pressure is adopted to study the effect of permeability evolution, and a thin layer of 20 cm around the lining is assumed to represent the grouting zone. In that case, same material as surrounding soil is applied in that thin layer. In order to investigate the influence of both stiffness and permeability evolution on the model responses, the time dependent stiffness constitutive model (TDE) is applied to that thin layer for simulating the grout hardening in consecutive consolidation scheme (A.1). By analogy, it is assumed that only the ring exiting the tail shield experiences a fluid grouting pressure, and that all annulus grout behind that behaves as an elastic solid.

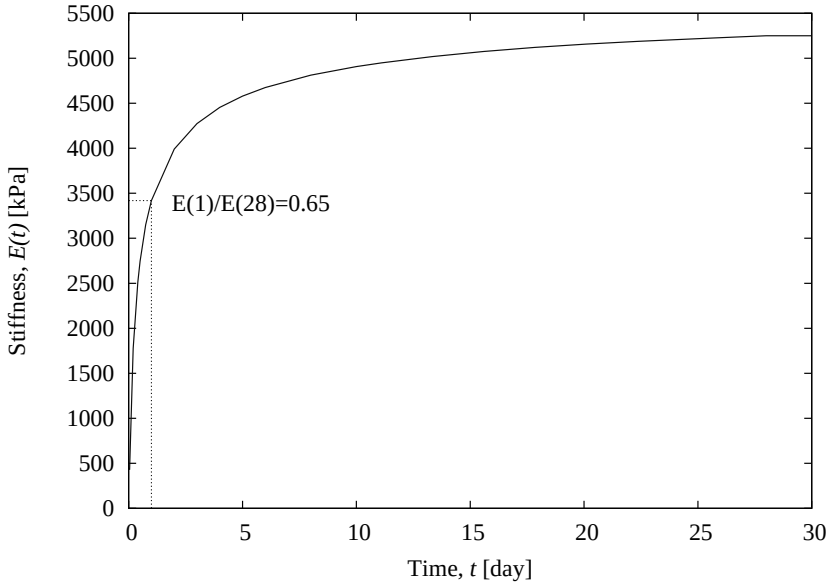

Figure 5.13: Increase of Young's modulus with time

Fig. 5.14 shows the influence of stiffness and permeability evolution on the model responses. Scenario "A.1-Consecutive" does not account for either stiffness or permeability evolution. Permeability evolution only is considered in scenario "A.1-with k^{f} evolution", these two scenarios have been described in the previous section. In scenario "A.1-with E evolution", TDE model is applied to describe the grout behavior, while infiltration process is not considered. In scenario "A.1-with E, k^{f} evolution", both stiffness and permeability evolutions are taken into account. As seen, when time dependent stiffness of grout is considered (without infiltration analysis), the lower stiffness of injected grout around the tunnel results in larger outward displacements of the lining segments. Subsequently, less uplift at tunnel invert and larger heave at tunnel crown are observed. Furthermore, the lower stiffness of grout leads to larger downward deformation of the soil domain above the tunnel crown and finally larger surface settlement is obtained. When both time dependent stiffness and permeability are taken into account, permeability evolution results in slower dissipation of excess pore pressure around the tunnel and subsequently, slightly less uplift of the tunnel can be derived. However, it should be noted that the effect of infiltration is less significant in comparison with the stiffness evolution, this might be attributed to the dominant influence of stiffness variation on the stress path. Within this framework, Fig. 5.14(d) shows the influence of stiffness evolution on the stress path at tunnel crown. Before TBM approaches the monitoring section, the stress paths are identical. In case that time dependent elastic stiffness is modeled, there is no significant decrease of effective mean stress when TBM passes through the monitoring section. Furthermore, smaller

effective stress is obtained when infiltration induced permeability evolution is considered, this is due to the fact that smaller permeability increase the excess pore pressure and subsequently, effective stress decreases.

Additionally, Fig. 5.14(e) shows the effect of time dependent stiffness of grout on the lining axial forces. When the stiffness evolution is considered, larger axial forces are obtained, which is consistent with the distribution of effective stresses (see Figs. 5.14(d)). Fig. 5.14(f) shows lower bending moments in the lining when stiffness variation is considered. This is because flexible grout material allows the adjustment of lining segments that develops lower bending moments. Although the influence of stiffness evolution on bending moments is not significant, its effect on axial forces is obvious. Therefore, it might be risky for lining structural design without considering hardening of the grout material.

5.6 Long-term displacements

In contrast to the soil with high permeability where the excess pore pressure fully dissipates after the lining installation (Figs. 5.7), the rate of excess pore pressure dissipation is very low in soil with lower permeability ($k^{\mathrm{f}} = 10^{-9}$ m/s). Accordingly, the system keeps deforming with time due to ongoing consolidation after construction phase. This section presents the soil deformations within an exploitation period of 1000 days by performing a consolidation analysis subsequent to the construction regardless of the type of the analysis during construction (e.g. undrained, consecutive and simultaneous schemes). The soil displacements and the excess pore pressure dissipation around the tunnel in 1000 days after construction are shown in Fig. 5.15. It should be noted that for the drained scheme of the tunnel excavation, no time dependent deformation is expected because no excess pressure is generated during the tunnel construction. Accordingly, the displacements at the end of the construction remain unchanged after 1000 days. These constant displacements are presented in Fig. 5.15(a) while the excess pore pressure is expectedly equal to zero during and after construction (see Fig. 5.15(b)).

According to Fig. 5.15(a), both crown and invert of the tunnel heave in the first 1000 days after construction period. The heave mostly relates to the shallow depth of the tunnel along with the time dependent dissipation of the positive pore pressure (suction) beneath the tunnel that allows appearance of the buoyancy effect. As the mechanical and hydraulic grouting pressures have been applied with respect to the actual stress state in the soil, no significant stress release/redistribution has occurred due to tunneling where the contraction (volume loss) has not applied to the lining elements. Therefore,

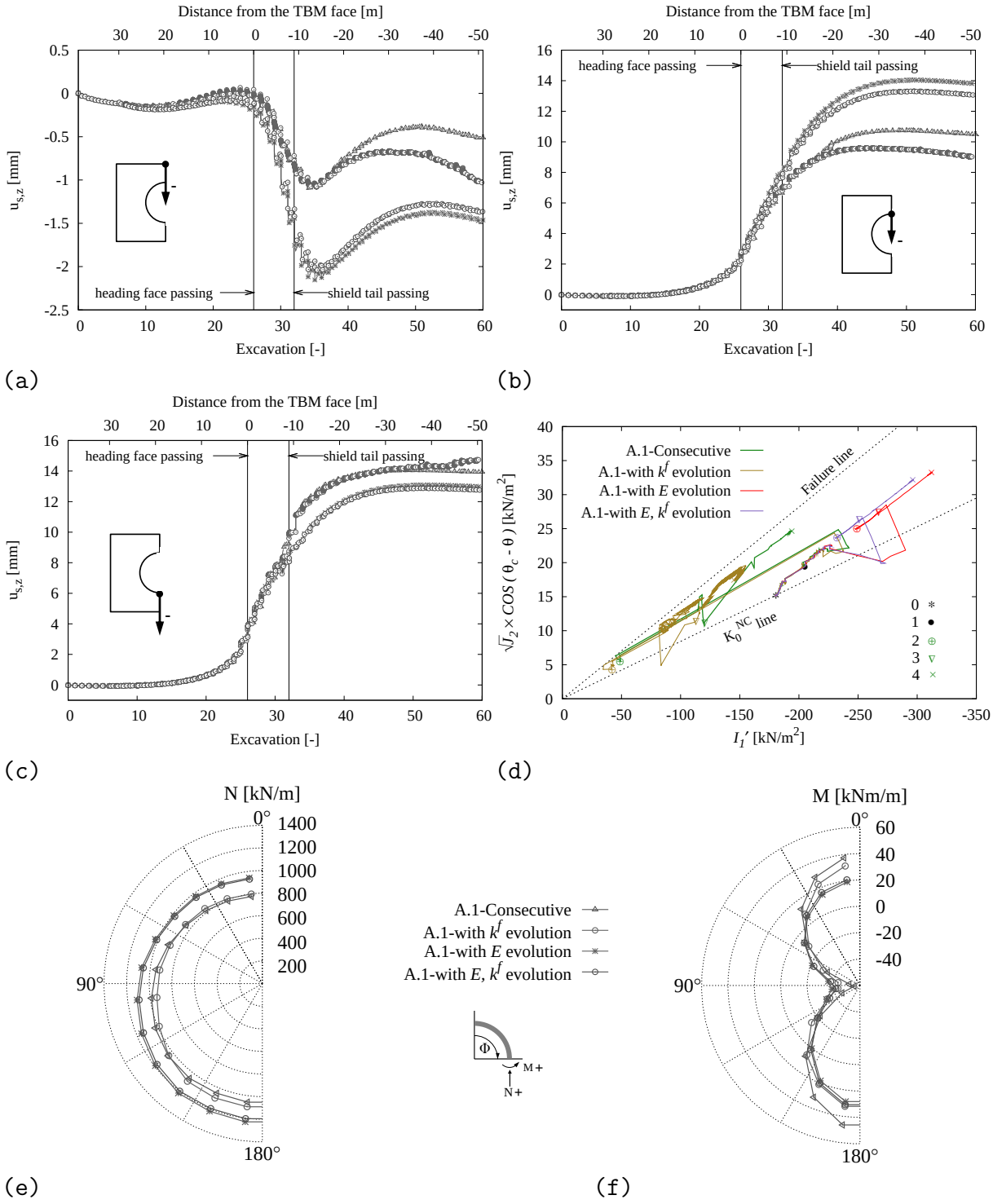

Figure 5.14: The effect of stiffness and permeability evolution on model responses for grouting simulated as pore pressure (variant II) for soil with high permeability ($k^{\mathrm{f}} = 10^{-5}$ m/s); (a) displacement at surface, (b) displacement at crown, (c) displacement at invert, (d) stress path at crown, (e) axial forces, (f) bending moments

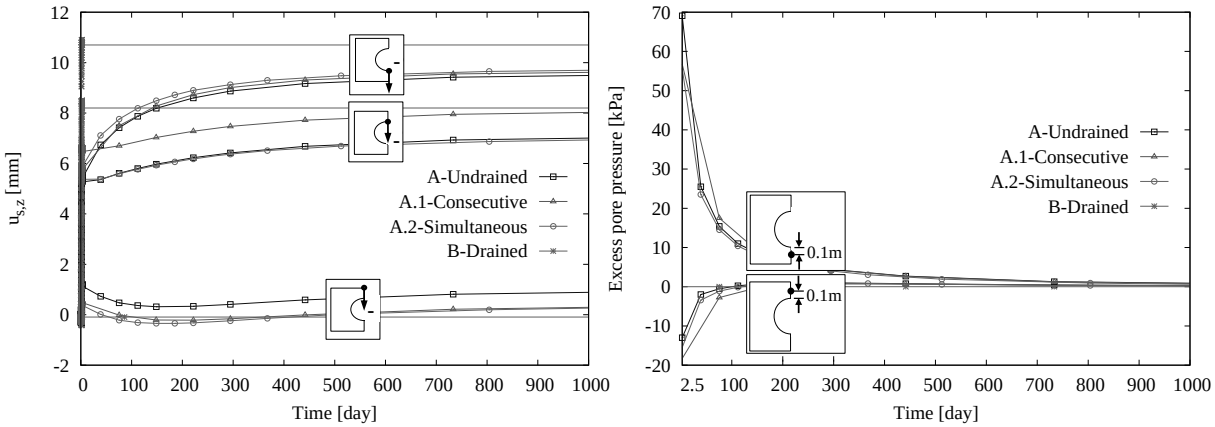

(a) (b)

Figure 5.15: Long term model responses for grouting simulated as pore pressure (variant II) for soil with low permeability ($k^{\mathrm{f}} = 10^{-9}$ m/s); (a) soil displacement, (b) excess pore pressure variation (suction is positive and compression is negative)

the behavior of the shallow tunnel is mainly governed by uplift due to unloading and the buoyancy effect. Since the drained construction analysis does not account for neither excess pore pressure nor suction, the deformations are higher in the construction stage and the subsequent consolidation analysis in 1000 days depicts no evolution in deformations. The suction decreases the volume of the soil beneath the tunnel while the soil expands gradually with dissipation of suction which takes more than 500 days. However, the excess pore pressure at the tunnel crown dissipates quicker (about 100 days), which induces a downward settlement of the soil between ground surface and tunnel crown.

5.7 Conclusion

In this chapter, the mechanized tunnel excavation in saturated soil is numerically investigated. The influence of soil permeability, method of simulating the grouting pressure, infiltration process and grout hardening on the ground displacements, pore pressures and lining forces have been taken into consideration. In addition, the influence of different numerical methods namely, drained, undrained and consolidation analyses (based on different concepts) on the model responses have been assessed. Based on the results obtained from these numerical analyses, the following remarks can be made:

1. The tunnel excavation may result in downward settlement or upward heave at the ground surface based on the permeability of the soil deposit and its embedment depth.

2. Considering the speed of construction and duration of standstills, different types of analysis can be defined to computationally address the real tunneling process.
3. The infiltration of grout material does not take place in soil with low permeability, while it strongly occurs due to backfill grouting in soil with high permeability. Considering the evolution of the permeability in the grouting zone and stiffness of the grout material significantly affects the ground surface settlement after passing the TBM and lining axial forces.
4. Different methods for simulating the backfill grouting do not significantly change the axial forces in the lining segments while dramatically affect the bending moments and settlements at the ground surface.
5. For the soil with low permeability, the complete dissipation of the excess pore pressure (and suction) takes almost 1000 days after finishing the construction stage.

6 Advanced process simulation

6.1 Introduction

According to the previous numerical anaylses, the three-dimensional numerical simulation of mechanized tunnel excavation is time and computational cost consuming. It is valuable to investigate the techniques for optimal numerical forward model, especially in case of parametric studies where intensive evaluations of numerical model are needed. Within this framework, three advanced process simulation techniques, namely adaptive constitutive modeling (Lavasan, Zhao & Schanz 2018), submodeling (Zhao, Lavasan & Schanz 2018) and hybrid modeling, are introduced in this chapter. Adaptive constitutive modeling aims to adequately describe the soil behavior in different sub-domains of the model by assigning appropriate constitutive models. The objective of submodeling is to cut a region of interest from the initial global model and continue the following simulation in this smaller scale model only. Based on submodeling technique, hybrid modeling is proposed to combine the capacity of the process-oriented submodeling to accurately describe the complex tunneling induced system behavior with the computational efficiency of metamodel (or surrogate model). After introducing the concepts and methodologies, these approaches are applied in the numerical simulation of mechanized tunnel excavation and their performances in predicting the model responses are evaluated.

6.2 Adaptive constitutive modeling

6.2.1 General concept

The general approach of adaptive constitutive modeling is to firstly assign and initiate the stresses in the domain based on basic constitutive model and then to exchange the basic model to the advanced one in a particular sub-domain in vicinity of the TBM due to the variation of boundary condition and stress/strain. Once the system behavior in

this sub-domain is not significantly affected anymore, the advanced constitutive model is switched back to the basic one.

In order to assign the appropriate constitutive model to relevant sub-domains, two crucial aspects should be carefully considered in the novel adaptive constitutive modeling approach. Firstly, how to determine the size of the sub-domain where advanced constitutive model has to be applied. The author suggests to determine the size based on the variation of plastic strain at the Gaussian points corresponding to each single element in the domain. Apparently, the advanced constitutive model should be assigned to the element when incremental plastic strain in Gaussian points of the element fulfills the predefined criteria. Likewise, the advanced soil model can be exchanged back to the basic model once the incremental plastic strain becomes smaller than a certain value and consequently fulfills the criteria for reassigning the basic model. Secondly, how to switch between the basic and advanced constitutive models as each model updates its own internal variables during stress-strain variation. Therefore, the variables corresponding to basic and advanced models should be compatible. Having identical or comparable internal variables for basic and advanced models guaranties appropriate transfer of stress-strain state from one model to another. Therefore, the author admits that the proposed concept is to hierarchical constitutive models developed in the same family group but having different levels of complexity. These models essentially have the same or compatible internal variables and update process of these variables should obey the same algorithm. This enables pursuing the analysis on the basis of current stress level calculated by the formerly assigned constitutive model. It should be noted that additional state variables might be needed when the basic model is exchanged to the sophisticated one. Under this situation, it is necessary to ensure that the state variables of advanced model are updated in accordance with the stress state variation when the basic model governs the domain. Such modification avoids eliminating the stress history due to constitutive model exchange.

In this part of the study, adaptive constitutive modeling is applied to mechanized tunneling. Due to complex mechanical incidents around the TBM, a sophisticated constitutive model is used to describe the system behavior in this highly affected subdomain (near-field). This area progressively moves in accordance with TBM advancement. Fig. 6.1 shows the schematic shape of near-field subdomain in two-dimensional coordination. The defined near-field turns to a cuboid block in 3D model with the size of width×height×length of $(2L + D) \times (2L + D) \times 2L$ where D is tunnel diameter. Different methods are available for defining the value of L. For instance, based on the distribution

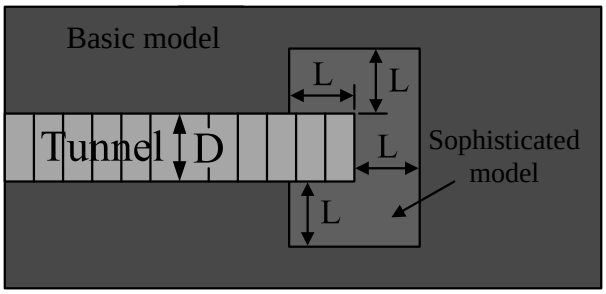

Figure 6.1: Schematic shape of near-field sub-domain (D is the tunnel diameter and L is assumed size of sub-domain)

of strain energy, stress gradient or plastic strain. In the numerical model of tunneling in this section, prior to tunnel construction, the soil domain is modeled by employing basic (Mohr-Coulomb) model. However, the basic model will exchange to advanced model (Hardening soil model with small strain) in the domains coincide with the near-field sub-domain. Thereafter, the basic model is reassigned with further TBM advancement. With this framework, the advantage of applying advanced constitutive model is to describe the plastic behavior of soil. Therefore, the incremental plastic strain in each element during tunnel excavation is derived for determination of the value of L. The detailed procedure will be explained in the following sections.

6.2.2 Numerical modeling procedure

The 3D numerical simulation of mechanized tunneling introduced in section 3.3 is adopted in this chapter to verify the model adaption approach. Two different tunnel overburden depths are considered, $1D$ and $5D$ depths represent the shallow and deep tunnels, respectively. Overcut, conicity of TBM and ground water level are not considered in this part of the study. The determination of required face support and grouting pressure can be found in section 2.2.2. The monitoring section for shallow and deep tunnels are defined to be $4.5D$ and $9D$ away from the model boundary, respectively.

The TBM shield and lining are simulated by the use of structural shell elements in accordance with an isotropic linear elastic model. The parameters of the shell elements representing the TBM and lining are given in Table 5.2.

Table 6.1: The parameters for hierarchical constitutive models

Parameter	φ'	ψ'	c'	E	E_{50}^{ref}*	E_{ur}^{ref}	G_0^{ref}	$\gamma_{0.7}$	m	ν	γ
MC	35	5	10	$f(z)$	-	-	-	-	-	0.3	17
HSS	35	5	10	-	35	100	130	1.5E-3	0.7	0.2	17
Unit	[°]	[°]	[kPa]	[MPa]	[MPa]	[MPa]	[MPa]	[-]	[-]	[-]	[kN/m^3]

Note: *$E_{50}^{\text{ref}} = E_{oed}^{\text{ref}}$ and p^{ref}=100 kPa.

6.2.3 Constitutive soil model adaption approach in mechanized tunneling

In the current numerical model, Mohr-Coulomb (MC) model is taken as the basic constitutive model, and Hardening soil model with small strain stiffness (HSS) is adopted as the advanced constitutive model. The corresponding model parameters are given in Table 6.1. Although, the hierarchical constitutive models are from the same family, the pre-failure behavior of MC model fundamentally differs from HSS model in both loading and unloading/reloading. In adaptive constitutive modeling of soil, as the basic MC and sophisticated HSS models are employed simultaneously at different sub-domains, the parameters have to be calibrated to achieve the best consistency in the results. Within this framework, the plasticity parameters in MC and HSS model are set to be identical, the distribution of elastic stiffness over depth in MC model is defined to be same as that in HSS model. The detailed approach has been introduced in section 3.4. It is worth mentioning that the elastic stiffness at small strain in HSS model is E_0 instead of E_{ur}.

As the main objective of this research, relevant constitutive models are supposed to be assigned to the sub-domains regarding its plastic strain level. Accordingly, the mechanized tunneling process is analyzed by adapting the advanced constitutive model to the sub-domain in the proximity of TBM, while, the basic model is assigned to the rest of the model. The relevant size of the near-field can be determined on the basis of the distribution of plastic strain in the domain.

Fig. 6.2 shows the distribution of volumetric and deviatoric plastic strain during one excavation for both shallow and deep tunnels when the tunnel head is at the monitoring sections. Here the basic model (modified MC model with depth dependent stiffness) is applied in the entire soil domain. As seen, the significant variation of plastic strain occurs near TBM face and around the grouting area. About $1.5D$ ahead the tunnel face and $1D$

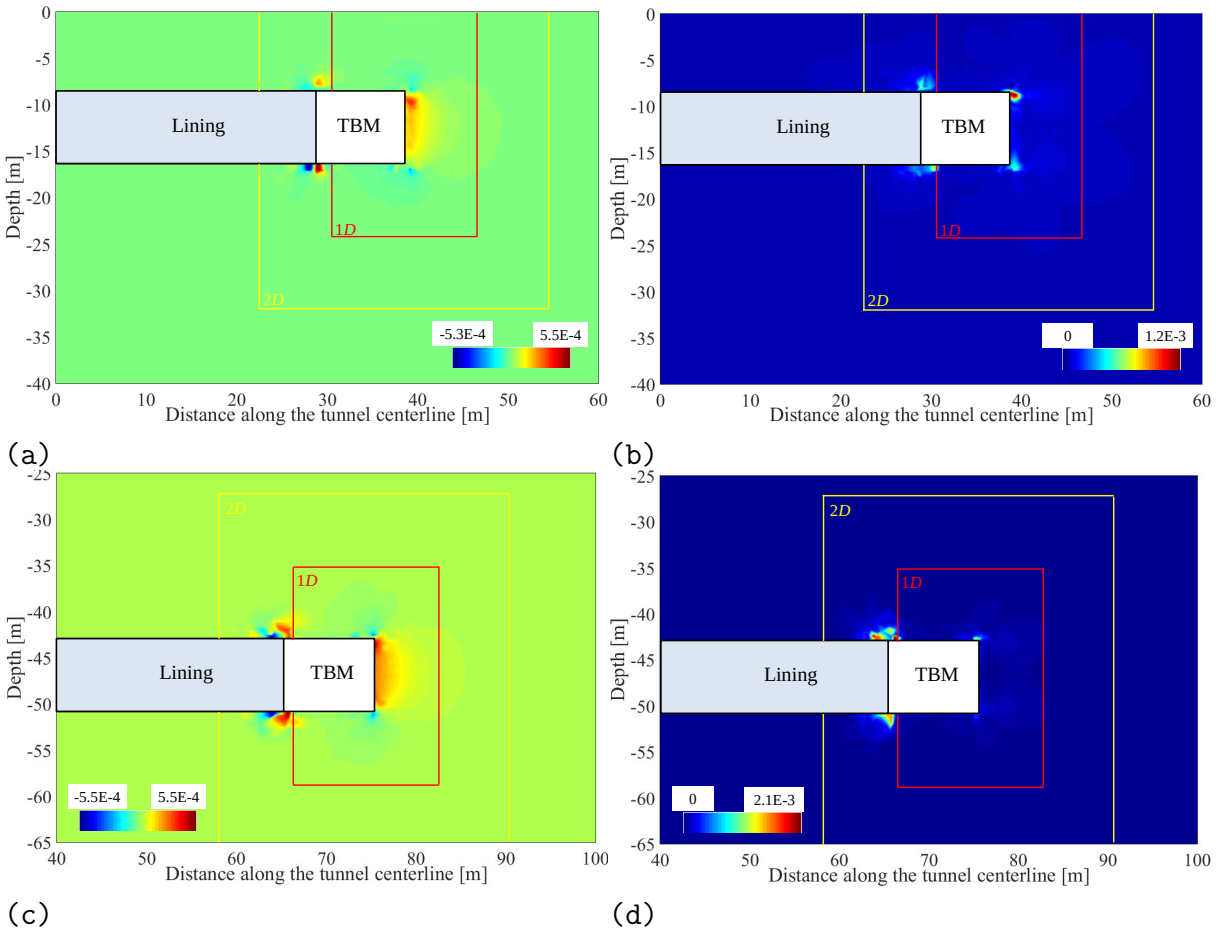

Figure 6.2: Distribution of plastic strain generated during excavation; (a) volumetric strain of shallow tunnel; (b) deviatoric strain of shallow tunnel; (c) volumetric strain of deep tunnel; (d) deviatoric strain of deep tunnel

behind the tail of TBM, the variation of plastic strain during this excavation is negligible for both shallow and deep tunnels. To better view the tunneling induced plastic zone, variation of plastic strain at tunnel crown and invert for each excavation with respect to the advancement of TBM is shown in Fig. 6.3. As seen for both shallow and deep tunnels, when the TBM face is about $1.5D$ away from the observation section, plastic strain at this cross section begins to be generated. When the tunnel face is about $2D$ ahead of the monitoring section, the plastic strain at the monitoring section keeps constant. Within this framework, the plastic zone for one excavation can be covered by the aforementioned cuboid (see Fig. 6.1) with approximately L=$2D$. In this study, the cuboid sub-domain around TBM with L=$1D$, $2D$ and $3D$ is assumed to investigate the effects of the model exchange in this domain on the model responses. This will be discussed more in detail in the next section by evaluating the soil deformations and stress paths.

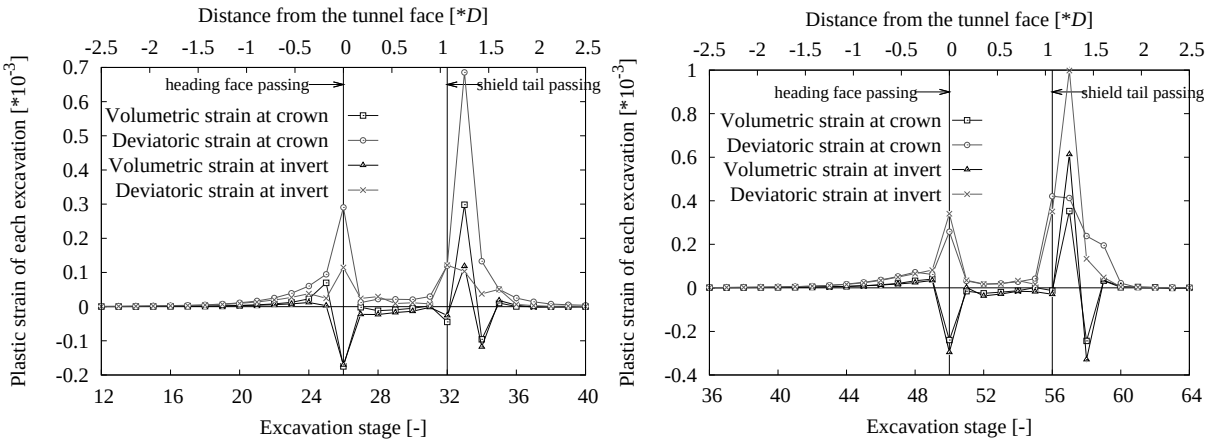

Figure 6.3: Variation of plastic strain for each excavation with the advancement of TBM for (a) shallow tunnel; and (b) deep tunnel

6.2.4 Evaluation of model response uncertainty using hierarchical constitutive models

Consider the fact that advanced constitutive model may induce higher degree of uncertainty on the model responses due to the larger amount of model parameters that are extracted from complex and costly experiments, this section aims to evaluate this kind of model response uncertainty by using different constitutive models. A 2D FE-model is created to simulate the construction process of shallow tunnel due to the fact that 2D simulation is time and resource saving for parametric study in comparison with the 3D modeling. The geometry of the 2D model is shown in Fig. 6.4. Compared to 3D FE-model, the face support and staged excavation process are neglected in the 2D model. Identical material properties and tunneling parameters (e.g., grouting pressure) are used in both 2D and 3D models. The designed numerical scenarios are shown in Table 6.2. Overall MC (depth dependent stiffness) and HSS model are applied in scenarios I and II respectively. While in scenario III, model adaption approach is used. HSS model is applied in the near field around the tunnel and the rest of soil domain is modeled by using MC model. In MC model, depth dependent stiffness E and shear strength parameters c', φ', ψ' are taken as the uncertain parameters using normal distribution. The mean values are given in Table 6.1 and coefficient of variance is defined as 10%. In HSS model, $c', \varphi', \psi', E_{50}^{\mathrm{ref}}, E_{oed}^{\mathrm{ref}}, E_{ur}^{\mathrm{ref}}$ are assumed to have 10% COV while parameters $G_0^{\mathrm{ref}}, \gamma_{0.7}$ are assumed to have larger uncertainty of 20% coefficient of variation (COV) due to the fact that complex experiments are needed for parameter determination. 200 sets of model

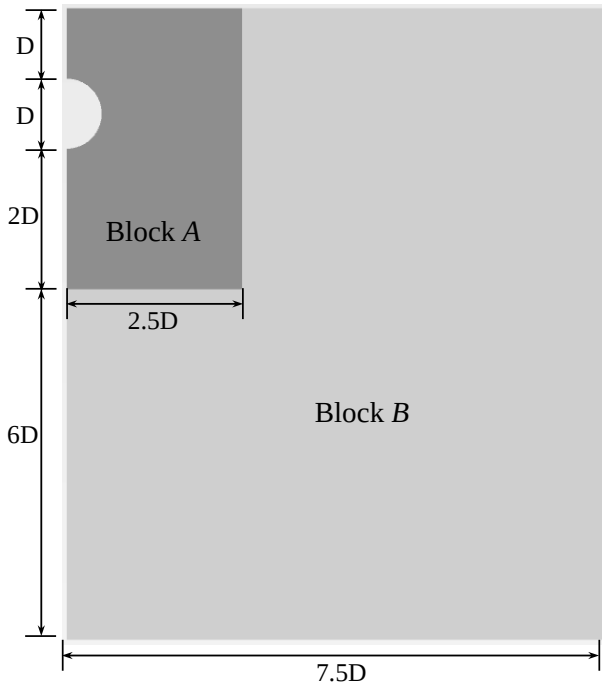

Figure 6.4: Geometry of the 2D model

parameters within the given distribution are created to calculate the mean value of maximum surface settlement (u_{max}) and corresponding COV, and the results are given in Table 6.2.

As seen in Table 6.2, when MC model is applied in the entire soil domain, least degree of model response uncertainty is obtained. However, the mean value of u_{max} is significantly underestimated compared to that obtained by applying HSS model. In contrast, HSS model results in largest degree of uncertainty due to greater amount of model parameters and higher values of COV. For scenario III where model adaption approach is applied, mean value of u_{max} is accurate and the uncertainty is reduced in comparison with scenarios II. Therefore, it can be deduced that adaption approach is available to adequately predict the model responses with less uncertainty. Accordingly, the complex in-situ or laboratory tests need to be conducted in the near field around the tunnel only, the total cost of parameter determination can be reduced.

6.2.5 Numerical results of adaptive constitutive modeling approach

In this section, the influence of the size of the sub-domain, where the adaptive constitutive soil modeling is conducted, on the model responses has been investigated (overall perspective). Apparently, an accurate model adaption entails proper determination of the

Table 6.2: Evaluation of model response uncertainty using different constitutive models

Scenario	Constitutive model	Uncertain parameters	Mean u_{max}	COV
I	A:MC, B:MC	E, c', φ', ψ'	2.9 mm	17.4%
II	A:HSS, B:HSS	$c', \varphi', \psi', E_{50}^{\text{ref}}, E_{oed}^{\text{ref}}, E_{ur}^{\text{ref}}, G_0^{\text{ref}}, \gamma_{0.7}$	5.5 mm	39.7%
III	A:HSS, B:MC	$E, c', \varphi', \psi', E_{50}^{\text{ref}}, E_{oed}^{\text{ref}}, E_{ur}^{\text{ref}}, G_0^{\text{ref}}, \gamma_{0.7}$	5.3 mm	30.2%

Note: When the mean values of model parameters are used in the constitutive models (see Table 6.1), u_{max} obtained in scenarios I, II, III are respectively 2.7 mm, 5.1 mm and 5.1 mm.

size of the near-field sub-domain subjected where the model adaption is carried out. To be specific, the variation of the stress path and soil deformation at different observation points with progressive construction process has been evaluated.

Stress path

Since the stress redistribution in soil around the tunnel dominantly affects the soil behavior, this part investigates the effect of model adaption on the variation of stress path at the crown and the invert of the shallow and deep tunnels. Fig. 6.5 shows the variation of the stress path in I_1' and $\sqrt{J_2}$ space for shallow and deep tunnels. It should be mentioned that θ is the Lode angle and $\tan\theta_c$=$\sin\varphi'/\sqrt{3}$ (see section 2.2.1). As seen, when the analysis conducted by employing basic model (modified MC model with depth dependent stiffness) or adaptive constitutive modeling in $1D$ around tunnel, the stress paths are different from those obtained by the advanced HSS model. The stress paths for advanced model and adaptive constitutive modeling approach are in good agreement while the adaption is conducted in a sub-domain around TBM face having the size of 2-3D for both shallow and deep tunnels. In Fig. 6.5, the excavation starts far from the observation point at phase 1. Due to the weight of the soil deposit and the face support pressure acting on the excavation zone, the stress path shows loading in the observation point at the top and bottom of the tunnel. This loading stress path continues while the TBM gets very close to the observation surface (phase 25 for shallow tunnel and phase 49 for deep tunnel). An unloading occurs when the observation cross section is under excavation (phases 25-32 and 49-55 respectively for shallow and deep tunnels) and it lasts up to grouting pressure being applied. The loading step due to grouting lasts for 2 steps

(phases 32-34 and 55-57 respectively for shallow and deep tunnels). By termination of the grouting process, the unloading stage occurs. Finally, the stress paths stay constant for both shallow and deep tunnels. According to Fig. 6.5, the basic MC model has ended up to the failure line; it occurs due to having no plasticity in pre-failure domain within basic model framework beyond the elasticity. However, the advanced model obeys a plasticity rule before reaching the Mohr-Coulomb failure line. As seen, neither the advanced model nor the model adaption approach have not ended up to failure line by mechanized tunneling process.

Ground surface settlements

The ground surface deformations induced by shallow and deep tunnelings are shown in Fig. 6.6. According to Fig. 6.6(a), when the basic model is uniformly assigned to the entire model, a significant heave at the ground surface is observed before the TBM reaches to the observation cross section. In contrast, the reference model (HSS model in the entire domain) indicates negligible deformation before excavation. By advancement of TBM towards the monitoring section, the difference between the responses on the basis of basic and advanced constitutive models becomes significant. However, no heave is detected for deep tunnel even in case of using basic model in the entire domain.

Apparently, the near-field subdomain is subjected to initial geostatic loading before excavation, unloading due to tunnel mass loss during the excavation and reloading due to grouting process. Fundamentally, the difference between modified MC and advanced HSS model can be attributed to identical stiffness for loading, unloading and reloading as well as having no hardening rule and plasticity before reaching the failure in the basic model. In addition, the advanced model addresses the initial stiffness increase at reversal loading (e.g. unloading and reloading). With reference to formulation of HSS model, the initial stress state of normally consolidated soils lays on the yield surface at loading condition that compromises the plastic straining while the soil become over-consolidated due to unloading. With respect to the double-hardening rule in the advanced model, the responses of the model around the excavation zone are more accurately assessed by advanced model rather than the basic model. According to Fig. 6.6(a), conducting adaptive constitutive modeling for shallow tunnels eliminates the unrealistic heave at the ground surface. When the model adaption area around the tunnel increases to be a cube-shaped zone with size of $L = 2D$, the obtained surface settlement is almost identical with that of reference model where advanced HSS model is applied to the entire domain (the difference of final settlement is less than 5%). Likewise, for the deep tunnels, the larger the model adaption

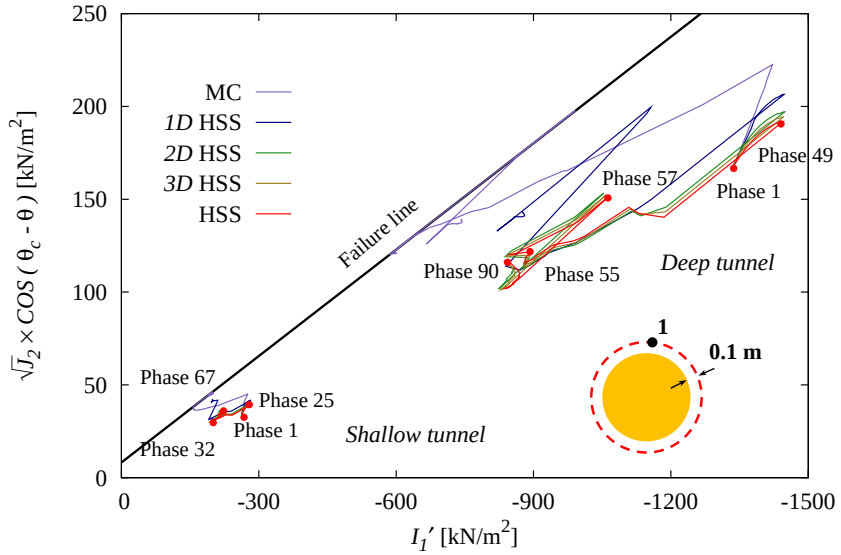

(a)

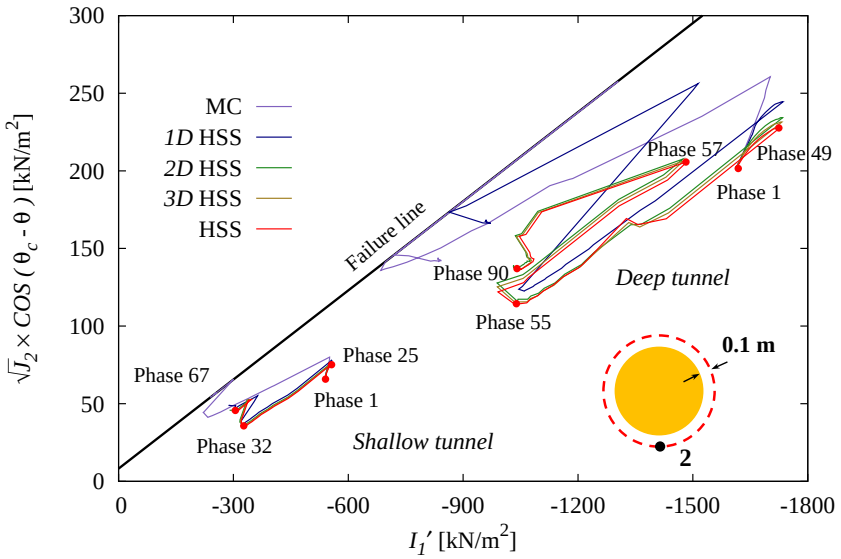

(b)

Figure 6.5: Variation of the stress paths in I_1' - $\sqrt{J_2}$ space; (a) tunnel's crown, (b) tunnel's invert

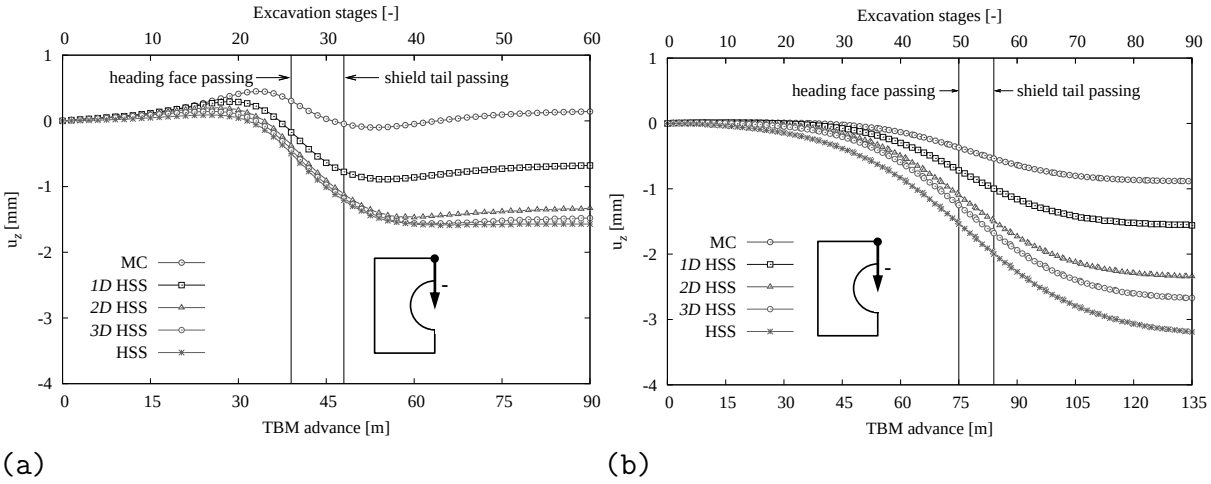

Figure 6.6: Vertical settlement of the ground surface during mechanized tunneling process; (a) shallow tunnel, (b) deep tunnel

area is, the better agreement between the model responses can be obtained in comparison with that of reference model (the differences of the final settlement compared with the reference model are 25% and 15% for $L = 2D$ and $L = 3D$, respectively). It is worth mentioning that these conclusions hold true when additional 0.5% tunnel volume loss is modeled using contraction factor in the tunneling simulation.

6.3 Submodeling

6.3.1 General concept

Submodeling is also known as the cut boundary displacement method or the specified boundary displacement method. The cut boundary is the boundary of the smaller model which represents a cut through a larger complete model. For the sake of nomenclature, the larger complete model is called global model and the smaller local model is called submodel. It should be noted that global model can be a submodel of a higher and larger more complex model. The global model is normally defined according to the materials, geometry and boundary conditions. This model is considered complex and to run a simulation on such a complete global model would require many time and computational resources, especially if intensive simulations are needed in parametric study, or there are certain regions of interest in this global model that need to be finely meshed. Therefore, once the global model has been simulated the nodal displacements of this model are saved. A submodel is created by "cutting" a portion out of this global model. After that, this

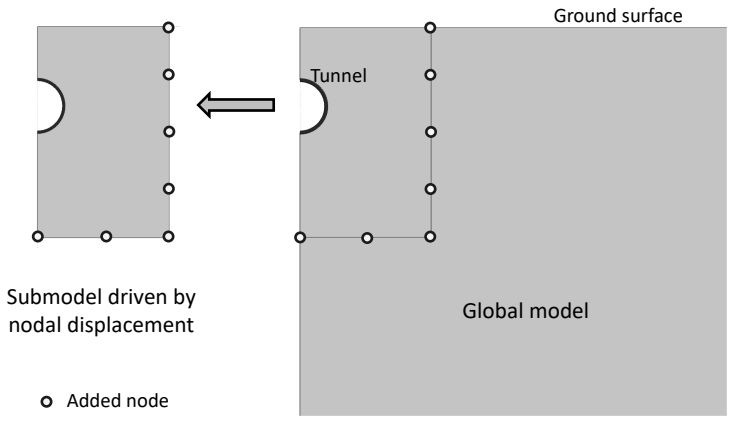

Figure 6.7: Driving the submodel by nodal displacement of the global model

submodel is a complete domain in its own. The submodel may or may not be defined with the same material law in comparison with the global model. However, it is defined with boundary conditions in terms of nodal displacements (derived from global model) at the "cut" boundaries. Fig. 6.7 shows graphically the transfer of boundary conditions from global model to submodel. Since the submodel is a portion of the global model, it requires less computational costs for solving (same mesh discretization) or can be refined in terms of mesh size using the same computational resources, which permits more detailed analysis.

Submodeling approach is based on St. Venant's principle, which states that if an actual distribution of forces is replaced by a statically equivalent system, the distribution of stress and strain is altered only near the regions of load application. The principle implies that when the actual boundary conditions of the submodel is replaced by the equivalent boundary conditions, there is no significant difference of the model response in the region which is not close to the boundary of the submodel. Although the size of submodel is defined by the user and depends on the particular problem, the appropriate size of the submodel should be checked that effects caused by the local phenomena must vanish at the submodel boundary.

Submodeling technique has been widely applied in structural engineering. For instance, to analyze the influence of a small hole in a relative large plate, stress concentration effect caused by crack, etc. While for the geotechnical problems, there are rare studies on the application of submodeling. This section aims to illustrate the methodology of applying Submodeling technique in mechanized tunnel simulation.

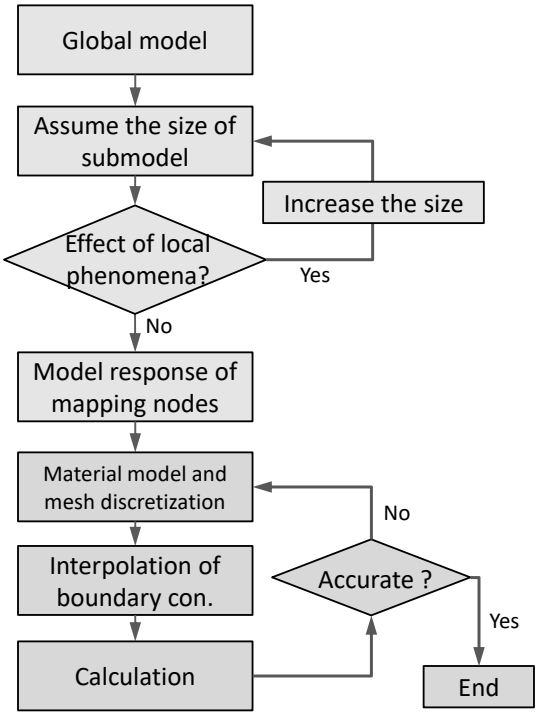

Figure 6.8: Methodology of Submodeling technique

6.3.2 Submodeling strategy for tunnel simulation

The general procedure of conducting submodeling for tunneling simulation is described as follows and the flow chart is shown in Fig. 6.8.

1. The global model has to be created and analyzed. Thereafter, the region of interest should be defined.

2. The size of the submodel should be defined on the basis of the region of interest. In case of tunneling simulation, the the submodel should embody the near field around the TBM including the constituent subsystems such as TBM, lining segments, face support, and grouting pressure. Afterward, it is essential to check that the effect of local phenomena is vanished at the boundary of the submodel.

3. The model responses (e.g., nodal displacements) at the cut boundary have to be derived from the global model and be applied to the boundaries of the submodel.

4. A mesh refinement and the advanced constitutive model adaption should be carried out in the submodel if a higher level of accuracy is expected in the calculation of the submodel.

5. The nodal displacements retrieved from the global model should be interpolated to find the distribution of the displacements on the cut boundaries.
6. The validity of the submodel to represent the local aspects should be verified. This validation is usually conducted based on the real measurements. In the present study, instead of real data, synthetic data obtained from a "reference model" that considers the entire domain with advanced constitutive model and fine mesh discretization are applied, is used.

One of the most important steps in this approach is to determine the appropriate size of the submodel by checking the local phenomena at the cut boundaries. In the current stage of this study, the concept of strain energy is utilized to determine the adequacy of the size of the submodel. The strain energy at j-th Gaussian point is calculated as:

$$W_j = V_j \sum_{i=1}^{n} \sigma_i \mathrm{d}\varepsilon_i \tag{6.1}$$

where V_j is the product of weight assigned to the j-th Gaussian point and the determinant of the Jacobian there, n is number of calculation steps, σ_i and $\mathrm{d}\varepsilon_i$ are stress and incremental strain at i-th calculation step, respectively. It should be noted that sum of $\sigma_i \mathrm{d}\varepsilon_i$ represents the density of strain energy. Once the solution of the global model is obtained, the strain energy gradient on the assumed submodel boundary can be derived. If the strain energy gradient tends to zero, this means that the effect of local phenomena is negligible. Subsequently, the size of the submodel is appropriate. It should be noted that there are many other methods to determine the appropriate size of the submodel, such as checking the resultant forces at the cut boundaries of the submodel with those coming from the global model by performing an iterative strategy. Although the strain energy concept is applied in the present study, the consistency of submodel and reference model is justified by comparing the stress distribution on the cut-boundaries and the unbalance force evolution in the submodel with the reference model. An example of determining the appropriate size of submodel based on strain energy concept is described in the following section.

6.3.3 Application - 2D tunneling simulation

- Introduction

In this section, Submodeling technique is applied to study the 2D tunneling induced ground movements and lining forces. 2D numerical model which has been introduced

Table 6.3: Constitutive model parameters for different soils − the Hardening Soil (HS) model

Soil type	φ'	ψ'	c'	E_{50}^{ref}	E_{oed}^{ref}	E_{ur}^{ref}	p^{ref}	m	ν	K_0^{NC}	γ
Soft	25	0	0	10	10	30	0.1	1.0	0.2	0.57	17
Stiff	35	5	10	35	35	100	0.1	0.7	0.2	0.43	17
Unit	[°]	[°]	[kPa]	[MPa]	[MPa]	[MPa]	[MPa]	[-]	[-]	[-]	[kN/m^3]

in chapter 3 is adopted here as well. The geometry of the numerical model is shown in Fig. 3.1(a). The tunnel has $1D$ overburden, here D=8.5 m is the diameter of the tunnel. TBM shield and lining properties are given in Table 5.2. Two different types of soil are used in this section to evaluate the distribution of strain energy, model parameters of soft and stiff soils are given in Table 6.3.

In the numerical simulation of tunneling process, $K0$ procedure is applied to generate the initial stress distribution. After that, soil inside the tunnel is deactivated to model the tunnel excavation. The contraction factor method is used to simulate the volume loss during excavation. In this study, high contraction factor (3.5%) is assumed to have larger mobilization of soil shear strength. Furthermore, the grouting pressure is simplified as a uniform load (200 kPa) which is applied on the surrounding soil to compensate the soil deformation. Finally the lining segment is installed.

- Strain energy

Fig. 6.9 shows the distribution of total strain energy at all Gaussian points of the global model by the end of tunnel excavation using HS model. As seen, significant strain energy variation in the near-field around the tunnel demonstrates that the stress/strain variation mainly takes place in the same zone. The negative strain energy is caused by unloading due to soil excavation (dilation), therefore, it is generated below the tunnel invert. Since elastic stiffness in soft soil is lower than that in stiff soil at the same depth, larger negative strain energy is obtained in the soft soil scenario. Furthermore, it is found that influencing zone of tunneling is larger in soft soil due to larger mobilization of shear strength. As the lining forces and ground movements are the most important model responses for tunnel design, the region of interest in this example is defined to be the soil domain around the tunnel. Therefore, a rectangular block with width and height of $(L + D/2)$ and $(L + 2D)$ respectively, is assumed to be the submodel that covers the region of interest

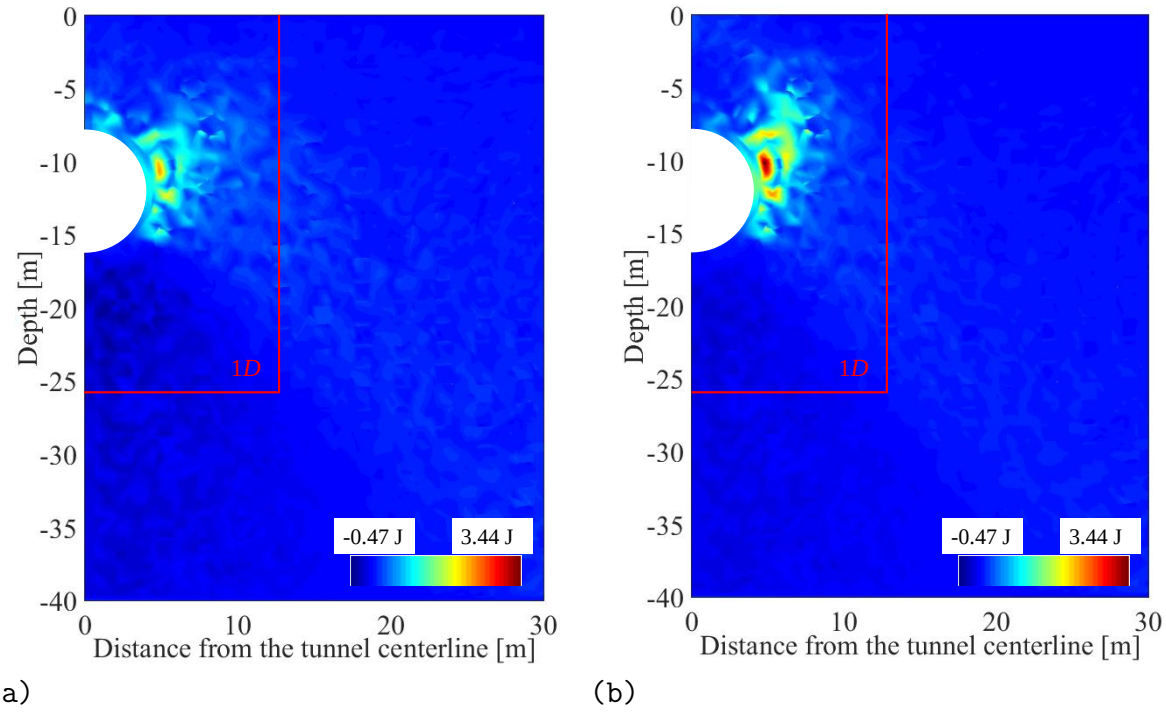

Figure 6.9: Submodeling for 2D tunnel simulation; (a) total strain energy distribution for soft soil scenario using HS model, (b) total strain energy distribution for stiff soil scenario using HS model

(see Fig. 6.7), here L depends on the distribution of strain energy. As shown in Fig. 6.9, when the submodel is assumed to be extended $1D$ beyond the tunnel (L=D), the strain energy gradient on the assumed boundary becomes negligible. In other words, a submodel that extends $1D$ around the tunnel embraces the influencing zone of tunneling process in both soft and stiff soils. Therefore, size of submodel in this tunneling model is defined using L=D.

In order to simulate the interaction between the submodel and the surrounding soil that is excluded in the submodeling calculations, nodal displacements at the boundary of submodel should be assigned. Fig. 6.10 shows the added mapping nodes on the cut boundary of the submodel. Nodal displacements of these nodes which lay on the cut-boundaries are obtained from the global model before being interpolated to generate the boundary conditions of submodel. As the position pf the nodes in the global model and submodel might be different, the nodal displacements are linearly interpolated between the nodes to find the distribution of the displacements on the submodel boundaries. An example of applying the distributed displacements on the submodel boundaries is shown in Fig. 6.10.

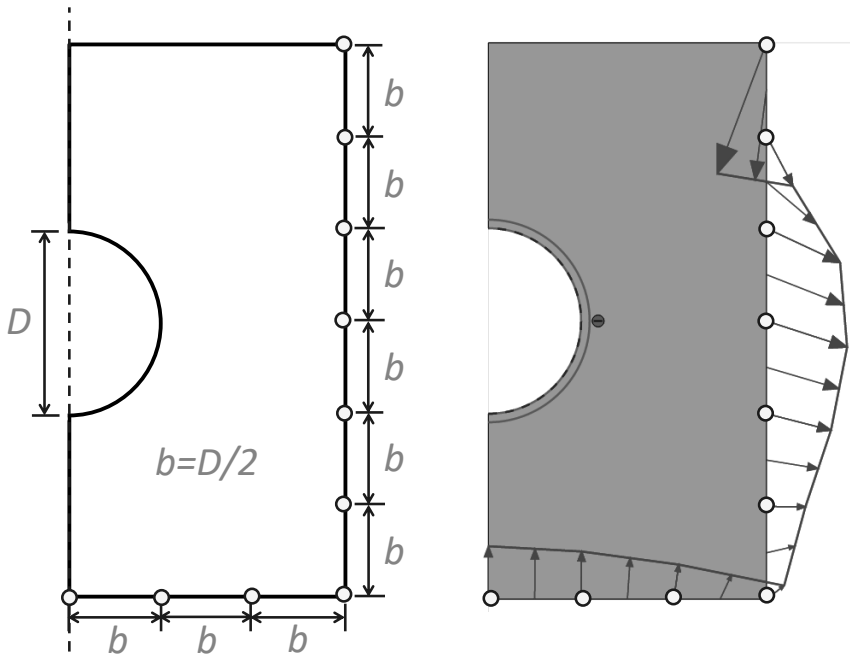

Figure 6.10: Added nodes on the boundary of the submodel (left) and an example of applying displacements on the submodel boundaries (right)

The numerical results are undoubtedly influenced by the mesh discretization in the model domain. In this study, since submodeling technique aims to evaluate more detailed system behavior in the region of interest, different mesh discretization is applied in the global model and the submodel, respectively. Additionally, a reference model is designed to check the accuracy of the proposed submodeling technique. To be specific, the reference model has the same geometry and tunnel parameters as the global model, while the mesh is globally finer than for the global model and the HS model is assigned to the entire domain. The mesh discretization in these three models is shown in Fig. 6.11.

- Results and discussions

In the first stage, the reliability of the proposed submodeling concept is verified by comparing the results of a simplified case where the same constitutive model (HS model) is applied to the submodel as well as global and reference models. The main objective at this stage is to ensure proper transfer of the information from the global model to the submodel and the influence of model discretization in 2D submodeling. The surface settlement profiles are shown in Fig. 6.12(a), and stress path for the point which is located 0.1 m above the tunnel crown is plotted in Fig. 6.12(b). As seen, the three models provide almost identical model responses. This means the submodeling technique is able to provide reasonable results that agree well with those obtained from the reference model. By

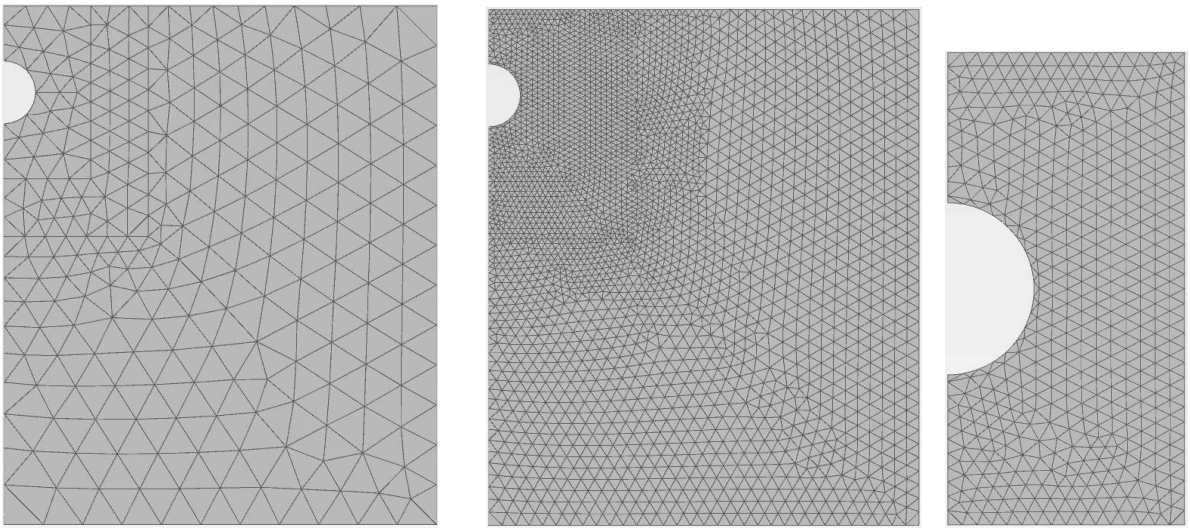

Figure 6.11: Adopted 2D mesh discretization for: (a) global model, (b) reference model, and (c) submodel

analogy, Figs. 6.12(c) and 6.12(d) show the lining radial displacements and axial forces calculated by different approaches. The submodel results are in a good agreement with those of the reference model. The slight difference between results can be attributed to (a) the coarser mesh discretization for the global model, (b) the nodal displacements at the the cut-boundary of the global model slightly differ from the those of the reference model, and (c) the simplification implied by assumption of linear interpolation of displacement profile on the boundaries of the submodel. As seen, the adequate agreement between the global model with HS constitutive relation and reference model reveals insignificant contribution of the discretization for this configuration.

In the second step, different constitutive models are used in the submodeling. To be specific, basic Mohr-Coulomb (MC) model is applied to the global model to have a preliminary evaluation of the model response. Thus, the size of the submodel, the nodal displacements on the boundary of the submodel are derived from the global model with basic MC model. Thereafter, advanced HS model is used in the submodel to better describe the soil behavior during tunnel excavation. As mentioned before, the MC model has same shear parameters as the HS model, while the elastic stiffness used in MC model is assumed to be depth dependent while the its distribution is similar to E_{ur} in HS model. According to the distribution of the strain energy distribution shown in Fig. 6.13, $1D$ size of submodel is applicable for this global model. The comparison of the model responses in Fig. 6.14 reveals that there is a huge disagreement between the results obtained by global

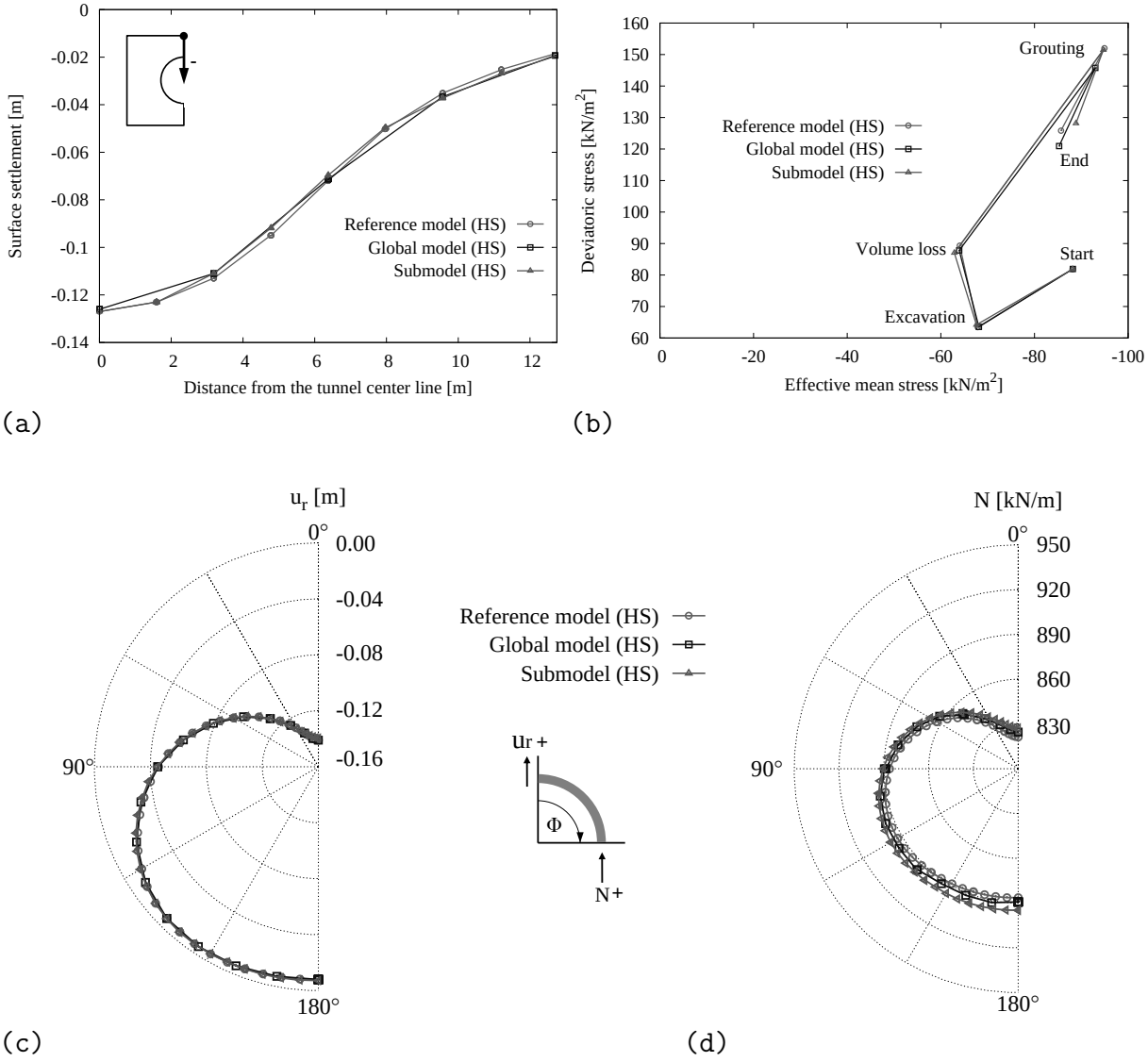

Figure 6.12: Application of submodeling technique in 2D tunneling simulation for stiff soil with HS model in global model; (a) surface settlements, (b) stress path at tunnel crown, (c) lining radial displacements, (d) axial forces

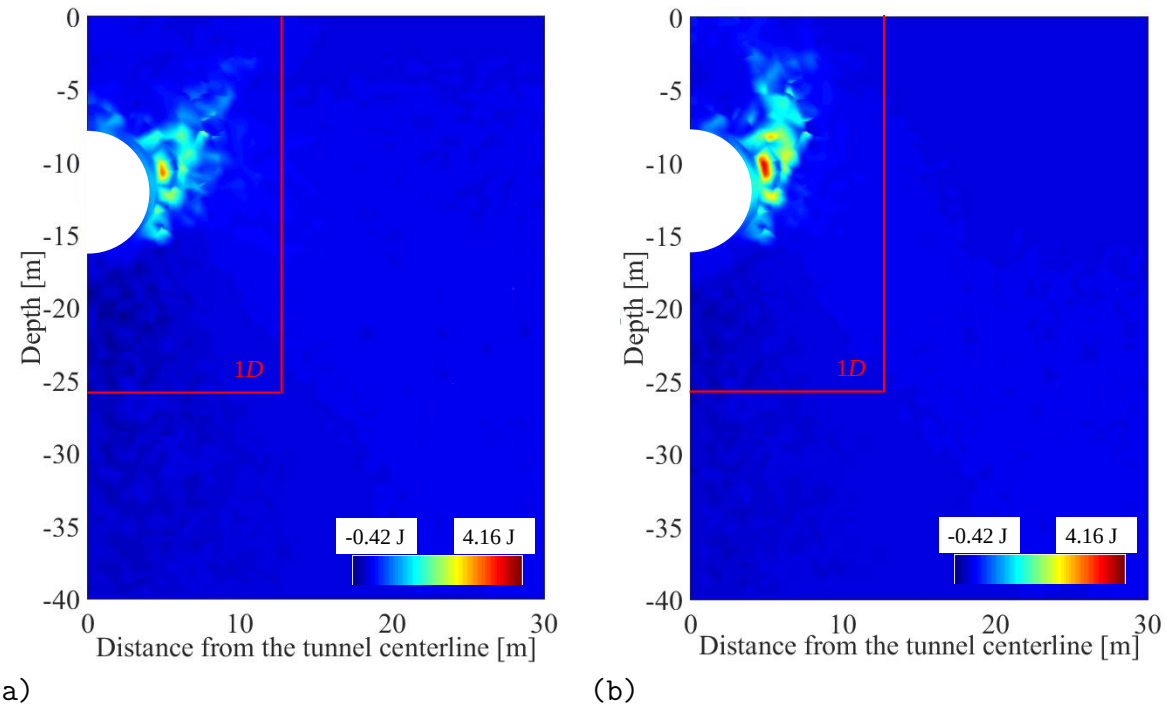

Figure 6.13: Distribution of total strain energy for (a) soft soil scenario using MC model, (b) stiff soil scenario using MC model

model and reference model. This is due to the deficiency of MC model which assumes an identical elastic stiffness during loading/unloading process and no plastic hardening. In contrast, when submodeling technique is applied and the advanced HS model is used to describe the soil behavior, although the boundary conditions of submodel are obtained from the global model where the basic model is applied, the submodel still provides results that agree well with those of the reference model.

It is to be noted that by using MC and HS model in the global model, although the strain energy distribution at the assumed submodel boundary shows that $L{=}D$ is applicable for the size of the submodel in both cases, the exact boundary conditions (nodal displacements) are different. In Fig. 6.14(a), the point on the ground surface that has horizontal distance of $1.5D$ (=12.75 m) from the tunnel center line is located on the boundary of the submodel. The settlement at this points obtained from MC model (global model) is underestimated in comparison to that of the HS model (reference model). Despite the different displacements on the cut-boundary of the submodel and the reference model at the same point, the settlement trough is in overall good agreement in comparison with the reference model.

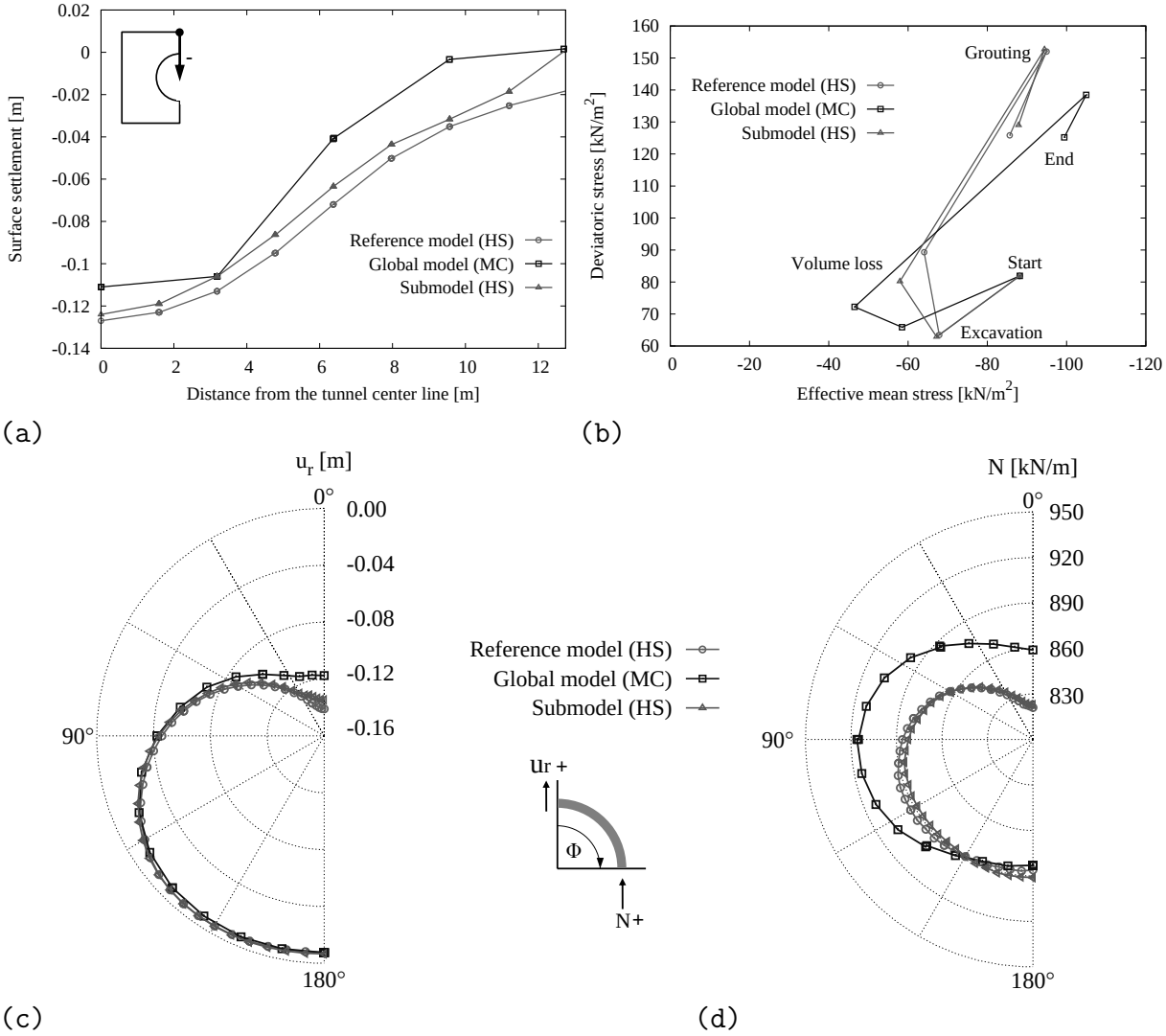

Figure 6.14: Application of submodeling technique in 2D tunneling simulation for stiff soil with MC model in global model; (a) surface settlements, (b) stress path at tunnel crown, (c) lining radial displacements, (d) axial forces

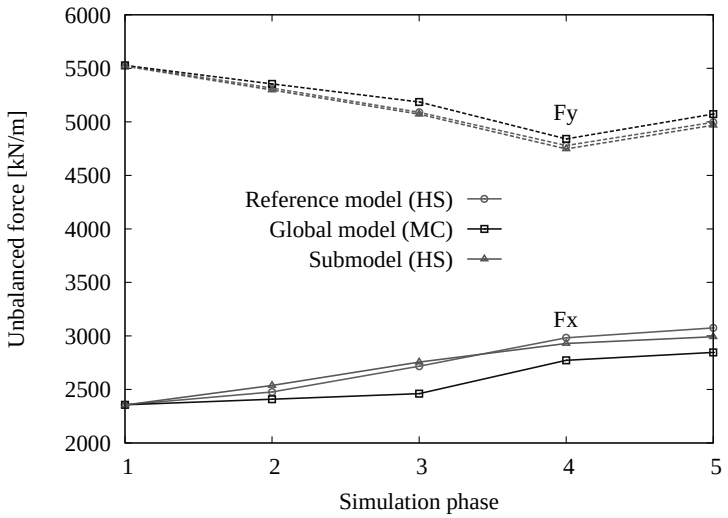

Figure 6.15: Unbalanced forces at the cut boundaries of the submodel during tunneling process for stiff soil scenario using MC model in global model [phase 1: excavation starts, phase 2: soil excavation, phase 3: tunnel volume loss, phase 4: grout injection, phase 5: final lining installation]

Additionally, when a different soil model is used for the submodel, different soil models can change the stiffness of the system. This might end up in a different stress distribution and different forces at the cut boundaries of the submodel. Therefore, the submodel needs to have a consistent force-displacement condition at the cut boundaries with that of the global model. Within this framework, it is essential to ensure that the unbalanced forces at the cut boundaries of the submodel coincide with the global model. Fig. 6.15 shows the horizontal and vertical unbalanced forces at the cut boundaries of the submodel during the tunneling process. With reference to the difference between the unbalanced forces on the cut boundary in the global, reference and submodel, it can be found that the change of the constitutive model in the submodel has made the stress-strain comparable with the reference model while the global model along with the MC model is inadequate for predicting the stress variation. In other words, although the displacement boundary conditions of the submodel are obtained from the global model using MC model, unbalanced forces at the boundary obtained via submodeling are consistent with that of the reference model.

According to the above discussions, it can be concluded that submodeling approach is able to accurately predict the tunneling induced model response. When the basic model is employed in the global model to obtain the boundary conditions of the submodel, the submodel is still adequate. It should be noted that the proposed submodeling has the

disadvantage that it requires two solutions for each simulation step (global model + submodel). However, for large domains the submodeling technique can save computational cost since the cost to solve a global model (coarse mesh with basic constitutive model) and a submodel (fine mesh with advanced constitutive model) can be less than the cost to solve a sufficiently fine discretized model (with advanced constitutive model).

6.3.4 Application - 3D tunneling simulation

- Introduction

The geometry of 3D global model is shown in Fig. 6.16, it is generally an extrusion of 2D model in the direction of tunnel axis. The soil and tunnel properties used in 3D simulation are same as those in 2D model (see stiff soil in Table 6.3 and Table 5.2). Based on the method for determining the support pressure that have been introduced in section 2.2.2, the face pressure at tunnel crown and invert is 88 kN/m^2 and 190 kN/m^2, respectively. The grouting pressure at tunnel crown and invert is respectively 138 kN/m^2 and 265 kN/m^2, respectively. Grouting pressure is applied at the tail of TBM as distributed load on the surrounding soil. The width of lining segment is 1.5m, thus, the tunnel advances 1.5m in each excavation step. Contraction factor at the tail of TBM is assumed to be 0.75% to model the volume loss around the tunnel due to overcut and conicity of TBM shield, and this contraction factor gradually decreases to zero towards the TBM head. One monitoring section is defined as $4D$ away from the model boundary. The current study aims is to apply submodeling technique to investigate the soil deformations and lining forces at the monitoring section.

In the first stage, the global model is calculated by using HS model, since the region of interest is the sub-domain in the near field around the TBM, strain energy distribution is evaluated in the transverse direction. By analogy to the 2D tunneling model, it is found that $1D$ domain covers the influencing zone of tunneling process. In order to determine the size of submodel in the longitudinal direction, the vertical displacement at tunnel crown of monitoring section is derived from the global model and shown in Fig. 6.17. As seen, soil begins to deform when the TBM head reaches $2.9D$ before the observation point. After the tunnel face is $4.9D$ ahead of the observation point, the settlement reaches steady-state condition. This means that the submodel should take into account all the the local phenomena due to excavation processes in this area (e.g. face pressure, grouting, tunnel advance) in order to assure proper for determination of the size of submodel in the longitudinal direction. Therefore, there should be a minimal horizontal distance between

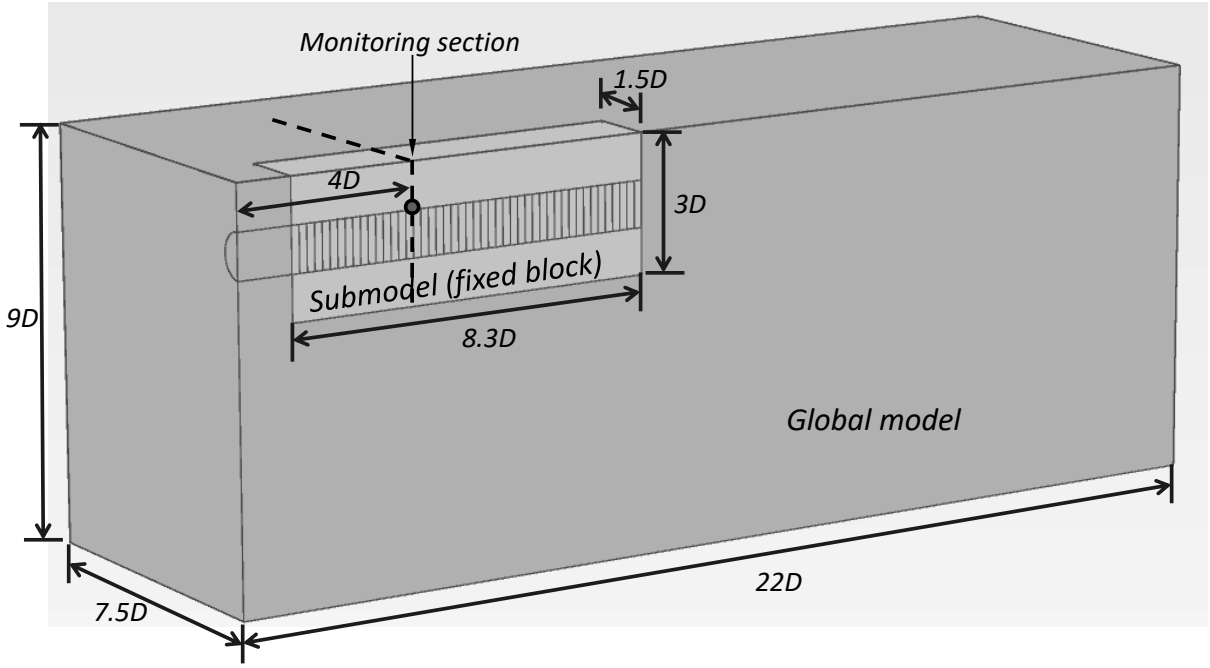

Figure 6.16: Geometry of 3D model for submodeling application

the final position of the tunnel face and the cut boundary of the submodel. In additional to applying the aforementioned strain energy concept, one alternative is to utilize the knowledge of tunneling influencing zone. To be specific, since the soil begins to deform when the tunnel face is $2.9D$ away from the monitoring section, the appropriate horizontal distance between the submodel boundary and final position of tunnel face can be defined as $2.9D$ to ensure that local phenomena is vanished at the cut boundary of the submodel. By doing so, the model response in the entire submodel domain is reliable, otherwise this local phenomena leads to questionable results for the areas between TBM and cut boundary only. If one aims to investigate the model responses in the domain far away from this area, this local phenomena is negligible. By doing so, the size of submodel in the longitudinal direction can be reduced for the purpose of saving computational cost. Within this framework, the geometry of submodel in this section is assumed to have a length of $8.3D$ at x-direction, $1.5D$ at y-direction and $3D$ at z-direction (see Fig. 6.16). Since the geometry of this submodel is independent of tunnel excavation, this approach is called "fixed block" submodeling. The schematic illustration of the model geometry in the longitudinal direction and tunnel excavation steps are shown in Fig. 6.18, here the green cluster represents the constant geometry of the submodel.

As mentioned before, influencing zone due to tunnel excavation is $2.9D$ in front and $4.7D$ behind the tunnel face, therefore, it is reasonable to update the geometry of the submodel

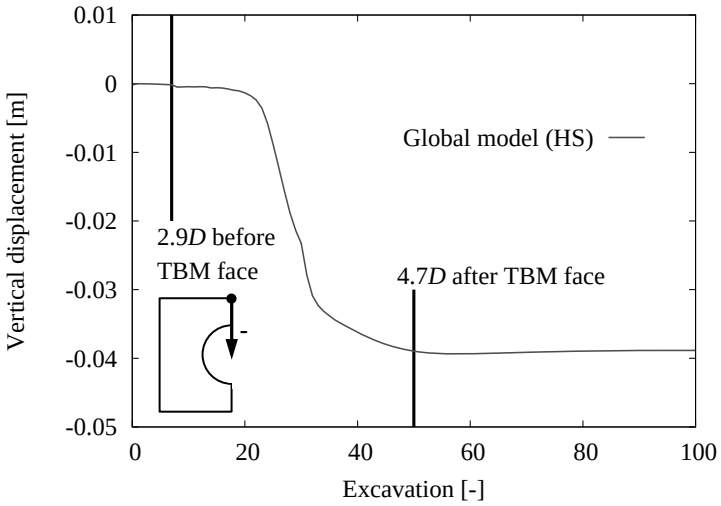

Figure 6.17: Vertical displacement at the observation point of the global model using HS model

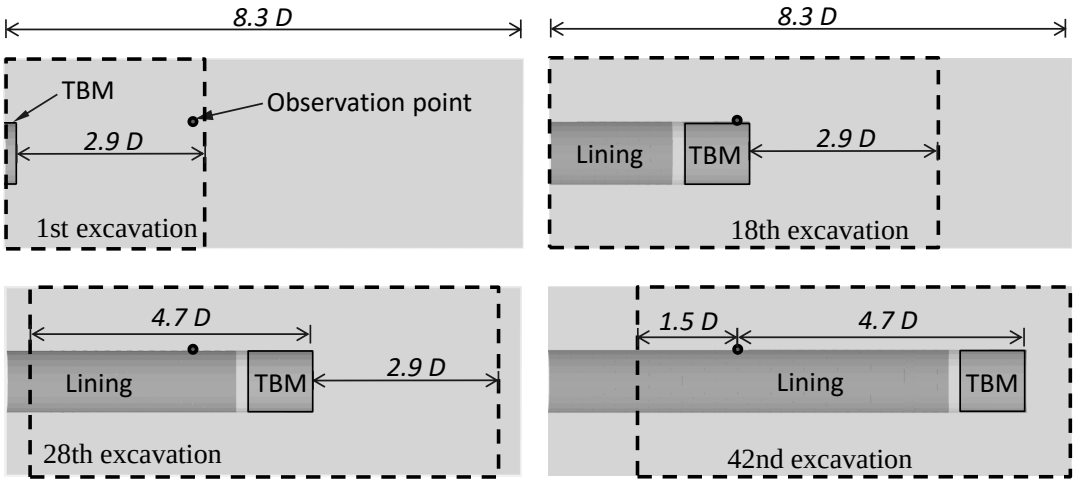

Note:
Green cluster represents the constant gemetry of the "fixed block" submodel
Dash line represents the variable geometry of the "moving block" submodel

Figure 6.18: Comparison of "fixed block" and "moving block" approaches for submodeling

according to the position of the TBM. Within this framework, "moving block" submodel is developed. The comparison between "moving block" and "fixed block" submodel is presented in Fig. 6.18. As seen, the dash line represents the variable geometry of the "moving block" submodel. Before TBM passes the monitoring section, the minimum distance between tunnel face and model right boundary is designed to be $2.9D$. In each excavation step, TBM advances 1.5m. Thus, 1.5m length (tunnel advance direction) of new soil cluster is activated in the subsequent excavation step. The maximum distance between tunnel face and model left boundary is designed to be $4.7D$ (based on Fig. 6.17). In contrast, when the tunnel face passes the monitoring section, the distance between tunnel face and model right boundary can be decreased in case that the influence of local phenomena on the behavior at the monitoring section is negligible. Additionally, the minimum distance between monitoring section and model left boundary is defined to be $1.5D$, this is for the purpose of avoiding boundary effect on the model responses. The advantage of "moving block" submodeling approach is that less computational resources are required compared to "fixed block" approach.

In both "fixed block" and "moving block" submodeling approaches, prescribed surface displacements are applied as the boundary conditions to drive the submodel. To be specific, the boundary surface of submodel can be split into many smaller rectangular sub-surfaces and each sub-surface has four corresponding nodes. The nodal displacements at these nodes can be derived from the global model in accordance with the position of TBM. After that, the average value of the nodal displacements at these four nodes is defined as the value of prescribed surface displacement for the corresponding sub-surface. By doing so for each sub-surface, the entire submodel can be driven. It should be noted that in each excavation step, the boundary conditions of the submodel need to be updated.

By analogy to the 2D tunneling simulation, different mesh discretization is applied in global model, submodel and reference model. The mesh discretization in these three models are shown in Fig. 6.19.

- Results and discussions

The vertical displacement at the tunnel crown of the monitoring section calculated by submodeling approach is shown in Fig. 6.20. In Fig. 6.20(a) the advanced HS model is used in global model to derived the boundary conditions for the submodel and HS model is used in submodel as well. While in Fig. 6.20(b), the basic MC model is applied in the global model and HS model is thereafter used in the submodel. In order to check the accuracy of the proposed submodeling method, by analogy to the 2D tunneling case, a reference model is created with fine mesh discretization and advanced HS model is applied

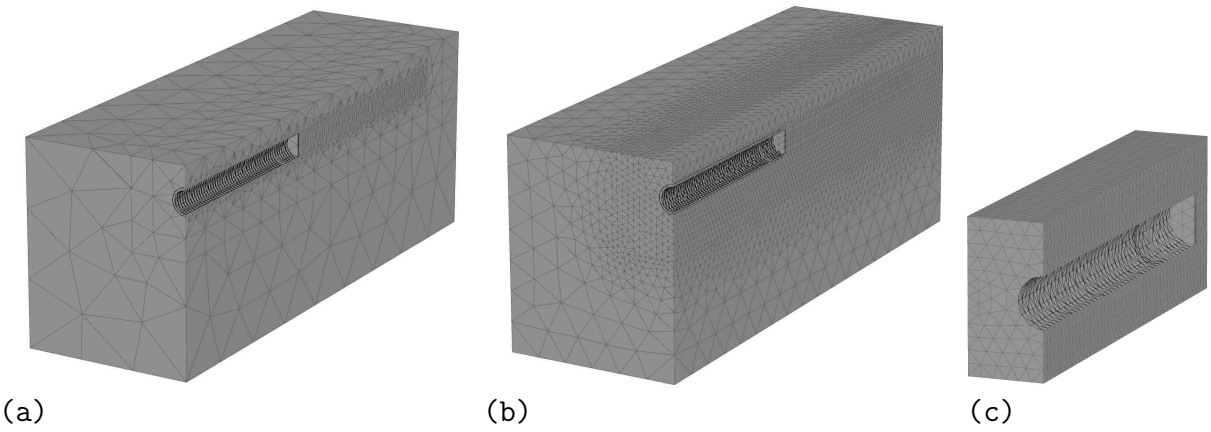

Figure 6.19: Adopted 3D mesh discretization for: (a) global model, (b) reference model, and (c) submodel

in the entire domain. The corresponding model responses are given in Fig. 6.20. As seen, there is a significant disagreement between the surface settlements obtained by the global model and the reference model, settlement is underestimated about 12% by the global model when tunnel face is $4.7D$ ahead of the monitoring section. This is due to the coarse mesh discretization in the global model. When MC model is used in the global model, this kind of discrepancy is larger (settlement is underestimated about 22% by the global model when tunnel face is $4.7D$ ahead of the monitoring section). However, the submodel provides almost same results as the reference model using both "fixed block" and "moving block" approaches. When the global model using MC model is applied to drive the submodel, the submodel is still applicable to provide adequate predictions.

Fig. 6.21 shows the lining forces and radial displacements calculated by using the submodeling technique. Here the advanced HS model is used in the global model. It is found that global model significantly underestimates the radial displacements and axial forces of the lining segments by the end of tunnel excavation, which is due to the insufficient mesh discretization. By adopting submodeling approach where the mesh discretization in the region of interest is refined, the obtained model responses are almost identical in comparison with the results of reference model.

Likewise, Fig. 6.22 shows submodeling results where MC model is utilized to describe the soil behavior in the global model. As seen, although the global model is not adequate in predicting the lining forces and radial displacements, it is adequate to provide the boundary conditions for driving the submodel. Accordingly, the submodel is able to well predict the tunneling induced lining behavior.

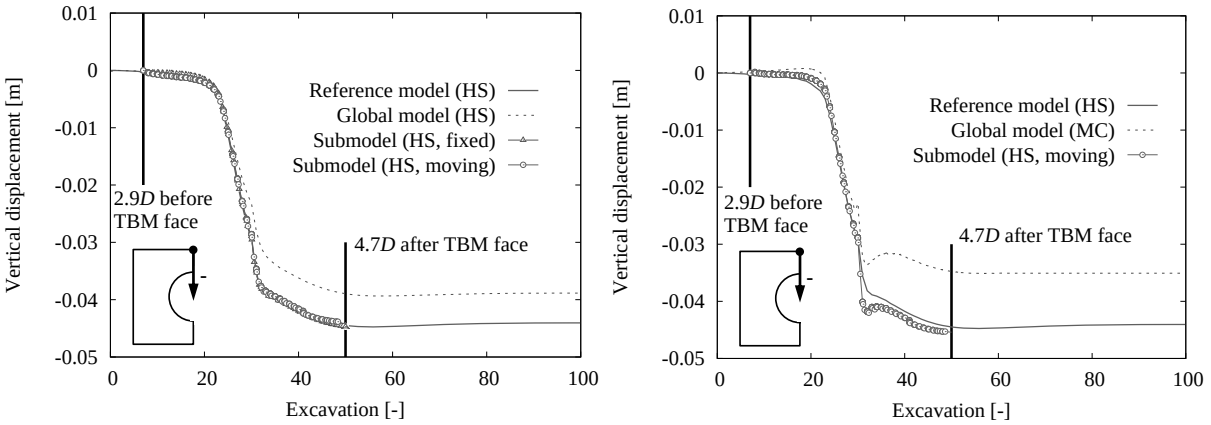

Figure 6.20: Vertical displacement at observation point using different approaches: (a) global model using HS model, (b) global model using MC model (tunnel advances 1.5m in each excavation step)

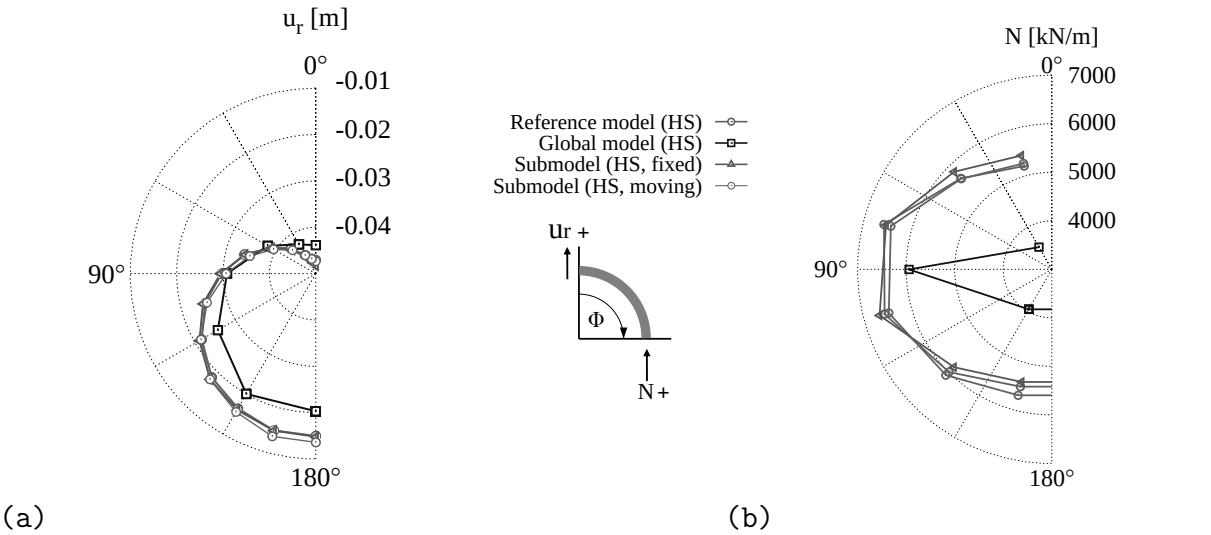

Figure 6.21: Application of submodeling technique in 3D tunneling simulation using HS model in global model: (a) lining radial displacements, (b) axial forces

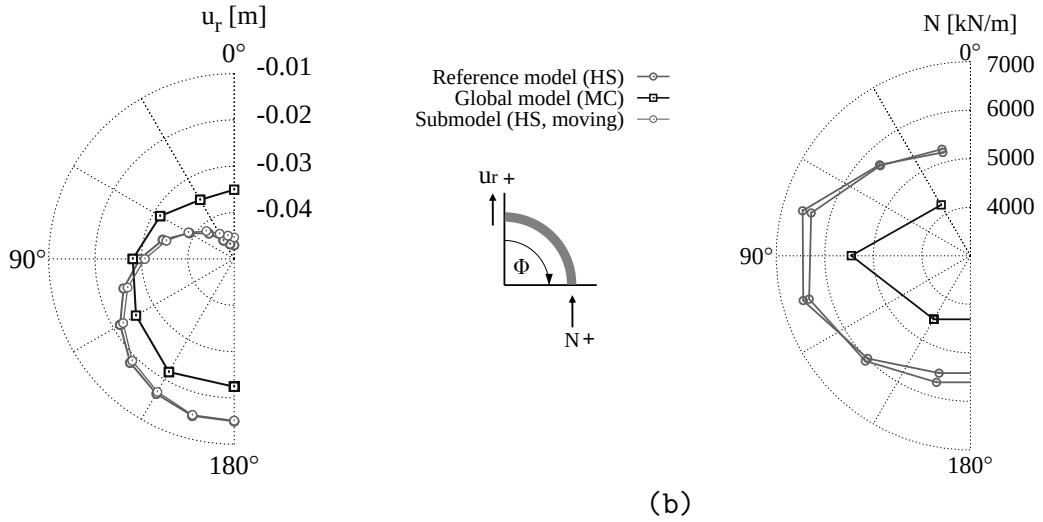

Figure 6.22: Application of submodeling technique in 3D tunneling simulation using MC model in global model: (a) lining radial displacements, (b) axial forces

Table 6.4: Comparison of calculation time for submodeling and conventional approaches (one computer with 8 kernels CPU)

Model	2D tunneling model	3D tunneling model
Global model (MC model)	20 s	30 min
Submodel (HS model)	40 s	60 min
Reference model (HS model)	180 s	200 min

Additionally, Table 6.4 shows the time needed for tunneling simulation using submodeling and conventional approaches. Based on the mesh discretization adopted in 2D/3D tunneling simulation, the calculation cost of submodeling method (2 simulation steps of global model and submodel) is significantly less than that of the reference model. It is foreseen that the submodeling method becomes a powerful tool in the parametric study of the tunneling problems.

6.4 Hybrid modeling

6.4.1 General concept and methodology

This section proposes a novel computational method for numerical simulation of mechanized tunnel excavation. This technique is called hybrid modeling that combines the capacity of a process-oriented simulation model (submodeling) for mechanized tunneling to accurately describe the complexities involved in the progressive excavation process and soil-tunnel interaction with the computational efficiency of metamodel (or surrogate model).

In the previous section, the concept and methodology of submodeling technique have been introduced. One of the key points in submodeling approach is to determine the appropriate boundary conditions of the submodel based on the global model. Although the global model is relatively coarse meshed and basic constitutive model might be applied, it is still time-consuming to run the global FE-model each time to derive the corresponding nodal displacements, especially in case of parametric study. To overcome this kind of computational problem, metamodeling approach where expensive FE-simulations are replaced by efficient mathematical regression functions (Khaledi et al. 2014), is applied. The regression function correlating the input and output data set is the so-called metamodel. Within this framework, metamodel can be used to generate the database of nodal displacements at submodel boundaries considering the variation of model parameters. After that, the submodel can be analyzed by recalling the boundary conditions for the corresponding model parameters from database without running the global model.

A conceptual illustration of hybrid modeling is shown in Fig. 6.23, the first step is to evaluate the global model and determined the submodeling area. This process has been illustrated in the previous sections. After that, there are three levels for the following hybrid modeling. In level 1, if the soil parameters are well known, it directly goes to level 3 where optimization of the tunneling process parameters (e.g., face pressure, grouting pressure, etc.) are conducted. If the soil parameters are uncertain, the model parameters that are of interest and their corresponding ranges are determined for the purpose of metamodel training, followed by checking the accuracy of metamodel. In this step, metamodel I correlates the soil parameters and submodel boundary conditions. Level 2 mainly deals with optimization of the soil parameters on the basis of the real measurements (for example, tunneling induced surface/subsurface settlements). It should be noted that if the mesh discretization in the submodel is changed or another constitutive model is

applied in the submodel, a new set of metamodel (metamodel II) should be trained to correlate the uncertain soil parameters and model responses that in accordance with the real measurements. By using optimization algorithm, the optimal soil parameters can be identified. Finally, level 3 aims to optimize the tunneling process parameters according to the user defined tolerance of the system behavior, for instance, allowable building settlement induced by tunnel excavation. In this process, the design process parameters are firstly used in the submodel (FE-simulation). When the FE-simulation models the i-th excavation step with the designed progress parameters, the model responses can be derived. If the tunneling induced building settlement is less than the tolerated level, the next excavation (i+1-th) step will be conducted in the FE-simulation. However, if the tunnel induced settlement exceeds the tolerated level, optimization of the process parameters for the current step is invoked. Subsequently, metamodel III can be created for the numerical simulation of current excavation step. Here the input and output of metamodel III are respectively process parameters and building settlement at the current i-th step. After that, optimization can be performed to provide the updated process parameters for the current excavation step and the tunnel advances for the next excavation step.

It is worth mentioning that the identified soil parameters from level 2 are used in the entire process of level 3. Since the variation of process parameters inevitably affect the soil behavior in the entire model, careful attention should be paid to their influences on the boundary conditions of the assumed submodel. The size of submodel in hybrid modeling should be adjusted to ensure that the submodel boundary conditions (nodal displacement from the global model) are not sensitive to the process parameters in the given ranges.

In the metamodeling approach, each input is assumed to be s dimensions that represent the different model parameters (soil constitutive model parameters or excavation process parameters), and there are m observation points in the outputs (nodal displacements at the submodel boundaries). For the training of a metamodel, firstly n_p (depends on the required accuracy) input parameter samples (n_p sample points with s dimensions) are generated via Latin Hypercube sampling method in the pre-defined ranges of the corresponding parameters. After that, the corresponding output values (n_p outputs for m observation points) can be obtained via FE-simulation. After that, the metamodel is the regression function mathematically correlating the inputs (s dimensions) with the output at each observation point. The type of regression function, e.g. polynomial regression or radial basis function, is chosen according to the complexity of the computational problem. According to Khaledi et al. (2014), the metamodel should be validated before its employment, the overall performance of metamodel is evaluated using one standard accuracy

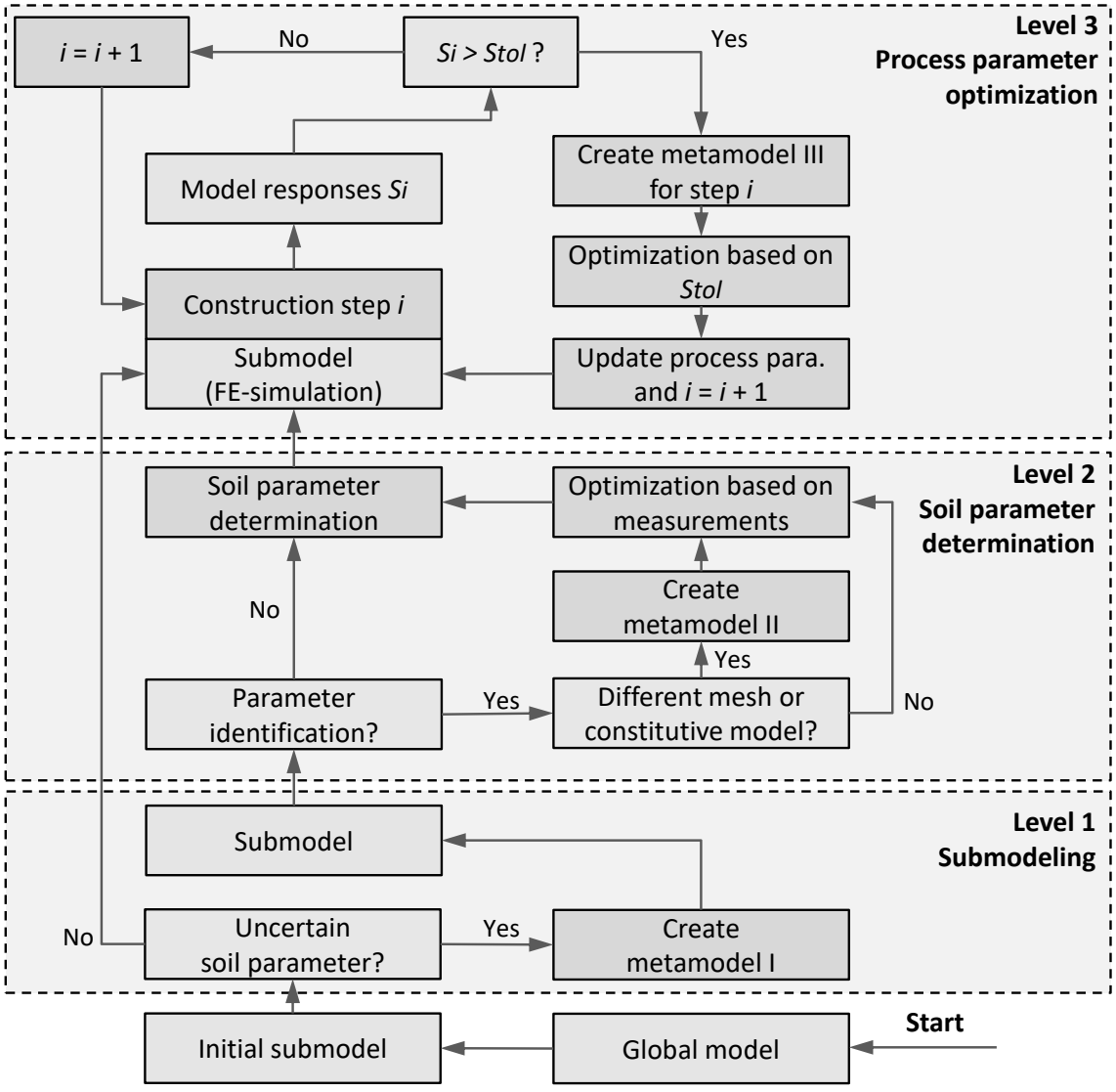

Note:
Metamodel I: submodel boundary conditions with respect to variable soil parameters
Metamodel II: model responses (in accordance with measurements) with respect to variable soil parameters
Metamodel III: model responses *Si* with respect to variable process parameters

Figure 6.23: General concept of hybrid modeling

measure: Normalized Root Mean Squared Error (NRMSE), which provides a global error measure over the entire design domain:

$$\text{NRMSE} = \left[\left(\sum_{i=1}^{n_p} \sum_{j=1}^{m} (u_j^i - \hat{u}_j^i)^2 \right) / \left(\sum_{i=1}^{n_p} \sum_{j=1}^{m} (u_j^i)^2 \right) \right]^{1/2} \tag{6.2}$$

where u_j^i is the exact value for the sample point x^i at the observation point j. $\hat{u}_j^i$ denotes the corresponding approximated value obtained by the metamodel. It should be noted that smaller value of NRMSE leads to more accurate metamodel.

The entire approach of hybrid modeling has been implemented in computational programing code *Python*. The metamodel is automatically trained according to predefined parameters ranges. Furthermore, global sensitivity analysis can be conducted to distinguish the relative importance of uncertain model parameters in determining the system behavior. By doing so, only the sensitive parameters are considered in the optimization process, which is efficient and computational cost saving.

6.4.2 Application of hybrid modeling in 3D tunnel simulation

In this section, the application of hybrid modeling approach in the 3D tunnel simulation is illustrated. As mentioned before, there are three levels for hybrid modeling, since level 2 mainly deals with parameters identification and is well studied in many literature, only the application of hybrid modeling in levels 1 and 3 is described in the following subsections.

Hybrid modeling of 3D tunnel simulation with uncertain soil parameters

In level 1 of hybrid modeling, the uncertainty of soil parameters is considered while the excavation process parameters (face pressure and grouting pressure) are assumed to be constant with the advancement of TBM. The numerical model and staged excavation process introduced in section 6.3.4 is used. The geometry is shown in Fig. 6.16. It is assumed that HS model is used to describe the soil behavior. The soil stiffness parameters $E_{50}^{\text{ref}}, E_{oed}^{\text{ref}}, E_{ur}^{\text{ref}}$ and friction angle φ' are uncertain and of interest for detailed analysis of submodel. The ranges of these parameters are given in Table 6.5. The remaining HS constitutive model parameters are assumed to be identical to the stiff soil parameters given in Table 6.3.

Table 6.5: Lower and upper bounds of selected parameters for meatmodel training

Parameter	Lower bound	Upper bound	Unit
φ'+	15	40	[°]
E_{50}^{ref}*	20	50	[MPa]
E_{ur}^{ref}	50	150	[MPa]

+If $\varphi' \geq 30°$, ψ'=φ'-30°; else ψ'=0
*$E_{50}^{\text{ref}} = E_{oed}^{\text{ref}} \leq 0.5 E_{ur}^{\text{ref}}$

In the first stage, strain energy concept is applied to determine the size of the submodel. Since the soil stiffness and strength parameters are variable, it is necessary to check the model responses under the combination of lowest soil stiffness and friction angle in the given ranges (worst case where largest mobilization of shear strength can be generated) for the applicability of submodel boundaries. In the present study, it is found that $1D$ area around the tunnel is able to cover the influence zone due to tunnel excavation.

In the second stage, 100 sets of parameters samples are generated within the given ranges, 480 nodes on the submodel boundary are defined as mapping nodes to derive the nodal displacements in each excavation step. In total, there are 20,640 nodal displacements (observation points in the metamodel) should be derived as the output of metamodel for one set of input parameters. The metamodel is trained based on these samples and corresponding output. After that, another 50 sets of parameters samples within the same ranges are generated to test the accuracy of trained metamodel. In the current study, Proper Orthogonal Decomposition with Radial Basis Function (POD-RBF) is employed in the metamodeling approach. According to Eq. 6.2, the NRMSE for the generated metamodel is 4.86%. By increasing up to 200 sets of parameters samples, the accuracy of metamodel is improved by having NRMSE of 0.85%.

In order to evaluate the accuracy of hybrid model, the following parameters set: $E_{50}^{\text{ref}} = E_{oed}^{\text{ref}}$=28 MPa, E_{ur}^{ref}=78 MPa and φ'=32° is adopted. The vertical displacements at tunnel crown of the monitoring section are shown in Fig. 6.24(a). As seen, when 100 samples are used to train the metamodel, the vertical displacements at tunnel crown at the end of excavation is slightly overestimated in comparison with the reference model (less than 4%). This is mainly caused by the inaccuracy of metamodel. When increasing the number of samples for the purpose of metamodel training, the accuracy of metamodel increases and the hybrid model approach gives excellent agreement with the reference model. By

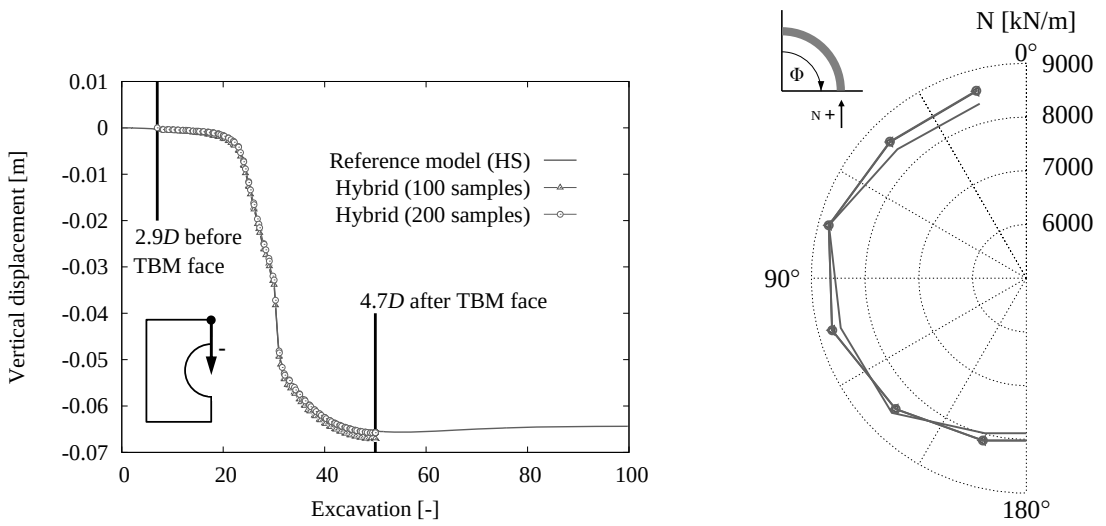

Figure 6.24: Evaluation of the hybrid modeling approach: (a) settlement profile at tunnel crown; (b) lining axial forces

analogy, Fig. 6.24(b) shows the comparison of lining forces using hybrid modeling approach. It is found that the axial forces calculated via hybrid model well agree with that of reference model. Although the less samples are used to train the metamodel which results in about 5% error, it provides sufficient accuracy in predicting the lining axial forces.

Hybrid modeling in the optimization of process parameters

In level 3 of hybrid modeling, since the aim is to optimize the process parameter according to the design requirement. A building is assumed on the ground surface in the numerical model described in the previous subsection, the geometry of the submodel is given in Fig. 6.25(a). The building is assumed be a square with length at each side of $1.5D$. The tunnel is excavated along the centerline of the building. As mentioned in Chapter 5, the building can be modeled as shell elements and the material properties are same as the ten-story building described in Table 4.6. For the process parameters, the design range for face pressure at tunnel crown is 143-238 kPa, and grouting pressure at tunnel crown varies between 199 kPa and 332 kPa. The range of the support pressure is based on the standard design in the previous section with 25% variance.

By analogy, in the first step, the size of submodel is determined on the basis of strain energy concept. Furthermore, it is ensured that the submodel boundary conditions are not

sensitive to process parameters in the given ranges. Then the hybrid model is built based on the ranges of the variable soil parameters. In this process, metamodel I is generated, the input and output are uncertain soil parameters and nodal displacements at the submodel boundaries, respectively. After that, the soil parameters should be identified based on the measurements via back analysis. However, for the sake of simplicity, it is directly assumed that the soil parameters have been identified as $E_{50}^{\mathrm{ref}} = E_{oed}^{\mathrm{ref}}$=28 MPa, E_{ur}^{ref}=78 MPa and φ'=32° in this part of the study. Then the submodel (FE-simulation) with identified soil parameters are applied in the following level 3 of hybrid modeling approach.

In the numerical analysis, the minimal face pressure and grouting pressure in the design range are firstly applied, and the tunneling induced settlement of the building (at the monitoring point) is derived at each excavation step and compared with the tolerated limit. If the building settlement reach 80% of the limit value, the optimization algorithm is invoked with the objective to optimize the tunneling induced building settlements do not exceed the tolerated limit. In this part of the study, consider the tunnel excavation process, three tolerated limits of the building settlement with respected to the position of TBM are taken into account. Namely: (1) before TBM face reaches the monitoring section, allowable settlement of the building is 1 cm; (2) when the TBM tail passes the monitoring section, the incremental settlement of the building should be less than 2 cm; (3) when the TBM tail is 12 m ahead of the monitoring section, the maximum incremental settlement of the building is 2 cm. After that, the variation of the building settlement becomes not significant.

Fig. 6.25 shows the settlements at the monitoring point and the optimized support pressures. The tunneling induced building settlements in comparison with the tolerated limits is given in Table 6.6. It is observed that the optimization process is first activated in the 18th excavation step, continuing with an updated face and grouting pressure in each step up to 20th excavation step where the TBM face passes the monitoring section. After that, the incremental displacements is of interest for optimization, the initial support pressure is sufficient to ensure that the incremental building settlement does not exceed the tolerance limit. At 25th excavation step, the optimization process is again invoked and continuing for 26th excavation step. By analogy, when TBM tail passes the monitoring section, the face pressure and grouting pressure are optimized from 31st to 34th step of excavation. According to Fig. 6.25(b), using the optimized process parameters induces less building settlements in accordance with the predefined tolerated limit. Additionally, the optimized support pressures are applied in the global model where fine mesh discretization and same constitutive model are used. The results is plotted in Fig. 6.25(b) as the reference model

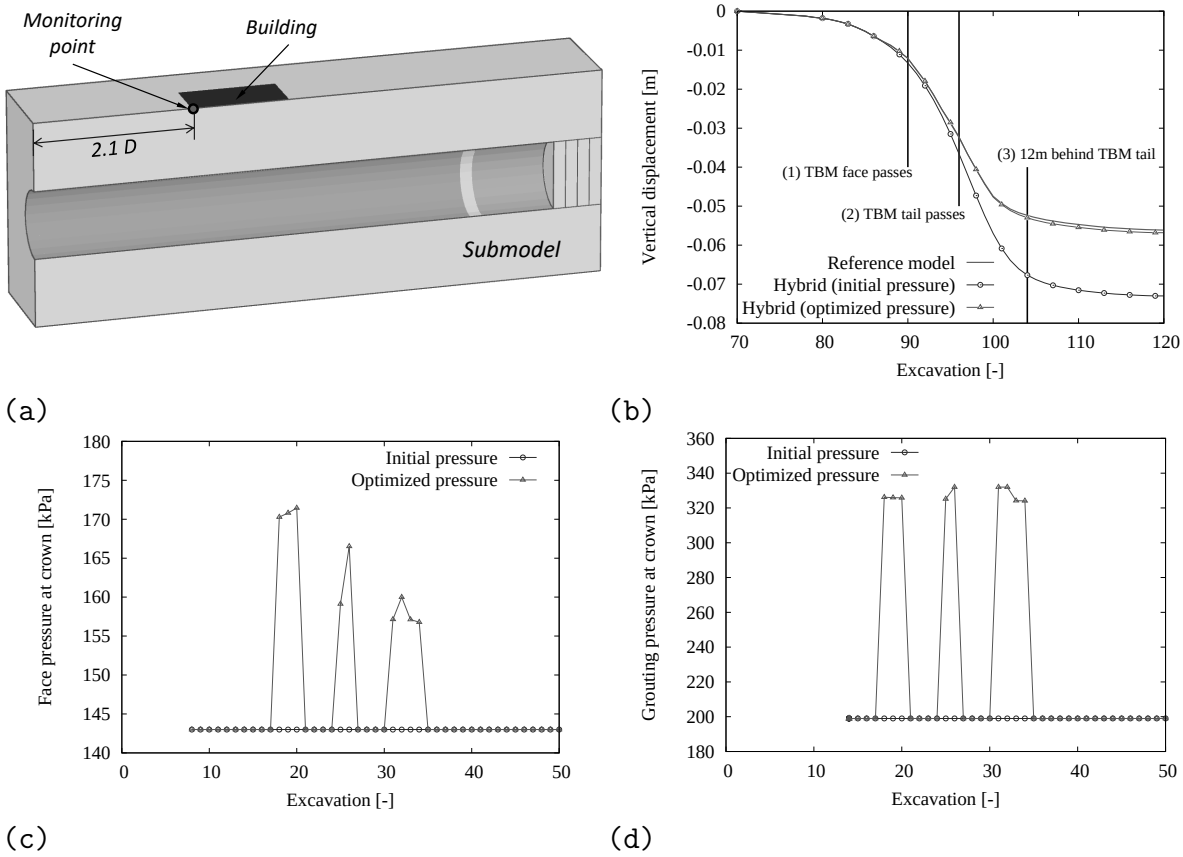

Figure 6.25: Application of hybrid model; (a) model geometry, (b) settlement development at the monitoring point, (c) initial and optimized face pressure, (d) initial and optimized grouting pressure

responses. As seen, the hybrid model provides almost identical results as the reference one.

The advantages of this hybrid modeling approach can be summarized as: (1) the FE-simulation of tunneling process is conducted in a smaller scale in comparison with the initial global model, which is time and computational cost saving; (2) hybrid model provides an efficient way to update the submodel boundary conditions for different types of soil; (3) more advanced constitutive model can be defined in the submodel to better capture the system behavior without updating the submodel boundary conditions; (4) the excavation process parameters can be modified in each excavation step according to the tolerated model responses without changing the boundary conditions of submodel. Therefore, hybrid modeling is a powerful tool for studying the detail model responses in the near filed around the tunnel by taking into account the uncertainty involved in the model parameters and structural design requirement.

Table 6.6: Comparison of tunneling induced building settlement at the monitoring point using hybrid modeling approach

	Total displacements		Incremental displacements			
Stage	Initial	Optimized	Initial	Optimized	Tolerated limit	Unit
(1)	-0.013	-0.012	-0.013	-0.012	-0.010	[m]
(2)	-0.037	-0.032	-0.023	-0.020	-0.020	[m]
(3)	-0.068	-0.053	-0.031	-0.021	-0.020	[m]

6.5 Conclusions

This chapter introduces three advanced process simulation techniques for tunnel modeling, which can reduced the cost of computational efforts and experimental tests. Firstly an innovative adaptive constitutive modeling concept is illustrated. It accounts for constitutive model exchange in the near-field sub-domain which is strongly affected by tunnel excavation. The model adaption was carried out by taking into account a family of hierarchical constitutive models based on Mohr-Coulomb shear failure concept. Secondly, the submodeling approach, where a smaller scale model is cut from the global model, is introduced. It is found that submodeling approach is a powerful tool to obtain detailed information in the near field of tunneling. Finally, a novel computational method for numerical simulation of mechanized tunnel excavation, namely hybrid modeling is introduced, it combines the capacity of a process-oriented submodeling with the computational efficiency of metamodel. Based on the analysis performed in the present study, the following general remarks could be outlined:

1. The zone which is subjected to loading, unloading and reloading due to tunnel excavation can be numerically simulated by a advanced model while the less affected far-field sub-domain can be sufficiently simulated by a basic constitutive model. Since the model exchange process is dependent on the stage of tunneling process, it is more wise to select the models from a hierarchical family group.

2. Distribution and variation of plastic strain at the Gaussian points are used to determine the size of the area where sophisticated model is employed to describe the soil behavior. Conducting adaptive constitutive modeling in a cube-shaped zone sized $2D$ around the TBM face leads to an excellent agreement with the results of advanced model uniformly assigned to the entire domain.

3. The appropriate size of the near-field sub-domain as well as the hierarchical constitutive models and their contributing parameters play a significant role in the design of laboratory tests and in-site investigation strategy.

4. Submodeling (both "fixed" and "moving" block approaches) is a powerful tool for detailed analysis in the near field around tunnel with reduced computational costs in comparison with traditional simulation method.

5. The size of the submodel can be determined based on the strain energy distribution. The assumed submodel boundary is accepted when the strain energy gradient at the cut boundaries of the global model tends zero.

6. The submodel model may or may not apply the same constitutive model as the global model to describe the system behavior. In both cases, the submodel provides reasonable results compared to those obtained by the reference model. Apply different constitutive models respectively in submodel and global model can benefit the design of experiments.

7. Hybrid modeling is able to provides accurate model responses in the near field around the tunnel with reduced computational cost especially in parametric study.

8. Hybrid modeling is applicable in the optimization of process parameters in each excavation step without updating the submodel boundary conditions, accordingly the tunneling induced soil settlements can be kept below a tolerated level with the advancement of TBM.

7 Tunnel case study

7.1 Introduction

This chapter describes two case studies. The first case study consider the mechanized tunnel excavation under the ground water level via slurry shield TBM. The detailed numerical simulation procedure considering the sub-systems will be highlighted, sensitivity analysis is conducted to study the influence of soil parameters on the tunneling induced model response. After that, the uncertain model parameters are optimized on the basis of the measured surface settlements. The second case study is based on the tunneling model tests, it mainly focuses on the design of optimal monitoring strategies based on the sensitivity field, which significantly benefits the in-situ and laboratory tests for the purpose of parameter identification/update.

7.2 Western Scheldt tunnel

The Western Scheldt tunnel (Dutch: Westerschelde tunnel) is a shallow twin road tunnel under the estuary of the Scheldt river in the Netherlands and it was constructed by slurry shield machine. The east line is the one investigated in the current study. The geology along the tunnel is made up of different sand and clay formations. The mechanical properties of the soil layers around the excavation zone were obtained based on conventional in-situ and laboratory tests. The groundwater level is influenced mainly by the North Sea and it is about 1.5 m below the ground surface during tunnel excavation. Ground settlements above the excavation domain were measured during the tunneling process.

Consider the fact that different clay and sand layers are involved in the tunneling domain, large number of soil constitutive model parameters are required for the numerical simulation. However, it is difficult to obtain the values of all constitutive model parameters as this is related to the expensive or time-consuming in-situ and laboratory tests as well as because not all parameters can be directly derived from the test data. Therefore, these

uncertain model parameters should be guessed according to the engineering judgment. Subsequently, uncertainty of these model parameters inevitably induces model response uncertainty. Furthermore, when the sophisticated constitutive model is applied to describe the soil behavior, larger uncertainty might be introduced due to more complex laboratory or in-situ tests. In order to reduce/quantify this kind of uncertainty, parametric study can be conducted (Khaledi, Mahmoudi, Datcheva & Schanz 2016). In the first step, global sensitivity analysis is conducted to rank the input parameters' importance in determining the surface settlement. This can also reduce the dimension of back analysis problem. In the second step, back analysis is conducted to identify the uncertain model parameters. After that, model calibration and verification are conducted based on the real measurements. Within this framework, this methodology is apply in this case study of Western Scheldt tunnel.

7.2.1 Numerical simulation of shield supported tunneling

To simulate the staged construction process, finite element code *Plaxis* is utilized. It is modeled the excavation in clay and sand layers by means of slurry shield TBM. A length of 88 m tunnel excavation is simulated to conduct model calibration and validation. The tunnel has a diameter D=11.33 m and an inclination of 4.3%. Furthermore, the TBM-shield including the cutter head is defined to be 12 m long. The tunnel lining consists of ring-shaped prefabricated concrete segments. After a preliminary study of boundary effects, the 3D FE-model is set up with dimensions of 150 m (almost 13D) long in X-axis direction, 100 m (almost 9D) wide in Y-axis direction and 71 m (almost 6D) deep in Z-direction (Fig. 7.1). These dimensions only represent half of the model due to the symmetry condition assumed with respect to the vertical plane that goes through the tunnel crown and invert. After a series of trial analyses (Zhao et al. 2015), a spacial discretization with a total number of 103,278 (10-node tetrahedral) elements is adopted and the typical shape of the mesh generated for the numerical simulation are shown in Fig. 7.1. Moreover, a constant water level of 1.5m below the surface is assumed in the numerical simulation.

In the present simulation, the grouting pressure is modeled by a uniformly distributed load acting on the soil elements that directly follow the TBM-shield to avoid the collapse of surrounding soil. In this research, the value of grouting pressure is chosen as 150 kN/m^2 based on the measured data. In case of Western Scheldt tunnel construction, the face pressure distribution was varying during excavation process. Based on the geotechnical report, the measured face support pressure remained at a low level for the first several

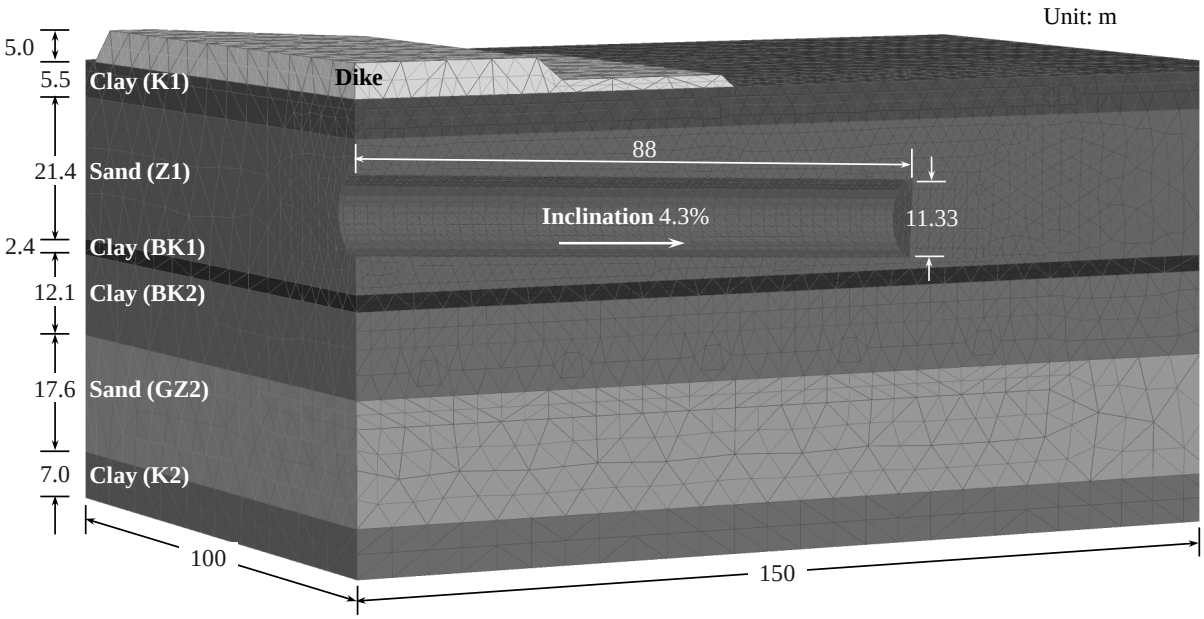

Figure 7.1: Geometry and FE-discretization of 3D model

excavation steps. Thereafter, the pressure began to increase and finally the pressure reached a relatively high level compared to the face pressure applied at the beginning. This happened due to the fact that the overburden increased with the advancement of TBM. In initial numerical simulation, the pressure is simulated by a non-uniformly distributed load that increases from the tunnel crown (137 kN/m^2) towards the tunnel invert (250 kN/m^2) and this distribution is kept constant with the advancement of TBM. The value is defined according to the average face pressure during the whole excavations. In order to simulate the volume losses due to overcut zone and conicity of TBM, contraction factor is used. If only considering the conicity of TBM-shield, the contraction factor at front and tail of TBM are 0 and 2.8%, respectively. By taking into account the volume loss due to TBM overcut, contraction factor in the prediction with initially guessed parameters is assumed to be increased linearly from 1.4% at the TBM face to 3.8% at the tail of TBM, and it keeps constant as 3.8% along the lining segments.

In order to reproduce the soil behavior during excavation, an advanced elasto-plastic soil constitutive model, namely Hardening Soil model considering small strain stiffness (HSS), is used. The soil parameters used in this research are given in Table 7.1. Due to the fact that TBM advances at a quite low speed and the permeability of sand layer (Z1) is high, fully drained analysis has been conducted. The values of parameters used in this research are all effective values. The following relations of friction angle (φ') , dilatancy angle (ψ'), K_0 value for normal consolidation (K_0^{NC}), secant stiffness in standard drained triaxial

test (E_{50}^{ref}) and tangent stiffness for primary oedometer loading (E_{oed}^{ref}) are also applied in HSS model: $\psi' = \varphi' - 30°$ and $\psi' = 0$ if $\varphi' < 30°$, $K_0^{\mathrm{NC}} = 1 - \sin\varphi'$, $E_{50}^{\mathrm{ref}} = E_{oed}^{\mathrm{ref}}$. The dilatancy angle controls the amount of plastic volumetric strain developed during plastic shearing. Clay is normally characterized by a very low amount of dilation and $\psi' = 0$ was applied in this research. As for sand, the dilatancy angle was assumed to depend on the internal friction angle, namely $\psi' = \varphi' - 30°$ when $\varphi' > 30°$ (Bolton 1986). Secant stiffness in standard drained triaxial test (E_{50}^{ref}) and tangent stiffness for primary oedometer loading (E_{oed}^{ref}) are independent input parameters in the HS model. However, according to Schanz (1998), the stiffness parameter of sand E_{50}^{ref} can be assumed to be equal to E_{oed}^{ref}. Additionally, based on the local sensitivity analysis (Zhao, Lavasan & Schanz 2014), the ground settlement are little sensitive to the E_{oed}^{ref}. Within this framework, $E_{50}^{\mathrm{ref}} = E_{oed}^{\mathrm{ref}}$ is assumed to be applied to all soil layers. The TBM-shield and lining segments are simulated as circular plate elements obeying linear elastic model. Based on the report of Brodesser (2012), material characteristics are given in Table 7.2.

The interaction between the shield skin and the surrounding soil as well as lining segments and the surrounding soil are modeled by using interface elements (Brinkgreve et al. 2014). The excavation stage is modeled via a step-wise procedure, where all soil layers except dike layer are activated to obtain the equilibrium state in initial phase. Then dike layer is activated in second phase to initiate the stress level in the soil deposit due to soil weight. The progressive advancement of the TBM is performed by a sequence of 2.0 m soil excavations for a total number of 44 steps. In this sequence, the first 6 excavation steps represent the advancement of the 12 meter-long TBM shield. After that, in each consequential excavation, the soil in front of TBM is deactivated, the shell segments are activated with assigned TBM-shield material, both face support and grouting pressure are activated. The installation of the lining proceeds by assigning the lining material to the corresponding shell elements.

Compared to 3D model, 2D numerical simulation of mechanized tunneling does not take into account the inclination of the tunnel, consequential advancement of the TBM and face support. However, it provides a good approximation of the model response for a defined observation section and it is popularly applied in engineering practice. For the comparison of model responses in 3D and 2D models, a simplified 2D FE-model is created to simulate the construction of Western Scheldt tunnel. To be specific, the 2D model simulates the cross section where several observation points (points 1-8 in Fig. 7.3) are located. Same soil mechanical properties are used in 2D and 3D models. After studying the influence of different mesh sizes on the numerical results, a discretized mesh with a total number of

Table 7.1: Soil constitutive parameters for HSS model: initial set

Para.	Soil layers							Unit
	Dike	K1	Z1	BK1	BK2	GZ2	K2	
γ_{unsat}	19	18	18	18	17	17	17	[kN/m^3]
γ_{sat}	20	20	19	21	19.3*	20.2*	20	[kN/m^3]
φ'	28**	22**	30	28**	28**	34	35	[°]
ψ'	0	0	0	0	0	4	0	[°]
c'	5**	5**	6.4*	20**	20**	11.4*	40	[kN/m^2]
K_0^{NC}	0.53	0.63	0.50	0.53	0.53	0.40	0.36	[-]
E_{50}^{ref}	30**	24**	35**	25	30	30	50	[MPa]
E_{oed}^{ref}	30**	24**	35**	25	30	30	50	[MPa]
E_{ur}^{ref}	90**	60**	80**	60	100	90	180	[MPa]
ν_{ur}	0.20	0.20	0.20	0.20	0.20	0.20	0.20	[-]
OCR	1.0**	1.0**	1.0**	2.7*	2.8	2.5*	3.0	[-]
G_0^{ref}	160**	150**	140**	65	100	110	150	[MPa]
$\gamma_{0.7}$	0.0002	0.0002	0.0002	0.0002	0.0002	0.0002	0.00015	[-]
p^{ref}	0.1	0.1	0.1	0.1	0.1	0.1	0.1	[MPa]
m	0.7	0.7	0.5	0.7	0.7	0.5	0.7	[-]
R_f	0.90	0.90	0.90	0.90	0.90	0.90	0.90	[-]

* The value is directly taken from the geotechnical report (Brodesser 2012)

** The value is proposed through a guess (Those without any mark are defined according to the reported tests)

Table 7.2: Material properties of TBM-shield and tunnel lining

Parameter	Tunnel lining	TBM-shield	Unit
Thickness(d_t)	0.45	0.35	[m]
Elastic modulus (E)	22	210	[GPa]
Unit weight (γ)	24	38	[kN/m^3]
Poisson's ratio (ν)	0.1	0.3	[-]

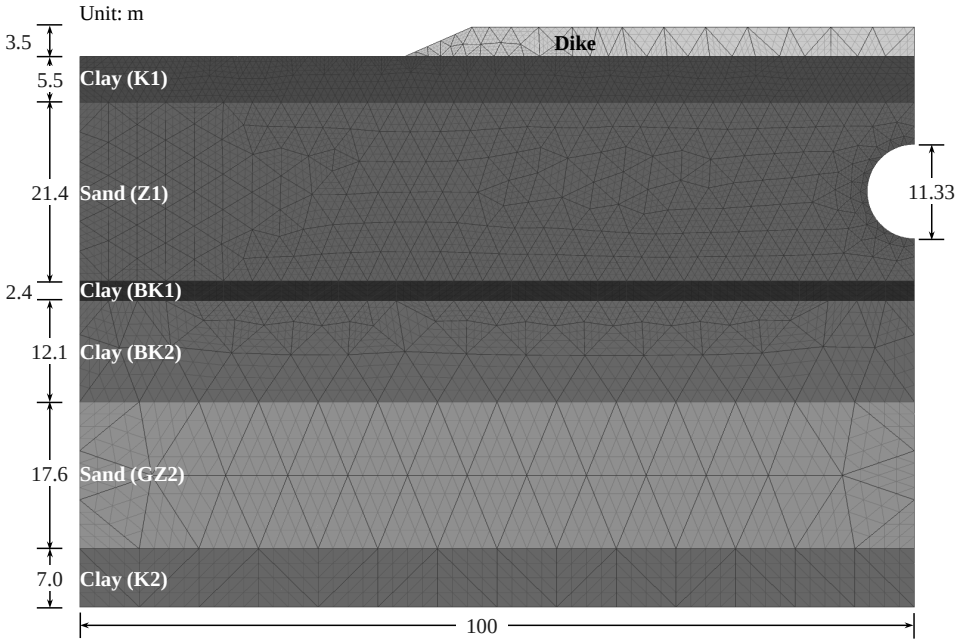

Figure 7.2: Geometry and FE-discretization of 2D model

1,001 15-node triangular elements is adopted. Geometry and FE-discretization are shown in Fig. 7.2.

According to the geotechnical report on Western Scheldt tunnel project, a clay layer (K1) lies above the sand layer (Z1). Soft soil model (in the framework of *Plaxis*) is based on modified Cam-Clay model and specially developed for normally consolidated clays, clayey silts or peat. It can deal well with primary compression of fine grained soils. This model reproduces the soil behavior by using two parameters λ^* and κ^*. Stress dependent stiffness and distinction between primary loading and unloading-reloading are also considered. Compared to HSS model, less input parameters are required in soft soil model. Within this framework, soft soil model is applied to K1 layer and HSS model is assigned to the remaining layers to simulate the tunnel excavation. The results will be compared to the case in which HSS model is applied to all soil layers.

7.2.2 Prediction with initially guessed parameters

Fig. 7.3 shows the vertical deformation contour (u_z) calculated with initially guessed parameters (Table 7.1), as well as the location of observation (measurement) points in longitudinal (A,B,...,E) and transverse (1,2,...,8) directions. The deformation pattern indicates that the soil at the ground surface settles while the invert of the tunnel heaves.

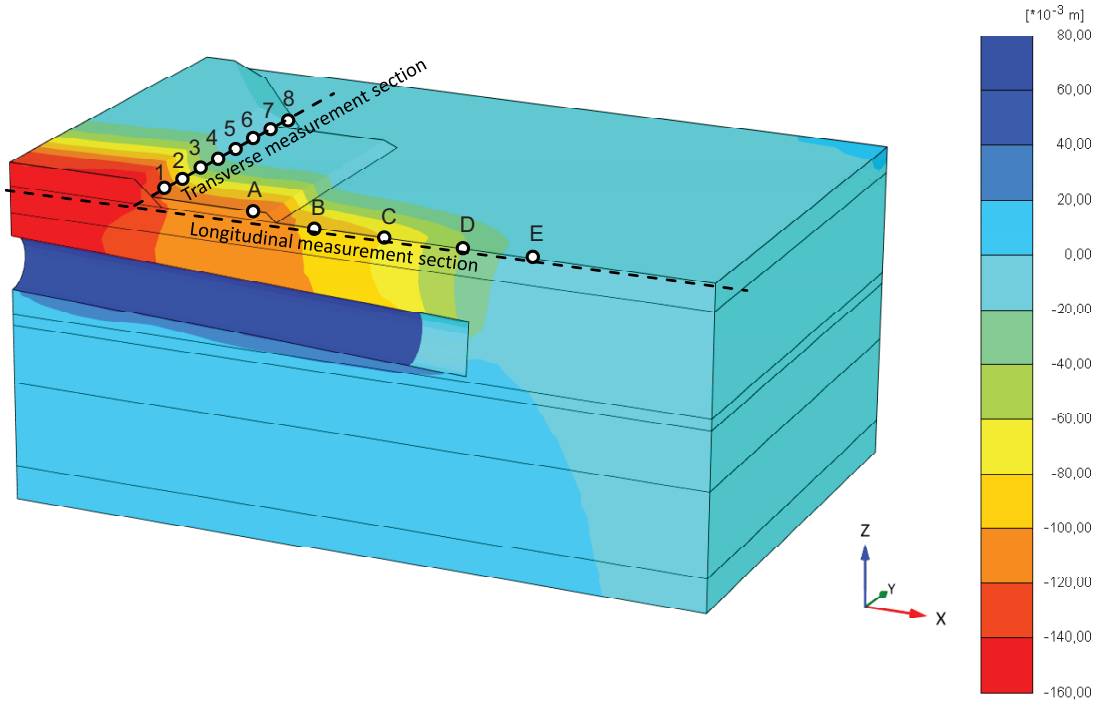

Figure 7.3: Vertical displacements in Z-direction at 44-th excavation

This deformation regime has been obtained for all sets of parameters in the search range. The up-heave at the bottom of the tunnel is related to unloading due to the weight loss caused by the excavation.

Fig. 7.4 shows the transverse and longitudinal surface settlement profiles predicted with initially guessed parameters. It can be seen that transverse surface settlements at points 2-5 and longitudinal surface settlements at points A,D,E predicted with initially guessed parameters are far away from the field measurements. It is to be noted that the disagreement between the field measurement and numerical prediction is due to a number of factors, among them are the limitations of the isotropic constitutive model employed (Mašín 2009), the uncertainty about the amount of over-excavation, the possible pressure drop at the TBM face, etc. What has been done in this research is an exercise, under the assumption that these factors are lumped together under the uncertainty on the values of the constitutive parameters.

7.2.3 Global sensitivity analysis

In order to improve the agreement between the calculated and observed data, sensitivity analysis is used to overall evaluate the sensitivity of input parameters in dike, K1 and Z1

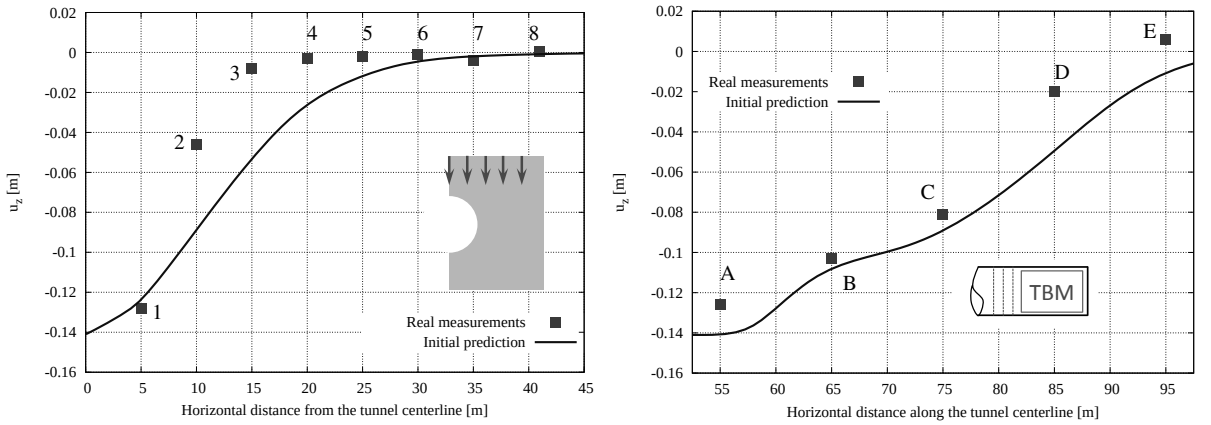

Figure 7.4: Prediction of (a) transverse surface settlement (b) longitudinal surface settlement

layers. According to a former study of Zhao, Lavasan & Schanz (2014), it was found that the surface settlement is not sensitive to parameters of dike layer and soil layers below the tunnel, while the stiffness and friction angle of K1 and Z1 layers play important roles in the surface settlement. Within this framework, Global Sensitivity Analysis (GSA) is performed to distinguish the key parameters that govern the model response. Related mechanical properties with the lower and upper bounds of uncertain parameters are given in Table 7.3, these values are defined based on literature and engineering judgment.

During the tunnel construction, the largest surface settlement is one of the most significant model response which should be considered. In both transverse and longitudinal directions, the affected zone of soil deformation caused by staged excavation is also crucial. Within this framework, Fig. 7.5 defines the important model responses whose sensitivity to input constitutive parameters has to be evaluated. L1 is the maximum vertical displacement in both transverse and longitudinal directions. L2 is the distance from tunnel centerline to the first point whose settlement is less than 5% of L1. L3 and L4 are the horizontal distances from face of TBM to the first point (opposite of excavation direction) whose vertical displacement is maximum and from face of TBM to first point (excavation direction) whose vertical displacement is less than 5% of L1, respectively.

Fig. 7.6(a) shows the sensitivity of L1 to input parameters. It is obvious that the most sensitive parameter is friction angle of Z1 layer, the relative importance of this parameter is almost 6 times higher than other parameters. It can be explained that the plastic deformation is the dominating part of soil deformation for point with largest settlement. Hence, effect of friction angle on maximal vertical displacement is significant. Fig. 7.6(b)

Table 7.3: Lower and upper bounds of constitutive parameters for HSS model

Soil layer	Parameter	Lower bound	Upper bound	Unit
clay K1	φ'	15	30	[°]
	E_{oed}^{ref}	15	28	[MPa]
	E_{ur}^{ref}	40	80	[MPa]
	G_0^{ref}	120	160	[MPa]
	$\gamma_{0.7}$	0.00015	0.00025	[-]
sand Z1	φ'	30	40	[°]
	E_{oed}^{ref}	28	50	[MPa]
	E_{ur}^{ref}	60	100	[MPa]
	G_0^{ref}	120	160	[MPa]
	$\gamma_{0.7}$	0.00015	0.00025	[-]

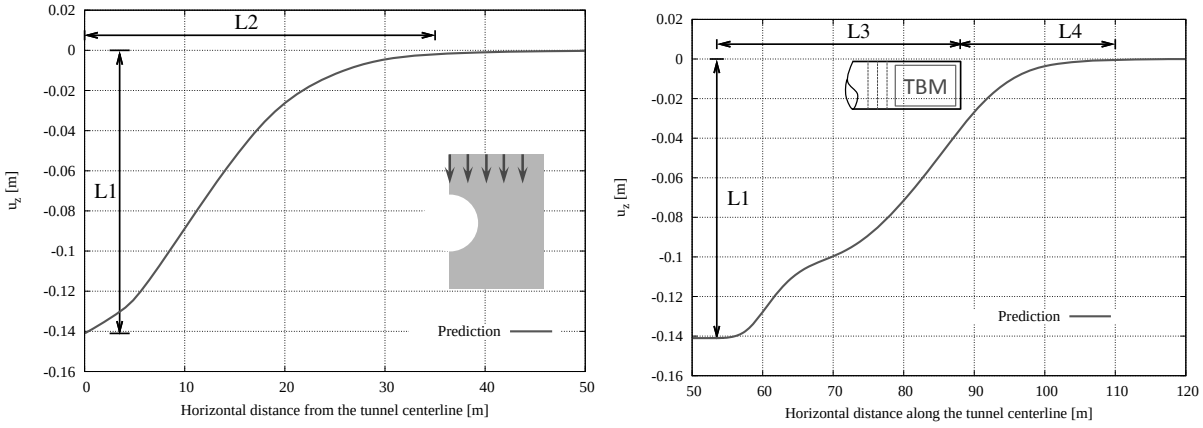

(a) (b)

Figure 7.5: Model response in: (a) transverse direction (b) longitudinal direction

shows the sensitivity of L2 to input parameters. It can be found that soil stiffnesses (E_{ur}^{ref} and E_{oed}^{ref}) of Z1 layer generate major influence. When TBM approaches the observation section, there is loading process in the soil. After TBM passes the cross section, soil body below the tunnel experiences unloading process and the consequential up-heave contributes to the small deformation of observation points which are far away from the tunnel. Then the dominating sensitivity of E_{oed}^{ref} and E_{ur}^{ref} are related to loading and unloading conditions, respectively. For surface points far away from tunnel centerline, the main soil behavior is elastic deformation and there is nearly no plastic deformation, which makes friction angle of Z1 less important. Figs. 7.6(c) and 7.6(d) present the sensitivity of L3 and L4 to input parameters, respectively. Nevertheless, parameters of sand layer (Z1) have the most influence; due to the fact that tunnel is excavated in this soil layer. However, L3 has relatively high sensitivity to parameters of K1 layer. This may happen due to the slope of dike layer between observation points A and B. When TBM passes through the area below the dike's slope, surface settlement of dike layer affects the ground settlement of clay layer. In this process, parameters of K1 layer play an important role. For ground surface in front of the TBM, there are small deformations due to soil's elastic behavior under loading condition, which makes G_0^{ref} of Z1 layer more effective.

Figs. 7.7 and 7.8 show the sensitivity of vertical displacements of surface points along the transverse and longitudinal directions to input parameters. In transverse direction, sensitivity of parameters of K1 layer keeps at a low level for all the observation points. This is due to the fact that tunnel is excavated in Z1 layer and major contribution of vertical displacement comes from Z1 layer. Friction angle of Z1 generates less influence as the observation points get far away from the tunnel, this is can be interpreted by decreasing the plastic deformation. On the contrary, E_{ur}^{ref} and G_0^{ref} have more effects on model response since the elastic deformation is the dominating part of soil's deformation. However, friction angle of Z1 layer is always the key parameter to model response. Likewise, in longitudinal direction where parameters corresponding to Z1 layer are more effective than those of K1 layer. For observation points at which large settlement occurs, the most important parameters are φ' and E_{oed}^{ref} (E_{50}^{ref}) of Z1 layer, especially the friction angle φ' whose sensitivity index keeps higher than 0.6. For observation points in front of TBM, vertical displacements show a gradually growing sensitivity to G_0^{ref} and gradually diminishing sensitivity to φ' of Z1 layer. This can be related to small strain deformation becomes dominated. However, friction angle still plays an important role in soil deformation. This is related with the effect of K_0, for observation points at which elastic deformation is the dominating deformation, K_0 also plays a pivotal role and there is a correlation between K_0 and φ' in this research ($K_0^{\mathrm{NC}} = 1 - \sin\varphi'$). Additionally, the elastic

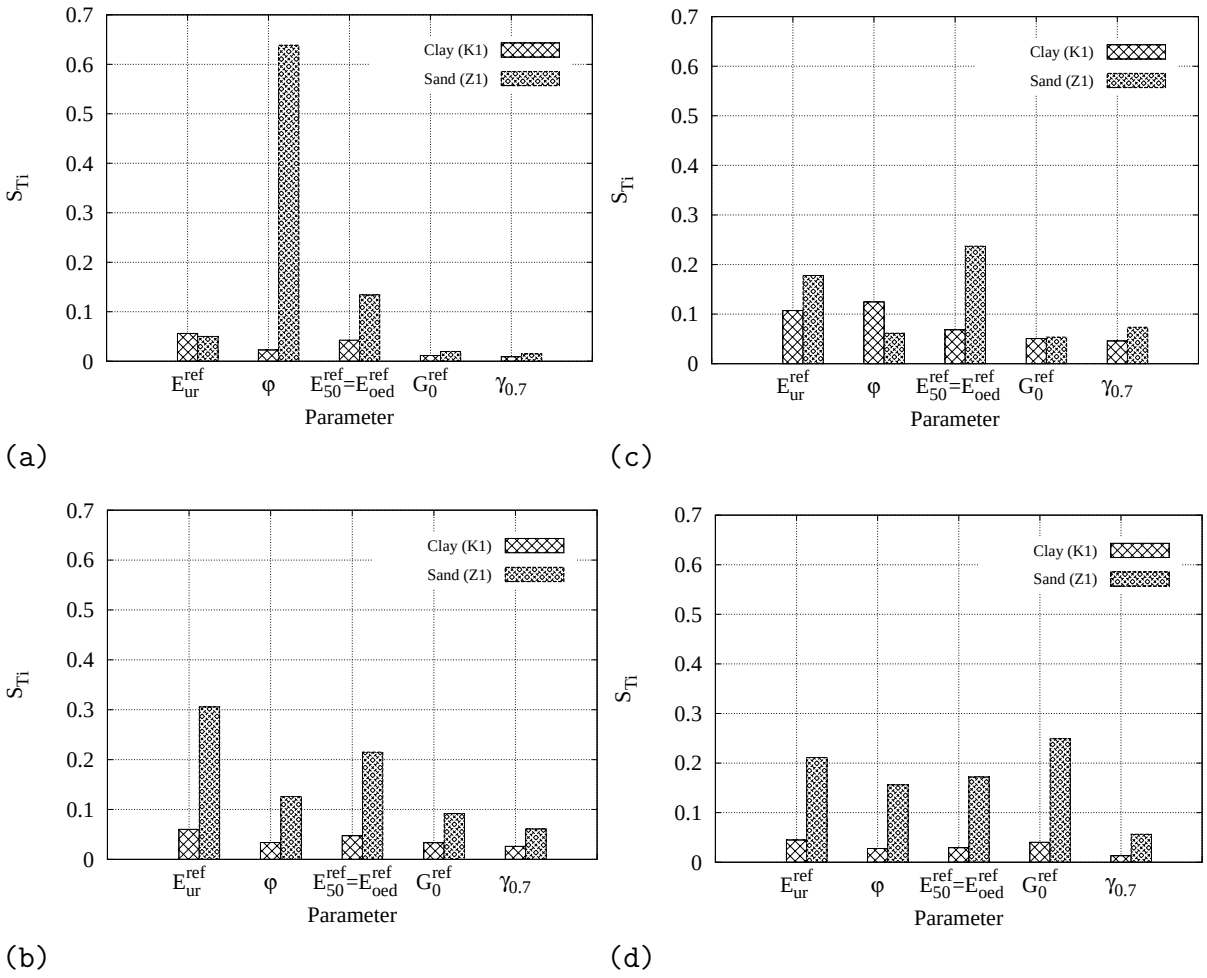

Figure 7.6: Total effect sensitivity index calculated for: (a) L1 (b) L2 (c) L3 (d) L4

domain in HSS model is controlled by hardening parameter γ^p, γ^p is calculated based on the plastic potential function which is related to friction angle and dilatancy angle. With the continuous deformation, the yield surface finally reaches the Mohr-Coulomb failure line. Within this framework, the elastic response is determined by the plastic parameter which defines the commencement of plastic range. It can be concluded that friction angle as a plastic parameter also controls the elastic deformation.

According to the result of GSA, vertical displacements of points 1-3 are mostly influenced by the friction angle and stiffness of Z1 and K1 layers. Therefore, φ', E_{oed}^{ref} (E_{50}^{ref}) and E_{ur}^{ref} of K1 and Z1 layers are selected as the input parameters in back analysis (bounds of parameters are same as those used in GSA).

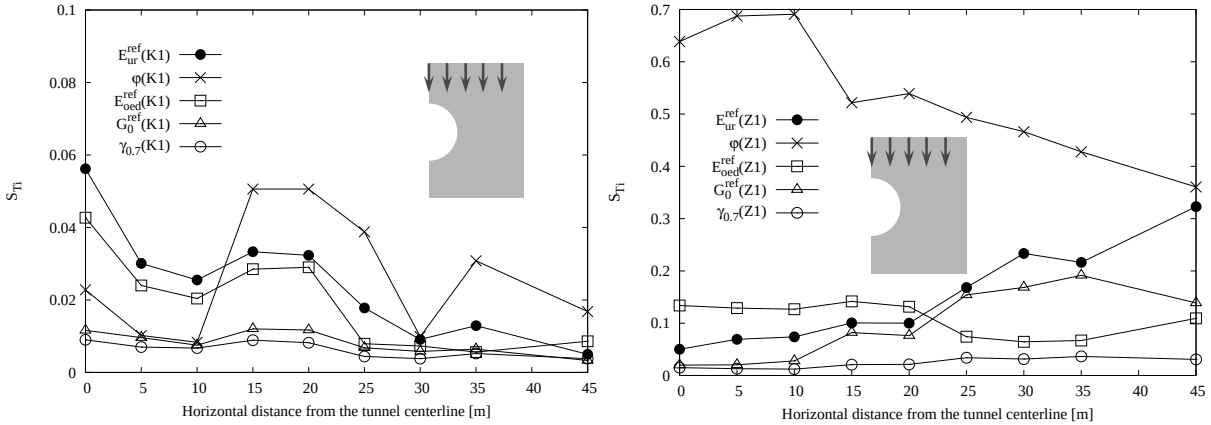

(a) (b)

Figure 7.7: Sensitivity of transverse surface settlement to input parameters of: (a) K1 layer (b) Z1 layer

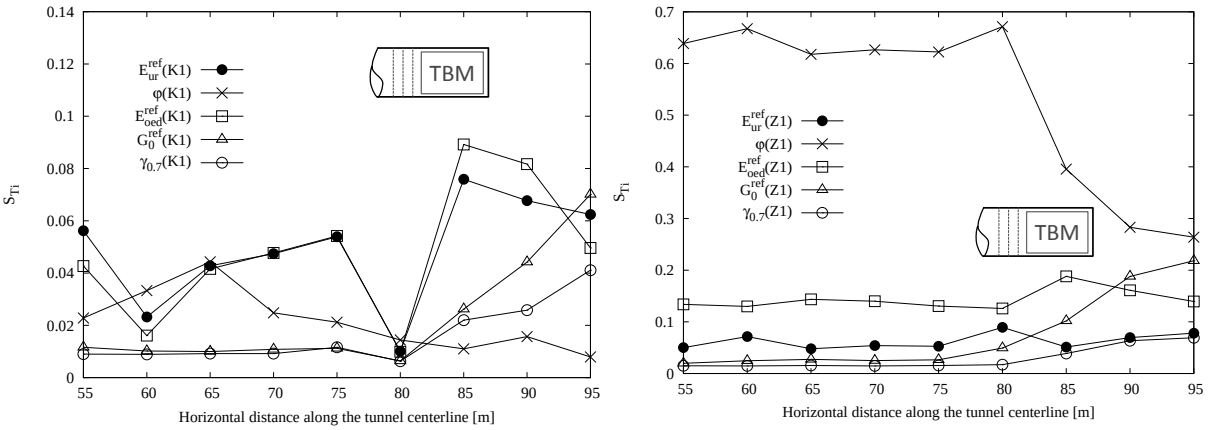

(a) (b)

Figure 7.8: Sensitivity of longitudinal surface settlement to input parameters of: (a) K1 layer (b) Z1 layer

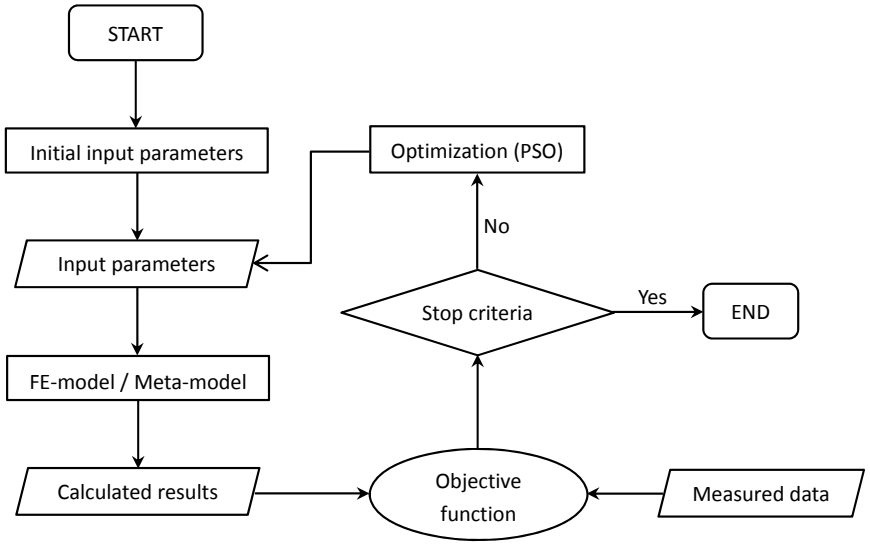

Figure 7.9: Concept of back analysis

7.2.4 Calibration and validation of the 3D model

In order to obtain the optimized values of related model parameters which can give a good match between predicted and measured values, back analysis is applied to conduct the parameter optimization. Fig. 7.9 presents the concept of the adopted back analysis. Within this framework, the optimization algorithm deals with minimization of the objective function defined as:

$$f(\mathbf{X}) = \frac{1}{N} \sum_{i=1}^{M} \left[w_i \ \left(y_i^{calc}(\mathbf{X}) - y_i^{meas} \right)^2 \right], \tag{7.1}$$

where $\mathbf{X}$ is the vector of input parameters of constitutive model to be identified; $y_i^{calc}(\mathbf{X})$ and y_i^{meas} are calculated result and field measurements respectively; N is the number of measurements. In this case, the largest disagreement between the calculated and measured settlements lies at points 2 and 3 (see Fig. 7.4), these two points are considered in the objective function to improve the prediction. Furthermore, point 1 has the largest vertical displacement among all the observation points which is one of the most significant model responses. In order to keep the good agreement between calculated and measured data at this point, it is included in the objective function. For point 1, the value of weighting factor is defined as the maximum ω_1=1.0 in order to keep the good agreement for the largest settlement. Predicted displacement of point 2 need to be improved more than other points, its weighting factor is defined as ω_2=0.5 and the weighting factor for point 3 equals 0.4. Particle Swarm Optimization (PSO) algorithm (Meier et al. 2009; Knabe et al.

Table 7.4: PSO parameters

PSO parameter	Value [-]
K_p	15
$\eta_{\max}$	0.9
$\eta_{\min}$	0.4
c_1	0.50
c_2	1.25
T_{max}	150
stop criterion	$f(X)$ <10^{-10}

2012) is selected here to minimize the objective function. Moreover, PSO algorithm is recognized to be very efficient in solving large, discrete, non-linear and poorly-understood optimization problems (Kang et al. 2004). It was particularly designed for a global minimum search and is considered to guarantee with high reliability not to terminate in a local minimum. In the framework of PSO algorithm (Kennedy & Eberhart 1995), there are two primary operations, velocity $V_k(t)$ and position $X_k(t)$ update as:

$$V_k(t) = \underbrace{\eta V_k(t-1)}_{\text{momentum}} + \underbrace{c_1 r_1 \left(X_k^L - X_k\,(t-1)\right)}_{\text{cognitive component}} + \underbrace{c_2 r_2 \left(X^G - X_k\,(t-1)\right)}_{\text{social component}}, \tag{7.2}$$

$$X_k(t) = X_k(t-1) + V_k(t), \tag{7.3}$$

where k=1,2,3,...,K_p. K_p is the total number of particles, and t is time. X_k^L is the best previous position of the k-th particle at current iteration, and X^G is the best particle among all the particles in the swarm. The parameters c_1 and c_2 are cognitive and social parameter, respectively. The parameters r_1 and r_2 are two independent random numbers in the range [0:1]. The parameter η is an inertia weight, it balances the global search (the best position of all particles among all search attempts) and local search (the best position of one particles in the last search attempt). In this case, η linearly decreases over time to have more chance to find the global optimum (Shi & Eberhart 1998). The used PSO parameters are listed in Table 7.4.

Fig. 7.10(a) shows the surface settlements profiles in transverse and longitudinal directions predicted with optimized parameters obtained within 3D back analysis. Two approaches are used, in the first one HSS model is assigned to all layers (Overall HSS), while in the second one soft soil model (in the framework of *Plaxis*) is assigned to K1 layer and

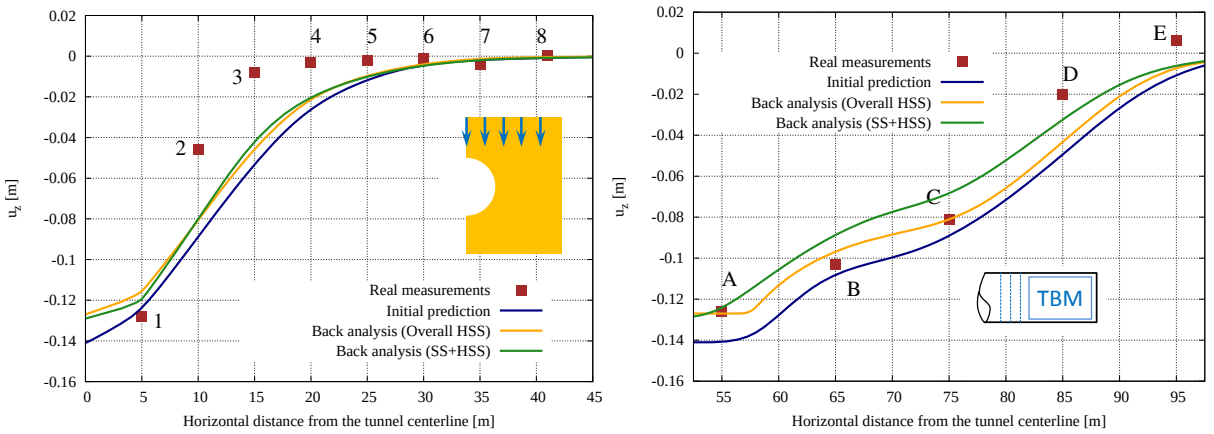

Figure 7.10: Optimization result in 3D model: (a) transverse direction (b) longitudinal direction

HSS model is assigned to the remaining layers (SS+HSS). As mentioned before in case of employing HSS model, the stiffness parameters and the friction angle of K1 and Z1 layers play the most important role for surface settlement. By analogy, for the soft soil model which is available as an in-built model in *Plaxis*, the corresponding stiffness parameters and friction angle are selected as parameters to be identified. The optimized values of the selected input parameters are given in Tables 7.5 and 7.6.

Using modified parameters obtained in back analysis makes the predicted displacements better match the field measurements. For back analysis with overall HSS model, in transverse direction the predicted surface settlement of points closed to the tunnel is decreased, this is due to the fact that increased friction angle and stiffnesses (E_{oed}^{ref} and E_{50}^{ref}) of Z1 layer decrease soil's elastic deformation. When soft soil model is applied, plastic deformation caused by ongoing large strain of clay above the excavated domain increases the displacement of point 1. Stiffness of Z1 layer in SS+HSS model is increased compared with that in overall HSS model, this results in decreasing the surface displacements of monitoring points far away from the tunnel centerline. In longitudinal direction, prediction with overall HSS model well matches the measured data, especially in points A-C. For SS+HSS model, displacements of points B-D decrease due to that stiffness of Z1 increases nearly three times. Accounting for the inclination of tunnel, with the advancement of TBM, the space between tunnel and clay layer becomes larger and then the effect of clay layer on ground surface settlement is less important. Vertical displacements of surface points decrease with the increased soil stiffness of Z1 layer.

Table 7.5: Optimized values of constitutive parameters for overall HSS model

Soil layer	Parameter	2D back analysis	3D back analysis	Unit [-]
clay K1	φ'	17.44	16.17	[°]
	E_{oed}^{ref}	23.498	24.082	[MPa]
	E_{ur}^{ref}	60.341	71.717	[MPa]
sand Z1	φ'	37.03	37.88	[°]
	E_{oed}^{ref}	39.502	33.508	[MPa]
	E_{ur}^{ref}	79.006	67.015	[MPa]

Table 7.6: Lower and upper bounds of constitutive parameters for SS+HSS model and the optimization result

Soil layer and Model type	Parameter	Lower bound	Upper bound	2D back analysis	3D back analysis	Unit
clay K1 (SS)	φ'	20	30	27.67	26.20	[°]
	λ^*	0.004	0.007	0.0062	0.0060	[-]
	κ^*	0.0012	0.0025	0.0017	0.0019	[-]
sand Z1 (HSS)	φ'	30	40	36.42	38.58	[°]
	E_{oed}^{ref}	60	150	93.731	91.856	[MPa]
	E_{ur}^{ref}	120	300	193.462	190.114	[MPa]

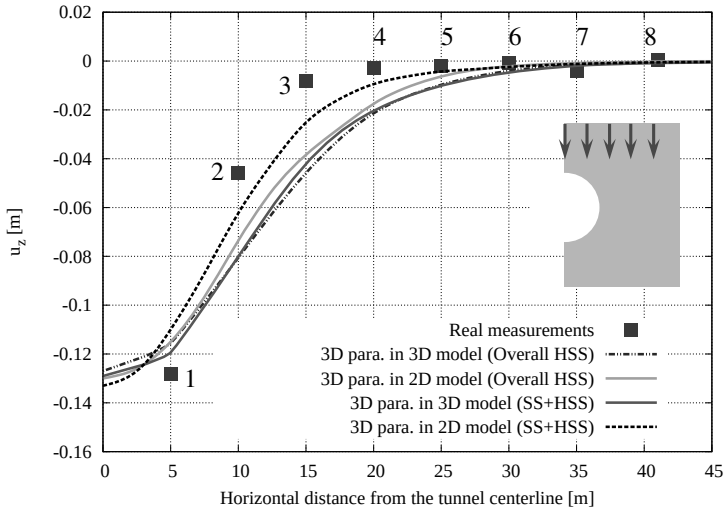

Figure 7.11: Compare of 2D and 3D model responses (transverse surface settlement) by using optimized parameters obtained in 3D back analysis

As optimized parameters have been obtained by back analysis in 3D model, these parameters are employed in the 2D model to check if the these parameters are also adequate in 2D model. Transverse surface settlement profiles calculated in 2D and 3D models are displayed in Fig. 7.11. As seen, these parameters are adequate in 2D model for the calculation of surface settlement. They give good fit between prediction and the field measurement. It can be concluded that both 2D and 3D models are adequate for prediction of the transverse surface settlements. However, 2D model only simulates one transverse cross section and neglects the limited length of embankment, slope of the tunnel, face pressure and consequential excavation process. On the contrary, these construction details are all taken into account in the 3D model. 3D model can provide the soil deformation along the tunnel axis with the advancement of TBM, while this is not available in 2D model. Due to these reasons, it is necessary to compare other model responses of 2D and 3D models beside the surface settlement.

Fig. 7.12(a) shows computational results for structural forces using different models. Since lining design is dominated by axial forces, the variation of axial force along the lining segment calculated with overall HSS model is investigated. As seen, the axial force calculated using both 2D and 3D models is always compressive and generally the axial force increases from tunnel crown towards tunnel invert. However, the value of the axial force obtained by the 3D model is much higher than that obtained within the 2D model. This may be attributed to the three dimensional arching effect of soil towards the end of the tunnel. Before TBM reaches the observation section, there is almost no arching action for the soil

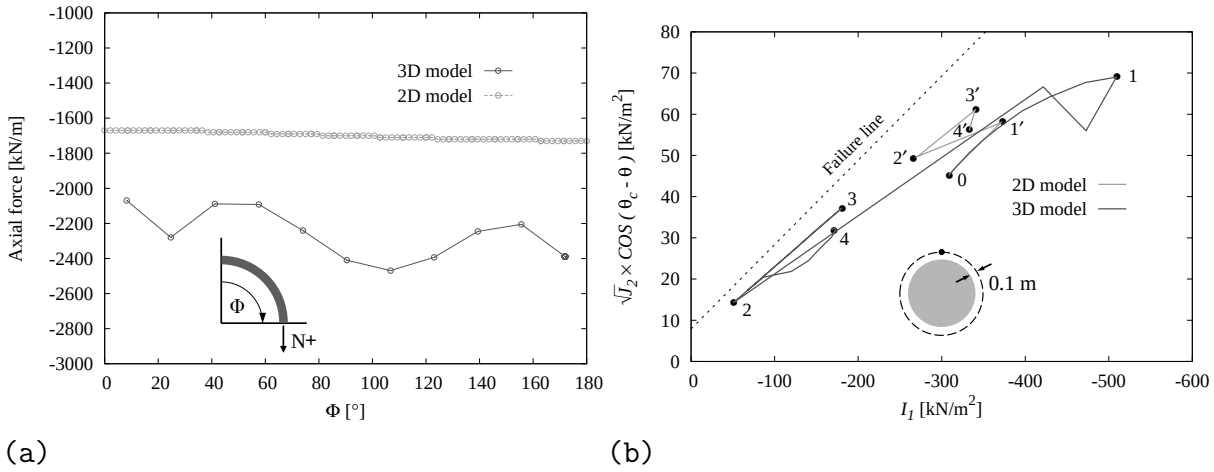

Figure 7.12: Different model responses of 2D and 3D models: (a) axial force (b) stress path (θ is the Lode angle, $\tan\theta_c$=$\sin\varphi'/\sqrt{3}$)

in the observation section. With the advancement of TBM, the arching action is gradually activated and induces stress release around the tunnel. When the lining segment is installed at the monitoring section, interaction between the lining and surrounding soil makes the lining to deform until a state when the support pressure of lining balances the released ground stress. However in 2D model, this step-wise aching effect is simulated as an immediately artificial support after soil excavation and this way may not be realistic.

Fig. 7.12(b) demonstrates the different stress paths for the monitoring point located 0.1 m above the tunnel crown. The stress path starts from the initial state, both models have the same start point (point 0). In 2D model, unloading occurs when contraction factor is activated (point 1'-2') to simulate the volume loss. Afterward, grouting pressure is applied (point 2'-3'), effective stress increases because of the reloading process. In 3D model, before TBM reaches the monitoring point (point 0-1), effective stress is increased due to the influence of face pressure. Volume loss during excavation (point 1-2) leads to the unloading process. The stress level is lower than that in 2D model, this is related to that effect of face support vanishes and the gradually increased contraction factor along the TBM shield. When grouting injection passes the section (point 2-3), effective stress increases which is coincident with that in 2D model. Nevertheless, stress paths of 2D and 3D models have the similar tendency for the monitoring point located 0.1 m above the tunnel crown, the actual stress states in different stages of tunnel excavation are different.

7.2.5 Calibration and validation of the 2D model

Fig. 7.13(a) shows the transverse surface settlements predicted with modified parameters obtained within 2D back analysis. The optimized values of selected input parameters are given in Tables 7.5 and 7.6. It is worth mentioning that the optimized parameter set obtained in 2D back analysis is different with that of 3D back analysis. This is because that 2D and 3D models consist different model features of the tunneling process. As mentioned before, the face pressure, conicity of shield, inclination of the tunnel and progressive excavation process are not considered in the 2D model, this means the 2D model has less uncertain model parameters to be identified compared to the 3D model. During back analysis, only the soil parameters are optimized to compensate the effects of other model features to have the best fit with the measured data. Therefore, 2D and 3D back analysis result in different optimized soil parameter sets.

Using modified parameters obtained in 2D back analysis improves the numerical prediction. The reason for the improvement of transverse surface settlement in different observation points is similar with the explanation in 3D model. In order to check if the optimized parameters obtained by 2D back analysis are adequate in 3D model, comparison of transverse settlement profiles in 2D and 3D models are shown in Fig. 7.13(b). It can be concluded that discrepancy between prediction and measurement is increased when the 2D parameters are used in 3D model especially for observation points 2-5, which means 2D parameters are not adequate in 3D model. This relates to the deficiency of 2D model which has been demonstrated in section 7.2.1. Comparing Figs. 7.11 and 7.13(b), optimized parameters obtained in 3D back analysis provide better prediction when they are employed in 2D model. While optimized parameters obtained in 2D back analysis give inadequate prediction for the 3D model. It can be concluded that 2D model is not adequate in this case without considering limited length of dike layer, inclination of the tunnel, face support and consequential excavation process. However, it is easier and cheaper to create and run the 2D model. According to Table 7.7, creating meta-model for 3D simulation costs much more time and resources than creating 2D meta-model. If one only cares about the maximum surface settlement of one monitoring section in this case, 2D model can be used to substitute 3D model. Additionally, 2D model cannot predict the longitudinal surface settlements.

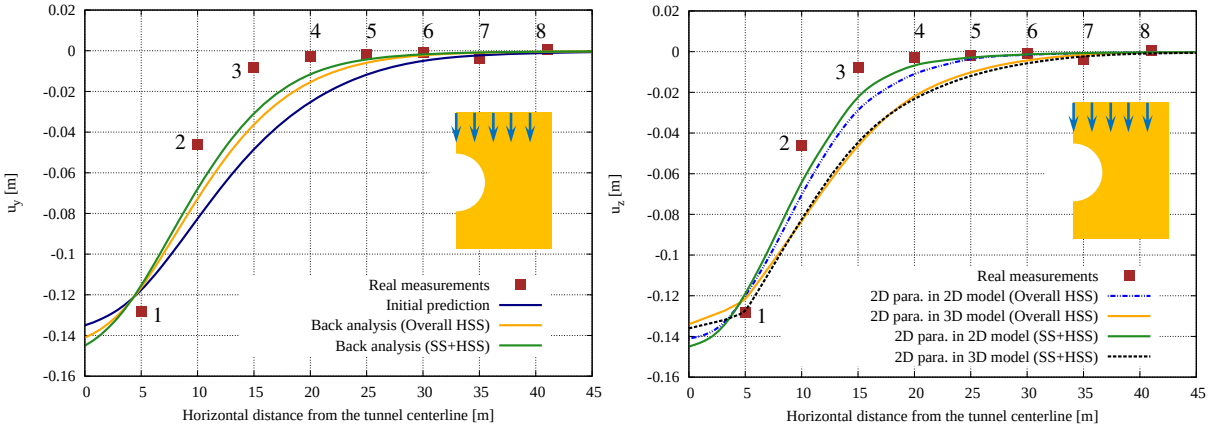

(a) (b)

Figure 7.13: Back analysis in 2D model: (a) transverse surface settlements (b) comparison of 2D and 3D model response by using optimized parameters obtained via 2D back analysis

Table 7.7: Comparison of calculation time cost of 2D and 3D models (one computer with 8 kernels CPU)

Calculation type	2D model	3D model	Unit
Single run of FE-model	0.08	6	h
Creating meta-model	16	1200	h
Single run of meta-model	$2{\cdot}10^{-4}$	$2{\cdot}\ 10^{-4}$	h
Back analysis with meta-model	0.25	0.25	h

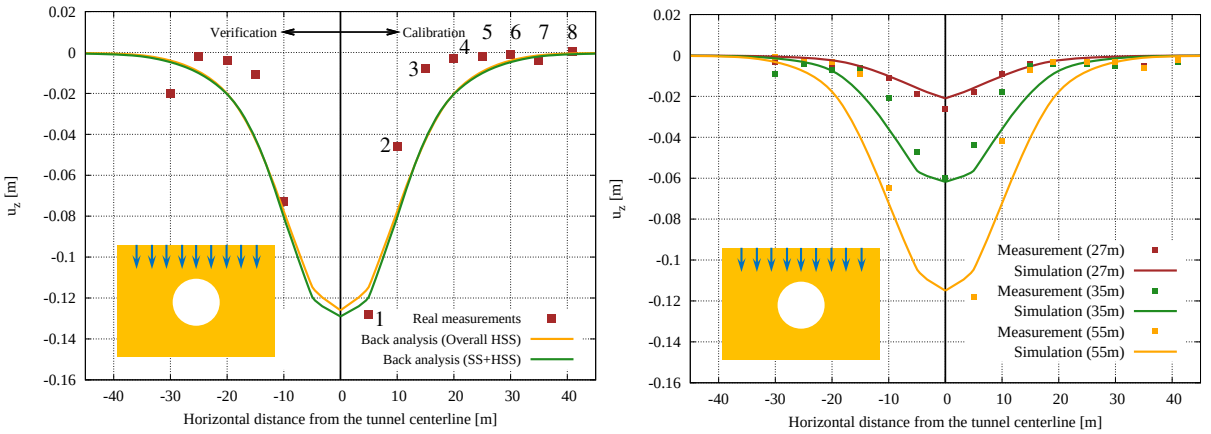

(a) (b)

Figure 7.14: Calibration and verification of transverse surface settlements: (a) at the end of tunnel excavation (b) verification of transverse surface settlements with respect to different length of tunnel excavation

7.2.6 Verification of the 3D model

In numerical simulation, predicted surface settlements in left and right sides of the tunnel are symmetric. However, surface displacements in reality are usually not symmetric due to the complex in-situ geologic layer distribution as well as possible error in measurement. The field measurements of surface settlements of Western Scheldt tunnel in both left and right sides are given in Fig. 7.14(a). For overall HSS model, the calibrated parameters obtained by back analysis are listed in Table 7.5, for SS+HSS model, the calibrated parameters are given in Table 7.6. In all scenarios, face pressure distribution and contraction factor are same as those used in initial prediction. Model calibration and validation are conducted based on the measured settlement in the right side of the tunnel. After validation, the model is verified based on the measured ground settlement in the left side of the tunnel. The result of model calibration and verification is depicted in Fig. 7.14(a). Using the optimal parameters set, the numerical model predicts the ground settlement very well. For verification, the model response is calculated with the calibrated parameters. It shows that predictions match well the field measurements, which means the assumptions and implementation of the numerical model are correct.

In addition to the ground settlement observed after 88 m length of tunnel excavation which has been shown in Fig. 7.14(a), vertical displacements of the monitoring points were also measured in different excavation stages. When TBM advanced 27 m, 35 m and 55 m, vertical displacements of observation points in both left and right sides of the

tunnel were recorded. By using the validated model, transverse surface settlements in the monitoring section are calculated with respect to different lengths of TBM advancement. Result of model verification (Overall HSS model) is shown in Fig. 7.14(b). As seen, good agreement is found when comparing the calculated result to the measured data. It can be concluded that 3D numerical model is very well capable to predict the surface settlements with respect to tunnel's construction process.

7.2.7 Conclusions

Numerical simulation is an important tool to provide reliable predictions of deformations for mechanized tunneling. However, it is often technically difficult to collect sufficient data of model parameters by in-situ and laboratory tests. Global sensitivity analysis plays a significant role in geotechnical application due to the uncertainty embedded in the subsoil properties, complicated constitutive model, etc. Especially for complex problems, such as the mechanized tunneling in this study, global sensitivity analysis can estimate the key parameters which govern the model response. To identify the most significant parameters, back analysis is carried out by using PSO algorithm for minimizing the disagreement between the observation data and calculated displacements. Model validation is conducted in both 2D and 3D numerical models. Based on the analyses performed in the present study, the following general conclusions can be outlined:

1. Sensitivity of surface settlement to constitutive model parameters are varying for different observation points. Plastic deformation of soil is most sensitive to friction and dilatancy angles. While soil's elastic deformation is more sensitive to stiffness and also related to the friction angle.

2. Less disagreement between the calculated surface settlement profile and the measured data is observed by assigning soft soil model instead of HSS model to the clay layer above the excavation domain.

3. Optimized parameters within 3D back analysis are adequate in both 3D and 2D models. Validated 3D model provides reliable prediction of the surface settlement profiles with the advancement of TBM as well as other model responses which cannot be well captured by 2D model.

4. One current shortage is that there is still space to improve the transverse surface settlement profile. It is foreseen to apply advanced constitutive model to take into

account anisotropy and destructuration. In addition, there are still several uncertain aspects affecting the ground settlement. This can also be seen in different measurement values at the right and left sides of the tunnel in the same plane.

7.3 Tunneling model test

The author has checked many literature and there is a lack of data where the displacements at the subsurface of soil domain are monitored during tunnel excavation underneath existing buildings. Fu et al. (2014) conducted a case study of twin tunnel excavation in Shenzhen, China. Two cross sections are designed for measurement of soil deformations at both surface and subsurface levels, while both cross sections are located at the greenfield. For the cross section where the buildings are located, only the building deformations are measured. In the work of Farrell et al. (2012), settlement responses of two buildings were reported in a tunnel excavation in Rome, Italy. However, the soil deformations were not mentioned. Similarly Dimmock & Mair (2008) presented the measurements of settlements of three buildings in London during construction of Jubilee Line Extension, while the displacements in the soil domain were not reported. In the work of Ritter et al. (2017), the influence of tunnel excavation on the building behavior is investigated via the centrifuge tests where relatively complex surface structure is fabricated by 3D printing. Nevertheless, a 3D numerical simulation is essential to capture all the model features, which is beyond the scope of the present study. Shanin et al. (2011) applied an apparatus to model the tunnel excavation in the laboratory. With this apparatus, 2D model tests were carried out to investigate the influence of tunnel excavation on the surface and subsurface settlements of soil domain. In their study, the effect of the interaction between the tunneling and existing nearby foundation was demonstrated as well. Thus, this tunneling model test is chosen as an alternative in the present study to validate the methodology of optimal sensor location by applying the field sensitivity obtained in section 4.3.

7.3.1 Introduction of the model tests

According to Shanin et al. (2011); Shahin et al. (2016), Fig. 7.15(a) shows a schematic diagram of the 2D model apparatus, it was constructed based on a device described by Adachi et al. (1994). The tunneling device consists of a central shim surrounded by 12 segments. These segments are strongly tightened all around the shim with rubber bands. There are two motors in this device, one for shrinking the tunnel and the other for moving the tunnel device in the vertical direction to fix it at a certain depth. These two motors can be controlled simultaneously. Consequently, the segments move inwardly and the diameter of the tunnel is reduced. By doing so, the volume loss around the tunnel can be reproduced.

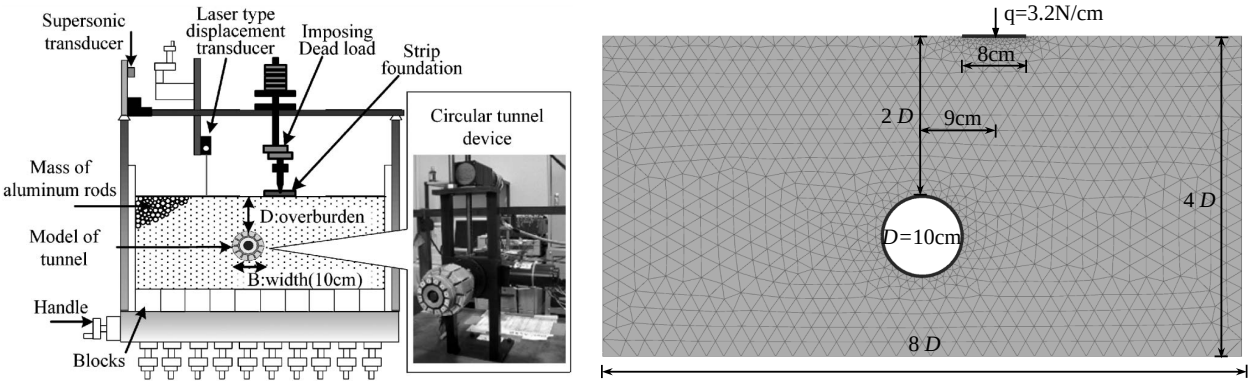

(a) (b)

Figure 7.15: (a) Schematic diagram of 2D tunnel apparatus, after Shanin et al. (2011), (b) Geometry and mesh discretization of 2D FE-model

In this device, the total diameter of the model tunnel is 10 cm. The tunnel device was set at a height of 10 cm measured from the bottom of the iron table to the tunnel invert. Several experiments were conducted to ensure that this height was enough to avoid boundary effect in their model tests. The distance between tunnel crown and ground surface is variable, in the current case study, this distance is chosen as 20 cm. To simulate the building loads, a strip footing which is made of an iron plate is used to model the foundation. The width and thickness are 8 cm and 1 cm, respectively. To impose the existing load, a constant dead load of 3.2 N/cm is placed in the center of the foundation before performing the tunnel excavation. They mentioned that this load was estimated from previous loading tests and it was around 1/2 of the bearing capacity of the ground. In this model test, aluminum rods were used to model the ground. The unit weight of the aluminum rods was 20.4 kN/m^3. For the initial stress condition, the value of K_0 was about 0.7 and it was carefully controlled by movable blocks at the bottom of the apparatus.

The resulting surface settlement of the ground is measured using a laser type of displacement transducer with an accuracy of 0.01 mm. Photographs are taken during the experiments and are used later as input data for the determination of ground movements based on the technique of Particle Image Velocimetry (PIV).

7.3.2 Calibration of the numerical model

Based on the aforementioned model test device, a same scale numerical model is created. The geometry and mesh discretization are shown in Fig. 7.15(b). To simulate the tunnel

Table 7.8: Calibrated model parameters

φ'	ψ'	c	E_{50}^{ref}	E_{oed}^{ref}	E_{ur}^{ref}	p^{ref}	m	ν_{ur}	γ
22.1°	2.8°	0	15 MPa	15 MPa	45 MPa	98 kPa	0.8	0.2	20.4 kN/m^3

excavation, contraction factor method is applied to model the tunnel volume loss. In the current study, a huge tunnel volume loss of 15.36% is applied based on the model tests. To keep the circular shape of the tunnel, elastic material with high rigidity is adopted to model the lining (EA=1.1·10^7 kN/m, EI=2.2·10^5 kNm^2/m). In the work of Shanin et al. (2011), an elasto-plastic subloading t_{ij}-model is used to describe the behavior of aluminum rods and the corresponding model parameters are calibrated on the basis of biaxial tests. In the current study, Hardening Soil (HS) model is used and the model parameters are derived according to the model parameters given in Shanin et al. (2011).

The calibration of model parameters is conducted via back analysis, which has been described in section 7.2.4. An optimized parameter set is obtained to provide an optimum fit between the numerical prediction and measurement of the biaxial tests. The measured biaxial results are shown in Fig. 7.16. In this back analysis approach, the objective function (see Eq. 7.1) is defined to evaluate the normalized differences between prediction and measurement. The minimum of the objective function may serve as a measure for comparison of the quality of different inverse analyses, and it can be found by the use of evolutionary algorithms.

The calibrated model parameters are presented in Table 7.8. Fig. 7.16 shows the experimental results of the biaxial tests for the mass of aluminum rods and the numerical prediction using HS model. As seen, the numerical results well match the measurements. It is worth mentioning that HS model is not able to capture the strain softening behavior of the material, therefore, the peak value of stress ratio in Fig. 7.16(a) is used for calibration of the friction angle of aluminum rods.

By using these model parameters, the tunnel excavation is simulated and the numerical prediction of the tunneling induced surface settlement profile is shown in Fig. 7.17. It is observed that the calibrated numerical model is able to well predict the tunneling induced ground movements. Therefore, this model is applied in the next subsection to validate the methodology of optimal sensor location.

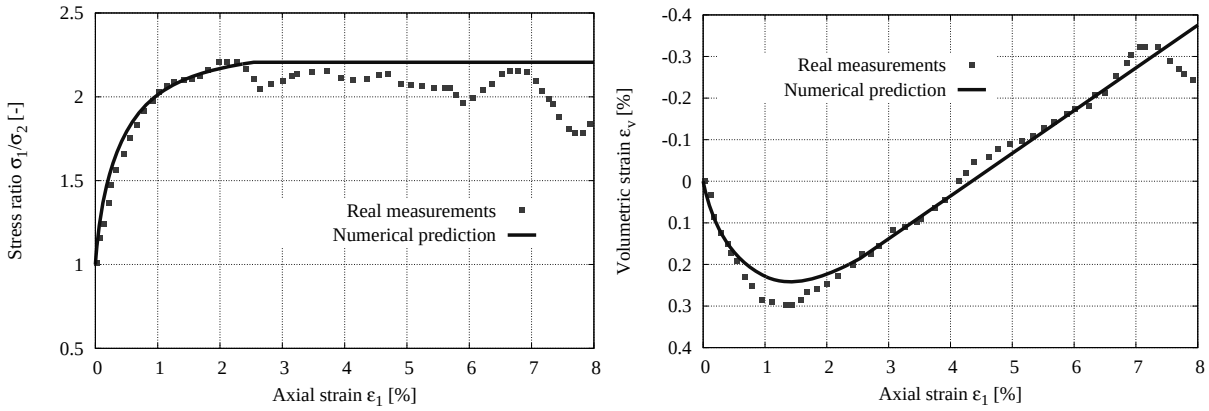

(a) (b)

Figure 7.16: Calibration of the constitutive model parameters: (a) stress-strain relation, (b) strain-dilatancy relation (negative volumetric strain represents dilation) under confining stress σ_2=19.6 kPa

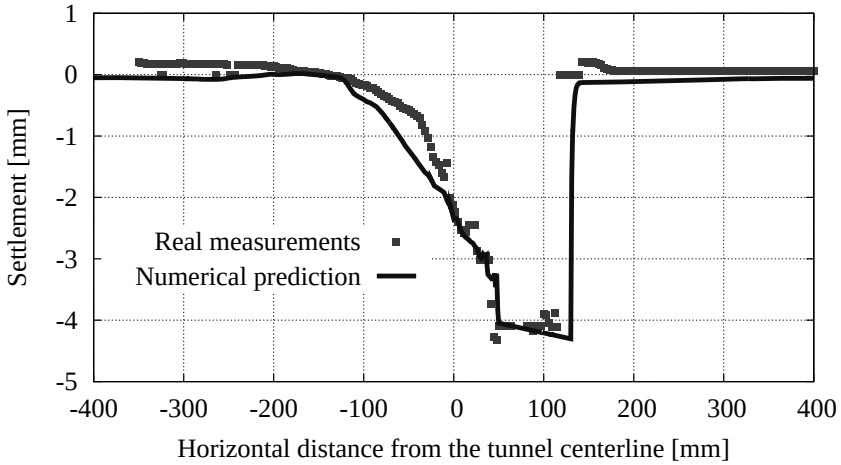

Figure 7.17: Comparison of numerical prediction and real measurements of the surface settlements

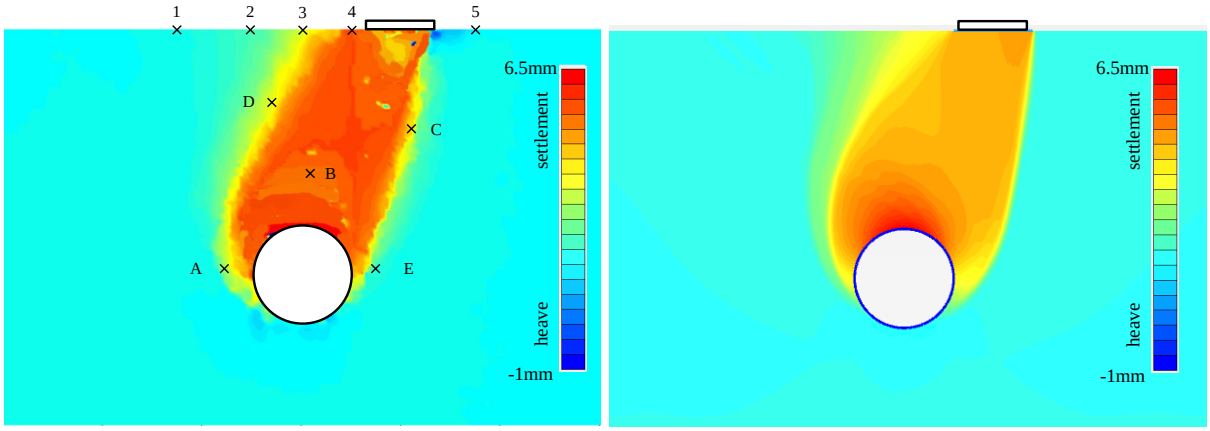

(a) (b)

Figure 7.18: Tunneling induced vertical displacements: (a) the model test results (after Shanin et al. (2011)) and illustration of the designed sensor locations, and (b) the numerical results

7.3.3 Evaluation of sensor locations

In order to evaluate the influence of different sensor locations on the parameters identification results, the model tests results are used and the soil stiffness (E_{50}^{ref}, E_{ur}^{ref}) and strength parameters (φ', ψ') are assumed as uncertain parameters and need to be identified.

Fig. 7.18 shows the tunneling induced vertical displacements of both the model tests and the numerical model. As seen, the calibrated numerical model is able to well predict the tunneling induced ground movements. The designed locations for the sensors are illustrated in Fig. 7.18(a). Three scenarios of sensor location are designed and the description of each scenario is given in Table 7.9. In scenario I, five sensors are placed on the ground surface. According to the discussion in section 4.3, the optimal sensor location areas are around the tunnel and between tunnel and foundation. Therefore, five sensors are placed at subsurface level and around the tunnel in scenario II. By comparison of scenarios I and II, the effect of different sensor locations on the parameter identification results can be investigated. Furthermore, according to the three optimal sensor locations suggested in section 4.3, 3 sensors are placed at points A, B and C only in scenario III to assess the possibility of reducing the number of sensors for the purpose of parameter identification. It should be noted that noise of measurement is not considered during parameter identification.

The aforementioned back analysis is applied to conduct parameter identification on the basis of measurements. It is to be noted that the current back analyses do not embed the

Table 7.9: Designed scenarios to evaluate the effect of different sensor locations

Scenario	Designed sensor locations	Measurement	Parameters to be identified
I	1, 2, 3, 4, 5		
II	A, B, C, D, E	Vertical displacements	E_{50}^{ref}, E_{ur}^{ref}, φ', ψ'
III	A, B, C		

knowledge of the parameters obtained from the former model calibration. In other words, only the ranges of the uncertain parameters (7.5 MPa$\leq E_{50}^{\mathrm{ref}} \leq$ 30 MPa, 22.5 MPa$\leq E_{ur}^{\mathrm{ref}} \leq$ 90 MPa, $15° \leq \varphi' \leq 30°$ and $0 \leq \psi' \leq 5°$) are assumed and blind parameter identification is conducted. For each scenario, 100 runs of back analysis were carried out. Afterwards, the mean value and coefficient of variance (COV) for each parameter are calculated and the results are presented in Table 7.10. It should be noted that the model parameters given in Table 7.8 are taken as the "true value", these values are compared with the identified parameters to evaluate the quality of the parameter identification. As seen in Table 7.10, scenario II has the minimum COV for parameters E_{50}^{ref}, E_{ur}^{ref} and φ', which means uncertainty of these optimized parameters is the least. It should be noted that the COV for parameter ψ' obtained in scenario II is not the minimum value, this may be because the optimal sensor location for identifying dilatancy angle is not in these designed positions as ψ' is not considered in aforementioned sensitivity field (see section 4.2). However, the mean value of optimized dilatancy angle in scenario II is most close to the true value. It is recommended that sensitivity field should be conducted for each uncertain parameter before determining the optimal locations for the sensors.

According to Table 7.10, by using five sensors in subsurface level around the tunnel is more efficient than five sensors at ground surface for the purpose of soil parameter identification (E_{50}^{ref}, E_{ur}^{ref} and φ'). Furthermore, when three sensors are placed optimally by means of sensitivity values (highest sensitivity information in the sensitivity field, such as Fig. 4.27) and applied in scenario III, despite of slightly larger COV of identified parameters in comparison with scenario II, the parameters are still in a tolerable range of accuracy. In other words, contrived design of monitoring scheme can result in obtaining more adequate information about system with less effort. Therefore, instead of installation of many sensors at the ground surface, less sensors can be placed at subsurface level on the basis of the sensitivity field (in the region with highest sensitivity information). By doing so, the soil properties can be identified with less uncertainty. This proves the

Table 7.10: Evaluation of different sensor locations

		Scenario I		Scenario II		Scenario III	
Parameter	True value	Mean	COV	Mean	COV	Mean	COV
E_{50}^{ref}[MPa]	15	16.88	0.30	14.30	0.25	16.64	0.29
E_{ur}^{ref}[MPa]	45	60.73	0.22	51.09	0.15	58.35	0.20
$\varphi'[^\circ]$	22.1	24.15	0.10	22.35	0.09	23.56	0.10
$\psi'[^\circ]$	2.8	3.22	0.17	2.95	0.22	3.17	0.27
Relative error		$4.24{\cdot}10^{-2}$		$5.91{\cdot}10^{-3}$		$3.05{\cdot}10^{-2}$	

applicability of reducing the numbers of sensors by having the sensitivity field of model response to model parameters. Furthermore, relative error for the optimized parameter set are obtained using Eq. 7.1 in comparison with the true value of corresponding parameters. The parameters identified in accordance with monitoring data from scenario II are the most accurate while the parameters determined by placing all the sensors at ground surface (scenario I) have the largest deviation from the true soil properties. Alternatively, adopting less sensors at the subsurface level leads to a tolerable relative error for the optimized soil properties. This comprehensively justifies the applicability of sensitivity field as a powerful tool for design of optimal sensor location.

7.3.4 Conclusion

Based on the study in section 4.3 where sensitivity analysis was conducted to evaluate the relative importance of soil-tunnel-building interaction in accordance with their influence on the tunneling induced ground movements, optimal sensor locations are suggested for the purpose of parameter identification and this methodology is validated via a case study of tunneling model tests. It can be concluded that sensitivity field is a powerful tool for design of optimal sensor location where instead of arranging all the sensors at ground surface, less sensors can be rationally placed at subsurface level to attain sufficient knowledge on the soil properties with less effort.

8 Conclusions and recommendations

8.1 Conclusions

In this research, the influence of the most important sub-systems, namely volume loss, tail void grouting, lining installation and progressive excavation on the model responses are studied. Special attentions are paid to the tunneling induced ground movements and the associated building's behavior. Tail void grouting induced time- and space-dependent stiffness and permeability of ground domain in the near field around the tunnel are considered in the hydro-mechanical coupling (consolidation) analyses of tunnel excavation in saturated soil. Three advanced process simulation techniques are proposed for the purpose of saving computational cost especially in parametric study. Finally two tunnel case studies are conducted. The main derived conclusions are categorized as follows.

Effects of sub-systems

Tunneling induced surface volume loss is triggered by the tunnel volume loss, the difference between them is attributed to the soil volume change which depends on the soil elasticity and plasticity parameters. The empirical Gaussian distribution curve can be modified based on the effect of tunnel volume loss on the surface settlement trough. Surface volume loss ratio and settlement trough width parameter can be respectively expressed as quadratic and linear equations of tunnel volume loss ratio. The value of K_0 governs the deformation mode of soil above the tunnel crown, higher value of K_0 may induce less settlement at the ground surface. When there is building on the ground surface, soil's friction angle, tunnel volume loss and horizontal distance from the tunnel are the dominant parameters in determining the building's settlements. While the overburden depth of tunnel as well as the soil-building contact properties highly affect the tilt of the building. By applying the sensitivity analysis in the entire domain of the model, it is found that for the purpose of identifying the soil's stiffness and strength, the optimal sensor locations to measure the vertical and horizontal displacements in the present study are (1) $D/2$ to

outer side of the tunnel with respect to the position of the building, (2) below or above the tunnel, and (3) $1D$ below the building and $2D$ horizontal distance to the inner side of the tunnel towards the intermediate zone between the tunnel and building. Consecutive and simultaneous consolidation schemes are developed as two numerical simulation methods for hydro-mechanical coupling analysis of tunneling problem. The consecutive scheme allows full generation of the excess pore pressure during excavation, which is preferred for tunneling in low permeable soil with high advance speed. Whilst the simultaneous scheme is preferred for slow advancing in high permeable soil due to the fact that consolidation and drilling coincide in each excavation step. The infiltration of grout material does not take place in soil with low permeability, while it strongly occurs due to backfill grouting in soil with high permeability. Neglecting the grouting induced evolution of the permeability and stiffness of ground domain in the near field around the tunnel could underestimate the surface settlements and lining axial forces after passing the TBM.

Advanced process simulation

The innovative adaptive constitutive modeling accounts for constitutive model exchange in the near field sub-domain which is strongly affected by tunnel excavation. The model adaption is suggested to be carried out by taking into account a family of hierarchical constitutive models. The zone which is subjected to loading, unloading and reloading due to tunnel excavation can be numerically simulated by an advanced model while the less-affected far field sub-domain can be sufficiently simulated by a basic model. The distribution and variation of plastic strain at the Gaussian points are used to determine the size of the area where advanced constitutive model is employed. The appropriate size of the near-field sub-domain as well as the hierarchical constitutive models can benefit the design of laboratory tests and in-situ investigation strategy. It is found that the submodeling approach is a powerful tool for detailed analysis in the near field around the tunnel with reduced computational costs in comparison with the conventional simulation method. The applicability of the assumed submodel boundary is suggested to be checked by the strain energy distribution. The submodel may or may not be defined with the same material law in comparison with the global model, and two submodeling techniques, namely fixed block and moving block approaches, are developed for tunneling simulation. The novel computational method hybrid model is proposed for numerical simulation of mechanized tunnel excavation. This approach combines the capacity of a process-oriented submodeling with the computational efficiency of metamodel. It is a powerful tool for parametric study and it is also applicable in optimization of process

parameters in each excavation step without updating the submodel boundary conditions, accordingly the tunneling induced soil deformations can be kept within the tolerated limit with the advancement of TBM.

Case study

According to the case study of Western Scheldt tunnel, it is found that sensitivity analysis is a powerful tool to elaborate the relative importance of the model parameters in determining the model responses. Sensitivity of soil deformation to constitutive model parameters are varying for different observation points. Plastic deformation of soil is most sensitive to friction and dilatancy angles. While the elastic deformation is more sensitive to stiffness and is related to friction angle as well. Sensitivity analysis can be used to quantify the model uncertainty and reduce the dimension of the back analysis problem. Optimized parameters within 3D back analysis are adequate in both 2D and 3D models. Validated 3D model provides reliable predictions of the surface settlement profile with the advancement of TBM as well as other model responses that cannot be well captured by 2D model. When the sensitivity information is applied in the entire model domain to form the sensitivity field, it becomes a powerful tool for design of optimal sensor location where instead of arranging all the sensors at the ground surface, less sensors can be conveniently and rationally placed at subsurface level to attain better knowledge on the soil properties with less efforts. This methodology is validated via the case study of tunneling model tests.

8.2 Works in the next step

Based on the work of adequate numerical simulation of mechanized tunnel excavation using finite element method conducted in the present study, the very interesting and potential development could be stated as follows:

1. Although the lining stiffness are reduced to take into account the effect of joints, the longitudinal joints in the lining segments could be further considered and explicitly simulated in the numerical analysis, which is more realistic for lining structural design.

2. In the present study, the variable permeability obtained from infiltration theory is manually updated in the simultaneous consolidation analysis. The grout infiltration

induced permeability evolution could be further implemented in the same framework of finite element code which is utilized for consolidation analysis.

3. In adaptive constitute modeling, the size of sub-domain where advanced model is applied is defined manually based on the incremental plastic strain. This approach could be further implemented in the finite element code. To be specific, when the incremental plastic strain at the Gaussian points using the basic constitutive model (e.g., MC model) fulfills the predefined criteria in certain domain of the model, the basic constitutive model is exchanged to the advanced one (e.g., HSS model). Thereafter, the basic constitutive model is re-assigned to the domain when the criteria of incremental plastic strain cannot be fulfilled.

4. The constitutive model employed in the present study does not account for the complex soil behavior, i.e., anisotropy and destructuration. These features of soil could be further considered in the numerical simulation by developing or employing more sophisticated constitutive models.

5. In the current Hybrid modeling approach, the effect of ground water is not considered. The hydraulic boundary conditions of the submodel can be further studied, and an approximate method can be developed to drive the submodel in Hydro-mechanical coupled analysis.

Bibliography

Adachi, T., Jun, L., Akinori, K. & Feng, Z. (2006), Numerical analysis of Biot consolidation problem based on an elasto-plastic constitutive model with strain softening in tunneling, *in* 'Proceedings 7th Geotechnical Symposium', Nagoya, Japan, pp. 105–110.

Adachi, T., Tamura, T., Kimura, M. & Aramaki, S. (1994), Experimental and analytical studies of earth pressure, *in* '8th Int. Conf. on Computer Methods and Advances in Geotechnics', pp. 2417–2422.

Addenbrooke, T., Potts, D. & Puzrin, A. (1997), 'The influence of pre-failure soil stiffness on the numerical analysis of tunnel construction', *Géotechnique* **47**(3), 693–712.

Ahmad, A., Hefny, A., Mansour, M. & Mansour, M. (2015), Three-dimensional analysis of Rod EL-Farag subway station, Greater Cairo metro, *in* '14th international Conference on Structural and Geotechnical Engineering'.

Ahrens, H., Lindner, E. & Lux, K. (1982), 'Zur Dimensionierung von Tunnelausbauten nach den "Empfehlungen zur Berechnung von Tunneln im Lockergestein"', *Die Bautechnik* **8**, 260–273.

Anagnostou, G. & Kovári, K. (1994), 'The face stability of slurry-shield-driven tunnels', *Tunnelling and Underground Space Technology* **9(2)**, 165–174.

Anagnostou, G. & Kovári, K. (1996), 'Face stability conditions earth-pressure-balanced shields', *Tunnelling and Underground Space Technology* **11(2)**, 165–173.

Arnau, O. & Molins, C. (2011), 'Experimental and analytical study of the structural response of segmental tunnel linings based on an in situ loading test. part 2: Numerical simulation', *Tunnelling and Underground Space Technology* **26**(6), 778–788.

Arnau, O. & Molins, C. (2012), 'Three dimensional structural response of segmental tunnel linings', *Engineering Structures* **44**, 210–221.

Atkinson, J. H. & Mair, R. J. (1981), 'Soil mechanics aspects of soft ground tunnelling', *Ground Engineering* **14**(5), 20.

Atkinson, J. H. & Sallfors, G. (1991), Experimental determination of soil properties, *in* '10th ECSMFE', pp. 915–956.

Atkinson, J. & Potts, D. (1977), 'Stability of a shallow circular tunnel in cohesionless soil', *Géotechnique* **27(2)**, 203–215.

Attewell, P., Yeates, J. & Selby, A. (1986), *Soil movements induced by tunnelling and their effects on pipelines and structures*, Blackie.

Bakker, K. (2003), 'Structural design of linings for bored tunnels in soft ground', *Heron* **48**(1), 33–63.

Balthaus, H. (1989), Tunnel face stability in slurry shield tunneling, *in* 'Proceedings of the 12th International Conference on Soil Mechanics and Foundation Engineering', pp. 775–778.

Bathe, K. (1982), *Finite element analysis in engineering analysis*, Prentice-Hall.

Benz, T. (2006), Small-strain stiffness of soils and its numerical consequences, PhD thesis, Universität Stuttgart, Germany.

Bezuijen, A., Huisman, M., & Mastbergen, D. (1996), Verdringingsprocessen bij gestuurd boren, Technical report, Boren Tunnels en Leidingen.

Bezuijen, A., Talmon, A., Kaalberg, F. & Plugge, R. (2004), 'Field measurements of grout pressures during tunnelling of the Sophia Rail tunnel', *Soils and Foundations* **44**, 39–48.

Biot, M. (1941), 'General theory of three-dimensional consolidation', *J. Appl. Phys.* **12**(2), 155–164.

Blom, C. B. M. (2002), Design philosophy of concrete linings for tunnels in soft soils, PhD thesis, Delft University of Technology.

Bobet, A. (2001), 'Analytical solution for shallow tunnels in saturated ground', *Journal of Engineering Mechanics* **127**(12), 1258–1266.

Bogdanovich, A. & Kizhakkethara, I. (1999), 'Three-dimensional finite element analysis of double-lap composite adhesive bonded joint using submodeling approach', *Composites Part B: Engineering* **30**(6), 537–551.

Bolton, M. (1986), 'The strength and dilatnacy of sands', *Géotechnique* **36**(1), 65–78.

Boscardin, M. & Cording, E. (1989), 'Building response to excavation-induced settlement', *Journal of Geotechnical Engineering* **115**(1), 1–21.

Brinkgreve, R. (1994), Geomaterial Models and Numerical Analysis of Softening, PhD thesis, Delft University of Technology.

Brinkgreve, R., Engin, E. & Swolfs, W. (2014), *Reference manual*, Delft, Netherlands.

Brodesser, M. (2012), Adäquates Simulationsmodell zur numerischen Analyse maschineller Tunnelvortriebe am Beispiel des Westerscheldetunnels, Bachelorarbeit, Ruhr-Universität Bochum, Germany.

Broere, W. (2001), Tunnel Face Stability & New CPT Applications, PhD thesis, Delft University of Technology.

Broere, W. (2003), Influence of excess pore pressures on the stability of the tunnel face, *in* 'Claiming the Underground Space', Amsterdan, The Netherlands, pp. 759–765.

Broms, B. & Bennermark, H. (1967), 'Stability of clay at vertical openings', *Journal of the Soil Mechanics and Foundations Division* **93(1)**, 71–94.

Bull, A. (1946), 'Stresses in the linings of shield driven tunnels', *Transactions of the American Society of Civil Engineers* **111**(1), 518–530.

Burland, J., Broms, B. & de Mello, V. (1977), Behaviour of foundations and structures, *in* 'Proc. 9th Int. Conf. Soil Mech. and Found. Eng.', pp. 495–546.

CEB-FIP model code (1990), *in* 'design code-comite Euro-international du Beton', Thomas Telford.

Celestino, T., Gomes, R. & Bortolucci, A. (2000), 'Errors in ground distortions due to settlement trough adjustment', *Tunnelling and Underground Space Technology* **15**(1), 97–100.

Ciptokusumo, J., Weide-Zaage, K. & Aubel, O. (2009), 'Investigation of stress distribution in via bottom of Cu-via structures with different via form by means of submodeling', *Microelectronics Reliability* **49**(9-11), 1090–1095.

Davis, E., Gunn, M., Mair, R. & Seneviratne, H. (1980), 'The stability of shallow tunnels and underground openings in cohesive material', *Géotechnique* **30(4)**, 397–416.

de Boer, R. (2000), *Theory of Porous Media: Highlights in Historical Development and Current State*, Springer.

Desari, G., Rawlings, C. & Bolton, M. (1996), Numerical modelling of a NATM tunnel construction in London clay, *in* 'Proc. Int. Symp. on Geotechnical Aspects of Underground Construction in Soft Ground', pp. 491–496.

Dias, D., Kastner, R. & Maghazi, M. (1999), Three dimensional simulation of slurry shield in tunnellingl, *in* 'Proceedings International Symposium on Geotechnical Aspects of Underground Construction in Soft Ground, Tokyo', Rotterdam: Balkema, pp. 351–356.

Dias, T. & Bezuijen, A. (2014), Tunnel modelling: Stress release and constitutive aspects, *in* 'Geotechnical Aspects of Underground Construction in Soft Ground', pp. 197–202.

Dias, T. & Bezuijen, A. (2015), TBM pressure models-Observations, Theory and Practice, *in* 'Geotechnical Synergy in Buenos Aires'.

Dimmock, P. S. & Mair, R. J. (2008), 'Effect of building stiffness on tunnelling-induced ground movement', *Tunnelling and Underground Space Technology* **23**(4), 438–450.

Do, N.-A., Dias, D., Oreste, P. & Djeran-Maigre, I. (2013), '2d numerical investigation of segmental tunnel lining behavior', *Tunnelling and Underground Space Technology* **37**, 115–127.

Dutta, S. & Roy, R. (2002), 'A critical review on idealization and modeling for interaction among soil-foundation-structure system', *Computers and Structures* **80**(20-21), 1579–1594.

Ehlers, W. & Bluhm, J. (2002), *Porous Media: Theory, Experiments, and Numerical Applications*, Springer.

Eilers, H. (1941), 'Die Viskosität von Emulsionen hochviskoser Stoffe als Funktion der Konzentration', *Kolloid-Zeitschrift* **97**, 313–321.

Eilers, H. (1943), 'Die Viskositäts- Konzentrationsabhängigkeit kolloider Systeme in organischen Lösungsmitteln.', *Kolloid-Zeitschrift* **102**, 154–169.

El-Nahhas, F., El-Kadi, F. & Ahmed, A. (1992), 'Interaction of tunnel linings and soft ground', *Tunnelling and Underground Space Technology* **7**(1), 33–43.

Elias, J. (2016), 'Adaptive technique for discrete models of fracture', *International Journal of Solids and Structures* **100-101**, 376–387.

Elsaied, A. (2014), 'Investigation of footing settlements adjacent to circular tunnels', *International Journal of Engineering Research and Technology* **3**(10), 373–378.

Engelbreth, K. (1961), 'Correspondence on Morgan, H.D., A contribution to the analysis of stress in a circular tunnel', *Géotechnique* **11**(3), 246–248.

Fargnoli, V., Boldini, D. & Amorosi, A. (2015), 'Twin tunnel excavation in coarse grained soils: Observations and numerical back-predictions under free field conditions and in presence of a surface structure', *Tunnelling and Underground Space Technology* **49**, 454–469.

Fargnoli, V., Gragnano, C., Boldini, D. & Amorosi, A. (2015), '3D numerical modelling of soil-structure interaction during EPB tunnelling', *Géotechnique* **65**(1), 23–37.

Farrell, R. (2010), Tunnelling in sands and the response of buildings, PhD thesis, Cambridge University.

Farrell, R., Mair, R., Sciotti, A., Pigorini, A. & Ricci, M. (2012), The response of buildings to tunnelling: A case study, *in* 'G. Viggiani(ed), Geotechnical Aspects of Underground Construction in Soft Ground', pp. 877–885.

Ferronato, M., Castelletto, N. & Gambolati, G. (2010), 'A fully coupled 3D mixed finite element model of Biot consolidation', *Journal of Computational Physics* **229**(12), 4813–4830.

Fillibeck, J. & Vogt, N. (2012), Prediction of tunnel induced settlements in soft grounds, *in* 'G. Viggiani(ed), Geotechnical Aspects of Underground Construction in Soft Ground', pp. 735–741.

Finno, R. & Clough, G. (1985), 'Evaluation of soil response to EPB shield tunneling', *Journal of Geotechnical Engineering* **111**(2), 155–173.

Franzius, J. & Potts, D. (2005), 'Influence of mesh geometry on three-dimensional finite-element analysis of tunnel excavation', *International Journal of Geomechanics* **5**(3), 256–266.

Franzius, J., Potts, D., Addenbrooke, T. & Burland, J. (2004), 'The influence of building weight on tunnelling-induced ground and building deformation', *Soils and Foundations* **44**(1), 25–38.

Franzius, J., Potts, D. & Burland, J. (2005*a*), 'The influence of soil anisotropy and K_0 on ground surface movements resulting from tunnel excavation', *Géotechnique* **55**(3), 189–199.

Franzius, J., Potts, D. & Burland, J. (2005*b*), 'The response of surface structures to tunnel construction', *Geotechnical Engineering* **159**(1), 3–17.

Fu, J. (2014), Modelling ground movement and associated building response due to tunnelling in soils, PhD thesis, Technische Universität Bergakademie Freiberg.

Fu, J., Yang, J., Zhang, X., Klapperich, H. & Abbas, S. M. (2014), 'Response of the ground and adjacent buildings due to tunnelling in completely weathered granitic soil', *Tunnelling and Underground Space Technology* **43**, 377–388.

Galli, G., Grimaldi, A. & Leonardi, A. (2004), 'Three-dimensional modelling of tunnel excavation and lining', *Computers and Geotechnics* **31**(3), 171–183.

Gavin, K. & Tolooiyan, A. (2012), 'An investigation of correlation factors linking footing resistance on sand with cone penetration test results', *Computers and Geotechnics* **46**, 84–92.

Goh, A., Zhang, F., Zhang, W., Zhang, Y. & Liu, H. (2017), 'A simple estimation model for 3D braced excavation wall deflection', *Computers and Geotechnics* **83**, 106–113.

Hardin, B. & Drenvich, V. (1972), 'Shear modulus and damping in soils: design equations and curves', *Journal of the Soil Mechanics and Foundation Division* **98**(SM7), 667–692.

Hawlader, B., Lo, K. & Moore, I. (2006), 'Analysis of tunnels in shaly rock considering three-dimensional stress effects on swelling', *Canadian Geotechnical Journal* **42**(1), 1–12.

Heaney, C., Bonnier, P., Brinkgreve, R. & Hicks, M. (2013), An adaptive mesh refinement algorithm based on element subdivision with application to geomaterials, *in* J. M. de Almeida, P. Diez, C. Tiago & N. Pares, eds, 'VI International Conference on Adaptive Modeling and Simulation ADMOS'.

Holt, D. & Griffiths, D. (1992), 'Transient analysis of excavations in soil', *Computers and Geotechnics* **13**(3), 159–174.

Hölter, R., Mahmoudi, E. & Schanz, T. (2015), Optimal sensor location for parameter identification in soft clay, *in* 'Application of Mathematics in Technical and Natural Sciences, Albena, Bulgaria', p. 030005.

Hölter, R., Zhao, C., Mahmoudi, E., Lavasan, A. A., Datcheva, M., König, M. & Schanz, T. (2018), 'Optimal measurement design for parameter identification in mechanized tunneling', *Underground Space* .

Hölter, R., Zhao, C., Mahmoudi, E., Lavasan, A. & Schanz, T. (2017), Optimal measurement setup for parameter identification in 3d-tunnelling cases, *in* 'EURO:TUN 2017 - IV International Conference on Computational Methods in Tunneling and Subsurface Engineering', pp. 465–472.

Horn, N. (1961), 'Horizontaler Erddruck auf senkrechte Abschlussflächen von Tunnelröhren', *In Landeskonferenz der Ungarischen Tiefbauindustrie* pp. 7–16.

Hudoba, I. (1997), 'Contribution to static analysis of load-bearing concrete tunnel lining built by shield-driven technology', *Tunnelling and Underground Space Technology* **12**(1), 55–58.

Iott, J., Haftka, R. & Adelman, H. (1985), *Selecting step sizes in sensitivity analysis by finite differences, Volume 86382 of NASA technical memorandum*, National Aeronautics and Space Administration, Scientific and Technical Information Branch.

ITA (1988), 'Guidelines for the design of tunnels', *Tunnelling and underground space technology* **3**(3), 237–249.

ITA (2001), Recommendations and guidelines for tunnel boring machines, Technical report.

ITA (2009), General report on conventional tunneling method, Technical report.

Jacky, J. (1944), 'The coefficient of earth pressure at-rest', *Journal of Society of Hungarian Architects and Engineers* pp. 355–358.

Jacobsz, S., Standing, J., Mair, R., Hagiwara, T. & Sugiyama, T. (2004), 'Centrifuge modelling of tunnelling near driven piles', *Soils and Foundations* **44**(1), 49–56.

Jancsecz, S. & Steiner, W. (1994), Face support for a large mix-shield in heterogenous ground conditions, *in* 'Tunneling'94', Institution of Mining and Metallurgy.

Jansen, M. (1999), 'Analysis of variance designs for model output', *Computer Physics Communications* **117**, 35–43.

Journel, A. & Alabert, F. (1989), 'Non-Gaussian data expansion in the earth sciences', *Terra Nova* **1**(2), 123–134.

Kämper, C., Putke, T., Zhao, C., Lavasan, A., Barciaga, T., Mark, P. & Schanz, T. (2016), 'Vergleichsrechnungen zu Modellierungsvarianten für Tunnel mit Tübbingauskleidung', *Bautechnik* **93**(7), 421–432.

Kang, Y., Lin, X. & Qin, Q. (2004), 'Inverse/genetic method and its application in identification of mechanical parameters of interface in composite', *Composite Structures* **66**(1–4), 449–458.

Kasper, T. & Meschke, G. (2004), 'A 3D finite element simulation model for TBM tunneling in soft ground', *International Journal for Numerical and Analytical Methods in Geomechanics* **28**, 1441–1460.

Katzenbach, R. & Breth, H. (1981), Nonlinear 3D analysis for NATM in Frankfurt clay, *in* 'Proc. 10th Int. Conf. Soil Mechanics and Foundation Engineering', Vol. 1, pp. 315–318.

Kennedy, J. & Eberhart, R. (1995), Particle swarm optimization, *in* 'Proceedings of IEEE International Conference on Neural Networks', Vol. 4, pp. 1942–1948.

Khaledi, K., Mahmoudi, E., Datcheva, M., König, D. & Schanz, T. (2016), 'Sensitivity analysis and parameter identification of a time dependent constitutive model for rock salt', *Journal of Computational and Applied Mathematics* **293**(Supplement C), 128–138.

Khaledi, K., Mahmoudi, E., Datcheva, M. & Schanz, T. (2016), 'Stability and serviceability of underground energy storage caverns in rock salt subjected to mechanical cyclic loading', *International Journal of Rock Mechanics and Mining Sciences* **86**(Supplement C), 115–131.

Khaledi, K., Miro, S., Koenig, M. & Schanz, T. (2014), 'Robust and reliable metamodels for mechanized tunnel simulations', *Computers and Geotechnics* **61**, 1–12.

Kilchert, M. & Karstedt, J. (1984), 'Schlitzwände als Trag- und Dichtungwände, Band 2, Standsicherheitsberechnung von Schlitzwänden', *DIN* pp. 28–34.

Kim, H. & Eisenstein, Z. (2006), 'Prediction of tunnel lining loads using correction factors', *Engineering Geology* **85**(3-4), 302–312.

Kim, S. & Tonon, F. (2010), 'Face stability and required support pressure for TBM driven tunnels with ideal face membrane-Drained case', *Tunnelling and Underground Space Technology* **25**, 526–542.

Klappers, C., Grüebl, F. & Ostermeier, B. (2006), Structural analyses of segmental lining - coupled beam and spring analyses versus 3D-FEM calculations with shell elements, *in* 'Proceedings of the ITA-AITES 2006 World Tunnel Congress, Safety in the Underground Space'.

Knabe, T., Schweiger, H. & Schanz, T. (2012), 'Calibration of constitutive parameters by inverse analysis for a geotechnical boundary problem', *Canadian Geotechnical Journal* **49**(2), 170–183.

Krause, T. (1987), Schildvortrieb mit flüssigkeits- und erdgestützter Ortsbrust, PhD thesis, Technischen Universität Carolo-Wilhelmina, Braunschweig.

Lavasan, A. A., Talsaz, A., Ghazavi, M. & Schanz, T. (2016), 'Behavior of shallow strip footing on twin voids', *Geotechnical and Geological Engineering* pp. 1–15.

Lavasan, A. A., Zhao, C. & Schanz, T. (2018), 'Adaptive constitutive soil modeling concept in mechanized tunneling simulation', *International Journal of Geomechanics* .

Lavasan, A. & Schanz, T. (2017), Numerical investigation of hydro-mechanical interactions at the tail void of bored tunnels due to grouting, *in* '9th International Symposium on Geotechnical Aspects of Underground Construction in Soft Ground', Sao Paulo, Brazil.

Lavasan, A., Zhao, C., Barciaga, T., Schaufler, A., Steeb, H. & Schanz, T. (2018), 'Numerical investigation of tunneling in saturated soil: The role of construction and operation periods', *Acta Geotechnica* **13**(3), 671–691.

Leca, E. & Dormieux, L. (1990), 'Upper and lower bound solutions for the face stability of shallow circular tunnels in frictional material', *Géotechnique* **40(4)**, 581–606.

Lee, K. & Rowe, R. (1991), 'An analysis of three-dimensional ground movement: The thunder bay tunnel', *Canadian Geotechnical Journal* **28**, 25–41.

Li, Z., Chan, T., Yu, Y. & Sun, Z. (2009), 'Concurrent multi-scale modeling of civil infrastructures for analyses on structural deterioration Part I: Modeling methodology and strategy', *Finite Elements in Analysis and Design* **45**(11), 782–794.

Liu, B. (1992), 'Theory of stochastic medium and its application in surface subsidence due to excavation', *Transactions of Nonferrous Metals Society of China* **2**(3), 17–24.

Liu, Y., Stratman, B. . & Mahadevan, S. (2006), 'Fatigue crack initiation life prediction of railroad wheels', *International Journal of Fatigue* **28**, 747–756.

Mair, R. & Taylor, R. (1997), Bored tunnelling in the urban environment, *in* '14th International Conference on Soil Mechanics and Foundation Engineering', pp. 2353–2385.

Mair, R., Taylor, R. & Bracegirdle, A. (1993), 'Subsurface settlement profile above tunnels in clays', *Géotechnique* **43**(2), 315–320.

Mair, R., Taylor, R. & Burland, J. (1996), Prediction of ground movements and assessment of risk of building damage due to bored tunnelling, *in* 'Proceedings of the International Symposium on Geotechnical Aspects of Underground Construction in Soft Ground', pp. 713–718.

Marshall, A., Farrell, R., Klar, A. & Mair, R. (2012), 'Tunnels in sands: the effect of size, depth and volume loss on greenfield displacements', *Géotechnique* **62**(5), 385–399.

Mašín, D. (2009), '3D modeling of an NATM tunnel in high K_0 clay using two different constitutive models', *Journal of Geotechnical and Geoenvironmental Engineering* **135**(9), 1326–1335.

Masini, L., Rampello, S. & Soga, K. (2014), 'An approach to evaluate the efficiency of compensation grouting', *Journal of Geotechnical and Geoenvironmental Engineering* **140**(12), 04014073.

Meier, J., Datcheva, M. & Schanz, T. (2009), Identification of obstacles ahead of tunnel face applying inverse approach, *in* 'Proceedings of ECCOMAS Thematic Conference on Computational Methods in Tunneling', pp. 673–680.

Melis, M. & Ortiz, J. R. (2014), Consideration of the stiffness of buildings in the estimation of subsidence damage by EPB tunnelling in the madrid subway, *in* 'Response of Buildings to Excavation Induced Ground Movements Conference', London.

Meyerhof, G. G. (1953), 'Some recent foundation research and its application to design', *The Structural Engineer* **31**, 151–167.

Miro, S., Hartmann, D. & Schanz, T. (2014), 'Global sensitivity analysis for subsoil parameter estimation in mechanized tunneling', *Computers and Geotechnics* **56**, 80–88.

Mohkam, M. & Wong, Y. (1989), 'Three dimensional stability analysis of the tunnel face under fluid pressure', *In G. Swoboda, editor, Numerical Methods in Geomechanics* pp. 2271–2278.

Molenkamp, F. (1998), 'A simple model for isotropic non-linear elasticity of frictional materials', *International Journal for Numerical and Analytical Methods in Geomechanics* **12**, 467–475.

Molins, C. & Arnau, O. (2011), 'Experimental and analytical study of the structural response of segmental tunnel linings based on an in situ loading test.: Part 1: Test configuration and execution', *Tunnelling and Underground Space Technology* **26**(6), 764–777.

Möller, S. (2006), Tunnel induced settlements and structural forces in linings, PhD thesis, Universität Stuttgart, Germany.

Möller, S. & Vermeer, P. (2008), 'On numerical simulation of tunnel installation', *Tunnelling and Underground Space Technology* **23**, 461–475.

Mollon, G., Dias, D. & Soubra, A. (2011), 'Rotational failure mechanisms for the face stability analysis of tunnels driven by a pressurized shield', *Int. J. Numer. Anal. Meth. Geomech.* **35**(12), 1363–1388.

Mollon, G., Dias, D. & Soubra, A. (2013*a*), 'Continuous velocity fields for collapse and blowout of a pressurized tunnel face in purely cohesive soil', *Int. J. Numer. Anal. Meth. Geomech.* **37**(13), 2061–2083.

Mollon, G., Dias, D. & Soubra, A. (2013*b*), 'Probabilistic analyses of tunneling induced ground movements', *Acta Geotechnica* **8**, 181–199.

Morgan, H. (1961), 'A contribution to the analysis of stress in a circular tunnel', *Géotechnique* **11**(1), 37–46.

Mori, A., Tamura, M., Kurihara, K. & Shibata, H. (1991), A suitable slurry pressure in slurry-type shield tunneling, *in* 'In G.E. Pearse, editor, Tunneling'91, London', Institution of Mining and Metallurgy, pp. 361–369.

Müller-Kirchenbauer, H. (1977), 'Stability of slurry trenches in inhomogeneous subsoil', *In 9th International Conference on Soil Mechanics and Foundation Engineering* pp. 125–132.

Nagel, F. (2009), Numerical modelling of partially saturated soil and simulation of shield supported tunnel advance, PhD thesis, Ruhr-Universität Bochum.

Nanninga, N. (1970), Foundation engineering, Technical report, Delft University of Technology.

Ninić, J. & Meschke, G. (2017), 'Simulation based evaluation of time-variant loadings acting on tunnel linings during mechanized tunnel construction', *Engineering Structures* **135**, 21–40.

O'Reilly, M. & New, B. (1982), Settlements above tunnels in the United Kingdom-their magnitude and prediction, *in* 'Tunnelling '82. Jones, M.J. (Eds.)', pp. 173–181.

O'Reilly, M. & New, B. (2000), Prediction and performance: A review of numerical analyses for tunnels, *in* 'The Second International Symposium on Getotechnical Aspects of Underground Construction in Soft Ground', pp. 409–418.

Oreste, P. (2007), 'A numerical approach to the hyperstatic reaction method for the dimensioning of tunnel supports', *Tunnelling and Underground Space Technology* **22**(2), 185–205.

Pan, X. & Hudson, J. (1988), Simplified three-dimensional hoek-brown yield criterion, *in* 'Proceedings of the International Society of Rock Mechanics (ISRM) Symposium', pp. 95–103.

Park, K. (2005), 'Analytical solution for tunnelling-induced ground movements in clays', *Tunnelling and Underground Space Technology* **20**(3), 249–261.

Paternesi, A., Schubert, P. & Schweiger, H. (2016), 'Verification of a rheological constitutive model for shotcrete through back analysis', *Geomechanics and tunnelling = Geomechanik und Tunnelbau* pp. 356–361.

Peck, R. (1969), Deep excavations and tunneling in soft ground, *in* '7th International Conference on Soil Mechanics and Foundation Engineering', pp. 225–290.

Peila, D., Borio, L. & Pelizza, S. (2011), 'The behaviour of a two-component backfilling grout used in a Tunnel-Boring Machine', *Acta Geotechnica Slovenica* **1**, 5–15.

Peila, D., Chieregato, A., Martinelli, D., Salazar, C., Shah, R., Boscaro, A., Negro, E. & Picchio, A. (2015), 'Long term behavior of two component back-fill grout mix used in full face mechanized tunneling', *Geoingegneria Ambientale e Mineraria* **1**, 57–63.

Pickhaver, J. (2006), Numerical modelling of building response to tunnelling, PhD thesis, University of Oxford.

Pinto, F. & Whittle, A. (2013), 'Ground movements due to shallow tunnels in soft ground. I: Analytical solutions', *J. Geotech. Geoenviron. Eng.* **140**(4), 04013040.

Pinto, F., Zymnis, D. & Whittle, A. (2013), 'Ground movements due to shallow tunnels in soft ground. II: Analytical interpretation and prediction', *J. Geotech. Geoenviron. Eng.* **140**(4), 04013041.

Potts, D. (2008), 'Contributions to Géotechnique 1948-2008: Tunnelling', *Géotechnique* **58**(5), 391–398.

Potts, D. M. & Addenbrooke, T. I. (1997), A structure's influence on tunnelling-induced ground movements, *in* 'Proceedings of the Institution of Civil Engineers: Geotechnical Engineering 125(2)', Sao Paulo, Brazil, pp. 109–125.

Potts, D. & Zdravković, L. (1999), *Finite Element Analysis in Geotechnical Engineering: Theory*, Finite Element Analysis in Geotechnical Engineering, Thomas Telford.

Potts, D. & Zdravković, L. (2001), *Finite Element Analysis in Geotechnical Engineering: Application*, Finite Element Analysis in Geotechnical Engineering, Thomas Telford.

Renner, J. & Steeb, H. (2015), Modeling of fluid transport in geothermal research, *in* 'Handbook of Geomathematics, W. Freedom et al. (Eds.)', Springer Berlin Heidelberg, pp. 1443–1500.

Ritter, S., Giardina, G., DeJong, M. J. & Mair, R. J. (2017), 'Centrifuge modelling of building response to tunnel excavation', *International Journal of Physical Modelling in Geotechnics* pp. 1–16.

Rohmer, J. (2014), 'Dynamic sensitivity analysis of long-running landslide models through basis set expansion and meta-modelling', *Natural Hazards* **73**(1), 5–22.

Rott, J., Mašín, D., Boháč, J., Krupička, M. & Mohyla, T. (2015), 'Evaluation of K_0 in stiff clay by back-analysis of convergence measurements from unsupported cylindrical cavity', *Acta Geotechnica* **10**(6), 719–733.

Rowe, R., Lo, K. & Kack, G. (1983), 'A method of estimating surface settlement above tunnels constructed in soft ground', *Canadian Geotechnical Journal* **20**, 11–22.

Sagaseta, C. (1987), 'Analysis of undrained soil deformation due to ground loss', *Géotechnique* **37**(3), 301–320.

Sakurai, S. (1978), 'Approximate time-dpendent analysis of tunnel support structure considering progress of tunnel face', *International Journal for Numerical and Analytical Methods in Geomechanics* **1**, 159–175.

Saltelli, A., Ratto, M., Andres, T., Campolongo, F., Cariboni, J. & Gatelli, D. (2008), *Global sensitivity analysis. The Primer*, John Wiley and Sons.

Saurer, E., Marcher, T., Schädlich, B. & Schweiger, H. (2014), 'Validation of a novel constitutive model for shotcrete using data from an executed tunnel', *Geomechanics and tunnelling = Geomechanik und Tunnelbau* **7**(4), 353–361.

Schanz, T. (1998), Zur Modellierung des mechanischen Verhaltens von Reibungsmaterialien, Habilitationsschrift, Mitteilung 45 des Instituts für Geotechnik, Universität Stuttgart.

Schanz, T., Vermeer, P. & Bonnier, P. (1999), The hardening soil model: Formulation and verification, *in* 'Proceedings of 1st International PLAXIS Symposium on Beyond 2000 in Computational Geotechnics', Balkema, pp. 281–296.

Schaufler, A. (2015), Multi-physical simulations of transport and infiltration of a suspension in granular porous media, PhD thesis, Ruhr-Universität Bochum.

Schaufler, A., Becker, C. & Steeb, H. (2013*a*), 'Infiltration processes in cohesionless soils', *Journal of Applied Mathematics and Mechanics* **93**(2-3), 138–146.

Schaufler, A., Becker, C. & Steeb, H. (2013*b*), Simulation of the backfilling process with annular gap grouting mortar, *in* 'Third International Conference on Computational Methods in Tunneling and Subsurface Engineering', pp. 587–597.

Schaufler, A., Becker, C., Steeb, H. & Scheuermann, A. (2012), A continuum model for infiltration problems, *in* '6th International Conference on Scour and Erosion ICSE6 Paris', pp. 663–670.

Schenkendorf, R., Kremling, A. & Mangold, M. (2009), 'Optimal experimental design with the sigma point method', *IET System Biology* **3**(1), 10–23.

Schmid, H. (1926), *Statische Probleme des Tunnel- und Druckstollenbaus.*

Schofield, A. (1980), 'Cambridge geotechnical centrifuge operations', *Géotechnique* **30**(3), 227–268.

Schuerch, R. & Anagnostou, G. (2013*a*), Analysis of the stand-up time of the tunnel face, *in* 'World Tunnel Congress', Geneva, Switzerland, pp. 709–714.

Schuerch, R. & Anagnostou, G. (2013*b*), The influence of the shear strength of the ground on the stand-up time of the tunnel face, *in* 'Tunnelling and Underground Space Construction for Sustainable Development', CIR Publishing Co., pp. 297–300.

Schulze, H. & Duddeck, H. (1964), Statische Berechnung schildvorgetriebener Tunnel, *in* 'Festschrift: Beton- und Monierbau Aktien-Gesellschafte', pp. 1889–1964.

Schweiger, H. (2008), 'The role of advanced constitutive models in geotechnical engineering', *Geomechanik und Tunnelbau* **1**(5), 336–344.

Schweiger, H. (2014), Implementation, validation and application of the shotcrete model, Technical report, Graz University of Technology.

Schweiger, H., Marcher, T. & Schädlich, B. (2014), Application of a new shotcrete constitutive model to numerical analysis of tunnel excavation, *in* 'GeoShanghai 2014, ASCE-GSP 242', pp. 890–899.

Sert, S. & Kılıç, A. N. (2016), 'Numerical investigation of different superstructure loading type effects in mat foundations', *International Journal of Civil Engineering* **14**(3), 171–180.

Shah, R., Peila, D. & Lucarelli, A. (2016), Tunneling with full face shielded machines: a study on the backfilling of the tail void, *in* 'World Tunnel Congress 2016', pp. 1505–1514.

Shah, R., Zhao, C., Lavasan, A., Peila, D., Schanz, T. & Lucarelli, A. (2017), Influencing factors affecting the numerical simulation of the mechanized tunnel excavation using fem and fdm techniques, *in* 'EURO:TUN 2017 - IV International Conference on Computational Methods in Tunneling and Subsurface Engineering', pp. 483–490.

Shahin, H., Nakai, T., Ishii, K., Iwata, T. & Kuroi, S. (2016), 'Investigation of influence of tunneling on existing building and tunnel: model tests and numerical simulations', *Acta Geotechnica* **11**(3), 679–692.

Shanin, H., Nakai, T., Zhang, F., Kikumoto, M. & Nakahara, E. (2011), 'Behavior of ground and response of existing foundation due to tunneling', *Soils and Foundations* **51**(3), 395–409.

Shen, J., Jin, X., Li, Y. & Wang, J. (2009), 'Numerical simulation of cutterhead and soil interaction in slurry shield tunneling', *Engineering Computations: International Journal for Computer-Aided Engineering and Software* **26**(8), 985–1005.

Shi, Y. & Eberhart, R. (1998), A modified particle swarm optimizer, *in* 'Proceedings of IEEE Congress on Evolutionary Computation', pp. 69–73.

Shin, J., Potts, D. & Zdravković, L. (2002), 'Three-dimensional modelling of NATM tunnelling in decomposed granite soi', *Géotechnique* **52**(3), 187–200.

Shirlaw, J., Richards, D., Ramond, P. & Longchamp, P. (2004), Recent experience in automatic tail void grouting with soft ground tunnel boring machines, *in* 'ITA World Tunnel Congress 2004-Underground Space for Sustainable Urban Development'.

Sobol', I. (1993), 'Sensitivity estimates for nonlinear mathematical models', *Mathematical Modelling and Computational Experiment* **1**, 407–414.

Spickermann, A., Schanz, T. & Datcheva, M. (2005), Numerical modelling of primary stress states in deep seated slope problems, *in* '18th ABAQUS Users' Conference'.

Stack, B. (1982), *Handbook of mining and tunnelling machinery*, John Wiley and Sons.

Steeb, H. (2008), Non-Equilibrium Processes in Porous Media, Habilitationsschrift, Saarland University Saarbrücken.

Surarak, C. (2010), Geotechnical aspects of the Bangkok MRT blue line project, PhD thesis, Griffith University.

Surarak, C., Likitlersuang, S., Wanatowski, D., Balasubramaniam, A., Oh, E. & Guan, H. (2012), 'Stiffness and strength parameters for hardening soil model of soft and stiff Bangkok clays', *Soils and Foundations* **52**(4), 682–697.

Swoboda, G. & Abu-Krisha, A. (1999), 'Three-dimensional numerical modelling for TBM tunnelling in consolidated clay', *Tunnelling and Underground Space Technology* **14**(2), 327–333.

Talmon, A. & Bezuijen, A. (2009), 'Simulating the consolidation of TBM grout at Noordplaspolder', *Tunnelling and Underground Space Technology* **24**(5), 493–499.

Tan, W. & Ranjith, P. (2003), 'Parameters and considerations in soft ground tunneling', *The Electronic Journal of Geotechnical Engineering* **8**(D), 1–17.

Tang, D., Lee, K. & Ng, C. (2000), Stress paths around a 3D numerically simulated NATM tunnel in stiff clay, *in* 'Proc. Int. Symp. on Geotechnical Aspects of Underground Construction in Soft Ground', pp. 443–449.

Thewes, M. & Budach, C. (2009), Grouting of the annular gap in shield tunnelling-an important factor for minimisation of settlements and production performance, *in* 'ITA-AITES World Tunnel Congress 2009-Safe Tunnelling for the City and Environment'.

Timoshenko, S. (1955), *Strength of materials, 3rd ed.*, D. Van Nostrand Company, Inc,.

Ucinski, D. (2005), *Optimal Measurement Methods for Distributed Parameter System Identification*, CRC Press, Boca Raton.

Vakili, K., Barciaga, T., Lavasan, A. & Schanz, T. (2013), A practical approach to constitutive models for the analysis of geotechnical problems, *in* 'Proceedings of 3rd International Symposium on Computational Geomechanics (ComGeo III)', Poland, pp. 738–749.

Vakili, K., Lavasan, A., Datcheva, M. & Schanz, T. (2014), The influence of constitutive modeling in the numerical assessment of mechanized tunneling, *in* 'Proceedings of 8th European Conference on Numerical Methods in Geotechnical Engineering', Vol. 2, pp. 889–895.

Vermeer, P., Bonnier, P. & Möller, S. (2002), On a smart use of 3D-FEM in tunneling, *in* 'Proc. 8th Int. Symp. on Numerical Models in Geomech.', pp. 361–366.

Vermeer, P. & Brinkgreve, R. (1993), *PLAXIS Version 5 Manual*, Rotterdam, a. a. balkema edition.

Vermeer, P. & de Borst, R. (1984), 'Non-associated plasticity for soils, concrete and rock', *HERON* **29**(3).

Verruijt, A. & Booker, J. (1996), 'Surface settlements due to deformation of a tunnel in an elastic half plane', *Geótechnique* **46**(4), 753–756.

Verruijt, A. & Booker, J. (1997), 'A complex variable solution fora deformation circular tunnel in an elastic half-plane', *International Journal for Numerical and Analytical Methods in Geomechanics* **21**(2), 77–89.

Verruijt, A. & Strack, O. (2008), 'Buoyancy of tunnels in soft soils', *Géotechnique* **58**(6), 513–515.

Voellmy, A. (1937), Eingebettete Rohre, PhD thesis, ETH Zürich.

Vorster, T., Klar, A., Soga, K. & Mair, R. (2005), 'Estimating the effects of tunneling on existing pipelines', *Journal of Geotech. Geoenviron. Engng* **131**(11), 1399–1410.

Vu, M., Broere, W. & Bosch, J. (2017), 'Structural analysis for shallow tunnels in soft soils', *Int. J. Geomech.* pp. 04017038–1.

Wang, L., Li, L. & Lv, X. (2009), 'Complex variable solutions for tunneling-induced ground movement', *International Journal of Geomechanics* **9**(2), 63–72.

Windels, R. (1967), 'Kreisring im elastischen Kontinuum', *Der Bauingenieur* **42**, 429–439.

Wong, K., Ng, C., Chen, Y. & Bian, X. (2012), 'Centrifuge and numerical investigation of passive failure of tunnel face in sand', *Tunnelling and Underground Space Technology* **28**, 297–303.

Wood, A. M. (1975), 'The circular tunnel in elastic ground', *Geotechnique* **25**(1), 115–127.

Wood, A. M. (1976), 'Discussion: The circular tunnel in elastic ground', *Géotechnique* **26**(1), 231–237.

Wood, T. (2016), On the Small Strain Stiffness of Some Scandinavian Soft Clays and Impact on Deep Excavations, PhD thesis, Chalmers University of Technology.

Xue, J., Chen, J., Liu, J. & Shi, Z. (2014), 'Instability of a geogrid reinforced soil wall on thick soft Shanghai clay with prefabricated vertical drains: A case study', *Geotextiles and Geomembranes* **42**(4), 302–311.

Yang, J., Liu, B. & Wang, M. (2004), 'Modeling of tunneling-induced ground surface movements using stochastic medium theory', *Tunnelling and Underground Space Technology* **19**(2), 113–123.

Zhang, D., Huang, H., Hu, Q. & Jiang, F. (2015), 'Influence of multi-layered soil formation on shield tunnel lining behavior', *Tunnelling and Underground Space Technology* **47**, 123–135.

Zhao, C., Lavasan, A. A., Barciaga, T., Zarev, V., Datcheva, M. & Schanz, T. (2015), 'Model validation and calibration via back analysis for mechanized tunnel simulations-The Western Scheldt tunnel case', *Computers and Geotechnics* **69**, 601–614.

Zhao, C., Lavasan, A. A., Hölter, R. & Schanz, T. (2018), 'Mechanized tunneling induced building settlements and design of optimal monitoring strategies based on sensitivity field', *Computers and Geotechnics* **97**, 246–260.

Zhao, C., Lavasan, A., Barciaga, T., Hölter, R., Datcheva, M. & Schanz, T. (2014), Constitutive parameter adjustment for mechanized tunneling with reference to subsystem effects, *in* '8th International Conference on Numerical Methods and Applications', Borovets, Bulgaria, pp. 217–225.

Zhao, C., Lavasan, A., Barciaga, T., Kämper, C., Mark, P. & Schanz, T. (2017), 'Prediction of tunnel lining forces and deformations using analytical and numerical solutions', *Tunnelling and Underground Space Technology* **64**, 164–176.

Zhao, C., Lavasan, A. & Schanz, T. (2014), Sensitivity analysis of the model response in mechanized tunnelling simulation - A case study assessment, *in* 'Proceedings 4th International Conference on Engineering Optimization', Lisbon, Portugal, pp. 491–496.

Zhao, C., Lavasan, A. & Schanz, T. (2018), 'Application of submodeling technique in numerical modeling of mechanized tunnel excavation', *International Journal of Civil Engineering* .

Zienkiewicz, O., Chan, A., Pastor, M., Schrefler, B. & Shiomi, T. (1999), *Computational Geomechanics with Special Reference to Earthquake Engineering*, Wiley.

Zienkiewicz, O. & Humpheson, C. (1977), Viscoplasticity: a generalized mode for description of soil behaviour, *in* 'Numerical methods in geotechnical engineering', McGraw-Hill, pp. 116–147.

Zienkiewicz, O., Owen, D. & Cormeau, I. (1974), 'Analysis of viscoplastic effects in pressure vessels by the finite element method', *Nuclear Engineering and Design* **28**, 278–288.

ZTV (2012), Teil 5, Tunnelbau, *in* 'Zusätzliche Technische Vertragsbedingungen und Richtlinien für Ingenieurbauten', Bundesanstalt für Strassenwesen.

Schriftenreihe des Lehrstuhls für Grundbau, Boden- und Felsmechanik der Ruhr-Universität Bochum

Herausgeber: H.L. Jessberger

1 (1979) **Hans Ludwig Jessberger**
Grundbau und Bodenmechanik an der Ruhr-Universität Bochum

2 (1978) **Joachim Klein**
Nichtlineares Kriechen von künstlich gefrorenem Emschermergel

3 (1979) **Heinz-Joachim Gödecke**
Die Dynamische Intensivverdichtung wenig wasserdurchlässiger Böden

4 (1979) **Poul V. Lade**
Three Dimensional Stress-Strain Behaviour and Modeling of Soils

5 (1979) **Roland Pusch**
Creep of soils

6 (1979) **Norbert Diekmann**
Zeitabhängiges, nichtlineares Spannungs-Verformungsverhalten von gefrorenem Schluff unter triaxialer Belastung

7 (1979) **Rudolf Dörr**
Zeitabhängiges Setzungsverhalten von Gründungen in Schnee, Firn und Eis der Antarktis am Beispiel der deutschen Georg-von-Neumayer- und Filchner-Station

8 (1984) **Ulrich Güttler**
Beurteilung des Steifigkeits- und Nachverdichtungsverhaltens von ungebundenen Mineralstoffen

9 (1986) **Peter Jordan**
Einfluss der Belastungsfrequenz und der partiellen Entwässerungs-möglichkeiten auf die Verflüssigung von Feinsand

10 (1986) **Eugen Makowski**
Modellierung der künstlichen Bodenvereisung im grundwasserdurchströmten Untergrund mit der Methode der finiten Elemente

11 (1986) **Reinhard A. Beine**
Verdichtungswirkung der Fallmasse auf Lastausbreitung in nichtbindigem Boden bei der Dynamischen Intensivverdichtung

12 (1986) **Wolfgang Ebel**
Einfluss des Spannungspfades auf das Spannungs-Verformungsverhalten von gefrorenem Schluff im Hinblick auf die Berechnung von Gefrierschächten

13 (1987) **Uwe Stoffers**
Berechnungen und Zentrifugen-Modellversuche zur Verformungsabhängigkeit der Ausbaubeanspruchung von Tunnelausbauten in Lockergestein

14 (1988) **Gerhard Thiel**
Steifigkeit und Dämpfung von wassergesättigtem Feinsand unter Erdbebenbelastung

15 (1991) **Mahmud Thaher**
Tragverhalten von Pfahl-Platten-Gründungen im bindigen Baugrund,
Berechnungsmodelle und Zentrifugen-Modellversuche

16 (1992) **Rainer Scherbeck**
Geotechnisches Verhalten mineralischer Deponieabdichtungsschichten
bei ungleichförmiger Verformungswirkung

17 (1992) **Martin M. Bizialiele**
Torsional Cyclic Loading Response of a Single Pile in Sand

18 (1993) **Michael Kotthaus**
Zum Tragverhalten von horizontal belasteten Pfahlreihen aus langen Pfählen in Sand

19 (1993) **Ulrich Mann**
Stofftransport durch mineralische Deponieabdichtungen:
Versuchsmethodik und Berechnungsverfahren

20 (1992) **Festschrift anlässlich des 60. Geburtstages von**
Prof. Dr.-Ing. H. L. Jessberger
20 Jahre Grundbau und Bodenmechanik an der Ruhr-Universität Bochum

21 (1993) **Stephan Demmert**
Analyse des Emissionsverhaltens einer Kombinationsabdichtung im Rahmen der
Risikobetrachtung von Abfalldeponien

22 (1994) **Diethard König**
Beanspruchung von Tunnel- und Schachtausbauten in kohäsionslosem Lockergestein
unter Berücksichtigung der Verformung im Boden

23 (1995) **Thomas Neteler**
Bewertungsmodell für die nutzungsbezogene Auswahl von Verfahren zur Altlastensanierung

24 (1995) **Ralph Kockel**
Scherfestigkeit von Mischabfall im Hinblick auf die Standsicherheit von Deponien

25 (1996) **Jan Laue**
Zur Setzung von Flachfundamenten auf Sand unter wiederholten Lastereignissen

26 (1996) **Gunnar Heibrock**
Zur Rissbildung durch Austrocknung in mineralischen Abdichtungsschichten
an der Basis von Deponien

27 (1996) **Thomas Siemer**
Zentrifugen-Modellversuche zur dynamischen Wechselwirkung zwischen Bauwerken
und Baugrund infolge stoßartiger Belastung

28 (1996) **Viswanadham V. S. Bhamidipati**
Geosynthetic Reinforced Mineral Sealing Layers of Landfills

29 (1997) **Frank Trappmann**
Abschätzung von technischem Risiko und Energiebedarf bei Sanierungsmaßnahmen
für Altlasten

30 (1997) **André Schürmann**
Zum Erddruck auf unverankerte flexible Verbauwände

31 (1997) **Jessberger, H. L. (Herausgeber)**
Environment Geotechnics, Report of ISSMGE Technical Committee TC 5
on Environmental Geotechnics

Herausgeber: Th. Triantafyllidis

32 (2000) **Triantafyllidis, Th. (Herausgeber)**
Boden unter fast zyklischer Belastung: Erfahrung und Forschungsergebnisse (Workshop)

33 (2002) **Christof Gehle**
Bruch- und Scherverhalten von Gesteinstrennflächen mit dazwischenliegenden Materialbrücken

34 (2003) **Andrzej Niemunis**
Extended hypoplastic models for soils

35 (2004) **Christiane Hof**
Über das Verpressankertragverhalten unter kalklösendem Kohlensäureangriff

36 (2004) **René Schäfer**
Einfluss der Herstellungsmethode auf das Verformungsverhalten von Schlitzwänden in weichen bindigen Böden

37 (2005) **Henning Wolf**
Zur Scherfugenbänderung granularer Materialien unter Extensionsbeanspruchung

38 (2005) **Torsten Wichtmann**
Explicit accumulation model for non-cohesive soils under cyclic loading

39 (2008) **Christoph M. Loreck**
Die Entwicklung des Frischbetondruckes bei der Herstellung von Schlitzwänden

40 (2008) **Igor Arsic**
Über die Bettung von Rohrleitungen in Flüssigböden

41 (2009) **Anna Arwanitaki**
Über das Kontaktverhalten zwischen einer Zweiphasenschlitzwand und nichtbindigen Böden

Herausgeber: T. Schanz

42 (2009) **Yvonne Lins**
Hydro-Mechanical Properties of Partially Saturated Sand

43 (2010) **Tom Schanz (Herausgeber)**
Geotechnische Herausforderungen beim Umbau des Emscher-Systems
Beiträge zum RuhrGeo Tag 2010

44 (2010) **Jamal Alabdullah**
Testing Unsaturated Soil for Plane Strain Conditions: A New Double-Wall Biaxial Device

45 (2011) **Lars Röchter**
Systeme paralleler Scherbänder unter Extension im ebenen Verformungszustand

46 (2011) **Yasir Al-Badran**
Volumetric Yielding Behavior of Unsaturated Fine-Grained Soils

47 (2011) **Usque ad finem**
Selected research papers

48 (2012) **Muhammad Ibrar Khan**
Hydraulic Conductivity of Moderate and Highly Dense Expansive Clays

49 (2014) **Long Nguyen-Tuan**
Coupled Thermo-Hydro-Mechanical Analysis: Experimental and Back Analysis

50 (2014) **Tom Schanz (Herausgeber)**
Ende des Steinkohlenbergbaus im Ruhrrevier: Realitäa und Perspektiven für die Geotechnik Beiträge zum RuhrGeo Tag 2014

51 (2014) **Usque ad finem**
Selected research papers

52 (2014) **Houman Soleimani Fard**
Study on the Hydro-Mechanical Behaviour of Fiber Reinforced Fine Grained Soils with Application to the Preservation of Historical Monuments

53 (2014) **Wiebke Baille**
Hydro-Mechanical Behavior of Clays - Significance of Mineralogy

54 (2014) **Qasim Abdulkarem Jassim Al-Obaidi**
Hydro-Mechanical Behavior of Collapsible Soils

55 (2015) **Veselin Zarev**
Model Identification for the Adaption of Numerical Simulation Models - Application to Mechanized Shield Tunneling

56 (2015) **Meisam Goudarzy**
Micro and Macro Mechanical Assessment of Small and Intermediate Strain Properties of Granular Material

57 (2016) **Oliver Detert**
Analyse einer selbstregulierenden interaktiven Membrangründung für Schüttkörper auf geringtragfähigen Böden

58 (2016) **Yang Yang**
Analyses of Heat Transfer and Temperature-induced Behaviour in Geotechnics

59 (2016) **Alborz Pourzargar**
Application of suction stress concept to partially saturated compacted soils

60 (2017) **Hanna Haase**
Multiscale analysis of clay-polymer composites for Geoenvironmental applications

61 (2017) **Kavan Khaledi**
Constitutive modeling of rock salt with application to energy storage caverns

62 (2017) **Nina Silvia Müthing**
On the consolidation behavior of fine-grained soils under cyclic loading

63 (2017) **Elham Mahmoudi**
Probabilistic analysis of a rock salt cavern with application to energy storage systems

64 (2017) **Negar Rahemi**
Evaluation of liquefaction behavior of sandy soils using critical state soil mechanics and instability concept

65 (2018) **Chenyang Zhao**
A contribution to modeling of mechanized tunnel excavation